Honda R&D

Technical Review



2025

Vol.37



Comment on the Cover

The second-generation fuel cell system is a symbol of efficiency and sustainability, and is represented here by soft, swirling loops that evoke the flow of energy. The layers of fine, curving lines of the loops are inspired by the beautiful layers of cells that form stacks. The smooth blending of color gradients combines lightness and strength, and evokes the harmony of advanced technology and feelings of optimism for the future.

I hope that when you see this image, you will get a sense of the beautiful possibilities inherent in the second-generation fuel cell system, its stack, and its associated technologies.



Design Center
Maki FUNAMOTO

Technical Review

2025

Honda R&D

CONTENTS

Contribution

Working Toward Introducing Reliability Design . . . . . Shinsuke Sakai 1

Special Edition for Fuel Cell

Development of New Fuel Cell System . . . . . .Hiroyasu OZAKI, Kaoru YAMAZAKI, Takayuki OGAWA
. . . . . .Shuto MANIWA, Taneaki MIURA, Todd W. HUSTON 13

High-durability and Cost-effective Fuel Cell Stack with New Structure
. . . . . Choichi ISHIKAWA, Manabu IWAIDA, Hideharu NAITO
Shigeru INAI, Hiromichi YOSHIDA, Nobuyoshi MUROMOTO 20

Development of High-durability and Low-cost UEA for Fuel Cell Stack
. . . . . .Takashi KATO, Akira NAKAHARA, Takuya OHKURA
Masakuni YAMAMOTO, Satoru TERADA, Akihiro NODA, Nagayuki KANAOKA 27

Development of High-durability and Low-cost Fuel Cell Bipolar Plate
. . . . . Kazuo NUNOKAWA, Hiroshi SHINKAI, Satoshi OYAMA
Kentaro ISHIDA, Shuhei GOTO 34

High-speed Inspection Technology for Fuel Cell MEAs Using Split-terminal Resistance Measurement System
. . . . . .Hiroaki KAWANISHI, Hiroyuki YAMAGISHI, Kensuke NANBA 41

Development of Hydrogen Ventilation Structure for Fuel Cell Systems . . . . . Sena TAKEKOSHI 49

Construction of One-dimensional Humidifier Model in Fuel Cell System
. . . . . .Shuto MANIWA, Yohei HIDAKA
Koichi KIMURA, Nobuki KOIWA 56

Application of Acoustic Emission Technology to Damage Analysis of High-Pressure Container for Fuel Cell Vehicles
. . . . . Takanori SUZUKI, Takashi KUWAYAMA, Masamichi KAWABE
Ichiro HARADA, Toshihiko KANEZAKI 66

Introduction / Case Study

Development of Power Exporter e: 6000, External Power Output Device, with Three-phase 200 V AC Output Function
. . . . . Yuuna YAHAGI, Tomoyuki KOZU, Takuya ODAKA
. . . . . Kenta YAGASAKI, Takahiro FUKUI, Kosuke IHARA 72

Technical Paper

Enhancement of Feeling in Turn Focusing on Pitching Behavior . . . . . Naoto OHKUBO 80

γ' Precipitation-hardened Cobalt-free Heat-resistant Steel Strip for Exhaust Gaskets Work at 900℃
. . . . . Hiroki YAMAMOTO, Isamu SAITO
Yoshiki KUMAGAI, Yoshinori SUMI 87

Evaluation of Anodized Aluminum Corrosion Resistance by Constant Current Anodic Polarization Test
. . . . . Hideaki MIYASHITA, Kohei TOMITA
Yuki YAMAGUCHI, Takahiro KUWABARA 95

Automated Test Scheduling Using Vehicle Routing Problem Methodology
. . . . . Atsushi ARISAKA, Takeshi MIYAZAKI, Kazuki FUKUI 101

Working Toward Introducing Reliability Design

Shinsuke Sakai, Ph.D.*

1. Introduction

My main activities so far have been primarily in fields related to pressure vessels and piping, with very little crossover into the automotive industry. Recently, I participated in a NEDO project[1] related to on-vehicle hydrogen tanks for automobiles, which gave me the opportunity to learn about this type of activity. This exposure to activities in fields that I'd had little experience in beforehand helped me to become aware of issues and complications in this field. I feel that reliability design is a subject that cannot be avoided when it comes to considering the development of this field in Japan. Therefore, I have decided to summarize this topic in this paper.

The "Reliability Design" mentioned in the title is the key phrase here. I'd imagine that few people have considered the design of hydrogen tanks from the perspective of reliability design in the past. However, G.W. Mair from BAM in Germany has really emphasized the importance of introducing the concept of "reliability design" for pressure tanks such as hydrogen tanks[2].

In the past, safety in terms of standards in the machinery field has often been secured through the safety factor. In the mechanical engineering field, there are opportunities to learn about the safety factor through lectures on the core academic field of "Material Mechanics." The definition of the safety factor as written in the textbook[3] on material mechanics that I studied at the time was "Allowable Stress = Material Strength/Safety Factor," and I was taught that the safety factor is determined empirically. Safety factors based on this concept are called empirical safety factors or deterministic safety factors. While not all of the safety factors listed in today's standards in the machinery field may be determined empirically, it seems that the basic concept has not changed greatly since then. Design using safety factors is extremely simple and can be said to be a convenient method for both designers and regulators.

If the impact from the damage to a mechanical structure is not large, it is considered reasonable to perform safety management by using a simple deterministic safety factor like this. On the other hand, since enhancement in the performance of mechanical products has been sought after in recent years, there are limits on performing safety management with just a deterministic safety factor. For example, damage in the event of an accident may become more severe when enhancement in performance is pursued. The concept of risk-based design, or reliability design, is important for rational design in these situations.

In this paper, I shall provide an outline on trends in related standards, applicable examples, current issues, and more, starting with introductory content so that even readers unfamiliar with reliability engineering will be able to understand. In addition, since the English expression for "Safety Factor" is "Safety Factor," it should really be called "Safety Coefficient," but since the term "Safety Factor" is also widely used, I've decided to use both terms in this paper without differentiating between them.

2. Tolerance Method Complications

The definition for allowable stress that I learned from lectures on material mechanics when I was a student was given as follows[3].

$$\text{Allowable stress} = \frac{\text{Standard strength}}{\text{Safety factor}} \qquad (1)$$

Safety is confirmed by evaluating stress in mechanical evaluation and confirming that the maximum stress does not exceed allowable stress. It was stated that the method for determining the safety factor is based on past experience. This concept of safety design is extremely simple, and the fact that it's easy for regulators to confirm safety can be said to be an advantage. If it's a simple mechanical structure, it's not practical to expend a great deal of effort on designing it, and it's thought that there is a rationality in adopting this level of design method.

However, various shortcomings may be exposed in safety factors determined empirically when the basis is not clear. Let's look at a few examples of this.

1. The size of the safety margin cannot be clearly stated since it's not clear which damage mode it's being designed for.
2. Even if attempts are made to rationalize the safety margin, it's challenging to provide an explanation linked to the basis.
3. The designer will not understand the incentive behind creating a better design if the basis for the safety factor is unclear.
4. The safety factor tends to be overestimated in methods for explaining safety using the safety factor, and it's not easy to lower the safety factor once it has been determined.

* Visiting professor, Yokohama National University

Table 1 Historical background on Sec. VIII safety factor reduction

Year	Details
1915	Code for power boiler, 1st ed.
1925	Sec. VIII, 1925 ed. Tensile strength safety factor set to 5.
1942/43	Safety factor reduced from 5 to 4 based on national request to secure strategic supplies (materials).
1998	Increase in requests to reduce the safety factor from 4 to 3.5, based on enhanced material performance and enhancement of standard specifics over past 50 years.

A high degree of safety is required in particular in cases like those where hydrogen tanks are installed in fuel cell vehicles, so it's thought that complications like these will become more prominent. Even now, it's thought that the safety factor in material mechanics is taught using nearly the same content. In addition, it's thought that the fundamentals of Japanese safety standards are based on the empirical safety factor. While a lot of mechanical structures may be realized through methods based on this type of tolerance method, rational safety margins should be optimized in the future in order to bring out top performance in mechanical products. It will be extremely important in these cases to introduce reliability design rather than the empirical safety factor.

One aspect of the safety factor can be understood by looking at the historical background of the values of the safety factor in the field of pressure vessels and piping, a field in which I've been deeply involved. Japan's design standards for pressure vessels refer to the standard of the American Society of Mechanical Engineers (ASME), the Boiler and Pressure Vessel Code. The design standards for pressure vessels in particular are specified in Section VIII, but around 1998, a dramatic change was made to reduce the safety factor for the tensile strength of material from 4 to 3.5. Looking at the literature[4] that summarizes the basis for this provides a glimpse of a cross section of the characteristics of the safety factor. Table 1 summarizes the historical background on safety factor reduction based on the literature.

In 1915, boilers were in widespread use in the United States. In modern times, one rarely hears anything about large boiler accidents, but at that time, accidents involving fatalities were practically a daily occurrence in the U.S. Standardization for design standards was not in place at that time, and the need to do so in order to enhance the situation was recognized. This resulted in an opportunity that led to the publication of the first edition of the ASME standards. Sec. VIII, the standards for pressure vessels including boilers, was published in 1925, and the safety factor for the tensile strength of pressure vessels in use at that time appears to have been set at 5. There is no clear basis for this value, and it's assumed that it was set based on experience and opinions of people close to the project. Boiler-related accidents declined thanks to the standardization of boiler standards, and large boiler-related accidents caused by issues at the time of design were successfully avoided for the most part thanks to the standards being revised further as time went on. However, the safety factor that had been established continued to be used without any changes in its value. This value was first reduced during World War II in 1942/1943. This was done based on a national request for the procurement of strategic supplies rather than for engineering reasons. As a result, the safety factor was reduced from 5 to 4, but this also made it possible to reduce the thickness of pressure vessels, allowing them to be utilized as strategic supplies. In other words, it was reduced through pressure in conjunction with a national request for reasons completely unrelated to engineering, demonstrating how ambiguous the safety factor value was. However, reducing the safety factor to 4 did not result in an increase in boiler-related accidents, and it remained unchanged for the next 50 years. However, if both material performance and the level of technical management increase and are reflected in the standards, accidents related to the design standards would no longer occur, and the industry would likely demand further reductions in the safety factor. In 1998, the safety factor was reduced from 4 to 3.5 based on a technical report[4] published by the WRC. Along with verifying increases in the level of technical management in detail, increases in material performance were also verified through this report, but it does not appear that the basis for setting the safety factor value to 3.5 was clearly stated. Optimizing the safety factor based on experience like this is generally applicable for mechanical products as well and could be called a widespread concept in the machinery field.

There are no complications with the tolerance methods themselves, which are based on the empirical safety factor. It's important to use them appropriately to address the complications for which these methods are applied, and complications will be exposed if they are not used appropriately. In fact, it's considered that there have been no major complications with most of the mechanical products made by design standards based on the empirical safety factor in the past. It's clearly not efficient to exert a great deal of effort to make a strict design even for design for normal use range, and in this case, the application of the tolerance method could be called appropriate. However, challenges accompany this when addressing things through the empirical safety factor when there's a desire to operate under extreme conditions to bring out the performance of a mechanical product, or when it's necessary to help

ensure high reliability in light of the severity of an accident. It's desirable to clarify the limit state for exhibiting the performance of a mechanical product and to design it with the distance between operating conditions and the limit state (in other words, the safety margin) as the management target. This is precisely the concept of reliability design. It's important to use the tolerance method and reliability design appropriately depending on the application in question.

3. Definition of Reliability Design

3.1. Concept of Reliability Design

The words of the Russian playwright Anton Chekhov (1860–1904) are quoted at the beginning of G.W. Mair's book, and I referred to these in the process of learning about trends in the stochastic treatment of on-board hydrogen tanks.

> There is no certainty(safety),
> only different degrees of uncertainty(danger).
> Anton Pawlowitsch Tschechow (1860–1904)

Along with symbolizing the essence of books, these words also express the essence of reliability design. My personal interpretation would be, "There is no such thing as safety (as defined by the tolerance method), only different degrees of danger." The method for evaluating this degree of danger is reliability engineering, and the method for designing according to these results is reliability design.

In Fig. 1, Chekhov's words have been visualized as an engineering conceptual diagram. The upper half shows the tolerance method, or deterministic method, widely used in the traditional mechanical engineering field. In this method, tolerance is set based on the empirical safety factor. It's judged to be dangerous if stress rises even a little bit above the tolerance and safe if it falls even a bit below the tolerance. In other words, the judgment is either/or. On the other hand, the lower half of the figure shows the conceptual diagram for the stochastic method used in reliability design. There's a wide gray zone between safety and danger; therefore, it's not an either/or judgment. This gray zone is the area expressed by the "different degrees of uncertainty (danger)" in Chekhov's words. When it is in this area, decisions are made based on evaluations without judging whether it's safe or dangerous. If it approaches danger, it's necessary to make an effort to shift it even a little bit toward safety, but usage is permitted once that effort has been made. Accordingly, as it should be clear from the comparison with the tolerance method, the usable range is expanded based on the premise of performing evaluation. Representative examples of evaluations are reliability evaluation and risk evaluation. Design based on reliability evaluation is called "reliability-based design," and design based on risk evaluation is called "risk-based design."

Figure 2 shows a conceptual diagram for decision-making in risk-based engineering that corresponds to Fig. 1. The horizontal length of the inverted triangle shown in the center indicates the size of the risk being evaluated. In other words, the top end shows where risk is the largest, and the bottom end shows where there is zero risk. To clarify the contrast between the risk method and tolerance method, the risk method is shown to the left of the triangle, and the tolerance method is shown to the right. In the case of the risk method, judgment for decision-making is divided into the three areas formed by the black lines. The uppermost area is where the risk value is excessive and unacceptable, while the lowermost area is the area where the risk value is sufficiently small and widely acceptable. The intermediate area is tolerable and acceptable, but it's necessary to make an effort to reduce the risk as long as it remains in this area. The risk values that divide these three areas are set as appropriate depending on the equipment subject to evaluation and the usage environment. This concept is called "As Low As Reasonably Practicable (ALARP)" and is a concept proposed by the British Health and Safety Executive (HSE). This concept is one widely used as a method for making risk-based engineering decisions. This intermediate area corresponds to the gray zone in the bottom row of Fig. 1 and is also called the ALARP area.

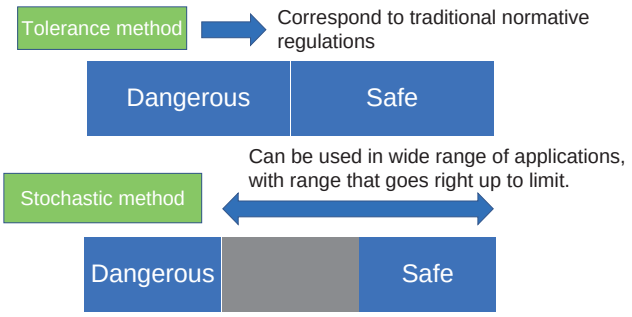


Fig. 1 Differences between stochastic design method and allowable stress method

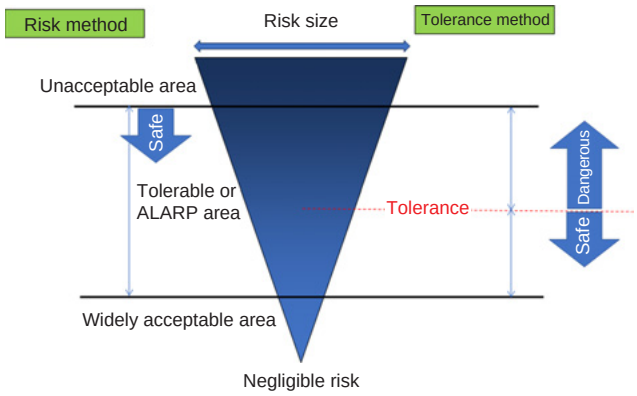


Fig. 2 Concept of decision-making for risk-based engineering

Based on recognizing that there's risk associated with most machines, efforts to reduce risk are required for machines included in the ALARP area. According to the definition from ISO Guide 73, areas below the ALARP area are judged to be safe. On the other hand, in the case of the tolerance method on the right side, judgment on whether it's safe or dangerous is performed by either/or when it's beyond a certain tolerance. In these cases, compared to the risk method, the area that is treated as safe is narrower, but various complications arise in conjunction with this. First of all, if it's judged to be "safe," it's natural that there will be less awareness for shifting to the safer side in response to that result, and there may be no effort to do so at all in some cases. On the other hand, under the risk method, effort to reduce risk is required as long as it is within the ALARP area. Next, if it's judged to be "dangerous" under the tolerance method, then it will never be accepted no matter how much effort is put forth. Under the risk method, if something is within the ALARP area, it will be accepted by reducing the risk. In other words, designers are rewarded for their efforts. However, in the case of the risk method, risk evaluation is required for decision-making in contrast to the tolerance method, and there's no denying that a lot of effort and labor are necessary.

The concept of reliability design will be explained using a simple RS model in which the only design variables are strength (R) and load (S). If R and S vary, the contour lines of the probability density function on the RS plane will be concentric ellipses, as shown in Fig. 3. The position of the vertex of the probability density function corresponds to the mean value of two random variables. What's important in reliability design is to quantitatively show how much of a safety margin there is rather than to judge safety in terms of black or white. To do this, it's necessary to clearly indicate the damaged area in Fig. 3 and to investigate its relative relationship with the state of distribution for RS. The limit state function $g(R, S)$ is defined for this reason. An area where this function is negative indicates damage, and one where it's positive indicates that it is undamaged.

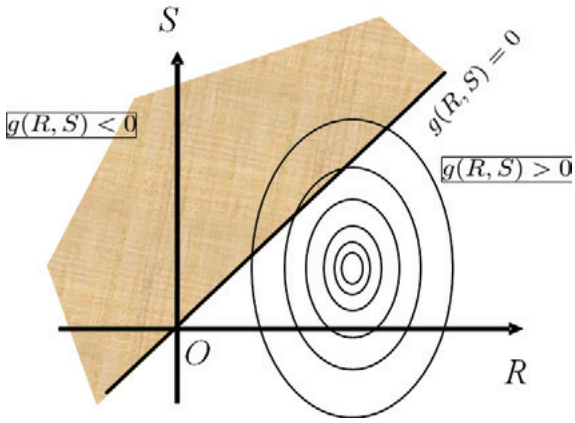


Fig. 3 Reliability design concept explanatory diagram

The boundary line where this is 0 is called the "limit state curve." In other words, it's defined by Eq. (2).

$$g(R, S) = R - S \tag{2}$$

The part indicated with brown hatching area in the figure is the damaged area, and how easily damage may occur can be found by examining how far the limit state curve that is the boundary line for the damage is from the position of the mean value of R and S. The Advanced First Order Second Moment Method (AFOSM) is a method to quantitatively derive the safety margin from the limit state function and the statistical properties of each design variable.

The method of evaluating reliability based on the limit state function in this fashion is called the "limit state function method," and it would be good to briefly explain the significance of this method. As shown in Fig. 3, processing is simple when the only design variables are strength (R) and load (S), but this alone is not sufficient when aiming for a higher degree of design. The first complication is that the design variables that should be considered may include a variety of other variables aside from strength and load, such as dimensions, surface roughness, thickness reduction rate, internal pressure, weight, stress, and displacement. In this case, a general reliability evaluation method for multiple variables is required. The second complication is that the definition of limit state is that there can be many different ones, depending on the interest of the evaluator. In the case of Fig. 3, the physical limits of the damage are defined as the limit state, but in addition to this, some evaluators may be interested in the margin for the standard limit values. In addition, when there are multiple damage modes, it becomes necessary to set a limit state for each different damage mode. The limit state function method is a method that can be used to respond flexibly to these complications. In the limit state function method, limit state function $g()$ is defined as follows.

$$\begin{aligned} Z_i = g_i(X_1, X_2, \cdots, X_n) > 0 &\Rightarrow \text{Damage Mode } i \text{ does not occur} \\ \leq 0 &\Rightarrow \text{Damage Mode } i \text{ occurs} \end{aligned} \tag{3}$$

There's no limit to the number of design variables (X_1, X_2, $\cdots$, X_n), and Damage Mode i may be defined according to the designer's interests. An example of setting the limit state function is shown below.

$$\begin{aligned} &\text{When interested in maximum stress: } g = \sigma_{limit} - \sigma_{max} \\ &\text{When interested in maximum displacement: } g = \delta_{limit} - \delta_{max} \\ &\text{When interested in standard limit pressure: } g = p_{code} - p_{working} \end{aligned} \tag{4}$$

In this way, the limit state function method is a versatile, efficient reliability evaluation method, but its handling method is complicated, and there is an issue that it's challenging for general designers to understand. For example, if there are two design variables, as shown in Fig. 3, drawing can be done in two-dimensional space and is easy to understand intuitively. However, when there are three variables, it shifts to three-dimensional space, as

shown in Fig. 4, and if the function shape is complex, the limit state surface will be complicatedly curved, making it challenging to understand intuitively. If the number of variables increases beyond this, then it would need to be handled in a multidimensional space, making it even more complex. However, although strict handling of reliability evaluations like this may be necessary at the researcher level, designers and standards users do not necessarily need to master these techniques. For example, for the Partial Safety Factor Method, which incorporates reliability design into standards, reliability design is achieved by simple evaluation through simple calculations using a partial safety factor table prepared in advance based on reliability theory. The specifics of this will be explained in the next chapter. Therefore, familiarity with all aspects of reliability theory is not necessary to practice reliability design in the industry, there are cases where individuals would like to learn the fundamental theory behind it, so reference materials have been listed in the literature[5][6][7].

3.2. Partial Safety Factor Method Definition

The cutting edge of reliability engineering is performing strict evaluations after defining the limit state function indicated by Eq. (3), but in addition to specialized knowledge, designers also need a lot of effort and time to program and perform these evaluations for each design. To address this complication, a partial safety factor table is placed in the standard, allowing for simple reliability design to be achieved by a simple evaluation through simple calculations. The conceptual treatment is described below.

If X_1, X_2, ⋯, X_n are random variables, then variable Z evaluated through Eq. (3) is also a random variable. If the probability density function of Z is as shown in Fig. 5, then $Z = 0$ is the limit state and the area where $Z < 0$ is the damaged area, so the area of the blue part in the figure is damage probability (P_f). Various quantitative evaluations may be performed using P_f, but generally, it will be an extremely small value like 10^{-6}. Therefore, the reliability index (β) is often used. In Fig. 5, the distance between the mean value of Z (μ_Z) and limit state $Z = 0$ is an index for the safety margin. The standardized value derived from dividing this distance by the standard deviation of Z (σ_Z) is called the reliability index. β is often used as the symbol for the reliability index. During normal distribution of the random variables of design variables, the distribution of Z is often close to normal distribution as well, the following approximation relationship forms between P_f and β, and there is a one-to-one correspondence relationship.

$$P_f = \Phi(-\beta) \tag{5}$$

Here, $\Phi()$ is the standard normal cumulative distribution function. For example, in the field of architecture, values of β = 2, 3, etc. are set as reliability to be targeted (target reliability), and the partial safety factor table corresponding to them is provided in the standard. For example, for target reliability β_0, if partial safety factors α_1, α_2, ⋯, α_n for X_1, X_2, ⋯, X_n are prepared in advance by a reliability expert, then checking whether the design values X_1, X_2, ⋯, X_n set by a designer satisfy target reliability β is performed as follows.

$$\begin{aligned} &g(\alpha_1 x_1, \alpha_2 x_2, \cdots, \alpha_n x_n) > 0 \Rightarrow \text{Satisfies target reliability } \beta \\ &g(\alpha_1 x_1, \alpha_2 x_2, \cdots, \alpha_n x_n) \le 0 \Rightarrow \text{Does not satisfy target reliability } \beta \end{aligned} \tag{6}$$

If evaluated at this level, it could be handled by processing through simple calculations even with a designer unfamiliar with reliability engineering.

However, there are some precautions to keep in mind when using a partial safety factor table. When reliability design is performed with rough approximations, it is a simple and convenient method relative to strict reliability evaluation, but consideration should be given to its ease of use in terms of practicality. Now, let's imagine that we've

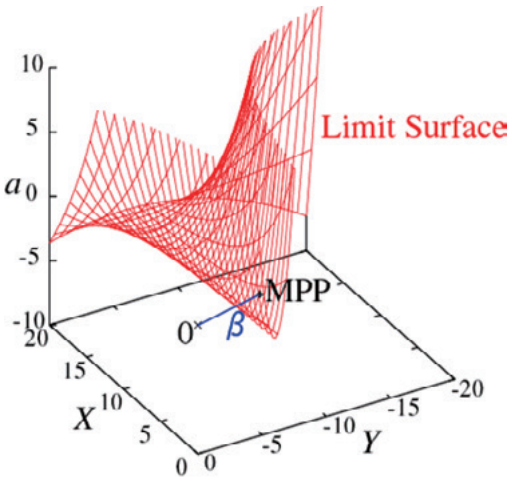


Fig. 4 Limit state curve when there are three random variables.

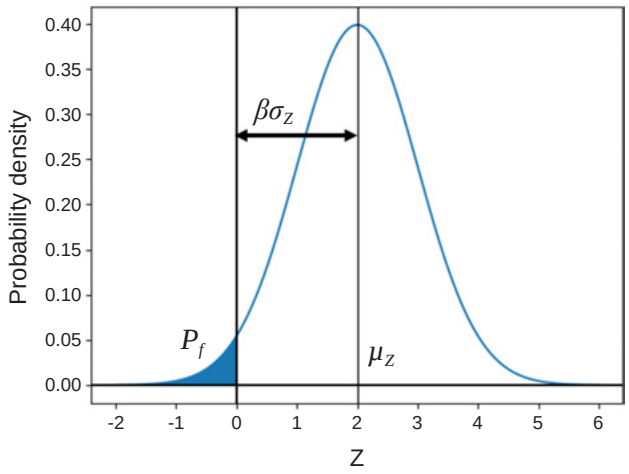


Fig. 5 Reliability index concept

Table 2 Example of complex partial safety factor table

Probability offailure	$a_0 < X_1 < a_1$, $b_0 < X_2 \leq b_1$				$c_0 < X_4 < c_1$, $d_0 < X_7 \leq d_1$			
	α_1	α_2	⋯	α_n	α_1	α_2	⋯	α_n
$P_f = 10^{-2}$ ($\beta = 2.0$)	1.1	2.5	⋯	3.8	1.3	1.1	⋯	1
$P_f = 10^{-3}$ ($\beta = 3.09$)	1.4	2.3	⋯	3.4	1.5	1.2	⋯	1
$P_f = 10^{-6}$ ($\beta = 4.75$)	1.6	2.1	⋯	3.2	1.9	1.3	⋯	1

Table 3 Role allocation for partial safety factor table development

Person in charge	Role	Description
Researcher	Develops physical models for target concerns and derives limit state function.	Advanced comprehension of limit state design methods is required.
Standards developer	Creates new partial safety factor tables for target concerns.	Comprehension of limit state design methods is required.
Standards user	Appropriate comprehension of partial safety factor tables is required.	Comprehension of details of limit state design method is not necessarily required, but being able to correctly understand how to read and evaluate table is required.

been given a partial safety factor table like Table 2 when there are n number of design variables.

Numerical values for the corresponding partial safety factors $\alpha_1 \sim \alpha_n$ are picked up according to the target reliability shown in the leftmost column. However, when the limit state function is non-linear and complex, the partial safety factor values may also change sensitively depending on the area of application. As a prerequisite for the Partial Safety Factor Method, they should be applied within a region where the partial safety factor value is almost constant. Therefore, it is necessary to investigate areas where the partial safety factor is almost constant and to set partial safety factors for each identified area, as shown in the top row of Table 2. Furthermore, since these values need to be calculated each time for target reliability, it's conceivable that the partial safety factor table corresponding to all of these would be complex. This needs to be enhanced from the perspective of practicality. An effective solution for this would be to calculate the sensitivity to the damage probability for each random variable. This sensitivity can be calculated easily using the limit state function method. Please refer to the literature[5][6][7] for details. The random variables that should actually be targeted can be narrowed down through sensitivity analysis. For example, in the case of a partial safety factor table created[8] for evaluating the reliability of localized thinning of pipe walls, in contrast to the nine random variables for the limit state function, the variables can be narrowed down to only the three that are sensitive to damage probability. In this case, the partial safety factor table could be made for only the three random variables, simplifying it and making it convenient in terms of practicality.

3.3. Role Allocation Between Industry and Academia for Reliability Design Promotion

A high level of specialized knowledge is required for making full use of the limit state design methods used in reliability design. Accordingly, it's not realistic for pure standards users to perform evaluations using the limit state design methods every time a design is created. Therefore, there is the Partial Safety Factor Method as a means of listing it in the standard, but the issue is the process for developing the partial safety factor table. This is where cooperation between reliability researchers, standards developers, and standards users is considered to be important. Examples of this allocation of roles are shown in Table 3. Among these, it's conceivable that roles could be allocated in such a way that universities and research institutes would be responsible for the researchers; industry and academia would both be responsible for developing standards; and the resulting product, the partial safety factor table, would be utilized by industries that use the standards.

4. Examples of Safety Factor Relaxation

As mentioned in Chapter 2, safety factors listed in standards have been amended due to various factors. This has not been done on the basis of scientific grounds, and social demands are considered to be one factor behind this. Safety factor optimization has been performed in a number of industrial fields in the past, even in Japan. I'll introduce two examples here to contribute to future investigation of safety factor optimization.

4.1. Introduction of Maintenance Standards for Pressure Equipment

Design is performed at the design stage for mechanical products in consideration of the safety factor written in the design standards. When devices designed and manufactured based on the design standards are added at the in-service stage for pressure equipment in plants, such as those in the nuclear power field, chemical industry, or oil refining industry, the standards for maintaining those are separate from the design standards and are called maintenance standards. Representative examples of these include the standards for the nuclear power field published by the Japan Society of Mechanical Engineers[9] and standards related to pressure equipment published by the High Pressure Institute of Japan[10][11]. Maintenance standards for the nuclear power industry were first established in 2000[12], but operational standards for maintenance standards did not exist before that, and Japan's concept of safety regulations has placed emphasis on the design stage, or design standards, for a long time. When securing safety for the maintenance stage according to the design standards, it's necessary to "maintain the state at the time of installation even if the state at the time of production is the in-service stage." However, mechanical equipment deteriorates over time. This has created a gap between safety maintenance practices and the spirit of legal compliance, and contradictions have surfaced in terms of the intention behind safety maintenance practices being contrary to the law. When looking at this from the safety factor perspective at the design stage in particular, not all information on design is collected, so the design is based on predictive behavior, and the safety factor should be set high to secure the safety margin. However, at the in-service stage, actual data is collected from the operation of the mechanical product, and the data predicted during design can actually be confirmed as well. Therefore, even if the safety factor is set excessively high at the design stage, it does not necessarily need to be operated at the same safety factor level at the in-service stage. In this way, the safety factor concept exists at both the design stage and the in-service stage, but the idea that the two numerical values do not need to be the same is firmly established. To clarify this distinction, for the nuclear power standards of the American Society of Mechanical Engineers (ASME), "Design Factor" is the term corresponding to safety factor used at the design standard stage, while "Structural Factor" is used at the in-service stage. It took 30 years from the time when maintenance standards were established by the ASME until maintenance standards were established in the nuclear power field in Japan.

Even though the introduction of maintenance standards will ease the safety factor, there are three important elements for that. Those three pillars are "investigation," "evaluation," and "repair/replacement." Investigations were conducted periodically even prior to the introduction of maintenance standards, but the act of evaluation was missing. When damage such as loss is detected, the harmfulness of that damage is evaluated through mechanical investigation, etc. If soundness is confirmed by the results from the evaluation, it is permissible to continue operating with some loss remaining. "Evaluation" regulations were published in 2000, "investigation" regulations in 2002, and "repair/replacement" regulations in 2004.

4.2. Introducing the Limit State Design Method to Mobile Crane Structure Standards

Around 2007, based on a request I received from the Japan Crane Association, I became involved in introducing the limit state design method to mobile crane structure standards. A mobile crane is shown in Fig. 6. The key to enhancing performance is to make it longer through weight reduction. Originally, Japan's advanced development technology for high-tensile steel should have had an advantage from the perspective of weight reduction, but in reality, Japanese manufacturers were at a disadvantage in international competition. The reason for this is that in Japan at that time, only allowable stress design methods were permitted under the mobile crane structure standards, while under the ISO standards[13][14] in Europe, it was possible to choose either the allowable stress design method or the limit state design method. Trying to make mobile cranes longer increases the risk of buckling and the amount of bending deformation. Therefore, it's important to achieve lengthening while being more aware of the limit state. Since there are limits in responding to the limit state under the allowable stress design method that's based on elastic design, Japanese mobile crane manufacturers were at an extremely disadvantageous position in terms of international competitiveness. Therefore, the task was given to incorporate the limit state design method into Japan's structural standards.

It was no easy task for Japan to develop an understanding for the introduction of the unfamiliar limit state design method, and no results were obtained despite a lot of time and effort being spent on this. As a result, when the ISO standards system was investigated, it was found that a standard regarding the general principles of reliability[15] does exist as a standard that serves as the basis for mobile crane standards[13][14]. On the other hand, the situation in Japan was that there were no corresponding JIS standards. It was expected that if corresponding JIS standards could be developed, then standards where the limit state function method is applied could be developed for each industry based on them, and that they would proliferate quickly. Therefore, appeals were made to related industrial fields and academic experts, and activities for the development of JIS standards were performed as a study group and subcommittee activity for the Japan Society of Mechanical Engineers. Ultimately, the High Pressure Institute of Japan became a development organization and JIS B9955:2017 was published[16]. The chapter structure of the JIS standards

is shown in Table 4. As shown in Chapter 5, the limit state design method was set as the basic concept, and the Partial Safety Factor Method is assumed to be applied as shown in Chapter 9. The mobile crane structure standards were revised in 2018, enabling designers to choose the most appropriate method (either the "allowable stress design method" or the "limit state design method") according to the usage of the crane, etc. When there's a desire to bring out the performance of a mechanical product with a stronger awareness of the limit state, it may not be possible to achieve it under the existing "allowable stress design method" from the perspective of the safety factor. The mobile crane structure standards could be called an example of a complication resolved by introducing the "limit state design method."

Table 4 JIS B 9955 Chapter Structure

Chapter 1	Scope of application
Chapter 2	Terms and definitions
Chapter 3	Symbols
Chapter 4	Requirements and concepts
Chapter 5	Principles of limit state design
Chapter 6	Basic variables
Chapter 7	Analysis models
Chapter 8	Principles of design based on probability
Chapter 9	Design through partial factor method
Chapter 10	Evaluation of mechanical products during in-service period



Fig. 6 Example of mobile crane (photo provided by KOBELCO Construction Machinery Co., Ltd.)

5. Importance of Stochastic Treatment

In the past, I've participated in activities to develop standards in a large number of fields, and my overall impression is that stochastic treatment is only used in a limited number of cases. Deterministic treatment is used the majority of the time. Considering the importance of bringing out the performance of mechanical products in a state closer to the limit state, the introduction of stochastic treatment may be inevitable in the future. This is considered to be the case in the automotive field when considering installing high-pressure hydrogen tanks in fuel cell vehicles. I'd like to share two things I've noticed from my past experiences.

The first is my experience in fields related to nuclear power. When looking only at Japan, it's hard to see where country stands in this field, and I developed a strong awareness of this complication while taking part in an international workshop related to nuclear power. The workshop, titled "Forging a New Nuclear Safety Construct" (Washington DC, December 4–5, 2012), was held by the American Society of Mechanical Engineers (ASME) following the Fukushima Daiichi nuclear power plant accident. While the specifics of this workshop are described in the literature[17], the purpose was to discuss a report published by ASME titled "Forging a New Nuclear Safety Construct" with individuals in leadership positions in the global nuclear power community. In this report, a new direction called the All Risk Approach was introduced as a direction for nuclear power in the future, and session moderator Kenneth R. Balkey asked me to report on the situation in Japan and to give my opinion on the matter. I explained that progress in Japan is slow, with little activity in terms of either a stochastic approach or a risk approach. In response to this, my recollection is that Mr. Balkey said something to the effect of, "Just as I thought. That's the Japanese mindset." At that time, I became painfully aware that this is how Japan is viewed by those outside of the country. In light of the importance of this report to the future of Japan's nuclear power field, I took part with other volunteers in completing the translation work, and the final product was published on the home page of the Japan Society of Mechanical Engineers[18]. However, looking at the situation since then, it's worrisome that it does not appear to have been fully utilized. I believe that risk-based engineering thinking and stochastic thinking will be extremely important in the future when considering how to bring out the performances of mechanical products through awareness of their limit states.

The second example is handling uncertainty when dealing with smaller samples of statistics. In these instances, in addition to the statistical properties of populations of random variables, it's necessary to handle the uncertainty known as the confidence level in English. While the term "confidence level" is used in the reliability terms in the JIS standards, etc., my personal opinion is that this translation is not appropriate. If the English term "confidence level" is used for "confidence level" when translating the English term reliability as "reliability," some may confuse it with the English term "reliability." However, the two concepts are quite different. Perhaps reflecting this situation, there are instances where the confidence level is not handled in the standard, or is handled incorrectly. While this is common sense to those familiar with statistics, it's an unfamiliar concept to those involved in engineering, and I feel that it's necessary to reconsider it, including our educational methods. For example, consider a case where the allowable stress value for tensile strength is determined in association with reliability. If the tensile strength has normal distribution and if the mean value and standard deviation (its parameters) are known, then the probability density function could be plotted as shown in Fig. 7. In this case, if there was a desire to determine allowable stress so that it would result in reliability R, it could be determined as the stress value S_A at the location of Point A in the figure. Here, Point A is determined as the position where the probability that the tensile strength will be less than or equal to S_A is 1-R. The value of 1-R is the area of the blue section in the figure, which is nothing but the probability of damage when the tolerance is set to S_A. However, in order to investigate the statistical properties of material strength, evaluation should be performed based on a finite number of samples (n). In this case, uncertainty accompanies the evaluation of the population. For example, the mean value and standard deviation, which are the parameters of normal distribution, will have a large degree of uncertainty if number of samples (n) is small. That uncertainty depends on n. Once the uncertainty has been taken into consideration, it will be necessary to give a value for the confidence level in order to determine the tolerance. An example of the tolerance for the U.S. MIL standards is

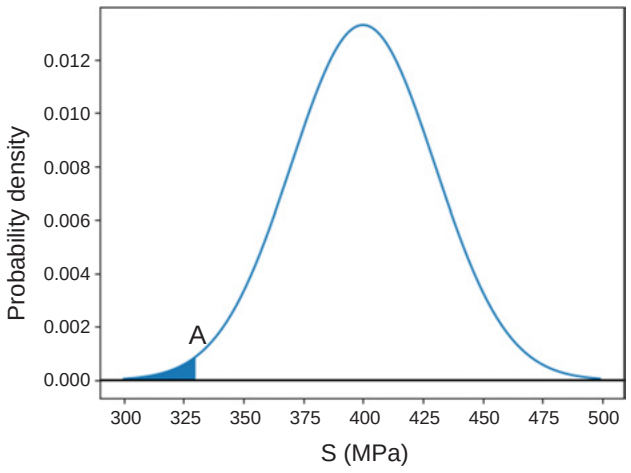


Fig. 7 Probability density function for tensile strength

Table 5 Examples of tolerance for MIL standard military aircraft

	Reliability	Confidence level
A-basis	99%	95%
B-basis	90%	95%

shown in Table 5 as a typical example adopted in the standards. Also, please refer to the explanatory article for technical details related to the handling of confidence levels[19]. When considering safety standards for hydrogen tanks, it may be challenging to secure the number of samples required for burst testing, so the complication with uncertainty related to small sample sizes may arise in these cases as well. In the next chapter, I will go over the method that G.W. Mair suggests for introducing a confidence level to manage this issue.

6. Safety Margin Optimization Concept

A high degree of safety is required for hydrogen storage tanks for fuel cell automobiles since they're used at high pressure levels. That said, it's preferable to avoid an excessive safety margin, so optimization is required. With hydrogen tanks, it's not possible to set up a large number of sample burst tests based on safety standards due to cost considerations. Therefore, as stated in the previous chapter, the uncertainty associated with small sample sizes needs to be handled. Since a high level of safety is required, it's natural to start with products designed and manufactured with a high safety factor as a starting point. G.W. Mair of BAM's concept[2] could be helpful when considering optimizing the safety factor in situations like this, so I'll introduce it briefly here. First, he suggests the application of a Monte Carlo simulation as a countermeasure for being unable to secure enough samples. Monte Carlo simulation refers to generating the value of a specific random variable using random numbers, applying the value generated to the evaluation subject, and giving consideration to the phenomenon. The principle is extremely simple, and since evaluation can be completed sufficiently even on a stock PC, it's fair to say that it's an effective method for supplementing burst testing. For example, Fig. 8 shows the results from evaluating pass/fail judgment for burst testing under the ISO 11119-3[20] standards through a Monte Carlo simulation. The horizontal axis shows the standard deviation, while the vertical axis shows the mean value, and both are standardized by the maximum service pressure (MSP). The specimens are judged to have passed the test if all three of them exceed the tolerance of 2.5 and are judged to have failed it if any of them are below that. Pass/fail judgment tests are conducted on three specimens at a time, and the results are shown for 100,000 tests. The value in yellow is the population value, and the mean value for groups of three and the standard deviation have a large amount of variation, as shown here. Also, the points in red show ones that failed the test, while the points in black show ones that passed. In this case, 59% are indicated as "passed." The ratio of ones that passed is called the Acceptance Ratio (AR). When the safety margin for tanks is excessive, it's only possible to get a 100% pass rate, and it's unlikely to see the size of the safety margin. The introduction of an index like the AR is considered to be helpful for visualizing the safety margin. When optimizing the mean value and standard deviation for the burst strength of hydrogen tanks from the perspective of the safety margin, a contour line for the AR values, which are combinations of the various mean values and standard deviations from the population, is effective. An example of a figure drawn like this is shown in Fig. 9.

G.W. Mair calls this figure an ISOASFALIA. The red line is the ISOASFALIA, and the values on the line are the AR values. Also, the boundary line for a reliability level of $1 - 10^{-6}$ is indicated by the black line in this figure. This

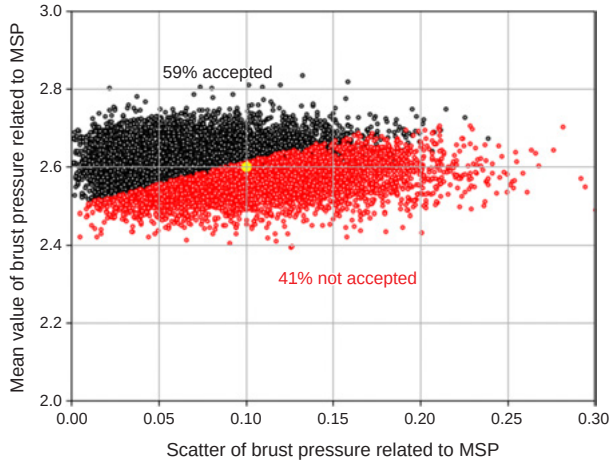


Fig. 8 Evaluation through Monte Carlo method for standard pass/fail

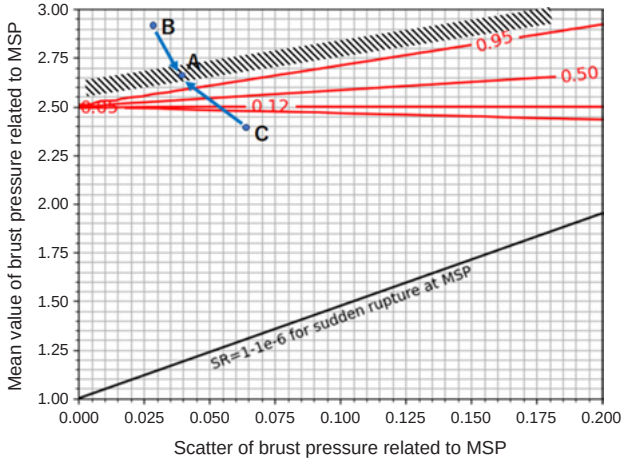


Fig. 9 Example of ISOASFALIA application

figure can be used to consider the safety margin while also considering the targeted reliability and the uncertainty of the small sample size.

For example, the concept of safety factor optimization is shown conceptually in Fig. 9. Imagine that the dashed line area is set as the optimization range in consideration of the AR values, and that among those, Point A is determined to be the target value. On the other hand, if we imagine the current value to be Point B, then shifting from Point B to Point A would be the optimization process. It's also conceivable that a great deal of effort and time would be required to reduce the margin from the excessive safety margin of Point B and shift to Point A. In cases like this, starting from a point with a smaller safety margin like Point C and moving closer to Point A might serve as a shortcut. In this way, this is considered to be an effective method for investigating the safety margin by visualizing various statistics.

7. Complications with Introducing Reliability Design

Finally, based on my experience, I would like to give my opinion on complications with introducing reliability design as a new phenomenon for industries. As shown in Fig. 10, I think that there are three major complications. Needless to say, the first of these is formulating standards and criteria. These should be officially recognized and formulated with international harmonization taken into consideration as well. When viewed from the perspective of stochastic treatment, I often feel that the current situation is still insufficient. The next important complication is the development of the databases required for carrying out various statistical considerations. I believe that developing databases on a public basis rather than keeping them confidential within specific organizations is important for the development of industry. With regard to this, in Japan, usage is often limited to within specific organizations, and this is an area where enhancement is desired. The final complication is the cultivation of human resources involved in these fields. One thing that could be considered to be an effective means would be the introduction of a qualification authentication system. For example, the High Pressure Institute of Japan employs a system for "risk management engineer certification for equipment, etc." to cultivate human resources involved in maintenance at plants, and the number of risk management engineers has grown dramatically with the start of this system. Cooperation between universities with specialized knowledge and industries would also be an effective means. In any case, I think that it's extremely important for industry to take the lead in moving forward on this.

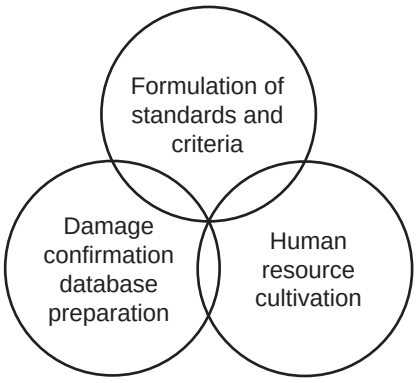


Fig. 10 Important elements for introduction of reliability design

8. Summary

Using on-board hydrogen tanks as the subject matter, I've presented the concept of reliability design, which is considered to be important to introduce in the future. In particular, I summarized my impressions from the perspective of someone from a different field. Based on my past experience, I also mentioned examples of reliability design and complications specific to Japan. In the future, it's believed that it will become extremely important to introduce reliability design once the limit state has been clarified further in order to bring out performance in mechanical products. This cannot be avoided, especially when considering optimizing the safety factor. Finally, I've summarized what are, in my personal opinion, the complications with introducing reliability design into industrial fields. I hope that this will prove useful as a reference.

Acknowledgements

Some of these results were obtained as a result of work commissioned by the New Energy and Industrial Technology Development Organization (NEDO) (JPNP20003). I would also like to thank Mr. Shigemitsu Kihara of BESTMATERIA Co., Ltd. for providing related materials.

References

[1] https://www.nedo.go.jp/activities/ZZJP_100182.html, (2023/6/29)
[2] G. W. Mair, 'Safety Assessment of Composite Cylinders for Gas Storage by Statistical Methods', Springer International Publishing, AG 2017, DOI: 10.1007/978-3-319-49710-5.
[3] Udoguchi, T., Kawada, Y., Kuranishi, M.: Zairyo Rikigaku, SHOKADO, (1973) (in Japanese)
[4] Evaluation of Design Margins for Section VIII, Div. 1 and 2 of the ASME Boiler and Pressure Vessel Code, WRC Bulletin 435, September (1998).
[5] Achintya Haldar and Sankaran Mahadevan, 'Probability, Reliability and Statistical Methods in

Engineering Design', John Wiley & Sons (2000), ISBN: 0-471-33119-8.
[6] Thomas A. Cruse, 'Reliability-Based Mechanical Design', MARCEL DEKKER, INC. (1997), ISBN: 0-8247-9793-0.
[7] Isaac Elishakoff, 'Safety Factors and Reliability: Friends or Foes?', Kluwer Academic Publishers (2004), ISBN: 1-4020-1779-0.
[8] Sakai, S., Iwasaki, A., Sasaki, T., Miyazaki, S., Ishizaki, Y., Kaida, T.: Development of Partial Safety Factor Table for Reliability Assessment of Local Metal Loss, Journal of High Pressure Institute of Japan, Vol. 57, No. 2, p. 66-72, (2019)
[9] The Japan Society of Mechanical Engineers (JSME): Code for Nuclear Power Generation Facilities -Rules on Fitness- on Fitness-for -Service for Nuclear Power Plants-, JSME SNA1-2020, (2020)
[10] High Pressure Institute of Japan: Assessment Procedure for Crack-Like Flaws in Pressure Equipment - Level 1, HPIS Z 101-1: 2008, (2008)
[11] High Pressure Institute of Japan: Assessment Procedure for Crack-Like Flaws in Pressure Equipment - Level 2, HPIS Z 101-2: 2011, (2011)
[12] Kashima, K.: Genshiryoku Iji Kikaku no Gaiyo, Japan Society of Maintenology, Maintenology, Vol. 4, No. 3, p. 11-16, (2005) (in Japanese)
[13] ISO 8686-1: Cranes-Design principles for loads and load combinations: Part1 General (1989).
[14] ISO 8686-2: Cranes-Design principles for loads and load combinations: Part2 Mobile cranes (2004).
[15] ISO 2394: General principles on reliability for structures, Third edition (1998).
[16] JIS B 9955: 2017, General principles on reliability for mechanical products
[17] Sakai, S.: Aratana Genshiryoku Gainen no Kouchiku wo Mezashite, ASME workshop report, Journal of the Society of Mechanical Engineers, Vol. 116, No. 1131, p. 123, (2013) (in Japanese)
[18] https://www.jsme.or.jp/shinsai3.11/ASME%20Presidential%20Report%20full_032.pdf
[19] Sakai, S.: Probabilistic method to determine allowable stress, Journal of High Pressure Institute of Japan, Vol. 60, Issue 1, p. 18-23, (2022)
[20] ISO 11119-3: Gas cylinders-refillable composite gas cylinders and tubes. Part 3: fully wrapped fibre reinforced composite gas cylinders and tubes up to 450L with non-load-sharing metallic or nonmetallic liners. ISO, Geneva, CH(2013).

■ Author ■



Shinsuke Sakai

Development of New Fuel Cell System

Hiroyasu OZAKI[1] Kaoru YAMAZAKI[1] Takayuki OGAWA[1]
Shuto MANIWA[1] Taneaki MIURA[2] Todd W. HUSTON[3]

ABSTRACT

In order to provide fuel cell durability, it is important to reduce iron (Fe) contamination to the polymer electrolyte membrane of the fuel cell stack and to control the humidity to an appropriate level. The new fuel cell system developed jointly with General Motors Company adopts a double-layer coating of titanium and carbon on the stainless steel bipolar plates of the fuel cell stack that reduces Fe elution to 1/10 the previous amount. In addition, the humidification level is increased by estimating the amount of water vapor with a highly accurate humidification model and using a high-efficiency water vapor transfer unit and an electric coolant mixing valve to perform active humidity control. The amount of water contained in the membrane was increased by lowering the coolant temperature and supplying air controlled to high humidity with a high degree of accuracy. As a result, the durability is more than double that of the previous system.

In addition, the start-up time in a low-temperature environment of -20°C was shortened to 1/9 that of the previous system by performing humidity conditioning control when the system is stopped and rapid warm-up control at start-up.

The fuel cell system cost was also reduced to 1/3 that of the previous system by reducing the cost of the fuel cell stack and simplifying the system.

1. Introduction

The utilization of hydrogen energy is attracting attention as a key technology for achieving a carbon-neutral society. Honda has engaged in research and development of fuel cells that extract electrical energy directly from hydrogen and the oxygen in the air. In 2002, the company released the FCX, the first fuel cell passenger vehicle, simultaneously in Japan and the U.S.[(1), (2)] This was followed in 2003 by development of an FCX equipped with a fuel cell system capable of start-up in sub-zero environments, which enabled use in cold regions[(3)]. In 2008, the FCX CLARITY was launched, considered the first sedan type to adopt a dedicated platform for fuel cell vehicles[(4)]. In anticipation of full-scale mass production, productivity was enhanced, and a downsized fuel cell system was developed in 2016 and positioned as the first generation. This first-generation fuel cell system (hereinafter, the previous system) was installed in the engine room to achieve release of the CLARITY FUEL CELL, considered the first fuel cell vehicle to seat five people, which increased practicality as a daily car[(5)]. In 2024, the CR-V e:FCEV was announced, which is equipped with the new second-generation fuel cell system introduced in this paper[(6)].

In order to help realize a carbon-neutral society, Honda will promote the expanded deployment of fuel cell systems not only in passenger vehicles but also in various applications. Hydrogen features a higher energy density compared to batteries, easy transport in various formats, and quick filling. Efforts will be made to expand use to applications that can take advantage of those characteristics, such as commercial use vehicles, construction machinery, and stationary power sources (Fig. 1). This paper introduces a new fuel cell system that features even greater durability, shorter start-up time at ultra-low temperatures, and further cost reduction with the goal of expanding adoption of fuel cell systems.

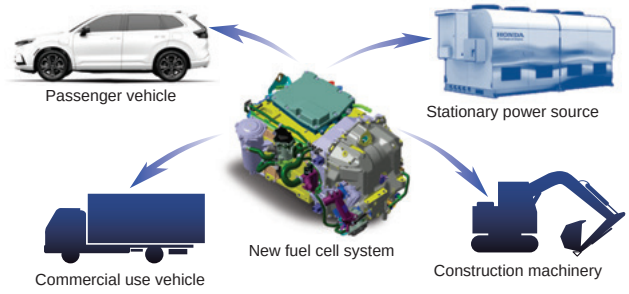


Fig. 1 New fuel cell system and various applications

[1] Innovative Research Excellence, Power Unit & Energy
E-mail: hiroyasu_ozaki@jp.honda
[2] American Honda Motor Co., Inc.
[3] General Motors Company

Table 1 Main specifications of fuel cell systems

		Previous fuel cell system	New fuel cell system
Major specifications	Fuel cell type	Proton exchange membrane	Proton exchange membrane
	Fuel cell power	103 kW	92.2 kW
	Fuel cell stack size	33 liters	33.8 liters
Main system configuration for durability	FC coolant temperature control	Thermostat valve	Electric coolant mixing valve
	Humidity control	Water vapor transfer bypass valve	
	Provide air circulation	EGR pump	– (Substitution by control)
	Provide H_2 circulation	Hydrogen pump	

2. Overview of Development

Figure 2(a) shows the previous fuel cell system, and Fig. 2(b) shows the new fuel cell system. It was considered important that the new system have even greater durability, better low-temperature environmental performance, and lower cost compared to the previous system, so the development goals were as follows. Table 1 shows the main specifications of the new and previous fuel cell systems.

(1) Further enhancement of fuel cell stack durability

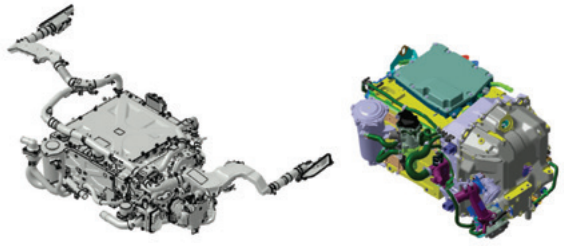
In order to promote compatibility with various applications, the target durability time was set to double that of the previous system. This was achieved by enhancing the amount of water contained in the polymer electrolyte membrane of the fuel cell stack, lowering the coolant temperature, and reducing the amount of Fe elution from the bipolar plates that comprise the fuel cell stack.

(2) Shorter warm-up time in low-temperature environments

In order to further enhance marketability in low-temperature environments, the target warm-up time at -20°C was set to 1/9 that of the previous system. This was achieved by adopting humidity conditioning control when the system is stopped and rapid warm-up control at start-up.

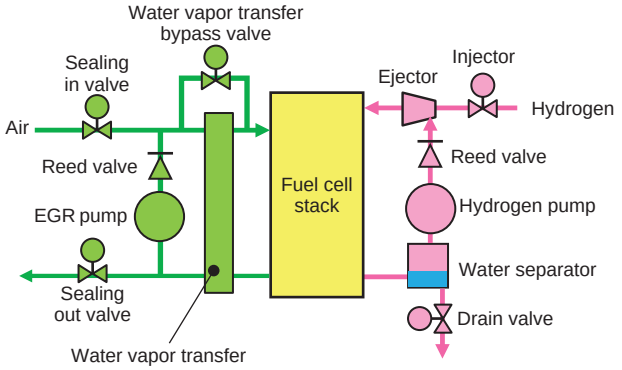
(3) Enhanced productivity and further cost reduction of fuel cell system

The target cost was set to 1/3 that of the previous system. This was achieved by simplifying the fuel cell stack structure as shown in Fig. 3(b), enhancing productivity, reducing the amount of precious metals used, and simplifying the system components.

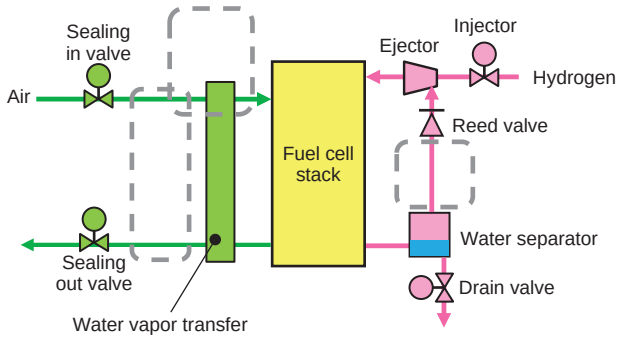


(a) Previous system (b) New system

Fig. 2 Appearance of fuel cell systems



(a) Previous system



(b) New system

Fig. 3 Comparison of system configuration

3. Further Enhancement of Fuel Cell Stack Durability

The polymer electrolyte fuel cells that are generally used for automobiles directly extract electrical energy externally by transferring hydrogen ions H^+ through polymer electrolyte membranes located in the center part. The fuel cell stack structure consists of a membrane electrode assembly (MEA) with catalyst layers and gas diffusion layers sandwiched around polymer electrolyte membranes, and bipolar plates in which flow channels for gas supplied as fuel and flow channels for coolant to cool the power generation parts are formed. The fuel cell stack humidification control system adopted in the new system like the previous system is described next. Figure 4 shows a diagram of the humidification system of the fuel cell stack. As the exhaust air from the fuel cell stack contains water produced by power generation, it is in the highly humid state. This highly humid exhaust air is passed through a water vapor transfer unit installed in the air supply system. As a result, the water vapor contained in the exhaust air is transferred to the air that is supplied to the fuel cell stack, thereby humidifying the supply air.

A key to enhancing the durability of the fuel cell stack is how to suppress changes over time, especially in the polymer electrolyte membrane that is responsible for the

transfer of hydrogen ions. It is known that the chemical stability of the polymer electrolyte membrane decreases when the amount of water contained in the membrane is insufficient and under high-temperature conditions[7, 8], and that changes over time are accelerated by contamination of the membrane by Fe eluted from components such as the bipolar plates[9]. However, if the fuel cell stack contains an excessive amount of water, the gas supply will be hindered, leading to changes in the electrodes over time, and thus it is necessary to adjust the amount of water contained to the appropriate range.

To address the decrease in the chemical stability of the membrane and changes in the electrodes over time, it is necessary to increase the amount of water contained in the membrane and lower the temperature within the appropriate ranges during power generation. The amount of water contained in the membrane and the relative humidity of the air supplied to the fuel cell stack are closely related, so the amount of water contained in the membrane was increased by lowering the coolant temperature and supplying air controlled to a highly humid state. This was achieved by the following three methods.

(1) Enhance the heat exchange performance of the fuel cell stack
(2) Enhance the accuracy of estimating the amount of water vapor in the air supplied
(3) Lower the coolant temperature

The heat exchange performance was enhanced by changing the cooling structure from the previous structure that provides one cooling layer for every two cells to a cell-by-cell cooling structure that provides one cooling layer for each cell[10]. Figure 5(a) shows the air and coolant flows inside the flow channels formed in the bipolar plates. The effect of the coolant on the relative humidity of the air is as follows. In the fuel cell stack, power generation produces water on the cathode, and the relative humidity of the air inside fuel cell stack increases toward the outlet. For this reason, a flow channel structure is adopted in which the air and coolant flow in parallel in the same direction in order to reduce condensation of the water vapor. In this flow channel structure, the humidified air entering the fuel cell stack undergoes heat exchange with the coolant supplied to the fuel cell stack before being supplied to the MEA, which is the power-generating part, in order to adjust the temperature of the air supplied to the MEA. The amount of saturated water vapor changes according to the temperature of this air, and thus the relative humidity of the air changes even though the amount of water vapor contained in the air remains the same. That is to say, the relative humidity of the air supplied to the MEA can be adjusted by controlling the coolant temperature at the stack inlet. Adoption of a cell-by-cell cooling structure as shown in Fig. 5(b) enhanced the heat exchange performance and reduced variation between cells compared to the previous system. This enabled performance of precise humidification control.

Enhancement of the accuracy of estimating the amount of water vapor in the air supplied is described next. The previous system applied the method of measuring the average impedance of the fuel cell stack to understand the state of the water contained in the membrane. A valve installed on piping that bypasses the water vapor transfer unit shown in Fig. 3(a) was operated based on that impedance information to control the relative humidity of the supplied air, thereby controlling the amount of water contained in the membrane[11]. However, there was the issue that the impedance measurement sensitivity is low in the high humidity environment that is the target of the new system, making it a challenge to accurately assess the amount of water contained in the membrane. Therefore, a new model was constructed that mathematically expresses the water vapor transfer principle in the water vapor transfer unit[12], and this mathematical model was then converted to an approximation function to create a control model with a low calculation load that can be implemented in system control. Use of this control model enabled onboard estimation of the amount of water vapor transfer in the high humidity region where high-precision control was not easy

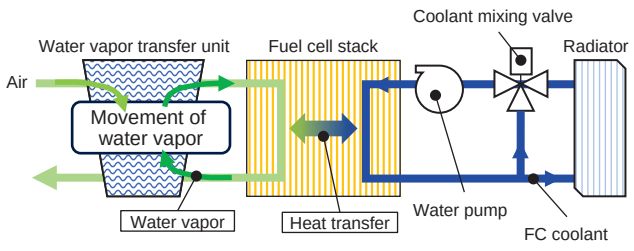
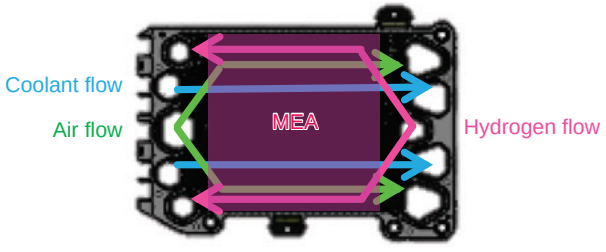
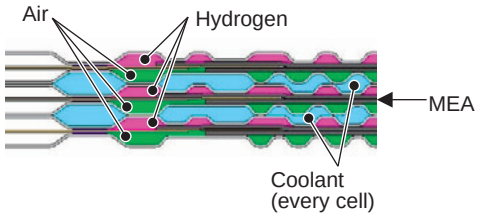


Fig. 4 Humidification system



(a) Fluid flow in stack



(b) Cross-sectional structure of stack (cell-by-cell cooling)

Fig. 5 Structure of flow channels

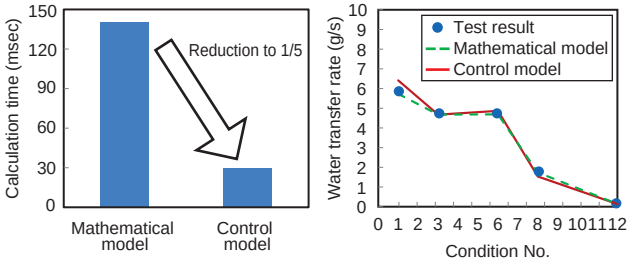
with the impedance-based method. Figure 6 compares the calculation times of both models, and shows the actual measurement results and model calculation results of the amount of water vapor transfer of the water vapor transfer unit under various power generation conditions of the fuel cell stack. The control model obtained equivalent estimation results while shortening the calculation time to approximately 1/5 that of the mathematical model, thus realizing both accuracy and a low calculation load.

In order to lower the coolant temperature, the cooling performance of the radiator was enhanced and a coolant mixing valve was applied that can electrically control the amount of coolant flowing to the radiator (Fig. 4). The previous system applied a thermostat valve that was passively opened and closed to achieve a constant target coolant temperature. By contrast, the opening of the coolant mixing valve can be adjusted at an arbitrary timing to achieve an arbitrary target coolant temperature. The amount of coolant flowing to the radiator is controlled by adjusting the opening of this valve, enabling the free mixing of coolant with a low water temperature that has been cooled by the radiator and coolant with a high water temperature that does not pass through the radiator. This enabled control at an arbitrary target coolant temperature calculated by the control model, and achieved the target relative humidity of the air supplied to the fuel cell stack.

Figure 7 shows an example of the behavior of the relative humidity of the air with or without this humidification control in constant current power generation. When the temperature of the air rises, as shown in Fig. 7(b), the humidification control model estimates a decrease in the relative humidity and lowers the coolant temperature. As a result, the relative humidity can be stably controlled to around the target value as shown in Fig. 7(a). Figures 8(a) and 8(b) show the respective frequency distributions of the coolant temperature and the relative humidity of the air during the evaluation power generation mode used in development. As shown in these figures, a higher amount of water contained in the membrane and a lower temperature could be achieved compared to the previous system.

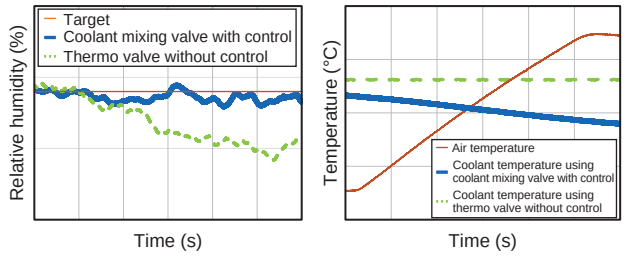
Acceleration of changes in the membrane over time due to Fe was addressed by coating the stainless steel base bipolar plates in the fuel cell stack with a double layer of titanium and carbon. This reduced the amount of Fe elution to 1/10 that of the previous system[10].

These initiatives to increase the amount of water contained in the membrane, lower the temperature, and reduce the amount of Fe elution from the bipolar plates more than doubled the durability of the fuel cell stack compared to the previous system.



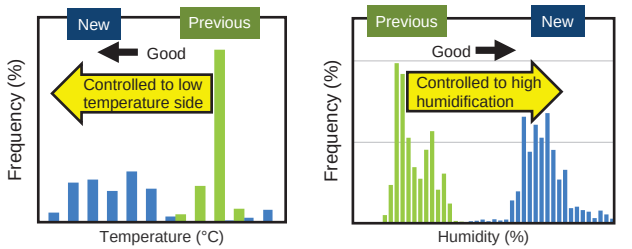
(a) Calculation time (b) Water transfer rate accuracy

Fig. 6 Performance of control model



(a) Changes in relative humidity (b) Changes in temperature

Fig. 7 Behavior of relative humidity



(a) Frequency distribution of temperature (b) Frequency distribution of humidity

Fig. 8 Operating temperature and humidity

4. Shorter Start-up Time in Low-Temperature Environments

In low-temperature and especially sub-zero environments, the power generation performance of the fuel cell stack decreases for reasons such as lower activity of the catalyst used in the fuel cell stack, and there is the issue that the fuel cell system is unable to supply the power output needed for vehicle operation at some temperatures. Therefore, in addition to warming up the fuel cell system after start-up until it can supply the required power output like the previous system, a goal for the new system was to shorten the start-up time in anticipation of expanding use to a wide range of applications.

First, a rapid warm-up method was applied to actively warm up the fuel cell stack by using the power generation loss (heat generation) that can occur when the amount of air supplied to the fuel cell stack in power generation is reduced compared to that in regular power generation[13]. Figure 9 shows the mechanism of this increase in the amount of heat generated. The more current that flows through a fuel cell, the larger the resistance component, and thus the voltage decreases and the resistance component becomes

heat, as shown in Fig. 9(a). In addition, when the amount of air is decreased, the resistance component increases and the voltage decreases even at the same current value, and thus the heat generation increases commensurately with the increase in resistance, as shown in Fig. 9(b). Figure 9(c) expresses these relationships in terms of energy and power generation efficiency. Power generation energy is the product of the flowing current value and the voltage value at that time, and heat generation energy is the heat due to the resistance component as described above. By increasing the current value and decreasing the amount of supplied air, the voltage decreases and the power generation efficiency drops. The heat generation energy increases due to the drop in power generation efficiency, and thus the start-up time can be shortened by making use of this increase in heat generation.

From the above, the fuel cell system would generate power at a high current in sub-zero environments for warm-up. However, due to the balance between the amount of water produced by power generation and the temperature of the fuel cell stack, the produced water may freeze and hinder the supply of gas, resulting in the issue that power generation cannot be continued. Therefore, by taking advantage of the fact that the dried polymer electrolyte membrane can absorb the produced water, the total amount of water produced in the time until the fuel cell temperature exceeds the freezing point was set to the amount that can be contained by the membrane or less, which realized the continuation of power generation[14]. As described in Chapter 3, the membrane in the new system is in a high water content state during regular power generation, making it necessary to dry the membrane for it to absorb the produced water. However, excessive drying leads to changes in the membrane over time, and thus drying is performed while controlling the relative humidity by performing humidity conditioning with power generation in advance. As the fuel cell temperature can be raised by power generation, the humidity conditioning time can be shortened at the same time.

Application of the above rapid warm-up control and humidity conditioning control achieved shorter start-up time at low temperatures. Figure 10 shows the start-up time in the low-temperature environment of -20°C. The start-up time is shortened to approximately 1/9 that of the previous model.

In addition, as shown in Fig. 11, this humidity conditioning is not performed immediately after fuel cell system stop. After fuel cell system stop is complete, the system is cooled in accordance with the ambient temperature, and humidity conditioning is automatically performed at the timing when the system temperature approaches the freezing point. As described previously, the fuel cell temperature rises due to power generation during humidity conditioning, and thus the period until the fuel cell temperature becomes equal to the ambient temperature can be extended compared to the case without

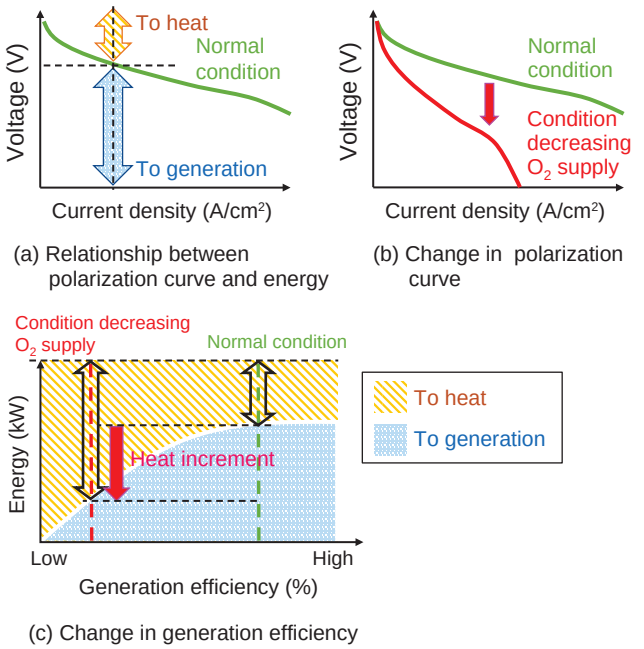


Fig. 9 Mechanism for heat increment

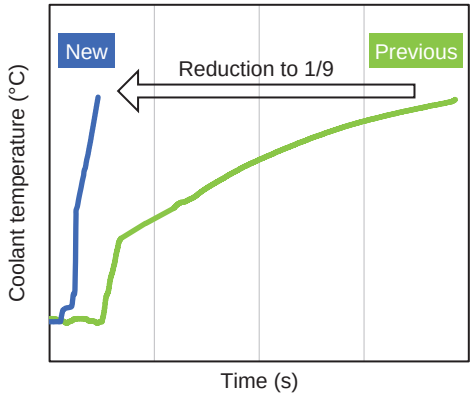


Fig. 10 Start-up time in low-temperature environment

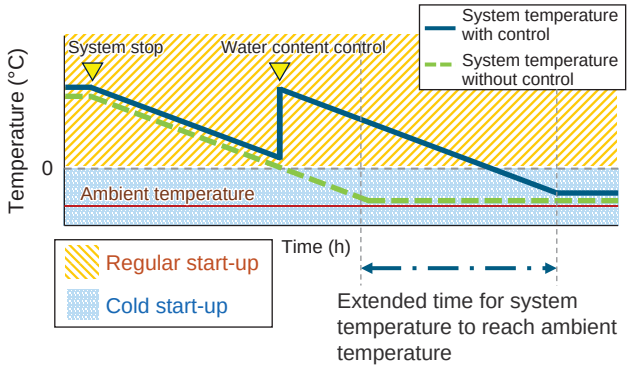


Fig. 11 Schematic diagram of system temperature changes

humidity conditioning. As a result, when performing start-up next under sub-zero ambient temperature conditions, the frequency of regular start-up can be increased in accordance with the amount by which the period that the fuel cell temperature is the freezing point or higher is extended. That is to say, the frequency of sub-zero start-up with a long warm-up time can be reduced.

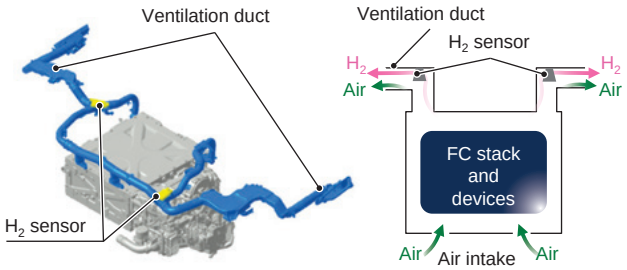
5. Enhanced Productivity and Further Cost Reduction of Fuel Cell System

Cost reduction measures were implemented in various aspects of the fuel cell stack from materials to production while providing the same or better performance than the previous system[10]. The parts composition was reviewed in accordance with the cell-by-cell cooling structure, enabling a reduction in the number of parts from 5 parts/2 cells[15] to 4 parts/2 cells. The surface coating of the bipolar plates was changed from gold plating to a double-layer coating of titanium and carbon. Regarding the seal structure between the bipolar plates of the fuel cell, in addition to the welded seal, a metal bead seal structure that combines metal bead and micro seals was newly developed, as shown in Fig. 12.

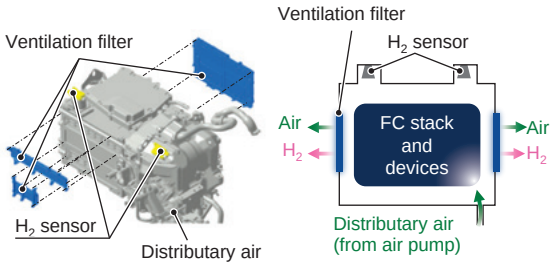
A 40% reduction in film thickness from conventional stacks was achieved by adopting novel, proprietary MEA coating processes and formulations[10]. In addition, equivalent performance is provided even with 80% less platinum in the MEA electrode parts compared with the previous stack[10]. Continuous production was achieved by fully automating fuel cell stack manufacture, as shown in Fig. 13[10]. This was realized with a joint venture plant of Honda and General Motors.

Figures 3(a) and 3(b) show the main auxiliary device configurations of the new and previous systems. As described in Chapter 3, the new fuel cell system achieved even greater stack durability by adopting an electric coolant mixing valve to control the humidification amount. This enabled a reduction in the number of auxiliary devices such as the hydrogen pump, EGR pump, reed valve, and water vapor transfer unit bypass valve that were installed as measures to enhance stack durability in the previous system, leading to a reduction in system cost.

When considering expansion of use to various applications, as shown in Fig. 1, the previous hydrogen ventilation system required specially designed ventilation ducts for each application, as shown in Fig. 14(a). The new hydrogen ventilation structure shown in Fig. 14(b)[16] is a forced ventilation system that constantly ventilates to achieve a safe concentration regardless of differences in installation conditions. This enabled a reduction in the number of specially designed parts and the construction of a system that is advantageous for multi-purpose deployment. Fewer parts also realized further cost reductions.



(a) Previous model



(b) New model

Fig. 14 Hydrogen ventilation systems

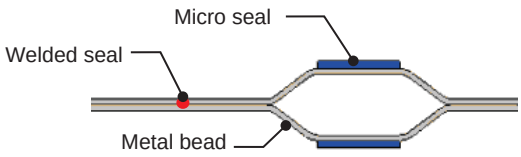


Fig. 12 New bipolar plate structure

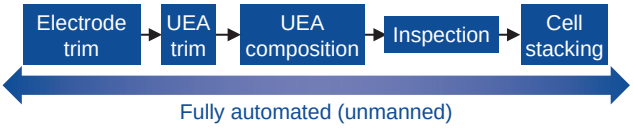


Fig. 13 Fuel cell stack manufacturing process

6. Conclusion

A fuel cell system that achieves enhanced durability and low-temperature environmental performance while reducing the cost was developed to realize deployment not only to passenger cars but also to various applications, with the goal of expanding adoption of fuel cell systems.

(1) Operating conditions with a lower temperature and higher humidification are used, the amount of humidification of the air input to the fuel cell is estimated onboard, and active control is performed with a water vapor transfer unit and a coolant mixing valve. In addition, coating the surface of the bipolar plates of the fuel cell with a double layer of titanium and carbon enabled a reduction in Fe elution to 1/10 the previous level. As a result, the

durability of the fuel cell achieved the target of double or more than the previous system.

(2) Regarding start-up in low-temperature environments, the start-up time at -20°C was reduced to the target of 1/9 the previous time by combining rapid warm-up control that controls the amount of input air and control that conditions the humidity of the polymer electrolyte membrane in advance before start-up.

(3) The number of parts comprising the fuel cell stack was reduced, a metal bead and micro seal structure was developed in addition to the welded seal of the bipolar plates, and the parts configuration was simplified. In addition, the amount of precious metals used was reduced and a new MEA manufacturing method and fuel cell assembly process were developed. Together with a simplified system configuration, the cost of the new fuel cell system achieved the target of 1/3 the previous system.

References

(1) Kawasaki, S., Ogura, M., Ono, T., Kami, Y.: Development of the Honda FCX Fuel Cell Vehicle, Honda R&D Technical Review, Vol. 15, No. 1, p. 1-6

(2) Ogawa, T., Kimura, K., Uchibori, K., Fujimoto, S., Shimizu, K.: Development of New Power Train for Honda FCX Fuel Cell Vehicle, Honda R&D Technical Review, Vol. 15, No. 1, p. 7-12

(3) Kawasaki, S., Uchibori, K., Murakami, Y., Shimizu, K., Fujimoto, S.: Development of New Honda FCX with Next-generation Fuel Cell Stack, Honda R&D Technical Review, Vol. 18, No. 1, p. 45-50

(4) Matsunaga, M., Fukushima, T., Ojima, K., Kimura, K., Ogawa, T.: Fuel Cell Powertrain for FCX Clarity, Honda R&D Technical Review, Vol. 21, No. 1, p. 7-15

(5) Kimura, K., Kawasaki, T., Ohmura, T., Atsumi, Y., Shimizu, K.: Development of New Fuel Cell Vehicle CLARITY FUEL CELL, Honda R&D Technical Review, Vol. 28, No. 1, p. 1-8

(6) Ozaki, H., Uenodai, A., Yamazaki, K., Maniwa, S., Ogawa, T.: Development of a new fuel cell system for new fuel cell vehicle, 2024 JSAE Annual Congress (Spring) Proceedings, No. 10-24, Publication code 20245041, (2024)

(7) Perry, M. L., Daring, R. M., Kandoi, S., Patterson, T. W., Reiser, C.: Operating Requirements for Durable Polymer-Electrolyte Fuel Cell Stacks, Polymer Electrolyte Fuel Cell Durability, Springer, p. 399-417, (2009), doi: 10.1007/978-0-387-85536-3_20

(8) Gittleman, C. S., Coms, F. D., Lai, Y. -H.: Chapter 2 - Membrane Durability: Physical and Chemical Degradation, Polymer Electrolyte Fuel Cell Degradation, ACADEMIC PRESS, p. 15-88, (2012), doi: 10.1016/B978-0-12-386936-4.10002-8

(9) Zatoń, M., Rozière, J., Jones, D. J.: Current understanding of chemical degradation mechanisms of perfluorosulfonic acid membranes and their mitigation strategies: a review, Sustainable Energy & Fuels, Royal Society of Chemistry, Vol. 1, Issue 3, p. 409-438, (2017), doi: 10.1039/C7SE00038C

(10) Ishikawa, C., Iwaida, M., Naito, H., Inai, S., Yoshida, H., Muromoto, N.: High-durability and Cost-effective Fuel Cell Stack with New Structure, Honda R&D Technical Review, Vol. 37, p. 20-26

(11) Iwanari, T., Miyajima, K., Furusawa, K., Inoue, M.: Real-time Measurement of Water Content of CCM in On-board Fuel Cell Stack System, Honda R&D Technical Review, Vol. 28, No. 1, p. 34-40

(12) Maniwa, S., Hidaka, Y., Kimura, K., Koiwa, N.: Construction of One-dimensional Humidifier Model in Fuel Cell System, Honda R&D Technical Review, Vol. 37, p. 56-65

(13) Manabe, K., Imanishi, H., Ogawa, T., Nonobe, Y.: Development of Fuel Cell Hybrid Vehicle Rapid Start-up from Sub-freezing Temperatures, Transactions of Society of Automotive Engineers of Japan, Vol. 41, Issue 6, p. 1379-1385, (2010), doi: 10.11351/jsaeronbun.41.1379

(14) Thompson, E. L., Jorne, J., Gu, W., Gasteiger, H. A.: PEM Fuel Cell Operation at -20°C. I. Electrode and Membrane Water (Charge) Storage, Journal of The Electrochemical Society, Vol. 155, No. 6, p. B625-B634, (2008), doi: 10.1149/1.2905857

(15) Kikuchi, H., Kaji, H., Nishiyama, T., Okonogi, D., Harata, H.: Development of New FC Stack for CLARITY FUEL CELL, Honda R&D Technical Review, Vol. 28, No. 2, p. 45-52

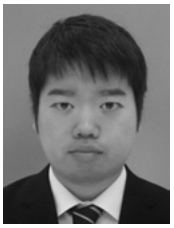
(16) Takekoshi, S.: Development of Hydrogen Ventilation Structure for Fuel Cell Systems, Honda R&D Technical Review, Vol. 37, p. 49-55

Author


Hiroyasu OZAKI


Kaoru YAMAZAKI


Takayuki OGAWA


Shuto MANIWA


Taneaki MIURA


Todd W. HUSTON

High-durability and Cost-effective Fuel Cell Stack with New Structure

Choichi ISHIKAWA[1] Manabu IWAIDA[1] Hideharu NAITO[1]
Shigeru INAI[1] Hiromichi YOSHIDA[1] Nobuyoshi MUROMOTO[2]

ABSTRACT

A new structure fuel cell stack developed jointly with General Motors realized twice the durability at 1/3 of the cost while maintaining the output and safety performance of the previous fuel cell stack.

In order to increase durability, control-based temperature and humidity management was adopted and the stack structure was enhanced to achieve less iron elution from the bipolar plates, better cooling performance, and more stable power generation due to the stack end unit parts, etc.

To achieve lower cost, first the current density of the Membrane Electrode Assembly was increased and the power consumption of auxiliary devices that compensate for stack power generation was lowered, enabling maintenance of the same net power as the previous system with fewer cell layers. Next, the structure was simplified while enhancing the cooling performance of the bipolar plates. In addition, less platinum is used in the electrode catalyst of the Unitized Electrode Assembly, the polymer electrolyte membrane was thinned, and a fully automated line was applied from assembly of the Unitized Electrode Assembly to the stacking process.

1. Introduction

Areas around the world are continuing to experience major disasters due to climate change, such as heavy summer rains, massive hurricanes, large-scale forest fires, and sea level rise due to melting ice as temperatures rise in the Arctic region. It has been pointed out that the global warming at the root of this, that is to say the increase in the global average temperature over pre-industrial (1850-1900) levels, reached 1.1°C in 2011-2020 and is likely to reach 1.5°C by 2040[(1)]. For this reason, hydrogen is attracting attention as an energy source to replace petroleum-derived fuels, as it does not emit CO_2 in use, which is a main factor in temperature rise[(2)]. Against this background, Honda is proposing the realization of “Use” to stimulate demand for hydrogen as part of measures to curb global warming[(3)].

Honda has worked to achieve practical application of fuel cell technology since the 1980s[(4)-(7)], and the CLARITY FUEL CELL[(8), (9)] equipped with the previous fuel cell system was launched to limited markets in 2016. As the next stage, development has proceeded on a new structure fuel cell system with enhanced durability and lower cost to enable deployment to a wide variety of markets. A new structure fuel cell stack developed jointly with General Motors realized twice or greater durability at 1/3 of the cost while maintaining the output and safety performance of the previous fuel cell stack. Honda is considering expanding application of this fuel cell stack to four areas including commercial use vehicles, construction machinery, and stationary power sources in addition to installation in a new fuel cell electric vehicle, as shown in Fig. 1[(10)]. This paper introduces the new structure fuel cell stack.

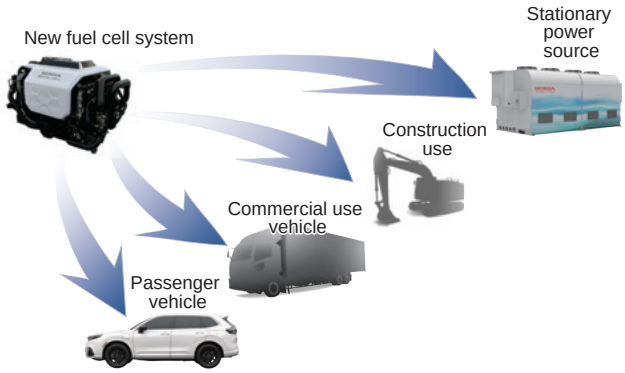


Fig. 1 Expanding application of fuel cell system

[1] Innovative Research Excellence, Power Unit & Energy
E-mail: choichi_ishikawa@jp.honda
[2] Honda Motor Co., Ltd.

2. Development Goals

The new structure fuel cell stack adopts a polymer membrane cell structure when stacked Membrane Electrode Assemblies (MEA) consisting of a polymer electrolyte membrane (PEM) sandwiched between hydrogen (anode) and air (cathode) electrodes, as shown in Fig. 2.

In this structure, hydrogen and the oxygen in the air are supplied to the MEAs, and chemical energy is directly converted into electrical energy by an electrochemical reaction. The power generation cell shown in Fig. 3 has a structure in which a Unitized Electrode Assembly (UEA) composed of an MEA and peripheral resin film is sandwiched between two bipolar plates (BPP) to configure flow channels that supply hydrogen and oxygen.

Factors such as contamination by iron and PEM drying due to higher temperatures in operation are known to promote PEM degradation in the MEA[11), 12)]. Durability was increased by implementing countermeasures to address these factors.

In addition, the MEA is a thin membrane that calls for high processing accuracy, and thus the manufacturing process is complex, and platinum (Pt) is also required, which is a cost issue in terms of popularization[13), 14)]. Therefore, a development goal was to achieve lower cost by simplifying the structure and material substitution.

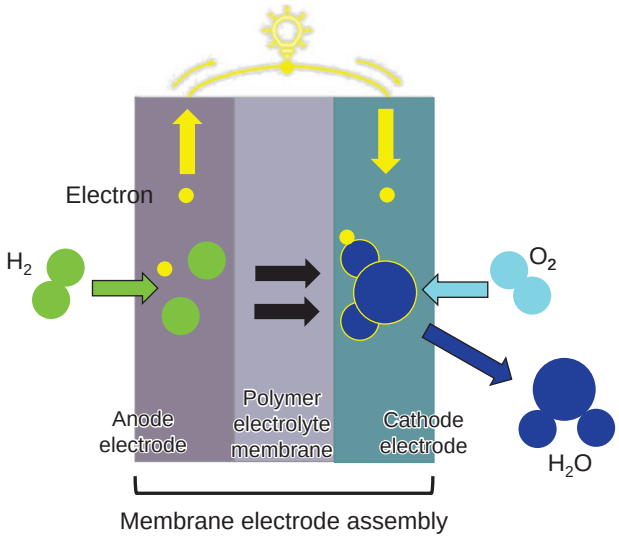


Fig. 2 Mechanism of electricity generation in stack

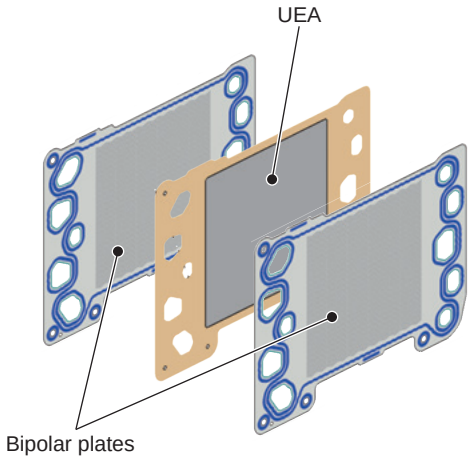


Fig. 3 Structure of cell in new stack

3. Lower Fuel Cell Stack Cost

Figure 4 compares the fuel cell stack cost for the previous and new structures. As the cell cost accounts for the majority of the stack cost, the current density of the MEA was increased and the power consumption of auxiliary devices that compensate for stack power generation was lowered while maintaining the same net power as the previous fuel cell system. This enabled to use 15% fewer cell layers compared with the previous stack.

In addition, as shown in Fig. 5, the fuel cell stack consists of a cell unit structure in which BPP and UEA are stacked, and a stack structure that functions to fasten and

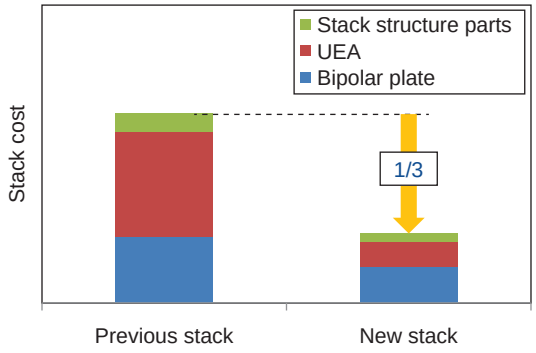


Fig. 4 Stack cost

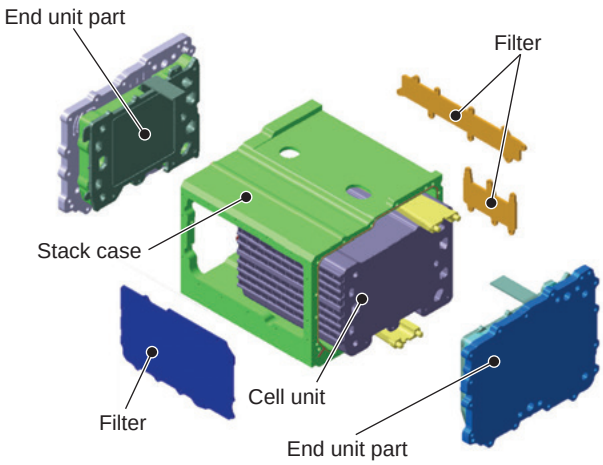


Fig. 5 New fuel cell stack

protect the cell unit. By lowering the cost of each of these parts, the new structure fuel cell stack realized a cost 1/3 that of the previous stack.

3.1. Simplification of BPP Structure and Review of Materials

In consideration of BPP cost, the base material surface coating was changed, the inter-cell seal structure was changed, and the peripheral covering structure used to help prevent water exposure was eliminated, as shown in Fig. 6.

As shown in "External shape" and "Coating structure" in Fig. 6, the BPP base metal surface that was a factor increasing cost was changed from the previous gold coating to a less expensive carbon (C) and titanium (Ti) coating. In addition, the previous BPP seal structure used a seal that covered the base material plate with rubber. As shown in "Seal structure," the new BPP structure was simplified by adopting a BPP structure in which two base material plates are sealed by welding, and a seal structure using metal beads and micro seals.

In addition, the previous BPP used a cell outer covering structure that covers the outer periphery of the cell with a resin frame and rubber to help prevent exposure of the metal areas after stacking. As shown in "Outer insulation structure," the new structure adopts the filter structure shown in Fig. 5 that helps prevent water exposure from the outside and also enables ventilation of the hydrogen, and eliminates the complex cell outer covering structure[13].

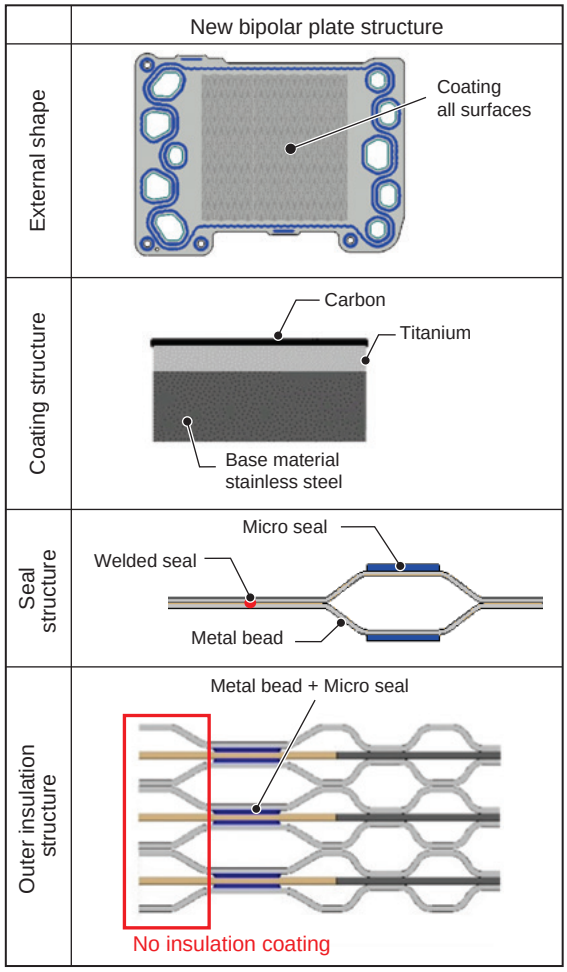


Fig. 6 Bipolar plate structure for cost reduction

3.2. Change in UEA Materials and Structure and Introduction of Fully Automated Production Line

The UEA adopted the structure shown in Fig. 7, and used just 1/5 of the amount of the precious metal Pt contained in the electrode layers compared with the previous UEA, which had been a factor increasing cost. In addition, the previous system used a membrane product (single membrane) from a cooperating supplier, but adoption of a proprietary coating process thinned the PEM to 3/5 of the previous thickness, which helped realize a lower UEA cost.

A Pt alloy catalyst with high catalytic activity was also used in the electrode layers. Increased catalytic activity and a thinner PEM resulted in lower resistance, which compensated for the decline in performance due to lower Pt content and provided output performance equivalent to or better than that of the previous UEA. Also, the peripheral resin structure no longer uses the flow channel structure present in the previous UEA structure, and instead adopts a structure with flow channels only on the BPP side[14].

In order to realize lower cost, the materials and structure were changed, and production technologies were also developed to increase production efficiency.

The previous processing times differed for each process, as shown in Fig. 8, making it a challenge to link and fully

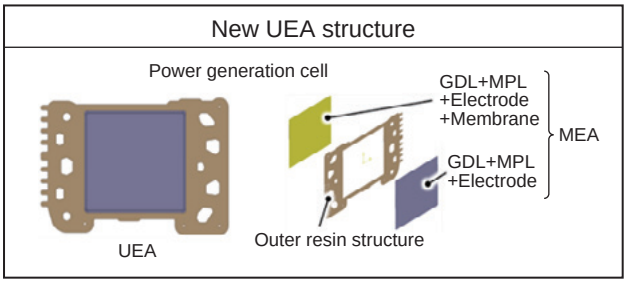


Fig. 7 UEA cost reduction structure

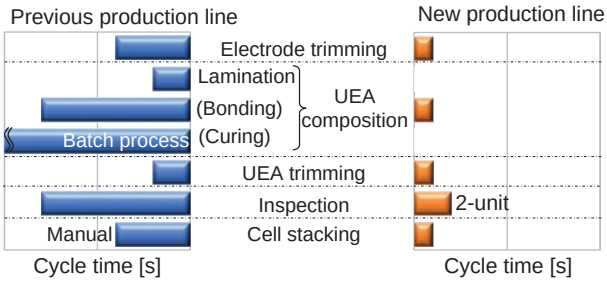


Fig. 8 Cycle time for each proces

automate the series of processes from electrode trimming to cell stacking. This limited the potential increase in production efficiency, and was a factor increasing cost. Therefore, the processes for the new structure fuel cell stack were consolidated and the processing times were shortened, realizing the fully automated line shown in Fig. 9. The processes in order from left to right of trimming the electrodes from the roll, laminating the trimmed electrodes with film, assembling the UEA, inspecting the quality, and then stacking with the BPP are all fully automated.

The details of that initiative are as follows. First, the previous peripheral resin structure used injection-molded parts, but the new structure UEA adopts a resin film. In addition, use of a sandwich structure at the junctions between the film and the electrodes enabled elimination of the impregnation (Bonding) process that melted the resin to create a physical joint in the previous model. The adoption of film coated with sealant that has finished primary curing as the material also enabled shortening of the adhesive Curing process time so that it completes within the Lamination process time. This realized integrated processing of the two types of electrodes and the resin film, and consolidated the UEA assembly process from three processes into a single process. In addition, the Electrode trimming, UEA trimming, and Cell stacking processes were fully automated, and technology that conforms to the specifications was developed for the UEA Inspection process. This achieved shorter and more uniform cycle times.

Furthermore, as stable material input is needed to realize a fully automated line, technology was applied to reliably pick and place sheet film material, as shown in Fig. 10. This film material is packed in containers in the flat stacked condition alternating with interleaf so that foreign matter does not adhere to the adhesive part. The film and interleaf are in close contact inside the container, and thus there was the issue that when the robot removes the interleaf, the film below may stick and be removed together with the interleaf. Therefore, a mechanism was adopted to pinch and peel off a part of the interleaf while holding down the periphery, as shown in Fig. 11, which realized stable pick and place operation.

The above realized a fully automated line from electrode roll loading to cell stacking, which increased production efficiency with 1/8 of the personnel and 1/3 of the depreciation cost per cell compared with the previous line.

3.3. Simplification of Stack Structure

The structural parts of the previous stack are divided into cell stack parts and structural parts that protect the cells, as shown in Fig. 12. The cell stack parts consist of

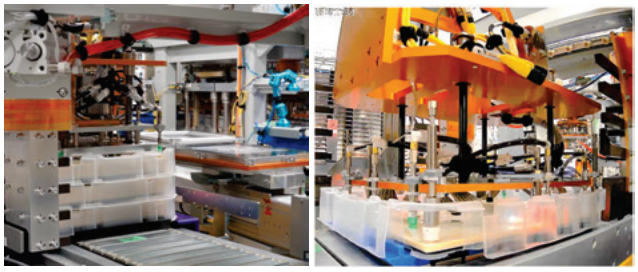


Fig. 10 Pick and place hand

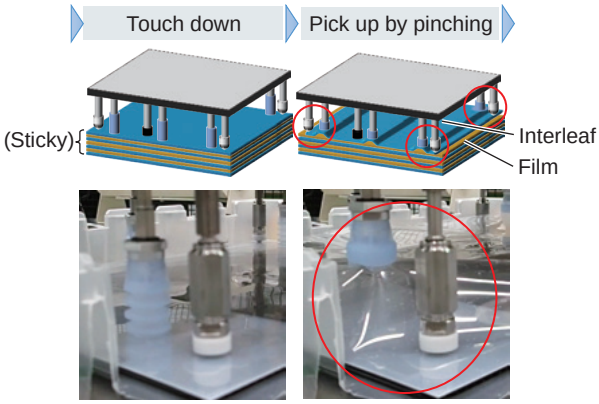


Fig. 11 Pick up by pinching

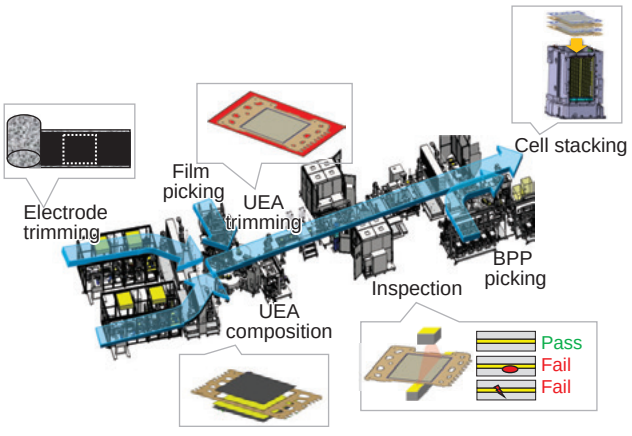


Fig. 9 Overview of new production line

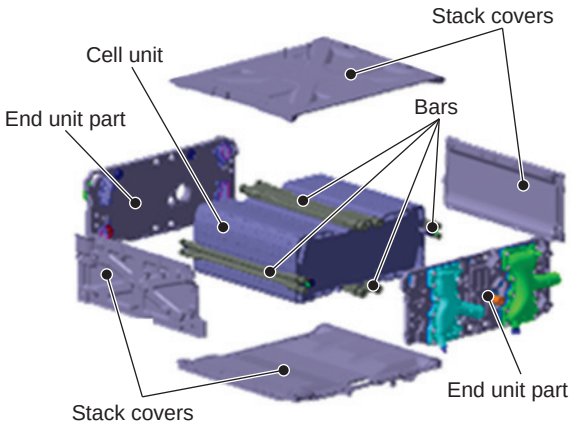


Fig. 12 Previous stack structure

the end unit parts and four bars that are used to stack the cells, and the structural parts that protect the cells are four stack covers that cover the outside of the cell stack. In order to use fewer parts, the new structure fuel cell stack has a stack case structure that performs the cell stacking and cell protective functions and integrates the four bars and stack covers of the previous stack into a single structure. This consolidated eight parts into one, as shown in Fig. 13.

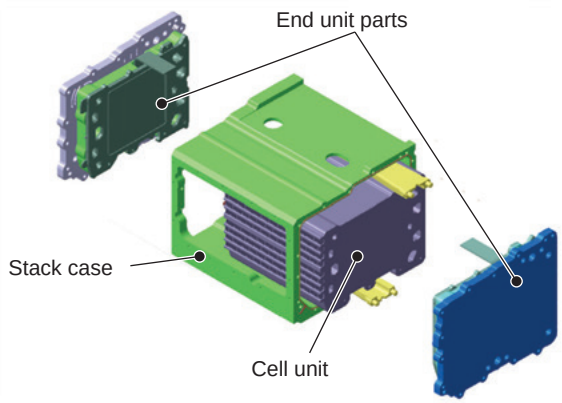


Fig. 13 New stack structure

4. Enhancement of Fuel Cell Stack Durability

The new structure fuel cell stack applies the following technologies to achieve twice the durability or greater through a combination of stack structure and control.

- Enhanced PEM durability by temperature and humidity control
- Less iron elution by changing the BPP coating
- Enhanced cooling performance by changing the BPP cooling structure and changing the aspect ratio
- Enhanced thermal insulation of stack end unit parts and measures to help prevent the entry of water from auxiliary device flow channels

4.1. Enhanced PEM Durability by Temperature and Humidity Control

It is known that when the PEM of a polymer electrolyte fuel cell contains an insufficient amount of water in the condition with a high membrane temperature, the chemical stability of the membrane drops, resulting in rapid decomposition[12]. This makes it necessary to maintain an appropriate membrane temperature and humidity. In order to achieve a lower coolant temperature, the amount of coolant is electrically controlled by an auxiliary device with enhanced performance[15]. In addition, use of a proprietary model to estimate the transfer rate of the water contained in the input air with high accuracy realized auxiliary device control that enables to suppress membrane degradation and maintain the optimum humidity.

4.2. Less Iron Elution by Changing the BPP Coating

Chemical deterioration of the PEM of a polymer electrolyte fuel cell progresses when contaminated by iron[11], and thus less iron elution from the BPP substrate is needed. The BPP structure uses a full-surface coating of carbon and titanium that suppresses exposure of the stainless steel base material, achieving 1/10 of the iron elution and increasing corrosion resistance.

4.3. Enhanced Cooling Performance by Changing the BPP Cooling Structure and Changing the Aspect Ratio

The new structure fuel cell stack uses a structure that successively stacks BPP and UEA, and flows hydrogen and air between the UEA and BPP and coolant inside the BPP, as shown in Fig. 14.

As shown in Fig. 15(a), the previous structure flowed coolant every two cells, meaning that some cells did not contact the coolant. The new structure adopts a cell-by-cell cooling structure in which the coolant comes into contact with every cell, as shown in Fig. 15(b). This achieved a lower temperature difference between cells.

In addition, the aspect ratio of the cell power generation part was changed, making it easier to achieve more even in-plane flow of the coolant inside the cells. This combination

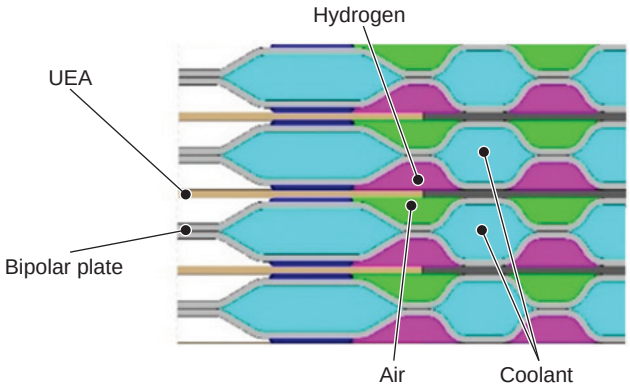


Fig. 14 Structure of cell unit in new stack

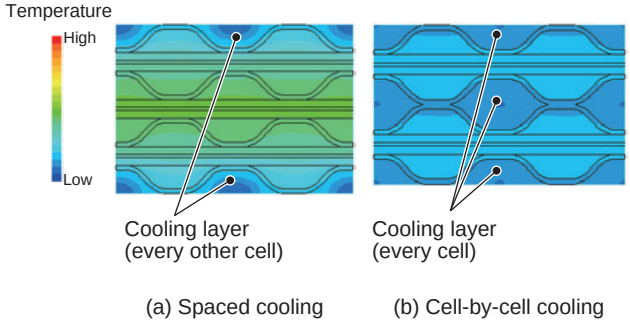


Fig. 15 Temperature distribution inside cell predicted by CFD

of the change in the cell cooling structure and the cell aspect ratio also lessened the in-plane temperature difference in both the horizontal and vertical directions, as shown in Fig. 16, and enhanced the cooling performance.

4.4. Enhanced Thermal Insulation of Stack End Unit Parts and Measures to Help Prevent the Entry of Water from Auxiliary Device Flow Channels

If the voltage becomes unstable, the electrodes degrade, leading to a drop in durability. In order to perform stable power generation, it is necessary to provide the stack end unit parts with thermal insulation performance and to help prevent the entry of water from the flow channels of auxiliary devices into the air and hydrogen flow channels of the fuel cell stack. In the new structure fuel cell stack, the thermal insulation effect was enhanced by providing insulator thickness, which helped to suppress the temperature drop due to natural heat dissipation from the cell end unit parts and achieve less temperature variance between cell layers. In addition, if water from the outside enters the UEA, power generation may become unstable, which is a factor resulting in lower UEA durability. Therefore, a water guiding channel was made in part of the insulator, as shown in Fig. 17, to realize a structure where water does not enter the UEA.

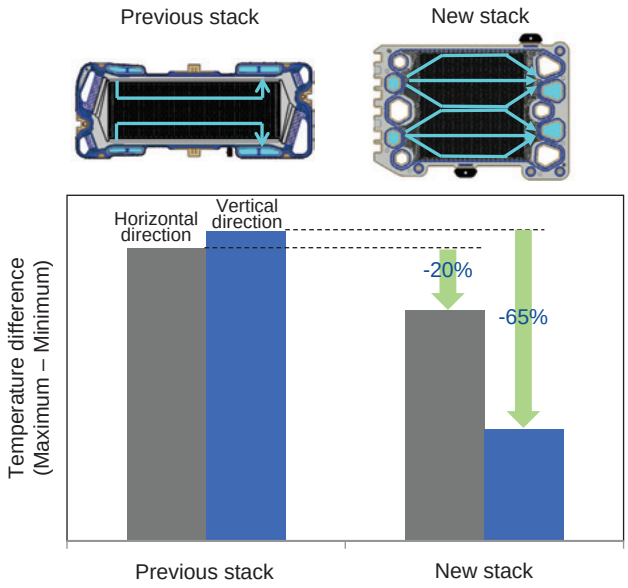


Fig. 16 Effect of changing cell aspect ratio

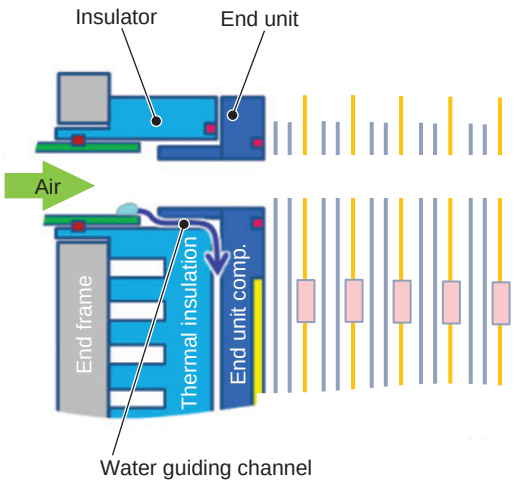


Fig. 17 New fuel cell stack end structure

5. Conclusion

This paper introduced a fuel cell stack with a new structure developed jointly with General Motors. The features of the newly introduced technologies compared with the previous fuel cell stack are summarized below.

(1) Introduction of the following technologies helped to suppress PEM degradation and increase durability.
- Enhancement of the cooling efficiency helped to reduce auxiliary device power consumption and equalize the PEM temperature, suppressing membrane degradation.
- Review of the BPP base material and the UEA coating material achieved lower cost and also suppressed iron elution to 1/10 or less of the previous stack.
- Review of auxiliary devices and flow channel structures enabled appropriate control of the amount of water vapor in the supply gas and the amount of water exhaust.

These technologies helped to suppress PEM degradation.

(2) Technologies such as the following helped to reduce the number of parts and shorten the production time, etc., resulting in lower cost.
- By increasing the current density of the UEA and lowering the power consumption of auxiliary devices, 15% fewer cell layers are needed compared with a previous fuel cell stack of the same output.
- Adoption of new BPP and UEA shapes achieved a simpler structure and enhanced cooling efficiency.
- The times required for each cell assembly line process could be leveled, which helped to realize full automation of the entire production process and enabled shortening of the production time.

As a result, the newly developed fuel cell stack achieved twice the durability at 1/3 of the cost while maintaining the same net power as the previous system.

References

(1) https://www.env.go.jp/content/000126429.pdf, (accessed 2024/7/9)
(2) https://www.meti.go.jp/shingikai/enecho/shoene_shinene/suiso_seisaku/pdf/20230606_2.pdf, (accessed 2024/7/9)
(3) https://global.honda/jp/hydrogen/, (accessed 2024/7/9)
(4) Kawasaki, S., Ogura, M., Ono, T., Kami, Y.:

Development of the Honda FCX Fuel Cell Vehicle, Honda R&D Technical Review, Vol. 15, No. 1, p. 1-6
(5) Ogawa, T., Kimura, K., Uchibori, K., Fujimoto, S., Shimizu, K.: Development of New Power Train for Honda FCX Fuel Cell Vehicle, Honda R&D Technical Review, Vol. 15, No. 1, p. 7-12
(6) Kawasaki, S., Uchibori, K., Murakami, Y., Shimizu, K., Fujimoto, S.: Development of New Honda FCX with Next-generation Fuel Cell Stack, Honda R&D Technical Review, Vol. 18, No. 1, p. 45-50
(7) Matsunaga, M., Fukushima, T., Ojima, K., Kimura, K., Ogawa, T.: Fuel Cell Powertrain for FCX Clarity, Honda R&D Technical Review, Vol. 21, No. 1, p. 7-15
(8) Kimura, K., Kawasaki, T., Ohmura, T., Atsumi, Y., Shimizu, K.: Development of New Fuel Cell Vehicle CLARITY FUEL CELL, Honda R&D Technical Review, Vol. 28, No. 1, p. 1-8
(9) Kikuchi, H., Kaji, H., Nishiyama, T., Okonogi, D., Harata, H.: Development of New FC Stack for CLARITY FUEL CELL, Honda R&D Technical Review, Vol. 28, No. 2, p. 45-52
(10) https://global.honda/jp/tech/Hydrogen_Fuel_Cell_System_FC/, (accessed 2024/7/9)
(11) Zatoń, M., Rozière, J., Jones, D. J.: Current understanding of chemical degradation mechanisms of perfluorosulfonic acid membranes and their mitigation strategies: a review, Sustainable Energy & Fuels, Royal Society of Chemistry, Vol. 1, Issue 3, p. 409-438, (2017), doi: 10.1039/C7SE00038C
(12) Perry, M. L., Daring, R. M., Kandoi, S., Patterson, T. W., Reiser, C.: Operating Requirements for Durable Polymer-Electrolyte Fuel Cell Stacks, Polymer Electrolyte Fuel Cell Durability, Springer, p. 399-417, (2009), doi: 10.1007/978-0-387-85536-3_20
(13) Nunokawa, K., Shinkai, H., Oyama, S., Ishida, K., Goto, S.: Development of High-durability and Low-cost Fuel Cell Bipolar Plate, Honda R&D Technical Review, Vol. 37, p. 34-40
(14) Kato, T., Nakahara, A., Ohkura, T., Yamamoto, M., Terada, S., Noda, A., Kanaoka, N.: Development of High-durability and Low-cost UEA for Fuel Cell Stack, Honda R&D Technical Review, Vol. 37, p. 27-33
(15) Ozaki, H., Yamazaki, K., Ogawa, T., Maniwa, S., Miura, T., Huston, T. W.: Development of New Fuel Cell System, Honda R&D Technical Review, Vol. 37, p. 13-19

Author


Choichi ISHIKAWA


Manabu IWAIDA


Hideharu NAITO


Shigeru INAI


Hiromichi YOSHIDA


Nobuyoshi MUROMOTO

Development of High-durability and Low-cost UEA for Fuel Cell Stack

Takashi KATO[1] Akira NAKAHARA[1] Takuya OHKURA[1]
Masakuni YAMAMOTO[1] Satoru TERADA[1] Akihiro NODA, Ph.D.[1]
Nagayuki KANAOKA[2]

ABSTRACT

Honda's newly structured fuel cell stack features a Unitized Electrode Assembly, which consists of a Membrane Electrode Assembly that generates electricity and an outer resin frame structure. Specifications of the Unitized Electrode Assembly were developed that have greater durability and lower cost than the previous fuel cell stack, while maintaining its output performance. Specifically, the amount of Pt was reduced to 1/5 that of the previous specifications due to increased activity by using a Pt alloy catalyst for the electrode catalyst, and the thickness of the electrolyte membrane was reduced to 3/5. For the outer resin structure, the cost was reduced to less than half that of the previous injection-molded product by using a general-purpose resin film.

As for the durability associated with the above-mentioned changes, the researchers developed degradation models for the various components of the Unitized Electrode Assembly and worked to increase the accuracy of those models. These efforts achieved both increased durability and lower costs by reflecting the material specification limit ranges in operation control based on the models obtained.

1. Introduction

Global warming has become so severe that in July 2023, UN Secretary-General António Guterres warned that the earth has entered the era of global boiling(1). At COP28, the 28th Conference of the Parties, in 2023, it became clear that humanity is falling short of achieving the 1.5°C target of the Paris Agreement adopted at COP21 in 2015(2). Meanwhile, moves are underway to reduce and absorb greenhouse gas emissions, which are a factor in rising temperatures.

Hydrogen, in particular, is important to help achieve not only carbon neutrality but also energy resilience(3).

Focusing on the potential of hydrogen energy, Honda began basic research on fuel cells in the late 1980s. Today, there is an urgent need to further increase durability and lower costs for a wide variety of applications, including not just passenger cars but also commercial vehicles and stationary power sources.

Against this background, Honda and General Motors have jointly developed a newly structured fuel cell stack that is more than twice as durable and has only 1/3 the cost of the previous fuel cell stack, while maintaining its output performance(4).

The Unitized Electrode Assembly (UEA) consists of a Membrane Electrode Assembly (MEA) that generates electricity and its outer resin frame structure. The previous UEA used a large amount of platinum (Pt) in the electrode catalyst and ionomer components, which are fluorinated polymer electrolytes that play a role in proton transport. These help to ensure durability, but also have a big impact on costs. Moreover, injection molding was used for the outer resin structure due to the configuration of the power generation cells. This requires a thickness of at least 250 μm to help ensure formability, and thus it was not easy to increase the power density by making the cells thinner.

2. Development Goals

The structure of the UEA in the previous stack is shown in Fig. 1. The power generation cell consists of two UEAs sandwiched within three stainless steel (SUS) separators(5). A stack consists of several hundred of these power generation cells stacked on top of each other. The

[1] Innovative Research Excellence, Power Unit & Energy
E-mail: takashi_kato@jp.honda
[2] American Honda Motor Co., Inc.

UEA consists of the MEA and an outer resin structure. The material cost breakdown of the previous UEA is shown in Fig. 2. As Fig. 2 shows, the cathode catalyst and electrolyte membrane make up a high percentage of the cost. Pt in the electrode catalyst, and ionomer, the main component of the electrolyte membrane, are expensive and not effective to mass-produce, and thus reducing use of these components is an effective way to lower the cost of the UEA.

Meanwhile, the gas diffusion layer (GDL) has the third greatest impact on cost, and in this case mass production seemed likely to reduce costs. Therefore, the researchers focused instead on simplifying the structure of the outer resin structure, which has the fourth greatest impact on cost. The outer resin structure can increase the power density.

Therefore, the goal of this development was to achieve the following while maintaining the same or greater output performance and durability of the previous fuel cell stack.

(1) Reduce the amount of Pt in the electrode catalyst
(2) Reduce the amount of ionomer in the electrolyte membrane
(3) Simplify the structure of the outer resin structure

In addition, the durability of the MEA is inversely related to the reduction in the amount of Pt and ionomer used[6]-[7], and thus ensuring durability while reducing costs is a challenge. For each UEA component, a degradation model was developed that can quantitatively represent the impact on durability and material degradation factors. Based on these models, controlling the operating environment so it is appropriate for each material's specification limits helped to ensure durability.

The structure of the UEA of the newly structured stack is shown in Fig. 3. The power generation cell consists of a single UEA sandwiched between two bipolar plates (BPPs)[4]. The technology that increased the UEA's durability and reduced its costs is discussed below.

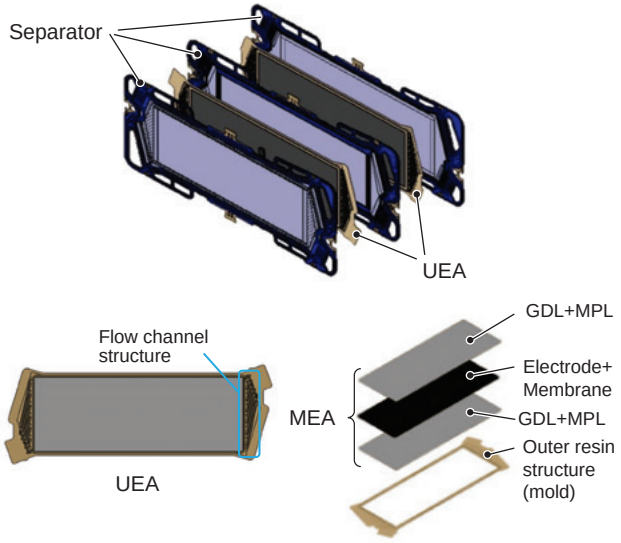


Fig. 1 Structure of previous power generation cell and UEA

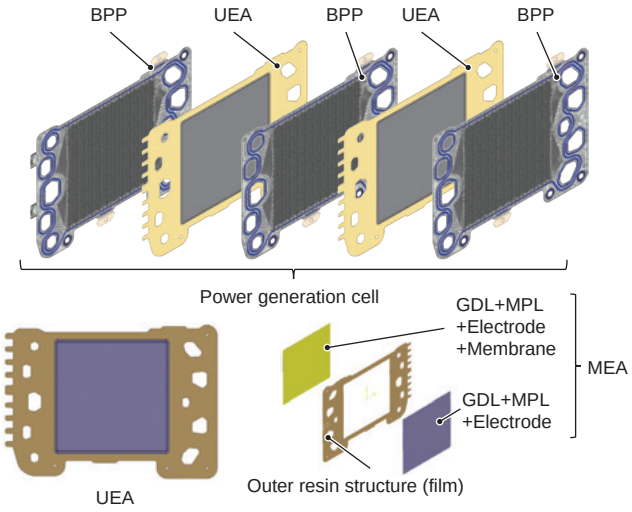


Fig. 3 Structure of new power generation cell and UEA

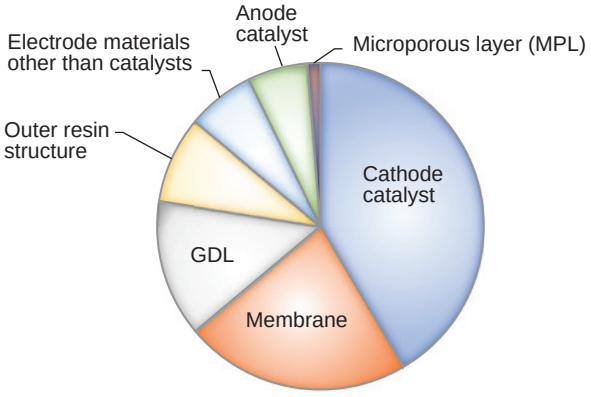


Fig. 2 Material cost breakdown in previous UEA

3. Reducing the Amount of Pt in the Electrode Catalyst

3.1. Pt Alloy Catalyst

Pt, a precious metal, is used in electrode catalysts. Therefore, reducing the amount of Pt is an effective way to reduce costs. However, reducing the amount of Pt also reduces the effective Pt surface area for generating power, resulting in lower power generation performance. Power generation performance is determined by multiplying the effective Pt surface area for generating power by the catalytic activity[8]. For that reason, a Pt alloy catalyst with high catalytic activity was adopted to increase activity as

compared to the Pt catalyst used in the previous UEA. The effect of using Pt alloy catalyst to increase performance is shown in Fig. 4. Porous carbon was used to support the Pt alloy, and Pt alloy particles were also supported in the carbon pores where ionomer could not penetrate. This suppresses catalyst poisoning by the ionomer[9], while the use of Pt alloy increases the efficiency of the oxygen reduction reaction[10], and as a result, activity is increased to more than double that of the previous Pt catalyst. The Pt alloy catalyst achieved the same catalytic activity as the previous catalyst, and thus the Pt surface area needed to obtain the same cell voltage as the Pt catalyst was reduced to about 1/4 that of the previous catalyst. In addition, to help ensure output, the voltage drop that may occur when the current density is increased needs to be suppressed. To suppress the voltage drop, the Pt alloy supporting rate was reduced to 3/5, which helped to ensure the oxygen reduction reaction at high current density and achieve the target cell output. Furthermore, a degradation model was developed as described in the next section to control the operating environment appropriately and suppress performance degradation.

As a result of the above, the amount of Pt per stack was reduced to 1/5, while the same power generation performance as before was maintained.

3.2. Suppression of Electrode Catalyst Degradation

Reducing the amount of Pt has a great impact on the cell voltage drop due to the decrease in effective Pt surface area for generating power. This makes it necessary to suppress the decrease in effective Pt surface area for generating power due to electrode degradation.

The mechanism of electrode catalyst degradation is shown in Fig. 5. In the power generation range of a fuel cell (0.6 to 0.8 V), the Pt surface is oxidized or reduced due to voltage fluctuations caused by load changes, and the Pt surface area decreases due to Ostwald growth, in which Pt repeatedly elutes and precipitates. When the voltage exceeds 0.85 V during startup or when power is being generated close to the open-circuit voltage, the amount of elution due to Pt oxidation increases. Furthermore, it is known that the presence of oxygen at the anode electrode during startup raises the cathode potential to about 1.5 V, which increases the Pt particle size and in addition degrades the carbon carrier[11]. Therefore, controls were implemented to help prevent the anode electrode from having an air environment during shutdown, which suppresses the rise in cathode potential. In addition, a degradation model was developed for the degradation that can happen during operation. Then, degradation was suppressed by setting certain operating conditions, such as lowering the temperature in conjunction with the electrolyte membrane as described below.

The electrode degradation model was developed by using a single cell with a power generation area of approximately 50 cm^2 and conducting durability tests using the experimental design method to confirm the degradation factors and their effect. Results of checking the impact of potential and hold time on degradation are shown in Fig. 6.

The effects of temperature and humidity were also confirmed by the experimental design method, similar to Fig. 6. A model consisting of temperature, humidity, and potential was developed as shown in Eq. (1). The higher the temperature, humidity, and potential, the greater the acceleration of degradation[12].

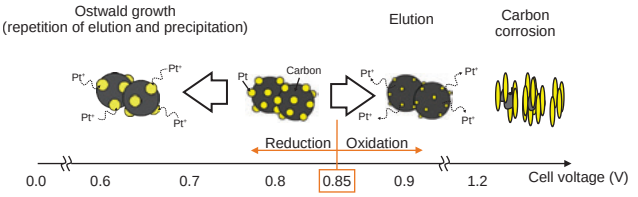


Fig. 5 Mechanism of electrode catalyst degradation

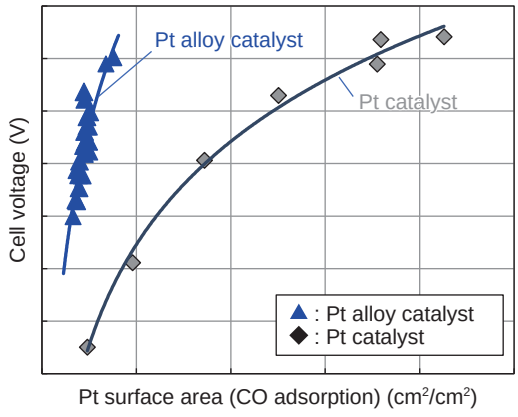


Fig. 4 Performance comparison of Pt catalyst and Pt alloy catalyst

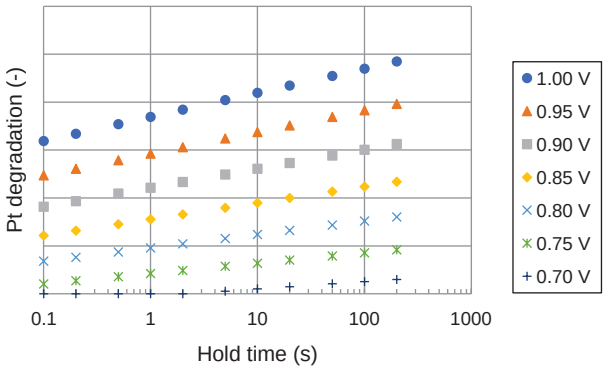


Fig. 6 Effect of potential and time on Pt degradation at 80°C

$$\theta_i = k_i(V, t) \times k_{Temp}(V, Temp) \times k_{RH}(V, RH) - r_i(V, t) \times r_{Temp}(V, Temp) \times r_{RH}(V, RH) \quad (1)$$

θ_i : Amount of decrease of effective Pt surface area for generating power
t : Time
$Temp$: Temperature
RH : Humidity
V : Potential
k : Coefficient on high-voltage side
r : Coefficient on low-voltage side

Figure 7 compares the effective Pt surface area for generating power as calculated in Eq. (1) based on operating history during FC system durability testing with actual values measured after durability testing was completed. Although the target performance was achieved, the measured results showed degradation had progressed more than predicted by the model. This may be because the temperature used in the calculations from the operating history is the temperature of the cooling water. This is because, due to the heat generated by overvoltage, the temperature near the catalyst is higher than the cooling water temperature. Using this discrepancy between actual and predicted values as the performance yields a difference of approximately 5 kW, but it was confirmed that the necessary durability was achieved. In future, a further increase in the accuracy of predictions of remaining life will be necessary.

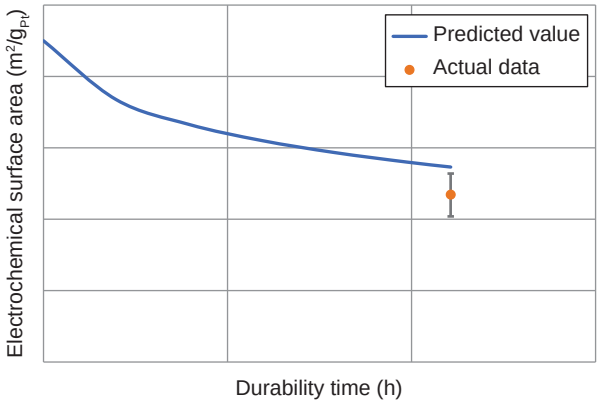


Fig. 7 Comparison of actual and predicted electrode degradation during FC system durability testing

4. Reducing the Amount of Ionomer in the Electrolyte Membrane

4.1. Thinner Electrolyte Membrane

Aside from reducing costs, a thinner electrolyte membrane would be an effective way to increase power generation performance by increasing proton conductivity and to increase water transfer from the cathode to the anode, thereby helping to ensure membrane water retention and suppress flooding in the power generation cell. However, as the electrolyte membrane needs to function as a gas barrier between the cathode and anode, a thinner membrane increases the amount of gas permeation, which could reduce fuel economy. For that reason, after considering power generation performance and the impact to fuel consumption, the thickness of the electrolyte membrane was reduced to 3/5 that of the previous stack by addressing the chemical and mechanical degradation associated with thinner membranes and by employing a new proprietary MEA coating process and formulation.

4.2. Dealing with Chemical Degradation of Electrolyte Membranes

There is both chemical and mechanical degradation of electrolyte membranes[13]. The mechanism of chemical degradation of the electrolyte membrane is shown in Fig. 8. OH radicals are formed by a reaction of H_2O_2, which is a byproduct of the power generation reaction, with Fe ions, etc. OH radicals can cause an unzipping reaction, in which the main chain ends of the electrolyte membrane are attacked, and main-chain scission, leading to a decline in the molecular weight. When main-chain scission occurs, the number of terminal groups increases, which promotes degradation at an accelerated rate[14]. Degradation is known to accelerate the higher the temperature and lower the humidification[15]. The formation of H_2O_2, which is how degradation begins, is also thought to be greatly affected by the amount of oxygen that permeates from the cathode side to the anode side. A reduction in membrane thickness increases the amount of gas permeation, which may accelerate degradation.

From the degradation mechanism shown in Fig. 8, the effects of temperature and humidity, as well as current and O_2 partial pressure, were confirmed using the experimental

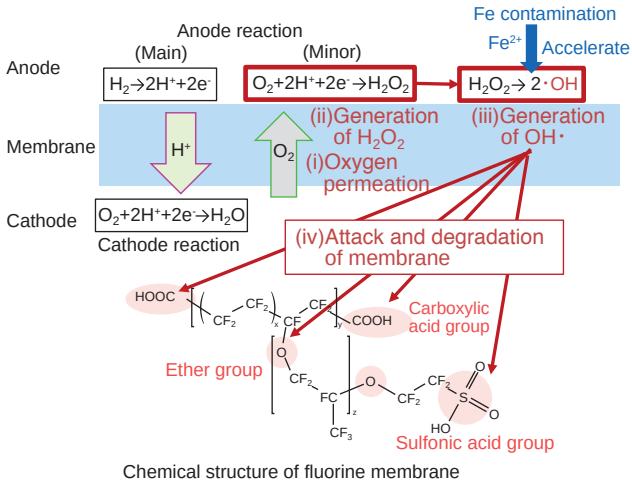


Fig. 8 Mechanism of membrane chemical degradation

design method in a single cell, similar to electrode degradation, and the electrolyte membrane degradation model shown in Eq. (2) was developed. Equation (2) shows the amount of chemical degradation stress, while Eq. (3) shows the relationship between the amount of stress and molecular weight retention rate. As with the electrodes, a degradation model was developed for durability, and the operating environment was controlled to help ensure it.

$$S_C = exp(C_{Temp} \times Temp + C_{RH} \times RH + C_J \times J + C_1) \times C_{P_{O2}} \times P_{O2} \quad (2)$$

$$Mw = exp(C_{Sc} \times S_C \times t) + C_2 \quad (3)$$

Sc : Chemical degradation stress
Mw : Molecular weight retention rate
t : Time
Temp : Temperature
RH : Humidity
J : Current density
P_{O2} : O_2 partial pressure
C : Coefficient for each degradation factor

As Eq. (2) shows, the degradation model consists of temperature, humidity, current density, and oxygen partial pressure. In particular, as low humidity accelerates membrane degradation all at once, operation is controlled so that the humidity input to the stack is kept above a certain level to help ensure durability[16].

Figure 9 compares the electrolyte membrane's molecular weight retention rate as calculated in Eqs. (2) and (3) based on operating history during FC system durability testing with actual values measured after durability testing was completed. The range of measured values indicates variation among measured values at multiple locations by their stacking position and within the cell plane. The measured values show that degradation progressed more than the predicted values suggested. Although it was confirmed that the necessary durability was maintained, this discrepancy is presumed to be because of accelerated degradation caused by Fe contamination. It has been confirmed that when deterioration acceleration caused by the maximum amount of Fe mixed in during durability testing is taken into account, it nearly matches the lower limit of variation of actual measured values.

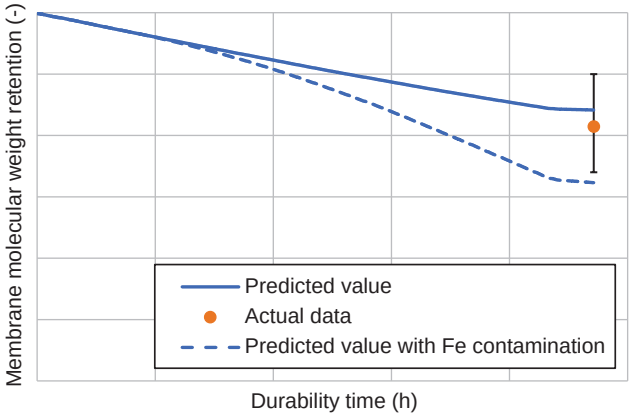


Fig. 9 Comparison of actual and predicted membrane degradation during FC system durability testing

4.3. Dealing with Mechanical Degradation of Electrolyte Membranes

Mechanical degradation of the electrolyte membrane caused by repeated swelling and shrinking of the electrolyte membrane due to changes in humidity is accelerated by cracks in the electrode[17].

The frequency of electrode cracks themselves was suppressed by using a more suitable electrode ink composition and by quality control of the surface properties. In addition, the use of high-strength membrane reinforcement increased the toughness of the electrolyte membrane against degradation stresses that may occur at cracks, thereby suppressing the impact of cracks.

5. Simplifying the Structure of the Outer Resin Structure

5.1. Resin Film

To simplify the structure of the outer resin structure, the flow channel structure was integrated with the separator, helping to eliminate the need for a flow channel structure in the resin frame of the UEA. In this UEA, the outer structure was simplified by switching to punch-molded general-purpose resin film[18]. Because film could be used, a structure was adopted in which a general-purpose resin film with a linear expansion coefficient close to that of SUS, the material used for the BPPs, is laminated together to form the UEA structure shown in Fig. 3.

Previously, precision injection molding was used, with expensive engineering plastic. Because of its molding properties, injection molding required a thickness of 250 μm or more, but using general-purpose resin film made it possible to reduce this thickness by more than 50%, which helped increase the volumetric output density. It also cut the cost per piece in half compared with the previous cost.

5.2. Strength Durability

As Fig. 3 shows, the resin film is sandwiched between BPPs. When power is being generated, stress may occur in the resin film due to the gas pressure differential between the cathode and anode gases flowing in the BPP flow channel. The resin film retention interval distance by BPPs was set to relieve the stress. Moreover, in fuel cells, where water is generated by the process of power generation, hydrolysis causes chemical degradation. For that reason, the mechanical strength was designed for the gas pressure differential between the cathode and anode, taking into

account the reduction in resin film strength due to chemical degradation.

Finite element method simulation was performed on the gas pressure differential. As Fig. 10 shows, the simulation confirmed the relationship between stress and the retention interval distance by BPPs. The stress was suppressed by controlling the distance between the restraints with BPPs. As a result, sufficient strength durability was achieved.

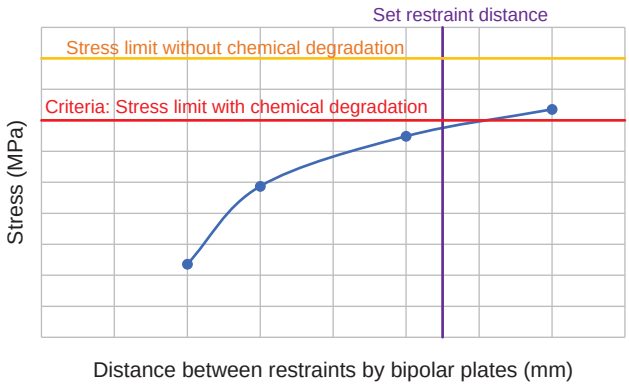


Fig. 10 Relationship between stress and retention interval distance by BPP

6. Conclusion

The low-cost UEA used in the newly structured fuel cell stack was developed in collaboration with General Motors and achieved the following compared with the previous UEA. It is more than twice as durable and has only 1/3 the cost of the previous fuel cell stack, while maintaining the previous fuel cell stack's output performance[4].

(1) By using Pt alloy catalyst, porous carbon, and a low supporting rate, which were predicted to inhibit degradation, the amount of Pt in electrodes was reduced to 1/5 that of the previous UEA.
(2) The thickness of the electrolyte membrane was reduced to 3/5 that of the previous fuel cell stack by addressing chemical and mechanical degradation and by using a proprietary coating process.
(3) By simplifying the structure of the outer resin structure, a resin film with a thickness reduced by half could be used.

References

(1) https://press.un.org/en/2023/sgsm21893.doc.htm, (accessed 2024/5/31)
(2) https://www.enecho.meti.go.jp/about/special/johoteikyo/cop28_01.html, (accessed 2024/5/31)
(3) https://www.enecho.meti.go.jp/about/whitepaper/2021/html/1-3-2.html, (accessed 2024/5/31)
(4) Ishikawa, C., Iwaida, M., Naito, H., Inai, S., Yoshida, H., Muromoto, N.: High-durability and Cost-effective Fuel Cell Stack with New Structure, Honda R&D Technical Review, Vol. 37, p. 20-26
(5) Kikuchi, H., Kaji, H., Nishiyama, T., Okonogi, D., Harata, H.: Development of New FC Stack for CLARITY FUEL CELL, Honda R&D Technical Review, Vol. 28, No. 2, p. 45-52
(6) Kocha, S. S.: Chapter 3 - Electrochemical Degradation: Electrocatalyst and Support Durability, Polymer Electrolyte Fuel Cell Degradation, ACADEMIC PRESS, p. 89-214, (2012), doi: 10.1016/B978-0-12-386936-4.10003-X
(7) Zatoń, M., Rozière, J., Jones, D. J.: Current understanding of chemical degradation mechanisms of perfluorosulfonic acid membranes and their mitigation strategies: a review, Sustainable Energy & Fuels, Royal Society of Chemistry, Vol. 1, Issue 3, p. 409-438, (2017), doi: 10.1039/C7SE00038C
(8) Vielstich, W.: Ch. 43 Proton exchange membrane fuel cell (PEMFC) down-the-channel performance model, Handbook of Fuel Cells: Advances in Electrocatalysis, Materials, Diagnostics and Durability, Wiley, Vol. 5 and 6, p. 631, (2009)
(9) Toyoda, A., Takahashi, T., Ida, A., Okumura, M., Nakamura, K., Yamashita, A.: Dai Ni Sedai Nenryo Denchi Sisutemu no Kaihatsu, 56th Kikai Shinkoushou Jyushousha Gyouseki Gaiyou, p. 25-28, (2922) (in Japanese), http://www.jspmi.or.jp/system/file/3/1381/N56-07.pdf, (accessed 2024/5/31)
(10) Toda, T., Igarashi, H., Uchida, H., Watanabe, M.: Enhancement of the Electroreduction of Oxygen on Pt Alloys with Fe, Ni, and Co, Journal of The Electrochemical Society, Vol. 146 No. 10, p. 3750-3756, (1999), doi: 10.1149/1.1392544
(11) Reiser, C. A., Bregoli, L., Patterson, T. W., Yi, J. S., Yang, J. D., Perry, M. L., Jarvi, T. J.: A Reverse-Current Decay Mechanism for Fuel Cells, Electrochemical and Solid-State Letters, Vol. 8, No. 6, p. A273-A276, (2005), doi: 10.1149/1.1896466
(12) Yamamoto, M., Matsumori, H.: Empirical Model for Polymer Electrolyte Fuel Cell Electrocatalyst Degaradation Using Platinum Stress, Honda R&D Technical Review, Vol. 28, No. 1, p. 41-49
(13) Jinnouchi, R.; Nenryo Denchi no Genri to Ouyou, Asakura Publishing Co., Ltd., 280p., (2023) (in Japanese)
(14) Hommura, S., Kawahara, K., Shimohira, T., Teraoka, Y.: Development of a Method for Clarifying the Perfluorosulfonated Membrane Degradation Mechanism in a Fuel Cell Environment, Journal of The Electrochemical Society, Vol. 155, No. 1, p. A29-A33, (2008), doi: 10.1149/1.2800171
(15) Perry, M. L., Daring, R. M., Kandoi, S., Patterson, T. W., Reiser, C.: Operating Requirements for Durable Polymer-Electrolyte Fuel Cell Stacks, Polymer

Electrolyte Fuel Cell Durability, Springer, p. 399-417, (2009), doi: 10.1007/978-0-387-85536-3_20
(16) Ozaki, H., Yamazaki, K., Ogawa, T., Maniwa, S., Miura, T., Huston, T. W.: Development of New Fuel Cell System, Honda R&D Technical Review, Vol. 37, p. 13-19
(17) Uchiyama, T., Kato, M., Ikogi, Y., Yoshida, T.: Mechanical Degradation Mechanism of Membrane Electrode Assemblies in Buckling Test Under Humidity Cycles, Journal of Fuel Cell Science and Technology, ASME, Vol. 9, Issue 6, 061005 (8 pages), (2012), doi: 10.1115/1.4007814
(18) https://global.honda/jp/tech/Hydrogen_Fuel_Cell_System_FC/, (accessed 2024/5/31)

Author


Takashi KATO


Akira NAKAHARA


Takuya OHKURA


Masakuni YAMAMOTO


Satoru TERADA


Akihiro NODA


Nagayuki KANAOKA

Development of High-durability and Low-cost Fuel Cell Bipolar Plate

Kazuo NUNOKAWA[1] Hiroshi SHINKAI[1] Satoshi OYAMA[2]
Kentaro ISHIDA[1] Shuhei GOTO[1]

ABSTRACT

A bipolar plate for a new structure fuel cell stack was developed jointly with General Motors Company. In order to achieve both lower cost and higher productivity while enhancing the functionality of the bipolar plate in this study, a bipolar plate structure that assumes high-cycle molding was developed. A coating consisting of carbon and titanium is applied to the stainless steel base material before stamping. The seal structure was changed from a multilayer rubber seal structure to a metal bead seal structure formed by stamping after coating and a welded seal structure. In addition, a structure without a rubber coating was adopted for high-cycle molding.

1. Introduction

Fuel cells are anticipated as circulation-type clean plants that do not emit CO_2 or harmful substances in order to address global warming and energy issues[(1)]. Honda has been working on the practical application of fuel cell technology since the 1980s[(2)]. This paper discusses the bipolar plate (BPP), which is one of the parts comprising the multilayer cell applied to a new structure fuel cell stack[(3)]. The multilayer cell adopts a cell structure that holds a single Unitized Electrode Assembly (UEA) with two BPPs and flows coolant, as shown in Fig. 1.

Figure 2 shows the functions demanded of the BPP.

(1) Supply hydrogen and oxygen gases to the UEA
(2) Flow coolant to cool the BPP and UEA
(3) Seal the hydrogen, oxygen, and coolant
(4) Provide conductivity between cells
(5) Provide corrosion resistance in the power generation environment

In addition, the BPP and UEA account for a high proportion of the cost ratio of a conventional fuel cell stack, as shown in Fig. 3.

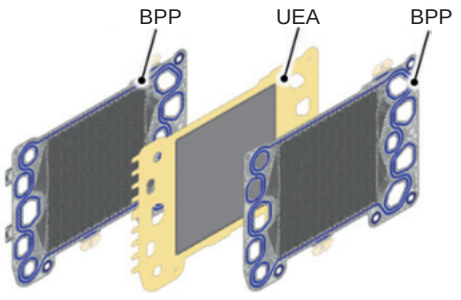


Fig. 1 Structure of BPP and UEA

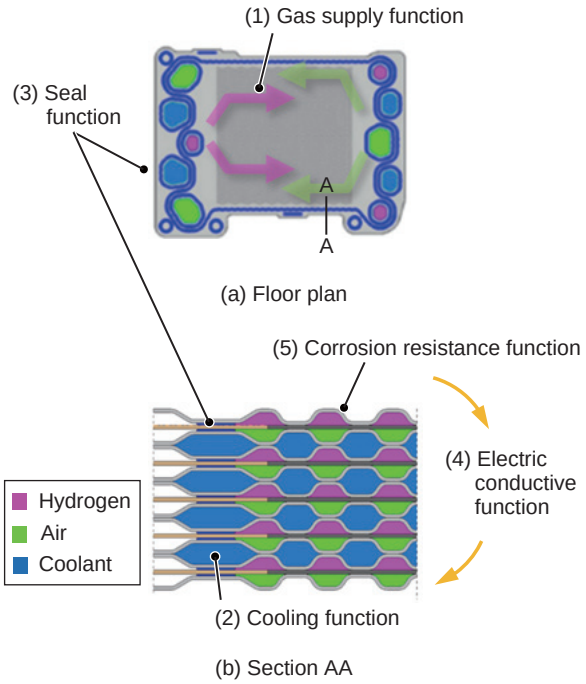


Fig. 2 Main functions of BPP

[1] Innovative Research Excellence, Power Unit & Energy
E-mail: kazuo_nunokawa@jp.honda
[2] Honda Motor Co., Ltd.

The breakdown of the BPP cost structure shows that sealing, coating, and stamping costs account for a high proportion, and lowering these costs was an issue. The conventional BPP[4] adopted a rubber seal structure using injection molding for the seal function, which resulted in a longer production cycle time and was an issue for mass production. Additional issues included the use of precious metals in coatings for corrosion resistance, and many coating quality inspections in BPP molding.

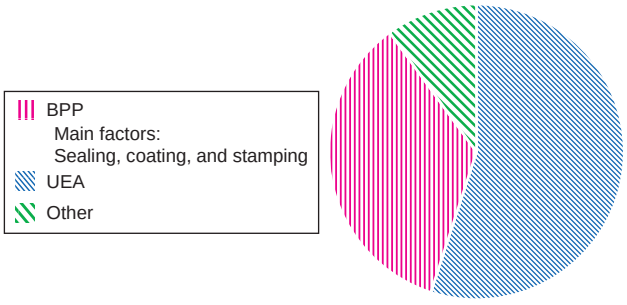


Fig. 3 Breakdown of conventional fuel cell stack cost

2. Development Goals

In order to achieve both lower cost and higher productivity while enhancing functionality compared to the conventional structure, a BPP structure that assumes high-cycle molding was developed.

Figure 4 shows a table comparing the conventional and new BPP structures. In order to achieve the target production volume set as a new structure, a seal structure that simplifies the manufacturing and inspection processes was needed. Therefore, the multilayer rubber seal structure was changed to a metal bead seal and welded seal structure. It was also necessary to achieve lower coating material and processing costs. Therefore, the coil was changed from the conventional gold-plating coating to a graphite-like carbon (GLC) coating.

The conventional BPP provided insulation with a perimeter rubber coating structure, but the new structure sets creepage and clearance distances and adopts a structure without a perimeter rubber coating, which enabled elimination of the insulation inspection process.

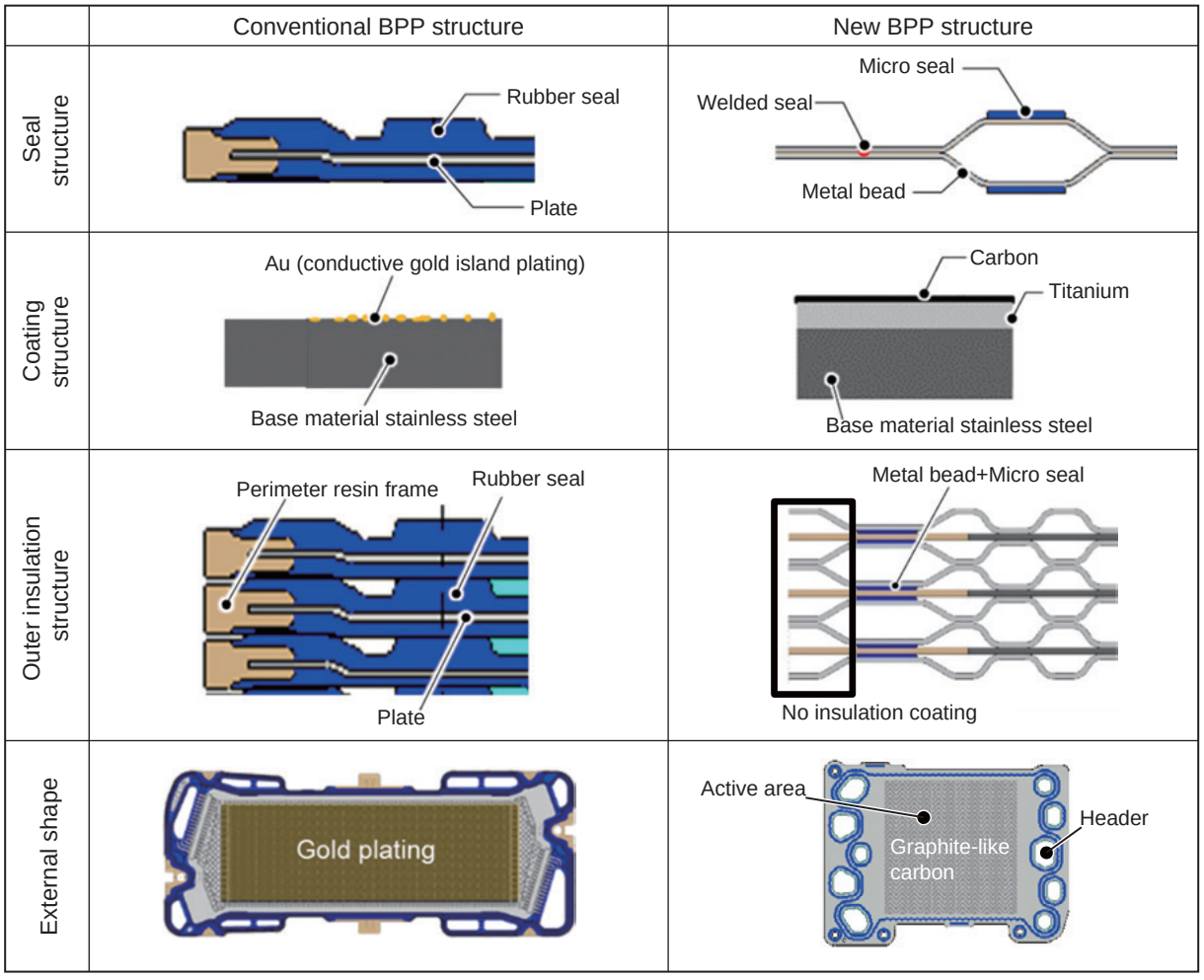


Fig. 4 Comparison of conventional and new BPP structures

3. Features of New BPP Structure

3.1. Feasibility of Metal Bead and Welded Seal Structure

The metal bead seal (MBS) structure consists of (a) metal bead parts molded by stamping and (b) micro seal rubber, as shown in Fig. 5, and seals by the reaction force in lamination and compression. In addition, cooling channels are formed by (c) welding Plate-A and Plate-B.

3.1.1. MBS structure settings

In MBS structures that make use of metallic elasticity, there is the issue that if the bead is subjected to a high load, the necessary seal line pressure may not be achieved due to plastic deformation, and gas or coolant may leak. The line pressure is the value obtained by dividing the load generated on the seal part by the length of the seal line.

When the vehicle vibrates in driving, the vibration also propagates to the stack, and a high load is generated on the BPP seal parts. A bead cross-sectional shape was set that can generate the line pressure needed to keep the seal function even in this case. Furthermore, the deceleration in a vehicle collision generates an internal load, and thus a shape that receives the load on the periphery of the BPP was provided, as shown in Fig. 6, to help prevent plastic deformation of the metal beads.

The compressive load characteristics of the MBS structure vary depending on the cross-sectional shape of the bead and the planar layout of the seal line. The compressive load characteristics can be changed by adjusting the bead cross-sectional shape (bead width), as shown in Fig. 7. The compressive load characteristics can also be changed according to the plane radius and angle of the seal line, as shown in Fig. 8. The above characteristics were used to achieve a design with uniform in-plane characteristics, which helped to prevent leaks due to local reduction of seal line pressure.

3.1.2. 2Hit stamping of flow channel area and MBS

In the new BPP structure, the amount of flow channel area warpage increases in stamping, resulting in uneven contact pressure in lamination and increasing the contact resistance of the active area. Therefore, measures were taken to increase the compressive load characteristics of the MBS.

As shown in Fig. 9, the reason for the flow channel warpage is that the inside of the flow channel stamp area becomes longer than the outside of the flow channel stamp area in the direction perpendicular to the flow channels. This difference is produced by springback in flow channel stamping.

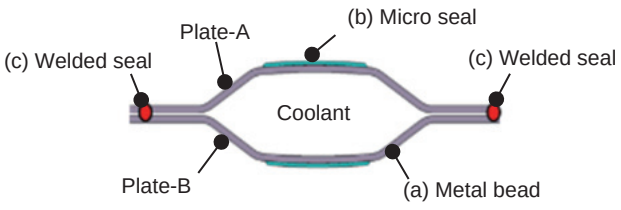


Fig. 5 Cross-sectional structure of MBS

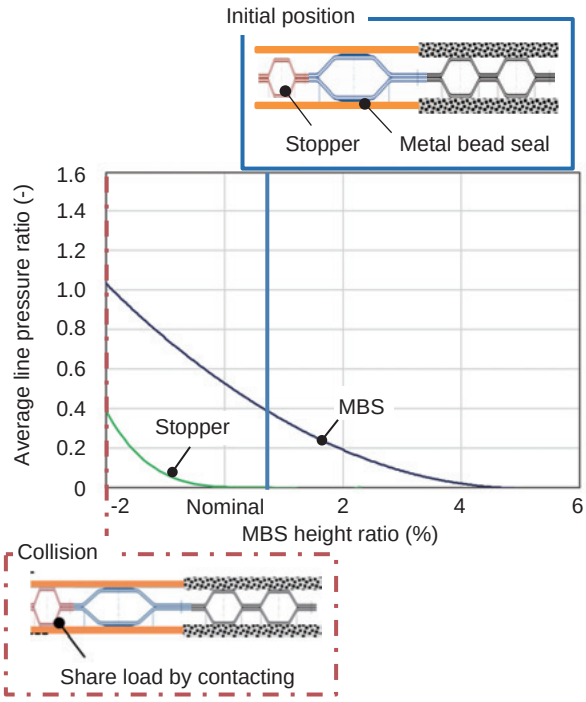


Fig. 6 MBS and stopper line pressure

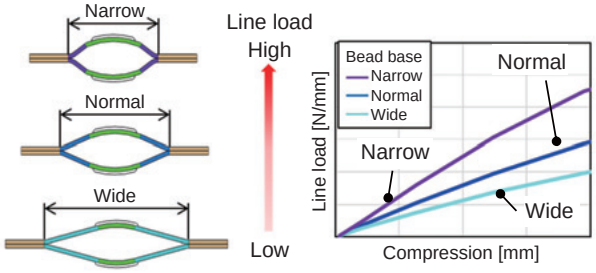


Fig. 7 Metal bead width and line load property

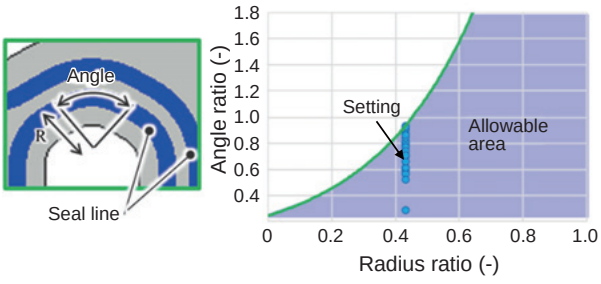


Fig. 8 Plane radius and angle setting

As a countermeasure, the flow channel stamping process was divided into two stages, as shown in Fig. 10. A two-stage stamping process flow channel structure was adopted in which the springback produced in the first stamping process stage (1Hit) is absorbed by bending the ridge line in the second stage (2Hit).

When the contact pressure of the active area was checked with Fuji film paper, this was confirmed to have the effect of helping to reduce contact pressure variance, as shown in Fig. 11. As shown in Fig. 12, the amount of flow channel area warpage was lower for 2Hit stamping specifications compared to only 1Hit stamping.

Next, in order to increase the MBS strength, a 2Hit-type structure was adopted within the same process as flow channel stamping, and work hardening of the base material was applied. A 2Hit metal bead seal structure was adopted that applies work hardening to the entire cross section by stamping the center of the MBS in the first stage and stamps the final MBS shape in the second stage, as shown in Fig. 13.

This increased the strength had the effect of increasing the most amount of the compressive load characteristics of the MBS, as shown in Fig. 14.

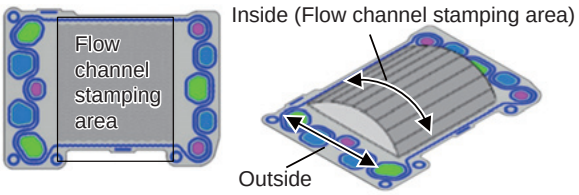


Fig. 9 Image of stamping area springback

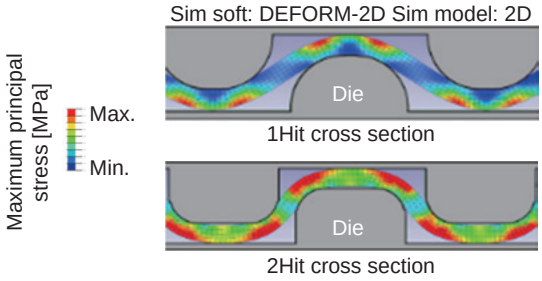


Fig. 10 1Hit and 2Hit of flow channel stamping process

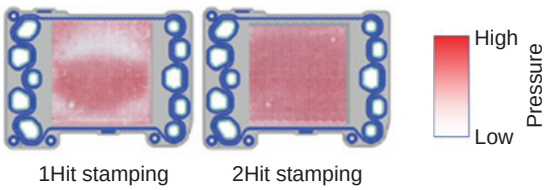


Fig. 11 Pressure of active area

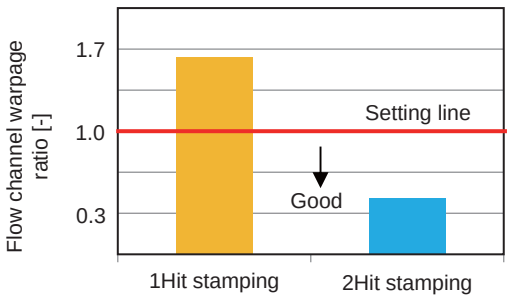


Fig. 12 Warpage of flow channel

3.1.3. Micro seal settings

The new BPP structure has a structure with micro seals placed on top of metal beads, as shown in Fig. 5. This results in a structure that can help lessen the drop in the seal line pressure due to compression set and keep the seal function as shown in Fig. 15. However, a thin seal makes it a challenge to keep the seal function in the event that foreign matter contaminates the seal in manufacturing.

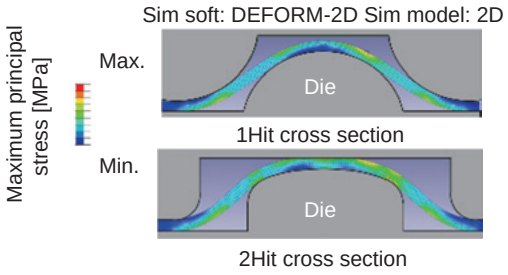


Fig. 13 1Hit and 2Hit of MBS stamping process

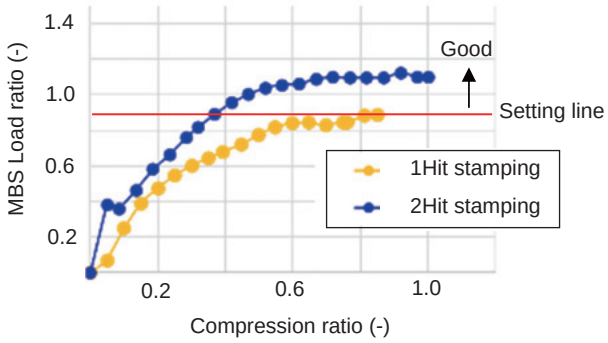


Fig. 14 MBS load characteristics

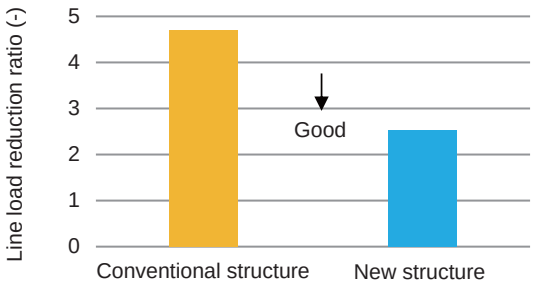


Fig. 15 Line load reduction comparison

Reduction of contamination by foreign matter calls for manufacture in a clean environment, but this is a factor that increases manufacturing costs. Therefore, the optimal thickness and width of the micro seal were set as shown in Fig. 16 based on the seal thickness that can keep the seal function even in the event of contamination by foreign matter and the manufacturing environment control conditions.

3.1.4. Welded seal structure settings

The BPP interface adopts a structure in which the coolant is sealed by joining the plates together by welding, as shown in Fig. 5. The weld width is defined as the faying length (FL), as shown in Fig. 17. The FL is set to provide bonding strength, as shown in Fig. 18, so that the joint does not break even when the operating pressure of the gas and coolant is applied to the weld.

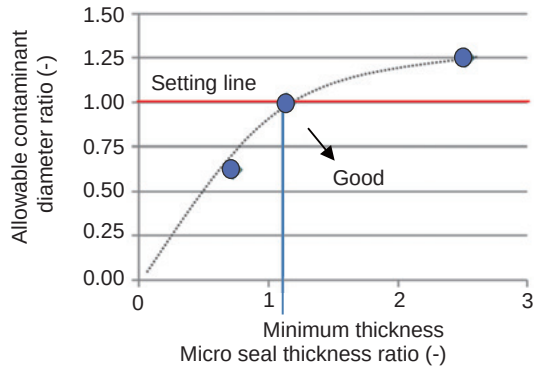


Fig. 16 Micro seal thickness setting

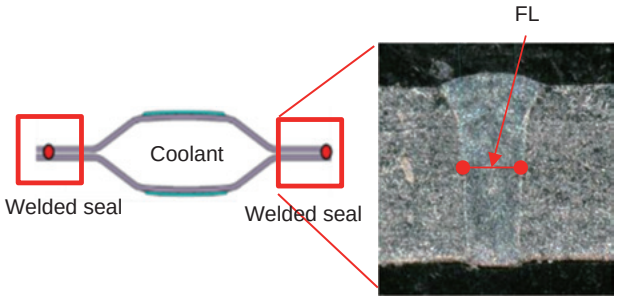


Fig. 17 FL Cross-sectional structure

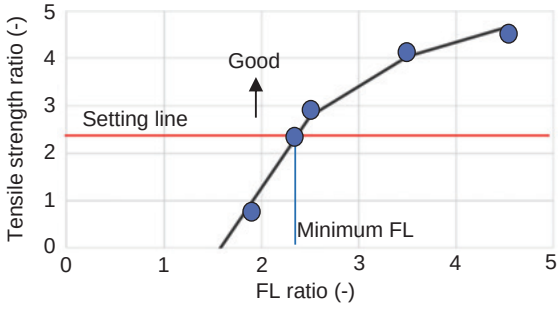


Fig. 18 FL and tensile strength

On the other hand, the bonding strength of the weld is generally enhanced by increasing the amount of heat input in welding to increase the width of the joint. However, large welding heat input may result in BPP warpage, which is a seal inconsistency factor. Therefore, the welding heat input condition was set to satisfy the amount of BPP warpage, as shown in Fig. 19. In addition, sensitization may occur in stainless steel welding[5]. Sensitization may cause stress corrosion cracking with the result that the seal function cannot be kept, so the welding conditions are set to help reduce the possibility of sensitization.

3.2. Achievement of Both Lower Cost and Corrosion Resistance Function with GLC Coating

In the conventional BPP, the surface of the stainless steel is treated with gold (sea-island structure gold plating) and then a passive film is formed on the exposed stainless steel areas to achieve both conductivity and corrosion resistance.

BPPs generally use stainless steel as the base material, and it is known that in an acidic corrosive environment with high temperature and humidity, iron ions are eluted due to damage to the passive film in the exposed stainless steel areas, which can reduce the durability of the ion exchange film[6]. This calls for enhancement of corrosion resistance performance for BPPs with stainless steel as the base material.

The newly developed BPP enhances corrosion resistance while suppressing exposure of the stainless steel base material and providing conductivity by coating the stainless steel base material with a GLC layer and an intermediate titanium (Ti) layer, which are less expensive than the conventional gold treatment, as described in Fig. 4 in the previous chapter.

In addition, the GLC layer and intermediate Ti layer are continuously coated on the stainless steel base material, and there is no need to coat the BPP by batch processing after stamping, which enhances production efficiency. The GLC layer and intermediate Ti layer provide reliable corrosion resistance, and coating with GLC and Ti layers helped to reduce the amount of iron ion elution to about 1/30 that of stainless steel even in an acidic corrosive environment with

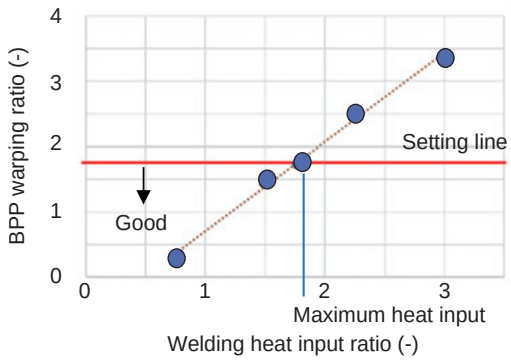


Fig. 19 BPP warpage by welding heat input

high temperature and humidity.

By contrast, if stamping is performed after surface treatment, the GLC layer and intermediate Ti layer become cracked due to elongation of the base material in stamping and scratched due to rubbing against the die, and exposure of the stainless steel base material was confirmed, as shown in Fig. 20.

It is known that the amount of iron ion elution from the BPP depends on the degree of exposure of the stainless steel base material. Therefore, when setting the cross-sectional shape of the flow channel, it is important to set a shape that takes into account elongation of the base material in stamping in order to suppress the degree of exposure of the stainless steel base material. By suppressing the stainless steel exposure ratio after stamping, the newly developed BPP achieved an amount of iron ion elution 1/10 that of conventional BPPs, as shown in Fig. 21, which also helped to lower the coating process cost.

3.3. Establishment of High-cycle Stamping of Flow Channel and Metal Bead Seal Parts

3.3.1. Elimination of resin molding and insulation inspection process

Conventional BPPs provided insulation with a perimeter rubber coating structure, but the new structure sets creepage and clearance distances based on IEC60664-1[(7)] for the cell (power generation parts), as shown in Fig. 22. In addition, adoption of a structure without a perimeter rubber coating enabled elimination of the insulation inspection process. Compared to the previous model, this helped to reduce the amount of rubber used by 6% per cell and the amount of resin used by 54%.

It also helped to reduce the resin molding and insulation inspection processes.

3.3.2. Productivity concept

Figure 23 shows the production process flow for the conventional and new structures. Surface treatment

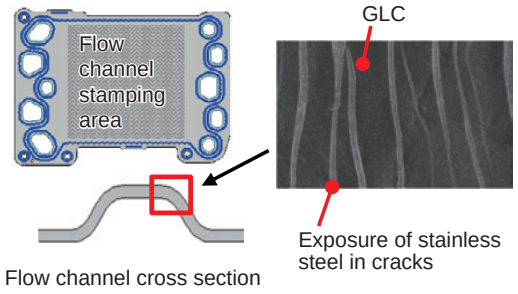


Fig. 20 Coating cracks on surface of flow channel

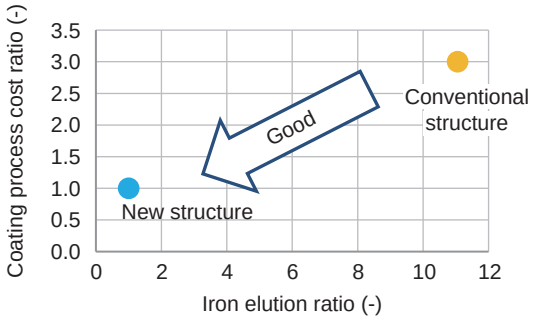


Fig. 21 Iron elution of BPP

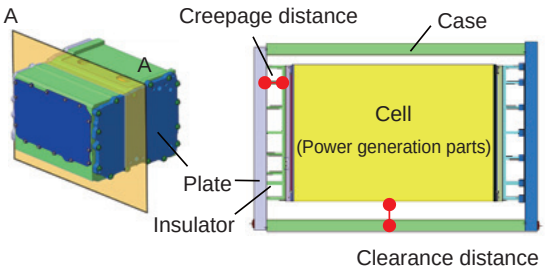


Fig. 22 Layout of creepage and clearance distances

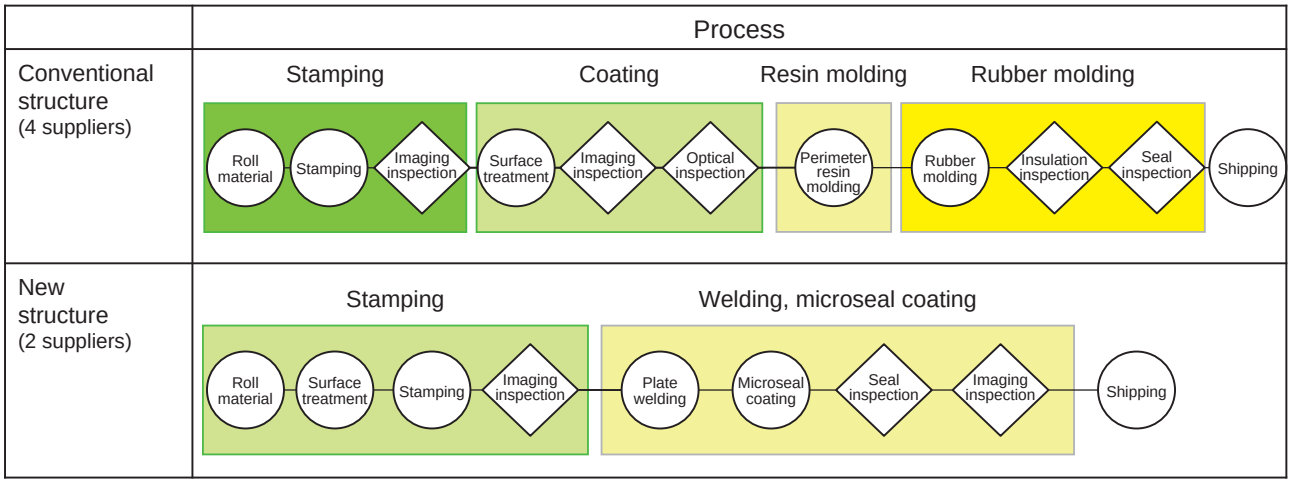


Fig. 23 Comparison of BPP processes between conventional and new structures

was conventionally performed in a separate process after stamping, but with the new structure, stamping is performed with a GLC-coated coil, which enables shortening of the process time while enhancing the cycle time.

Figure 24 shows the details of the MBS and flow channel area stamping process. The aforementioned 2Hit stamping is performed, and the laser engraving and inspection processes for quality control are fully automated.

By fully automating the resin molding, insulation inspection, laser engraving, and inspection processes, the new BPP structure achieved a production cycle time 1/20 that of the previous structure.

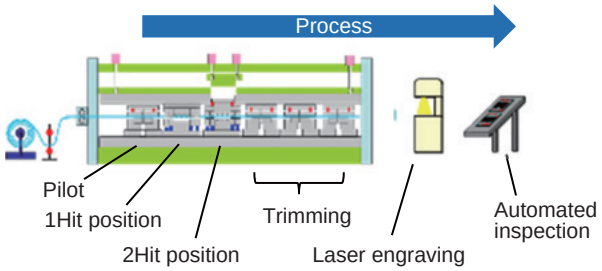


Fig. 24 Progressive stamping process flow

4. Conclusion

By enhancing productivity and reviewing materials and functions, a new BPP structure was developed that simultaneously achieves the seal function, corrosion resistance performance, and cost reduction. The following results were obtained.

(1) The metal bead parts were designed with a cross-sectional shape and planar layout that provide uniform in-plane compressive load characteristics, and a load-bearing structure was provided to enhance sealing performance in a collision. In addition, use of a metal bead and micro seal structure achieved a structure that can help lessen the drop in the line pressure and provide the seal function. The welding conditions of the welded seal part were set to help prevent BPP warpage and sensitization and to provide bonding strength.

(2) A 2Hit die structure is adopted and springback in stamping is suppressed to enhance flow channel warpage. At the same time, the metal bead seal parts were also changed to a 2Hit die structure and work hardening was added, enabling enhancement of the compressive load properties of the MBS.

(3) By applying a GLC coating to the coil and adopting a shape that takes into account the flow channels and suppresses the degree of exposure of the stainless steel in stamping, the amount of iron ion elution could be reduced to 1/10 that of the conventional structure.

(4) With the new structure, stamping is performed with a GLC-coated coil, which enabled shortening of the process time while enhancing the cycle time. In addition, creepage and clearance distances based on IEC60664-1 were set for the cell (power generation parts), and a structure without a perimeter rubber coating was adopted.

References

(1) https://global.honda/jp/stories/057.html, (accessed 2024/6/12)

(2) Matsunaga, M., Fukushima, T., Ojima, K., Kimura, K., Ogawa, T.: Fuel Cell Powertrain for FCX Clarity, Honda R&D Technical Review, Vol. 21, No. 1, p. 7-15

(3) Ishikawa, C., Iwaida, M., Naito, H., Inai, S., Yoshida, H., Muromoto, N.: High-durability and Cost-effective Fuel Cell Stack with New Structure, Honda R&D Technical Review, Vol. 37, p. 20-26

(4) Kikuchi, H., Kaji, H., Nishiyama, T., Okonogi, D., Harata, H.: Development of New FC Stack for CLARITY FUEL CELL, Honda R&D Technical Review, Vol. 28, No. 2, p. 45-52

(5) Nakazawa, T., Suzuki, S., Tanaka, Y., Komatsu, H.: Effect of High Temperature Dynamic Strain on Grain Boundary Sensitization in Type 304 Stainless Steels, The journal of the Japan Institute of Metals and Materials, Vol. 62, No. 9, p. 812-819, (1998) (in Japanese), doi: 10.2320/jinstmet1952.62.9_812

(6) Zatoń, M., Rozière, J., Jones, D. J.: Current understanding of chemical degradation mechanisms of perfluorosulfonic acid membranes and their mitigation strategies: a review, Sustainable Energy & Fuels, Royal Society of Chemistry, Vol. 1, Issue 3, p. 409-438, (2017), doi: 10.1039/C7SE00038C

(7) JIS C 60664-1: 2009, Insulation coordination for equipment within low-voltage systems - Part 1: Principles, requirements and tests

■ Author ■


Kazuo NUNOKAWA


Hiroshi SHINKAI


Satoshi OYAMA


Kentaro ISHIDA


Shuhei GOTO

High-speed Inspection Technology for Fuel Cell MEAs Using Split-terminal Resistance Measurement System

Hiroaki KAWANISHI[1] Hiroyuki YAMAGISHI[2] Kensuke NANBA[1]

ABSTRACT

New fuel cell stacks are being developed with the aim of improving productivity while maintaining the same quality for mass production. In particular, the time it takes to perform shorting inspection of the membrane electrode assembly is an issue that limits productivity, so development has been conducted to help reduce this time. Conventional shorting inspection on flat bases detects the electrical characteristic values of the entire membrane electrode assembly. In this approach, signals of local short circuits are small relative to the change in detected value due to the charge, and thus they could not be judged until the change was complete. In the development discussed in this paper, the detection sensitivity for signals in each local area was increased by using a split-terminal base. Shorting signals greater than the charge change were successfully detected locally. This lowered the impact on the inspection judgment, and the measurement waiting time caused by charging was lowered by 87% compared with the conventional method. In addition, the researchers developed an algorithm for synthesizing peripheral currents to deal with the misjudgment factor of a short circuit in the terminal gap, which presented an issue in the use of split bases. As a result, inspection total time was reduced to 10 seconds, thus contributing greatly to increasing cell productivity.

1. Fuel Cell Stacks

Fuel cells are expected to be used as a circular clean system for achieving carbon neutrality[(1)].

Honda has been working on the practical application of FC technology since the 1980s[(2)-(5)]. In 2016, it introduced the CLARITY FUEL CELL[(6), (7)] with the conventional fuel cell system.

For the next stage, Honda partnered with General Motors to develop a new fuel cell system that helped ensure high durability and low cost and thus helped enable deployment in diverse markets, including commercial vehicles, construction machinery, and stationary power sources[(8)]. With the production line for this newly structured fuel cell stack, the researchers achieved a fully automated assembly line, from electrode roll feeding to cell stacking[(9)].

As Fig. 1 shows, polymer electrolyte fuel cells convert chemical energy directly into electrical energy through an electrochemical reaction between hydrogen and oxygen. The formula for the chemical reaction is as follows.

Hydrogen electrode (–): $2H_2 \rightarrow 4H^+ + 4e^-$
Oxygen electrode (+): $O_2 + 4H^+ + 4e^- \rightarrow 2H_2O$

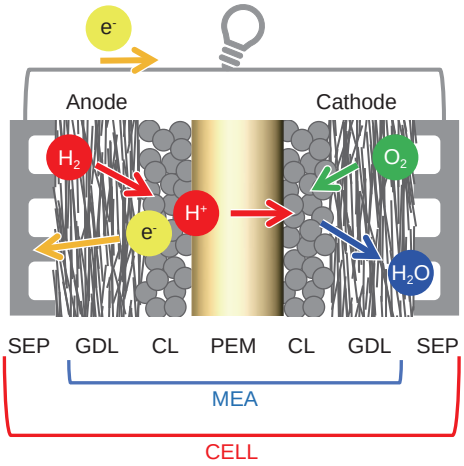


Fig. 1 Mechanism of electricity generation in FC stack

[1] Innovative Research Excellence, Power Unit & Energy
E-mail: hiroaki_kawanishi@jp.honda
[2] Honda Motor Co., Ltd.

A polymer electrolyte membrane (PEM), the conductor of hydrogen ions, is sandwiched between two catalyst layers (CL) and gas diffusion layers (GDL) for the hydrogen electrode and the oxygen electrode (air electrode), forming a membrane electrode assembly (MEA). This MEA is sandwiched between two separators (SEP), one on either side, and the structure is called a cell. These cells are stacked and fastened together to form a fuel cell stack.

2. Issues with Shorting Inspection

2.1. MEA Shorting Phenomena

Output performance and durability are key to fuel cell stack performance, and elements for maintaining them are the insulating quality of the electrolyte membrane and the function of shutting off gas. An example of a phenomenon that interferes with the insulating properties of the electrolyte membrane is the conduction between electrodes due to fibrous contamination, as in Fig. 2. Such conduction can cause electricity to flow between the electrodes, which may lead to a decline in electromotive force, and pinholes in the membrane when high voltage is applied between the electrodes, which can cause cross leakage of hydrogen and oxygen. This is why shorting inspection is performed.

2.2. Conventional MEA Shorting Inspection Technique

Because a short circuit in the electrolyte membrane can cause a drop in cell voltage and degradation of membrane durability, the following steps are performed in the conventional model using the shorting inspection system shown in Fig. 3 to confirm that there are no more than a certain number of short circuits.

The inspection steps are:

1. Clamp a pair of parallel plate electrodes with a constant load
2. Apply direct current with a constant voltage
3. Apply a charge until the measured value stabilizes
4. Measure the value of the current flowing between the two electrodes after charging
5. Judge as Pass or Fail relative to a threshold value

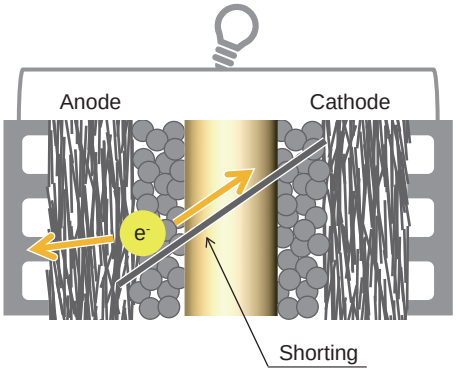


Fig. 2 Imaged figure of MEA shorting

The takt times for the conventional MEA shorting inspection process are shown in Fig. 4. The charging process accounts for 80% of the inspection time, and thus this is the rate-limiting process. This is because the MEA has a capacitor structure in which the insulator PEM is sandwiched from both sides by the conductor GDLs and CLs and has capacitance. To show the impact that capacitance has on judgment, Fig. 5 shows the change in the measured values of MEA current that resulted in a judgment of Fail in the inspection, and the conventional MEA shorting inspection threshold. This shows that the change in current value is saturated and that it takes about 20 seconds until a judgment can be made.

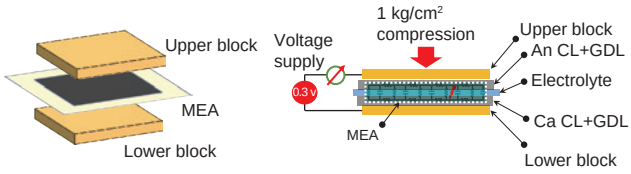


Fig. 3 Shorting inspection system of Honda's previous model

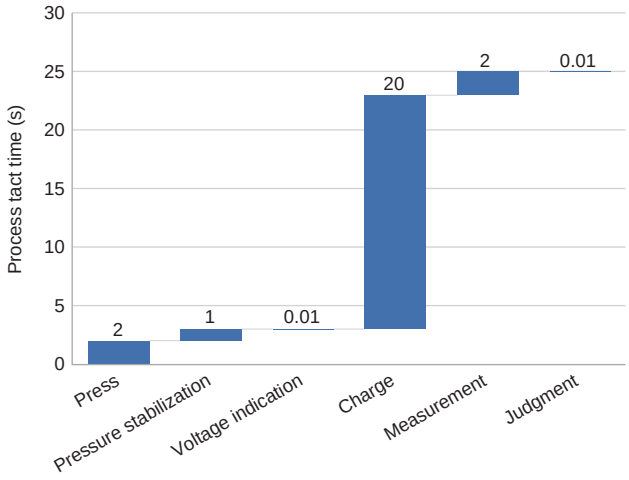


Fig. 4 Takt time of each process in shorting inspection

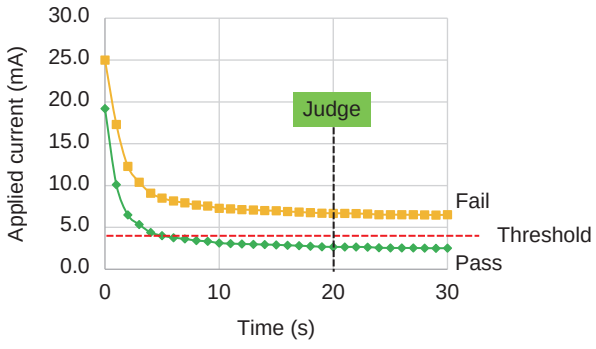


Fig. 5 Variation of measured values due to charging

3. Devising a Split Shorting Inspection System

In order to achieve greater productivity than that of conventional fuel cell stacks, the researchers focused on reducing the time required for charging, which is the rate-limiting step in the shorting inspection process, and devised a split-terminal base that extracts local shorting signals and lowers the impact of charging.

A common method to shorten charging time is to increase the applied current and voltage[10]. However, this method was already used when developing the conventional method and resulted in a charge time of 20 seconds, and thus no great advancement can be expected. Therefore, speeding up MEA shorting inspection required a method other than increasing the amount of charge to the capacitor component of the MEA.

Next, when measuring with the conventional uniform plate shown in Fig. 3, an issue is that the inrush current to a large-area capacitor is relatively large compared to the current of local short circuits. Before presenting a solution, an electrical schematic of the MEA is given below. The electrical properties of the MEA are considered to be an internal resistance resulting from the material, in addition to shorting resistance and capacitance. An electrical schematic of the MEA is given in Fig. 6. In a circuit where the locations with shorting and locations without it are separated from each other, as shown in the figure, the shorting signal is anticipated to be locally greater than the other components. As a solution, the authors actively extracted the shorting signal flowing locally, and worked to develop technology as described below to shorten the measurement waiting time resulting from charging by making the short circuit detection value relatively large compared to the change resulting from the charge.

(1) Develop a split-terminal base for extracting voltage of shorting signals[11]
(2) Develop an algorithm to synthesize shorting voltage generated at the split terminal gap[12]

These will be described in turn in the following sections of the paper.

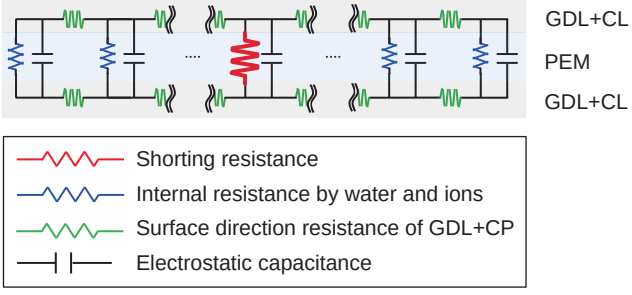


Fig. 6 Electrical schematic of MEA

4. Development of a Split-terminal Base

4.1. Basic Concept of the Split-terminal Base Device

Figure 7 shows the basic concept of the device, in which a multi-channel tester (R-5800i) from Nidec Advance Technology Corporation is connected to the inspection device circuit and voltage meter on a split-terminal base. In the measurement system that is used, shunt resistors whose resistance is known with high accuracy are connected under the split terminals, and the voltage across shunt resistance is measured to calculate the resistance of the MEA.

The following equation is used to calculate the local MEA resistance based on the ratio of series resistance and voltage.

$$\Omega_{MEA} = \frac{\Omega_{shunt} \cdot V}{V_{shunt}} - \Omega_{shunt}$$

Ω_{MEA}: MEA resistance (Ω)
Ω_{shunt}: Shunt resistance (Ω)
V: Voltage supplied from power supply (V)
V_{shunt}: Voltage across shunt resistance (V)

The following is a description of the verification to determine the specifications of the device capable of extracting shorting signals based on the basic concept.

To extract shorting signals with high accuracy, it is first necessary to establish a state in which a large amount of shorting current flows to the sensor directly below the shorting area in the circuit shown in Fig. 7. However, as the MEA electrical schematic in Fig. 6 shows, there are plane-direction conductive paths in the GDL and CL parts of the MEA as an inhibiting factor, which may cause shorting current to disperse in the plane direction. Suppressing this is a necessary condition for extracting the voltage of the shorting signal. The factors involved in dispersion are

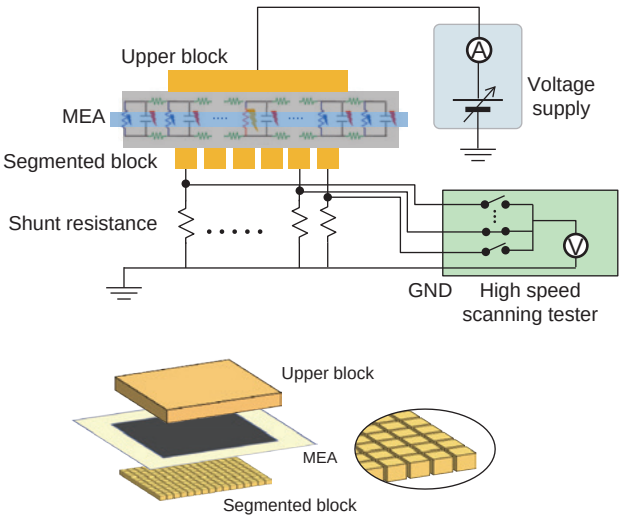


Fig. 7 Circuit diagram of shorting inspection system

terminal size, shunt resistance, and terminal pitch. The specifications were set for each of these.

4.2. Setting the Terminal Size

To evaluate current dispersion by terminal size, the shunt resistance, which is resistance in the terminal direction, was set to a fixed value of 10 Ω. The current dispersion, which is the relationship between the detection rate and distance at the peripheral terminals when the amount of current directly below the shorting area is 100%, was verified with four standards of split bases with terminal sizes ranging from 3.0 to 10.0 mm. The results are shown in Fig. 8. The results showed that smaller terminal sizes better suppressed current dispersion, and a terminal size of 3.0 mm was selected due to constraints imposed by the number of available tester channels.

4.3. Setting the Shunt Resistance

The basic policy for setting the shunt resistance was to make the shunt resistance in the direction directly below the short circuit smaller than the resistance of dispersion in the plane direction. However, to suppress measurement variation, the voltage detected by shunt resistance needs to be sufficiently large for the measurement accuracy of the tester. For this reason, it is necessary to increase the shunt resistance and increase the detection voltage.

As a result of the verification and to evaluate shunt resistance measurement accuracy and the challenge of current dispersion, Fig. 9 shows the voltage ratio of the adjacent terminal voltage when the terminal voltage at the center of the short circuit is 100%. A shunt resistance of 0.5 Ω was selected as the balance point because it has low current dispersion and a sufficiently high measurement accuracy of 1/10 at 3 σ with respect to the short circuit judgment threshold of 900 Ω.

4.4. Setting the Terminal Pitch

Theoretically, the narrower the terminal pitch, the shorter the distance in the plane direction, and thus the resistance in the MEA's plane direction would be relatively small compared to the resistance in the direction of the circuit directly below. This would make it easier for current to flow to adjacent terminals, resulting in lower accuracy. On the other hand, if the terminal pitch is widened, shorting areas are more likely to be present in the terminal gaps, which may result in a decline in accuracy due to signal dispersion and make it challenging to locate the short circuit, and thus the terminal pitch should be narrow. For that reason, the authors confirmed the impact of terminal pitch on current dispersion by taking measurements. For this verification, terminal size was set at 3.0 mm. The verification evaluated the degree of current dispersion with respect to distance when the voltage immediately below the short circuit was set to 100%. The results are shown in Fig. 10. No difference in current dispersion was observed between the 0.3 mm and 0.7 mm terminal pitch. Although the verification results confirmed the possibility of shortening the terminal pitch, 0.3 mm was set as the lower limit of the terminal pitch in consideration of the need to help prevent short circuits in the terminal gap during processing, and thus it was determined to use a terminal pitch of 0.3 mm.



Fig. 9 Measurement variation and detection signal ratio with adjacent terminals due to shunt resistor specification differences

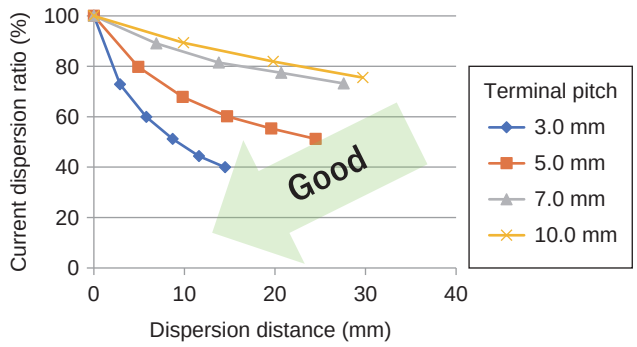


Fig. 8 Relationship between segment size and current dispersion

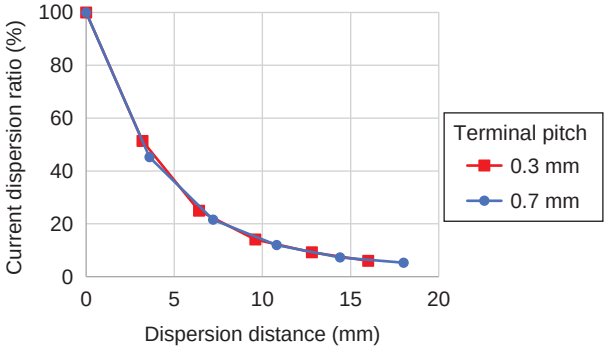


Fig. 10 Distance between terminals and current dispersion

4.5. Split Base Effect

A terminal size of 3.0 mm, a terminal pitch of 0.3 mm, and a shunt resistance of 0.5 Ω were selected as the final base specifications.

Figure 11 shows the voltage data for the X and Y positions obtained with the split base as the measurement results with a split base. The data confirmed that the signal was clearly detected. Figure 12 shows the results of cross-sectional observation of the center of shorting and non-shorting areas by X-ray CT. The cross-sectional observation results show that with the split base, it is possible to accurately detect the shorting phenomenon, as it was confirmed that the shorting area has a fibrous contamination that penetrates the membrane.

Next, the change in time of resistance to charging of shorting and non-shorting areas is shown in Fig. 13. Compared to non-shorting areas, shorting areas have a sufficiently small change in measured values and reach a steady state within 2.0 seconds. As non-shorting areas show a time change of more than 15 seconds, the charging effect is considered to be present in shorting areas as well. However, the shorting signal is large and less sensitive to changes due to charging, suggesting an apparent steady state. These results confirm that there is sufficient saturation in about 2.0 seconds to make an inspection judgment. The final inspection time was set at 2.6 seconds, as the time that can be allocated to charging to achieve the 10-second target time for the production process. In the end, there was an 87% reduction in charge time, from 20 seconds for the conventional system shown in Fig. 4 to just 2.6 seconds.

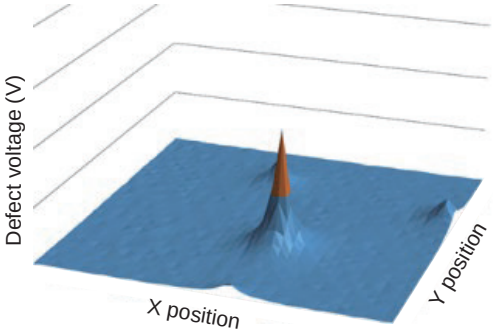


Fig. 11 Voltage measurement data on split-base MEA with short circuit

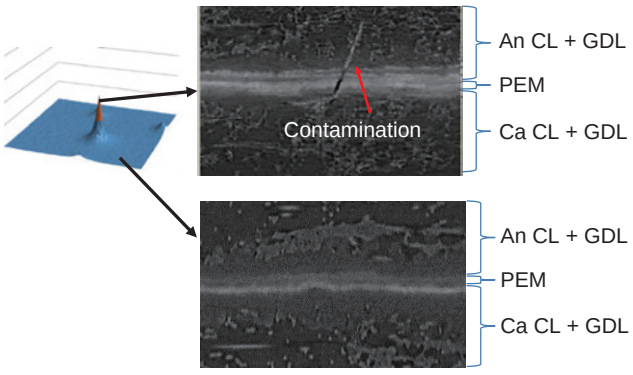


Fig. 12 X-ray CT image of shorting area

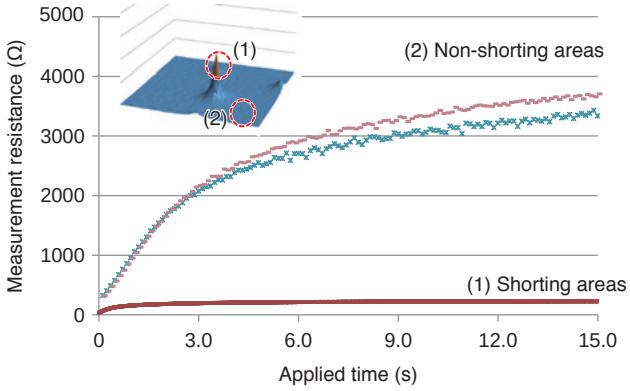


Fig. 13 Charge time variation between shorting and non-shorting areas

5. Development of Synthesizing Algorithm to Detect Short Circuits with Split Terminals

5.1. Issues with Detection Using Split Base

As shown in Fig. 14, a characteristic phenomenon resulting from split-terminal bases is that detection results differ depending on whether there is a short circuit on a terminal or one in the terminal gap. If it is in the terminal gap, the same level of current flows through adjacent terminals. Figure 15 shows the detection voltage of terminals A and B at the short circuit positions (1) and (2) in Fig. 14. These results indicate that if a short circuit is present in the terminal gap, the detection value per terminal may be low.

The following techniques were developed as a solution to this phenomenon:

(1) Synthesize the range of the voltage flowed to the split terminals

(2) Remove variability factors of range synthesis

5.2. Synthesis Process

Considering that the total amount of current flowing at a short circuit phenomenon at the terminal gap as shown in Fig. 14 would not change, the authors devised a method to help prevent a possible decline in judgment accuracy by synthesizing the dispersing current. To determine an appropriate synthesizing range, voltage values for expanding the synthesizing range were evaluated. The area was expanded to a square centered on the shorting area as a way to verify the range to synthesize. An image of the

synthesizing range is shown in Fig. 16. Figure 17 shows the results of the synthesis, with the horizontal axis showing the number of synthesized terminals, the vertical axis showing the synthesizing voltage values, and the curves in the plot showing data for different shorting MEAs. The synthesized value was calculated by combining the voltage V_{shunt} detected by shunt resistance as a parallel circuit, as shown in Fig. 6.

As a result of the synthesis of shorting voltages, it was confirmed that the sizes of results were interchangeable for the same synthesis range. Two factors may be responsible for this. The first is that the radial range centered on the short circuit does not perfectly coincide with the center as found by synthesis calculation in this method, and thus it is treated as variance if the synthesizing range is small. The second is that the voltage resulting from the internal resistance of the material as results from ions and water, as shown in Fig. 6, varies from MEA to MEA.

To address the latter, the calculation needs to consider the variation of internal resistance of each MEA, which will be discussed in the next section.

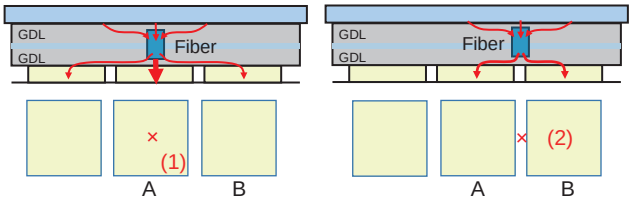


Fig. 14 Image of current bifurcation by segment and short-circuit position

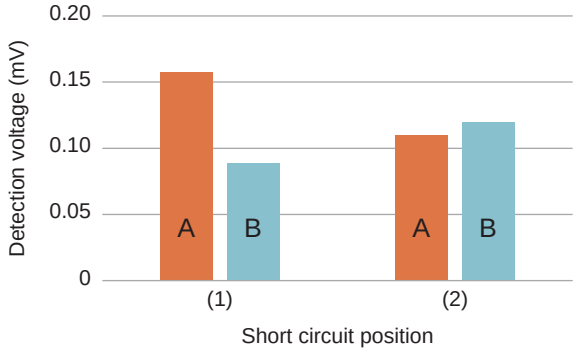


Fig. 15 Detection voltage value according to position of segment and short circuit

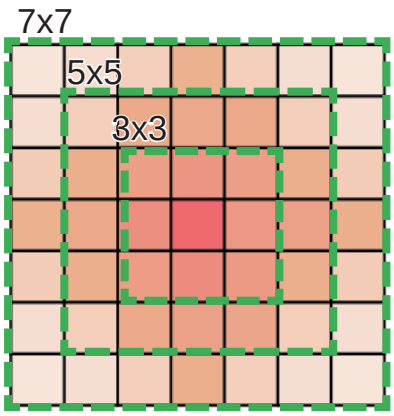


Fig. 16 Image of synthesizing range from the short circuit center

5.3. Removing Internal Resistance Voltage

To address variations in judgment results due to differences in the internal resistance voltage of each workpiece, the researchers considered the possibility of removing the internal resistance voltage from the calculation prior to the synthesis calculation.

Because it is necessary to clarify the distribution of the internal resistance voltage in order to properly remove it where it varies, the distribution of shorting resistance and the internal resistance voltage values was observed, as shown in Fig. 18.

The results show that the resistance distribution has two peaks. The distribution of lower resistance values indicates

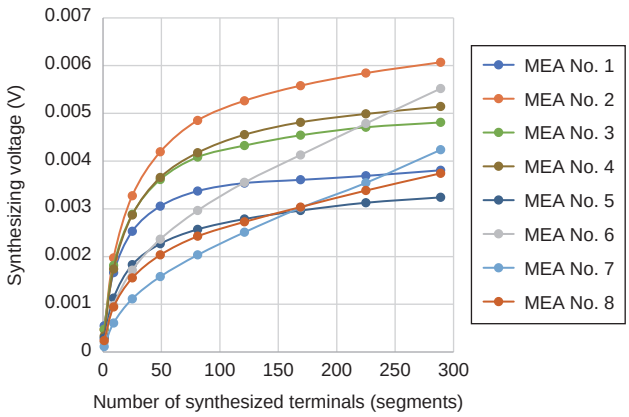


Fig. 17 Change in synthesizing voltage value relative to synthesizing range

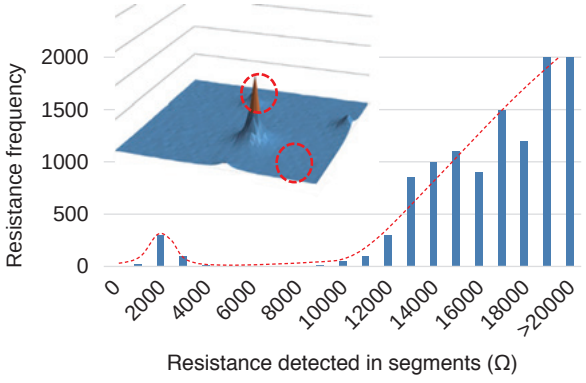


Fig. 18 In-plane resistance distribution of MEA

short circuits due to contamination. The distribution of higher resistance values can be considered a distribution of internal resistance rather than a short circuit. In the researchers' approach, 8000 Ω, which is at the base of the distribution, is taken as the lower limit of internal resistance, and the internal resistance voltage is removed as described by the following arithmetic steps. An image of this is shown in Fig. 19.

The arithmetic steps are:

1. Extract data of 8000 Ω or more from the data for all terminals
2. The average of the extracted data is taken to represent the internal resistance voltage of that MEA
3. The representative internal resistance voltage is subtracted from the data for all terminals
4. The data for terminals in the specified range from the center of each terminal is synthesized as a parallel circuit and used as the detection value
5. Judge as Pass or Fail relative to a threshold value

To confirm whether removal is effective and to determine an appropriate synthesizing range, voltage values for expanding the synthesizing range were evaluated, with the results shown in Fig. 20. The internal resistance fluctuation effect was eliminated without any interchange of the size relationship in the synthesis over a range of 100 terminals or more. There was increased robustness against fluctuation of measured values resulting from the material.

The synthesis condition was set to a synthesis range of 121 terminals, which is 11x11 terminals, in which no change of the size relationship is seen for each MEA.

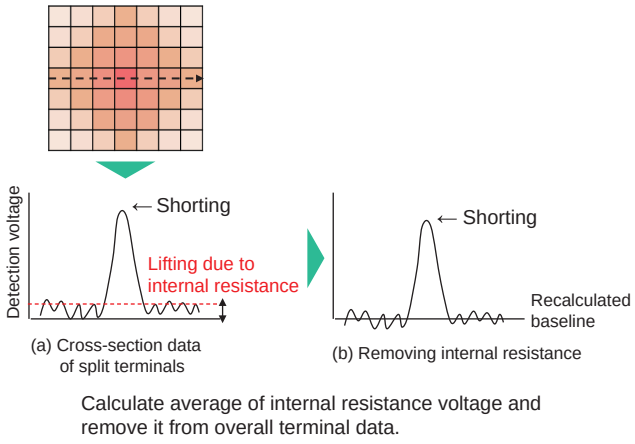


Fig. 19 Image of removal of base voltage lift due to internal resistance

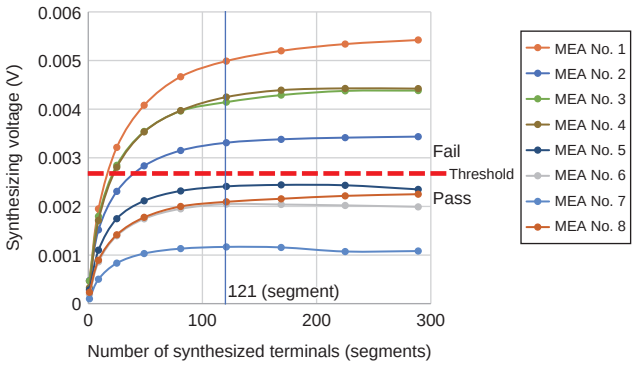


Fig. 20 Synthesizing range and voltage convergence

6. Conclusion

As a fast shorting inspection technology for fuel cell MEAs to increase the productivity of fuel cell stacks, the researchers developed a split-terminal base and a synthesizing algorithm to help prevent declines in judgment accuracy, which are characteristic of split terminals.

(1) Using a split-terminal base lowers measurement waiting time resulting from the charging required for shorting inspection by 87%.

(2) The synthesizing algorithm for short circuits in the gap between split terminals helps prevent a decline in judgment accuracy due to short circuits at locations with large measurement errors, such as the gap between split bases, and further increases the robustness of the inspection.

References

(1) https://global.honda/en/newsroom/news/2023/c230202eng.html, (accessed 2024/06/07)

(2) https://global.honda/en/tech/Hydrogen_Fuel_Cell_System_FC/, (accessed 2024/06/07)

(3) Kawasaki, S., Ogura, M., Ono, T., Kami, Y.: Development of the Honda FCX Fuel Cell Vehicle, Honda R&D Technical Review, Vol. 15, No. 1, p. 1-6

(4) Ogawa, T., Kimura, K., Uchibori, K., Fujimoto, S., Shimizu, K.: Development of New Power Train for Honda FCX Fuel Cell Vehicle, Honda R&D Technical Review, Vol. 15, No. 1, p. 7-12

(5) Kawasaki, S., Uchibori, K., Murakami, Y., Shimizu, K., Fujimoto, S.: Development of New Honda FCX with Next-generation Fuel Cell Stack, Honda R&D Technical Review, Vol. 18, No. 1, p. 45-50

(6) Matsunaga, M., Fukushima, T., Ojima, K., Kimura, K., Ogawa, T.: Fuel Cell Powertrain for FCX Clarity, Honda R&D Technical Review, Vol. 21, No. 1, p. 7-15

(7) Kimura, K., Kawasaki, T., Ohmura, T., Atsumi, Y., Shimizu, K.: Development of New Fuel Cell Vehicle CLARITY FUEL CELL, Honda R&D Technical Review, Vol. 28, No. 1, p. 1-8

(8) Kikuchi, H., Kaji, H., Nishiyama, T., Okonogi, D., Harata, H.: Development of New FC Stack for CLARITY FUEL CELL, Honda R&D Technical Review, Vol. 28, No. 2, p. 45-52

(9) Ishikawa, C., Iwaida, M., Naito, H., Inai, S., Yoshida, H., Muromoto, N.: High-durability and Cost-effective Fuel Cell Stack with New Structure, Honda R&D Technical Review, Vol. 37, p. 20-26
(10) Narita, S., Kobayashi, H.: Denki kairo riron, SHOKODO Co., Ltd., p. 210, (1978) (in Japanese)
(11) JP,2018-160371,A
(12) JP,2022-006899,A

■ Author ■


Hiroaki KAWANISHI


Hiroyuki YAMAGISHI


Kensuke NANBA

Development of Hydrogen Ventilation Structure for Fuel Cell Systems

Sena TAKEKOSHI[1]

ABSTRACT

A new hydrogen ventilation structure for fuel cell systems has been developed that uses a waterproof and dustproof filter for simplification towards multipurpose development of fuel cell powertrains. A 78% reduction in terms of volume was achieved compared to conventional model hydrogen ventilation structures for fuel cell systems with ducts installed. In this paper, under the assumption of normal operation and the possible occurrence of a hydrogen leak, it was confirmed that the hydrogen concentration in the hydrogen system and under the front hood was equal to or less than the unusual detection for hydrogen concentration through the hydrogen ventilation structure that was adopted. Furthermore, this structure newly introduces what is known as a "forced ventilation system," where part of the air supplied to the cathode electrodes is taken into the hydrogen ventilation structure, which has enabled reducing the concentration of hydrogen inside the hydrogen ventilation structure of the fuel cell system during normal operation compared to its concentration in conventional models.

1. Introduction

Fuel Cell Vehicles (FCV) are vehicles which run on kinetic energy converted from electricity that is generated through a reaction between hydrogen and oxygen. The hydrogen that serves as their fuel emits only water when it reacts with oxygen and does not emit any carbon dioxide, making FCV considered to possess outstanding potential as environmentally conscious vehicles(1). With the CLARITY FUEL CELL released in 2016, Honda aimed at creating a comfortable environment for sedans based on the idea of “man maximum” and “machine minimum,” and successfully installed the fuel cell powertrain under the front hood(2). One of the elements to achieve this was a structure which efficiently releases hydrogen that has passed through the fuel cell stack to the outside of the vehicle.

Figure 1 shows a fuel cell system installed in a 2016 model vehicle, as well as a diagram of the fuel cell system. The portion colored orange indicates the duct, which was installed above the fuel cell stack to utilize a ventilation method which took advantage of the difference in height to discharge the hydrogen that had passed through to the outside of the vehicle through the duct. In addition, in hydrogen ventilation structures for fuel cell systems (hereinafter, "hydrogen ventilation structures") in 2016 models, hydrogen system parts were covered with system covers to achieve a safety performance design for handling hydrogen. These covers were comprised of three elements: a barrier consisting of the stack case and system cover, a hydrogen sensor, and a duct. If the hydrogen system parts became damaged due to a vehicle collision, etc., it could result in hydrogen leaking inside of the structure. If there were a possibility that this could happen, it would be detected by the hydrogen sensor, and the hydrogen supply

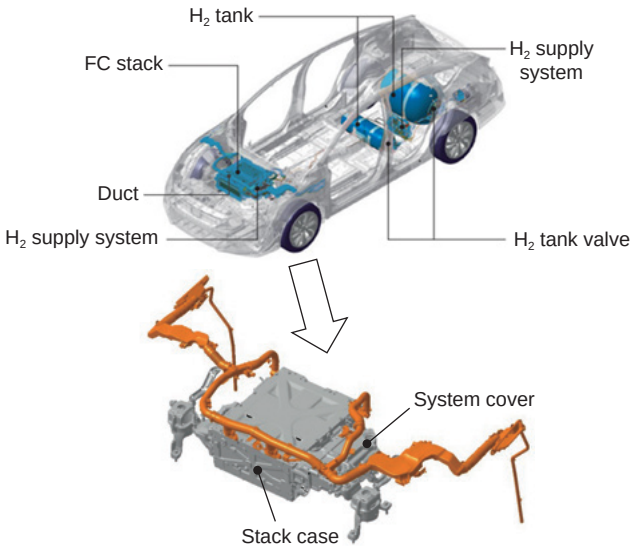


Fig. 1 Hydrogen ventilation structure of CLARITY FUEL CELL

[1] Innovative Research Excellence, Power Unit & Energy

would be shut off. Furthermore, the duct was used to vent the hydrogen to the outside of the vehicle once it had been reduced to a level of concentration where it would no longer be flammable[3]. In addition, since hydrogen molecules are small, even during normal operation, hydrogen at an extremely low flow rate of several cm^3/min would pass through the sealing material of the stack and be discharged into the hydrogen ventilation structure, so even the hydrogen discharged through permeation was constantly discharged to the outside of the vehicle through the duct.

On the other hand, in the development of fuel cell powertrains not only for passenger vehicles but also for commercial vehicles, there was an issue with versatility as it was necessary to design differently shaped ducts each time according to the applicable products. In addition, when assuming a fuel cell system with multiple linked powertrains to obtain the output, it was assumed that the design of the duct would become even more complicated.

Regarding the international regulations, a United Nations Regulation (UN-R134)[4] based on the UN's Agreement Concerning the Adoption of Uniform Technical Prescriptions for Wheeled Vehicles, etc. should be adhered to for fuel cell vehicle development. Enacted in 1958, this agreement attempted to unify the standards related to safety performance and the environment for each type of vehicle device and have them approved by all parties involved. The following information is related to the fuel cell vehicles themselves, as well as to their hydrogen storage containers and accessories. The items in this agreement related to this paper are shown in Table 1. The first requirement is that the concentration of hydrogen inside the passenger compartment should be below a standard value in the event that a hydrogen leak could occur during a single fuel cell system component malfunction located downstream from the main hydrogen shut-off valve of the tank. The second requirement is that a warning should be provided when a hydrogen leak could occur during a single fuel cell system component malfunction during operation, resulting in the concentration of hydrogen in the enclosed or semi-enclosed space in the vehicle exceeding 3%, and also that it is possible to isolate the storage system by shutting off the main hydrogen shut-off valve on the tank if this concentration exceeds 4%.

In addition to the aforementioned regulations, Honda implements development after first establishing its own target values in order to achieve a safety performance design for handling hydrogen. First, a hydrogen concentration sufficiently lower than a flammable concentration was established as a safety performance target for inside of the hydrogen ventilation structure during normal operation. The design helps prevent hydrogen from accumulating when it is released under the front hood, which is dotted with ignition sources and releases it to the exterior of the vehicle through gaps in the body. The safety performance target, which is based on satisfying the standards for hydrogen concentration in the passenger compartment listed in 7.1.4.2 on Table 1, has been set as inside the hydrogen ventilation structure. In addition, when hydrogen system parts are damaged and hydrogen leaks inside of the structure, the leakage is detected by a hydrogen sensor and the hydrogen supply is shut off. Should this happen, the requirements listed in 7.1.4.3 on Table 1 would be satisfied as well. Also, design standards have been established at Honda that help prevent ignition from possibly occurring: even if hydrogen is released under the front hood - which is dotted with ignition sources - from inside the hydrogen ventilation structure through the filter, limiting the amount of hydrogen leaking from the filter as the hydrogen supply is shut off, while suppressing it below a flammable concentration and helping to prevent it from igniting.

Table 2 shows a comparison of Honda's regulations and the international regulations. Vehicle conditions are divided into "Normal operation condition" and "Single malfunction condition," and the regulations and standards are listed in Table 2. While Honda has established hydrogen concentration regulations in the vehicle during the normal operation condition, there is no regulation for this in the international regulations. As noted previously, regulations have been established for the single malfunction condition in the international regulation: specifically, regulations for the hydrogen concentration inside the

Table 1 Excerpt from UN-R134

Item Number	Contents
7.1.4.2	Any single failure downstream of the main hydrogen shut-off valve shall not result in accumulations in levels of hydrogen concentration in the passenger compartment according to test procedure.
7.1.4.3	If, during operation, a single failure results in a hydrogen concentration exceeding 3.0 per cent by volume in air in the enclosed or semi-enclosed spaces of the vehicle, then a warning shall be provided. If the hydrogen concentration exceeds 4.0 per cent by volume in the air in the enclosed or semi-enclosed spaces of the vehicle, the main shut-off valve shall be closed to isolate the storage system.

Table 2 Comparison of regulations between Honda and UN-R134

Vehicle Condition	Honda	International Regulation (UN-R134)
Normal operation condition	• Hydrogen concentration in vehicle	No regulations
Single malfunction condition	• Hydrogen concentration in vehicle • Warning and hydrogen supply cutoff when concentration rises	• Hydrogen concentration in vehicle (passenger compartment only) • Warning and hydrogen supply cutoff when concentration rises

passenger compartment and a requirement for providing an alarm/shutting off the hydrogen supply when the hydrogen concentration increases. Honda has established hydrogen concentration regulations for each part of the vehicle rather than just for inside the passenger compartment and has also established regulations for providing warnings and shutting off the hydrogen supply when the hydrogen concentration increases. Therefore, in addition to incorporating the international regulations, Honda has established even higher safety performance standards and is conducting safety performance design to achieve them.

2. Development Goals

Figures 2 and 3 show the appearance of the CR-V e:FCEV with a simplified version of the hydrogen ventilation structure. Installing a waterproof and dustproof filter on the side of the stack case instead of a hydrogen discharge duct adds a ventilation function while simultaneously satisfying safety performance. As a result, as shown in Fig. 4, the hydrogen ventilation structure can be reduced by 78% in terms of volume compared to conventional models. Thus, the aims of development of this structure were defined as follows:

(1) It should satisfy the hydrogen concentration standards defined within Honda just as with conventional models, even if the hydrogen ventilation structure uses a waterproof and dustproof filter; and
(2) Safety performance should be established through a hydrogen ventilation structure using forced ventilation.

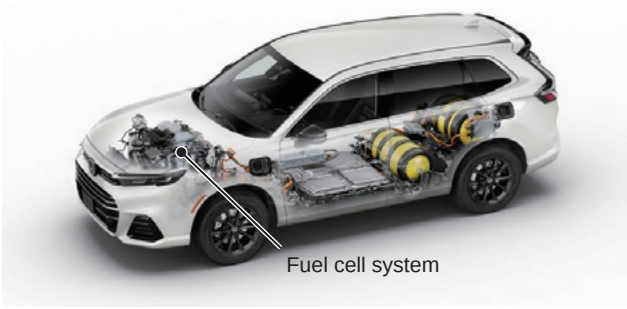


Fig. 2 FC system installation layout in CR-V e:FCEV

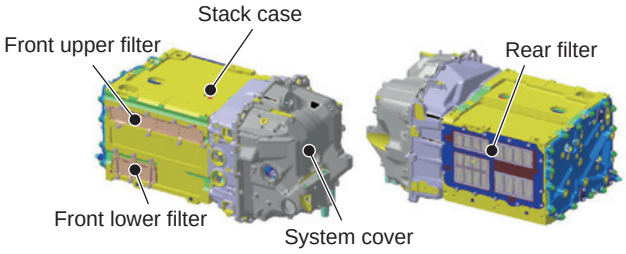


Fig. 3 FC system of CR-V e:FCEV

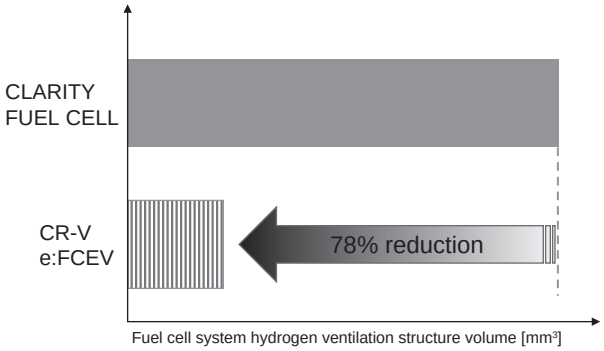


Fig. 4 Structure volume of hydrogen ventilation

3. Overview of Hydrogen Ventilation Structure

3.1. Forced Ventilation System

A forced ventilation system was newly introduced for this model to dilute the hydrogen in the hydrogen ventilation structure. Figure 5 shows a system diagram that includes a forced ventilation line. This structure splits off part of the air supply for the cathode electrode, and an orifice is installed midway to reduce the flow rate into the hydrogen ventilation structure. The flow rate of the air flowing into the forced ventilation line changes depending on the amount taken in, and if the air taken in increases, the air flow rate towards the forced ventilation line increases as well. During normal operation, hydrogen that passes through the fuel cell stack and is discharged inside the hydrogen ventilation structure is diluted by the air discharged from the forced ventilation line to this structure and is discharged under the front hood through the waterproof and dustproof filter. However, this forced ventilation system is only effective when the fuel cell system is running; it does not work when the vehicle is stopped and the fuel cell system is not running. Therefore, the hydrogen concentration inside the hydrogen ventilation structure should be less than the

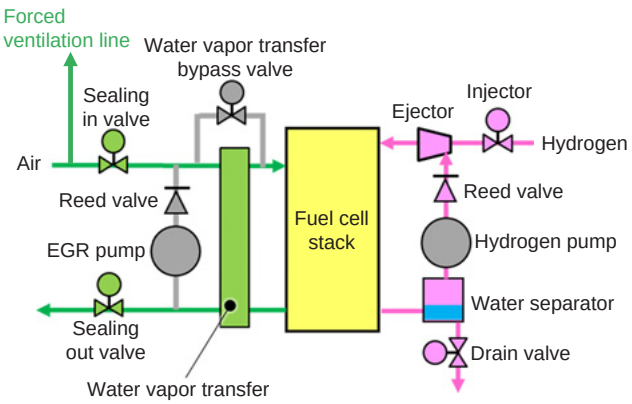


Fig. 5 Forced ventilation line in FC system

standard value even under ventilation conditions where only a waterproof and dustproof filter is used.

3.2. Waterproof and Dustproof Filter

Figure 6 shows the fuel cell stack composition. Filters are installed facing the front and rear of the vehicle in order to efficiently draw air into the stack case, which is part of the hydrogen ventilation structure, while driving. Figure 7 shows the front upper filter. While having the filter take up a large amount of surface area is desirable in order to draw air into the hydrogen ventilation structure from the front, touching the filter directly may cause dust to accumulate, making it unlikely to obtain desired ventilation performance. In addition, the filter could become damaged by force (e.g. from a person's finger) and come into contact with the electrified part inside of the stack case, which could result in an electric shock or a short circuit if water or dust entered. In this model, therefore, a filter cover is used with gaps above and below it to help prevent the accumulation of water and dust, as well as a structure with a gap that helps prevent the filter from being damaged by force.

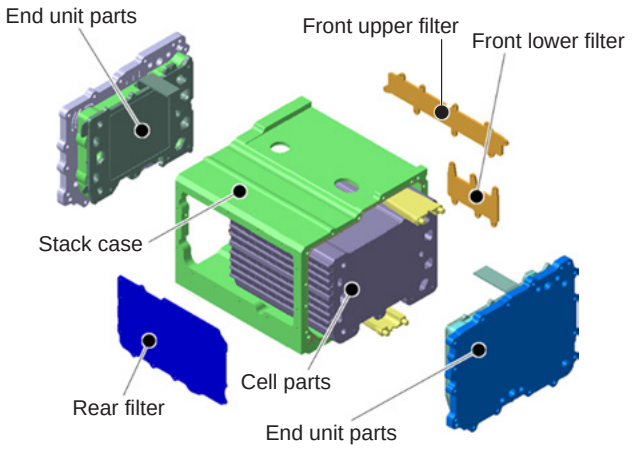


Fig. 6 FC stack of CR-V e:FCEV

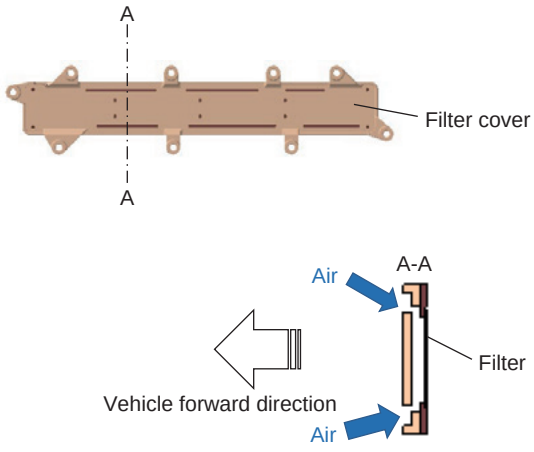


Fig. 7 Front upper filter assembly

3.3. Hydrogen Sensor Roles and Positioning

The hydrogen sensor should be positioned so as to immediately detect when a hydrogen leak may have occurred due to hydrogen system parts becoming damaged due to a vehicle collision, etc. On the other hand, if the detection threshold for irregular hydrogen concentration is exceeded during normal operation, the sensor would erroneously determine that a hydrogen leak may have occurred and stop the system operation, even if the parts have not been damaged, etc. Thus, when determining where to install the hydrogen sensor, the inside of the hydrogen ventilation structure should be ventilated appropriately to help ensure that the detection threshold it below that for irregular hydrogen concentration. It is important that there be no erroneous detections from the sensor that may have been caused by increases in hydrogen concentration inside the hydrogen ventilation structure when parts have not been damaged, etc., during normal operation. In addition, it is necessary to consider a position where the sensor is able to detect a malfunction immediately when one may occur. Figure 8 shows the hydrogen concentration distribution inside of the structure during normal operation. Taking the aforementioned concept into account, the sensor was installed near the front filter since installing it near the filter in the hydrogen ventilation structure would provide it with constant ventilation, and since installing it in the area of the stack case where hydrogen accumulates would allow it to be able to immediately detect malfunctions when they may occur.

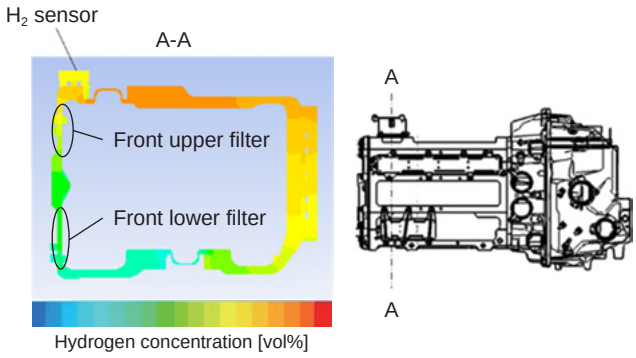


Fig. 8 H_2 sensor layout

4. Test Results

4.1. Test Verification Assuming Hydrogen Permeation

This section shows the test results for hydrogen concentration inside of the hydrogen ventilation structure during normal operation. Testing was made in conditions wherein no power was being generated, when the forced ventilation system could not be used, during normal operation. For hydrogen permeation, the permeation flow rate was reproduced using a jig while taking design variations in fuel

cell stack sealing into account. In addition, hydrogen sensors were installed in the upper and lower parts of the stack case where hydrogen may remain inside the hydrogen ventilation structure due to the nature of that structure. Figures 9 and 10 show the measuring positions of the hydrogen sensors. In addition, the hydrogen sensors mounted on the vehicle are in (2) and (5) of Fig. 9. Also, the verification conditions for testing considered the tilt of the vehicle in order to reproduce various driving situations. This was conducted in order to confirm that the hydrogen concentration did not exceed the detection threshold for irregular hydrogen concentration due to the tilt, which may cause hydrogen to tend to accumulate and help prevent efficient ventilation of the hydrogen inside of the hydrogen ventilation structure.

First, the results for the hydrogen concentration within the hydrogen ventilation structure while in a horizontal orientation are shown in Fig. 11. These results clarified that most of the measurement positions had a hydrogen concentration of less than half that of the detection threshold for irregular hydrogen concentration, and hydrogen was diffused almost uniformly within the hydrogen ventilation structure. The location with the highest concentration is the measurement position in (8) of Fig. 11, which was close to directly above the center of the stack case. However, this hydrogen concentration was roughly 60% compared to the detection threshold for irregular hydrogen concentration and was sufficiently lower than a flammable concentration.

Next, the results of the hydrogen concentration for the hydrogen ventilation structure with the vehicle tilted are shown in Fig. 12. The maximum concentration indicated was almost directly above the center of the hydrogen ventilation structure, the same as under the horizontal condition. Hydrogen tended to accumulate at the highest locations depending on the direction of the tilt, where the hydrogen concentration tended to increase. These results confirmed that the detection threshold for irregular hydrogen concentration is not exceeded even if the hydrogen sensor is installed in the upper part of the inside of the system ventilation structure.

4.2. Test Verification Assuming Hydrogen Leakage

A hydrogen sensor is used to detect when hydrogen leakage may occur, and the system has been designed to perform as well as possible by limiting the amount of hydrogen leakage if one could occur. This section shows the results from measuring the hydrogen concentration when hydrogen system parts become damaged and may cause

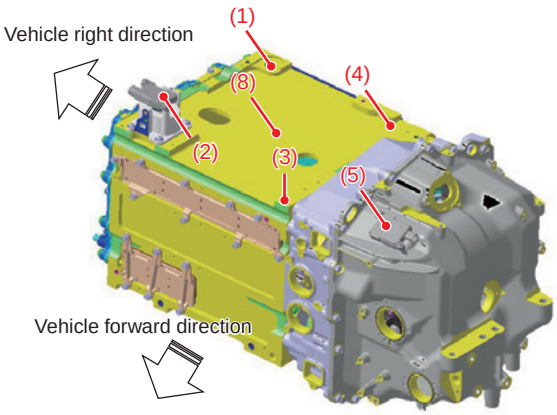


Fig. 9 Perspective view of FC system and hydrogen concentration measurement position

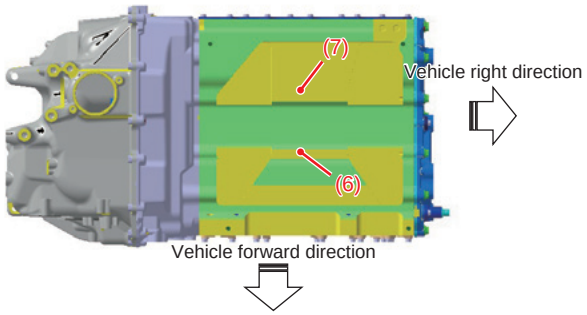


Fig. 10 Bottom view of FC system and hydrogen concentration measurement position

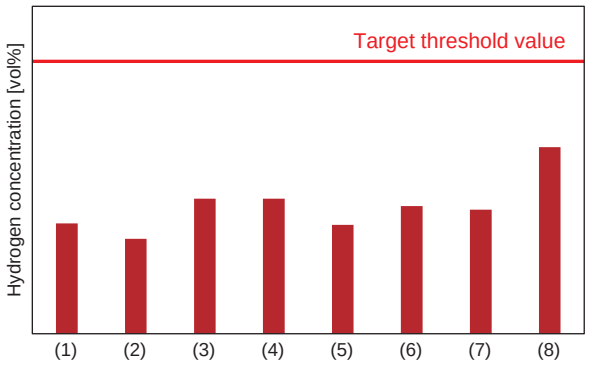


Fig. 11 Hydrogen concentration results for hydrogen ventilation structure in horizontal orientation

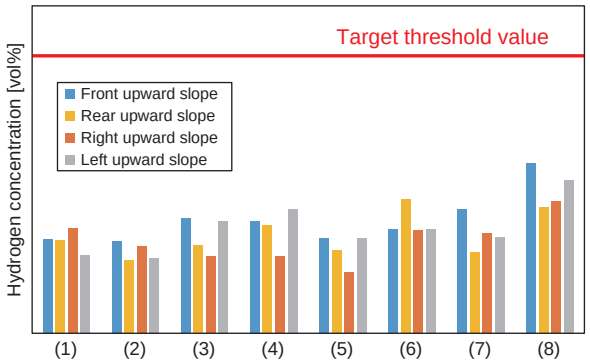


Fig. 12 Hydrogen concentration results for hydrogen ventilation structure in tilted orientation

hydrogen leakage, utilizing simulation of an actual vehicle. Testing was conducted with the leaking area positioned the furthest away in a straight line from the on-board hydrogen sensor, so that detection time would be the slowest, and assuming a hydrogen leak rate of several thousand cm^3/min max. Figure 13 shows the hydrogen concentration measurement positions. The testing method mirrored the behavior of an actual vehicle during a malfunction. First, hydrogen was discharged from the presumed leakage area to the inside of the hydrogen ventilation structure at the flow rate at which it is assumed that a hydrogen leak could occur. Next, hydrogen release was stopped once the concentration detected by the hydrogen sensor reached the supply shut-off level. At this point, the forced ventilation line would normally operate in an actual vehicle, but it is advantageous in reducing hydrogen concentration detection time. Thus, under the presumed operating conditions, testing was performed by simulating conditions that would not be advantageous for detection by allowing a minimum flow rate to be distributed as air towards the forced ventilation line to flow into the hydrogen ventilation structure.

The hydrogen that leaked into the hydrogen ventilation structure was released under the front hood through the waterproof and dustproof filter. By measuring the hydrogen concentration at each installation point, it was confirmed whether or not the hydrogen concentration at locations presumed to be fire sources was below the detection threshold for irregular hydrogen concentration.

First, the results of hydrogen concentration under the front hood in a horizontal orientation are shown in Fig. 14. Based on these results, the hydrogen concentration at all of the measurement positions was almost zero relative to the detection threshold for irregular hydrogen concentration. It is assumed that the hydrogen concentration did not increase since it was immediately released to the exterior of the vehicle from the gaps in the body after being released under the front hood from the waterproof and dustproof filter.

Next, Fig. 15 shows the results of hydrogen concentration under the front hood when it is assumed that the vehicle is tilted, as shown in Fig. 16. Based on these results, it was revealed that the hydrogen concentration was sufficiently low relative to the detection threshold for irregular hydrogen concentration, as it also was when the vehicle was horizontal. However, influence from the tilt was observed: for example, it was revealed that hydrogen concentration has a high value at the measurement positions in (c) of Fig. 13 that correspond to near the front side of the fuel cell system when the front part of the vehicle rises. In other words, based on these results, it can be concluded that the hydrogen diffuses under the front hood through the waterproof and dustproof filter.

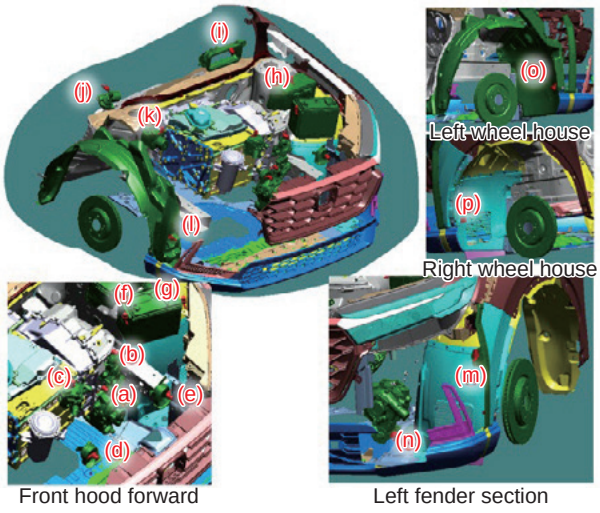


Fig. 13 Hydrogen concentration measurement positions

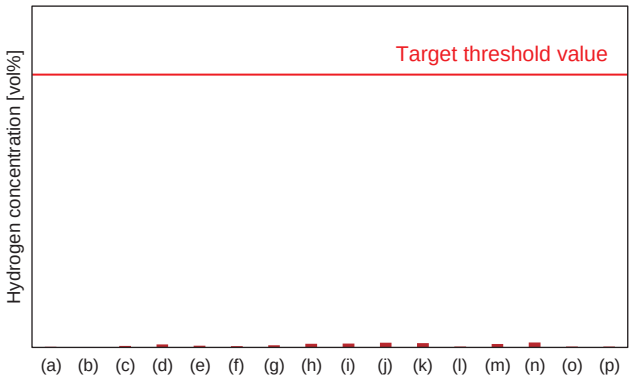


Fig. 14 Hydrogen concentration results in front hood in horizontal orientation

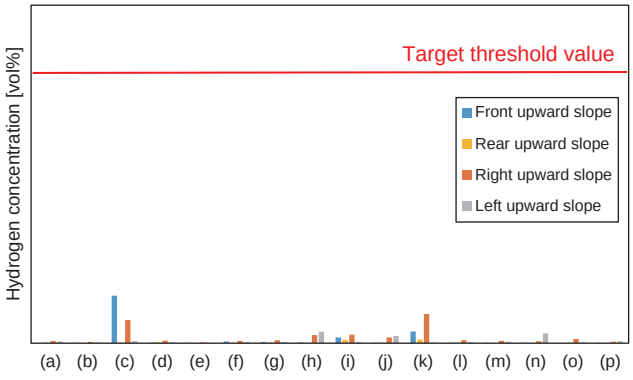


Fig. 15 Hydrogen concentration results in front hood in tilted orientation

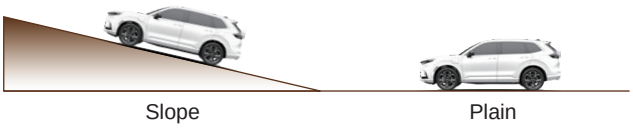


Fig. 16 Image of parking slope

4.3. Effects of Forced Ventilation Line

As mentioned previously, in order to further reduce the concentration of the hydrogen released under the front hood from the hydrogen ventilation structure, a forced ventilation system is being introduced to allow part of the air supply for the cathode electrodes of the fuel cell stack to flow into the hydrogen ventilation structure. Figure 17 shows the difference in maximum hydrogen concentration inside the hydrogen ventilation structure, depending on the presence or absence of a forced ventilation system. It was revealed that the inflow of air greatly diluted the hydrogen concentration within the hydrogen ventilation structure. Also, Fig. 18 shows the difference in detection time for on-board hydrogen sensors, depending on the air volume level from forced ventilation. Based on these results, it was revealed that detection timing could be increased by introducing a forced ventilation system, through which detection time was successfully reduced by 55%. The reason why the forced ventilation system was effective at detection during hydrogen leakage became clear from these results. It is assumed that the air from the forced ventilation system guiding the leaking hydrogen towards the hydrogen sensor facilitated this detection timing. In addition, the reason why the concentration value remains constant once the hydrogen concentration value exceeds the detection threshold is because it falls outside of the concentration detection range of the hydrogen sensor.

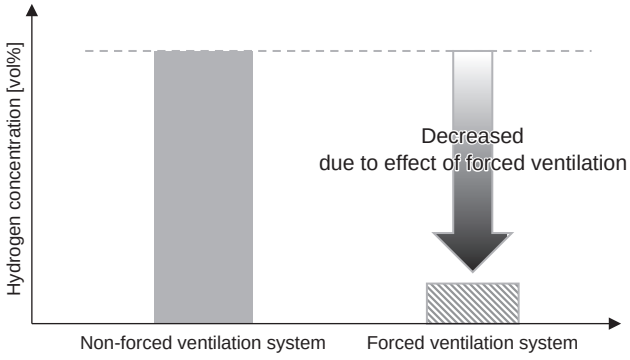


Fig. 17 Comparison of hydrogen concentration between non-forced ventilation system and forced ventilation system

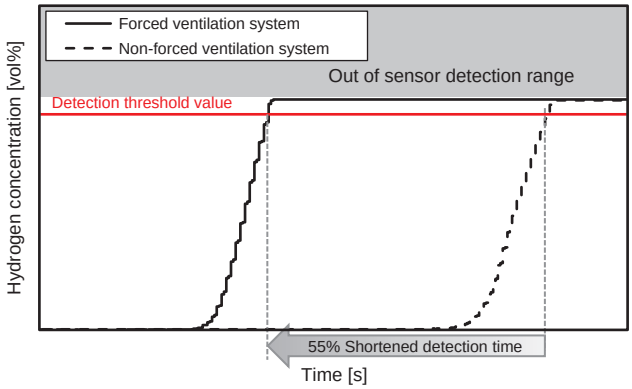


Fig. 18 Comparison of detection time between non-forced ventilation system and forced ventilation system

5. Conclusion

The following two points were confirmed for this mode: the volume of the hydrogen ventilation structure was reduced by 78% through fuel cell powertrain simplification; and a new hydrogen ventilation structure with a waterproof and dustproof filter was successfully adopted.

(1) Testing was conducted similarly on the conventional model during normal operation and during a malfunction, as well as under the presumption that the vehicle was tilted, and it was confirmed that the standards were satisfied, even with Honda's independent target values that are stricter than those of the international regulation.

(2) Introduction of a forced ventilation structure system together with positioning of the waterproof and dustproof filter reduced hydrogen concentration within the hydrogen ventilation structure during normal operation, and it was even possible to reduce the concentration to below the flammable state. Also, the timing for detecting hydrogen leakage through hydrogen sensors was increased by 55%.

References

(1) https://www.gov-online.go.jp/eng/publicity/book/hlj/html/201609/201609_02_jp.html, (accessed 2024/6/5)

(2) Kimura, K., Kawasaki, T., Ohmura, T., Atsumi, Y., Shimizu, K.: Development of New Fuel Cell Vehicle CLARITY FUEL CELL, Honda R&D Technical Review, Vol. 28, No. 1, p. 1-8

(3) Sasamoto, K., Suda, K.: Developing Method Using CFD to Design Hydrogen Isolation Structure with Waterproof and Dustproof Filters, Honda R&D Technical Review, Vol. 34, No. 1, p. 83-91

(4) https://unece.org/sites/default/files/2022-07/R134am4e.pdf, (accessed 2024/6/5)

■ Author ■



Sena TAKEKOSHI

Construction of One-dimensional Humidifier Model in Fuel Cell System

Shuto MANIWA[1] Yohei HIDAKA[1]
Koichi KIMURA[1] Nobuki KOIWA[1]

ABSTRACT

The phenomena inside a porous hollow fiber membrane humidifier were analyzed and a one-dimensional humidifier model that can estimate the water transfer rate was constructed to enable control of the water content in the fuel cell stack of a fuel cell system to the appropriate range. The calculation accuracy of the humidifier model was enhanced by investigating and considering the impact of the dry-up phenomenon that may lower the water transfer rate due to partial drying of the porous membrane. In addition, verification was performed by comparing the calculation results of the humidifier model with the results of humidifier evaluation tests and measurements of the water transfer rate in bench operation of the fuel cell system. The estimation accuracy of the humidifier model was confirmed to satisfy the target accuracy of ±15% or less that is needed for use in performance design and control optimization of fuel cell systems.

1. Introduction

Polymer electrolyte fuel cells are power generation devices with a low environmental load, and are attracting attention as a next-generation power source.

To help ensure the power generation performance of polymer electrolyte fuel cells, it is necessary to maintain the thickness of the Polymer Electrolyte Membrane (PEM) that functions to conduct hydrogen ions and to physically separate oxygen and hydrogen. OH radicals and hydrogen radicals generated as by-products during power generation chemically cleave the polymer chains of the PEM, and the cleaved polymer chains are exhausted out of the cell, which may reduce the membrane thickness. As a result, the amount of unreacted gas that permeates between the cathode and anode via the PEM increases and more hydrogen is consumed, which affects fuel efficiency performance. Insufficient water content in the PEM may impede radical transfer, resulting in higher concentrations and promoting the reduction in PEM thickness. This is also known to lower the chemical stability of the PEM, which accelerates aging[(1)-(3)].

Many fuel cell systems adopt humidifiers to humidify the air supplied to the fuel cell stack in order to provide the PEM water content (Fig. 1). High-humidity air (hereinafter defined as WET gas) is exhausted from the fuel cell stack and flows into the humidifier installed in the air supply system. The air supplied to the fuel cell stack (hereinafter defined as DRY gas) is humidified by the water vapor contained in the WET gas.

However, if the fuel cell stack has an excessive water content, the supply of hydrogen to the anode is impeded, the power generation efficiency drops, and aging is accelerated. It is important to control the relative humidity (RH) of the DRY gas in order to adjust the water content in the fuel cell stack to the appropriate range. This calls for estimation of the water transfer rate due to the humidifier, and multiple studies have been conducted to elucidate the humidification performance of humidifiers applied to fuel cell systems through experiments and modeling[(4), (5)].

Honda has adopted a porous hollow fiber membrane humidifier in its fuel cell system that can achieve both humidification performance and differential pressure strength.

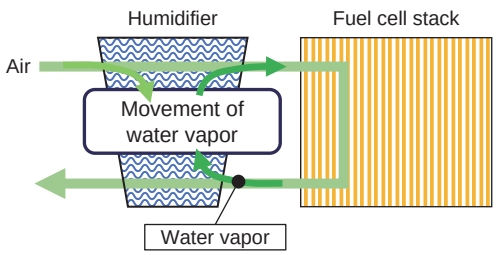


Fig. 1 Humidification system

[1] Innovative Research Excellence, Power Unit & Energy
E-mail: shuto_maniwa@jp.honda

2. Development Goals

Porous membranes are characterized by a drop in humidification performance under conditions with low WET gas RH. It is necessary to accurately understand the phenomenon of this drop in humidification performance in order to properly humidify the DRY gas, but to date there is insufficient research on the characteristics of porous membrane humidifiers. This study referred to this phenomenon as the dry-up phenomenon, and analyzed the factors by which it may occur.

A one-dimensional humidifier model that estimates the RH of the air supplied to the fuel cell stack from the operating conditions was constructed for use in performance design and control optimization of fuel cell systems. This humidifier model reproduces the effects of the dry-up phenomenon, and enhances the estimation accuracy under conditions with low WET gas RH. The target accuracy of the humidifier model was set to ±15% or less, considering variance factors in the fuel cell system and taking into account the model estimation error needed to help prevent PEM aging and flooding.

3. Construction of Humidifier Model

3.1. Mechanism of Humidification

This section describes the method by which the humidifier humidifies the fuel cell system. The humidifier functions to self-recover the generated water from the WET gas and to provide the DRY gas with the appropriate humidity needed for power generation. In the fuel cell system, the humidifier and the fuel cell stack form a circulatory system as shown in Fig. 2. Here, water circulates in a cycle in which (I) water vapor transfers due to the partial pressure difference between the WET gas and DRY gas, (II) the water vapor is exhausted from the fuel cell stack along with the water generated by power generation (part of the generated water permeates to the anode), and (III) the WET gas flows into the humidifier. Therefore, the water transfer rate due to the humidifier N_{wtr} [mol/s] is expressed in terms of the amount of water generated by the fuel cell stack N_{gen} [mol/s], the water content in the WET gas N_{wet} [mol/s], and the water transfer rate to the anode $N_{backdiff}$ [mol/s], as shown by the relationship in Eq. (1).

$$N_{wtr} = N_{gen} - N_{wet} - N_{backdiff} \quad (1)$$

Heat exchange takes place inside the humidifier between the WET gas, which has risen in temperature due to the reaction heat of the fuel cell stack, and the DRY gas, and this change in the gas temperature influences water transfer.

The humidifier consists of a humidifier module and heads that form flow channels, as shown in Fig. 3. The inside of the humidifier module is filled with thousands of hollow fibers, and DRY gas flows inside and WET gas flows outside the hollow fibers. Figure 4(a) shows a magnified view of the hollow fiber membrane cross section. There are pores on the order of several nm through which water is exchanged. The diameter of the hollow fiber membrane pores becomes smaller from the outer surface (WET gas side) shown in Fig. 4(b) toward the inner surface (DRY gas side) shown in Fig. 4(c)[6].

The hollow fiber membrane has a cylindrical structure that is advantageous for obtaining high differential pressure strength without additional support structures as compared to a flat membrane. In addition, whereas other exchange

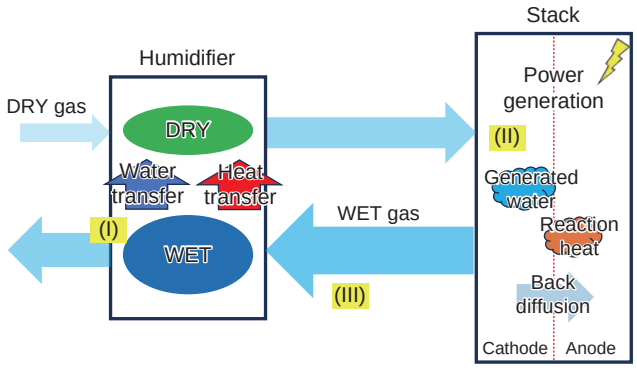


Fig. 2 Water circulation in fuel cell system

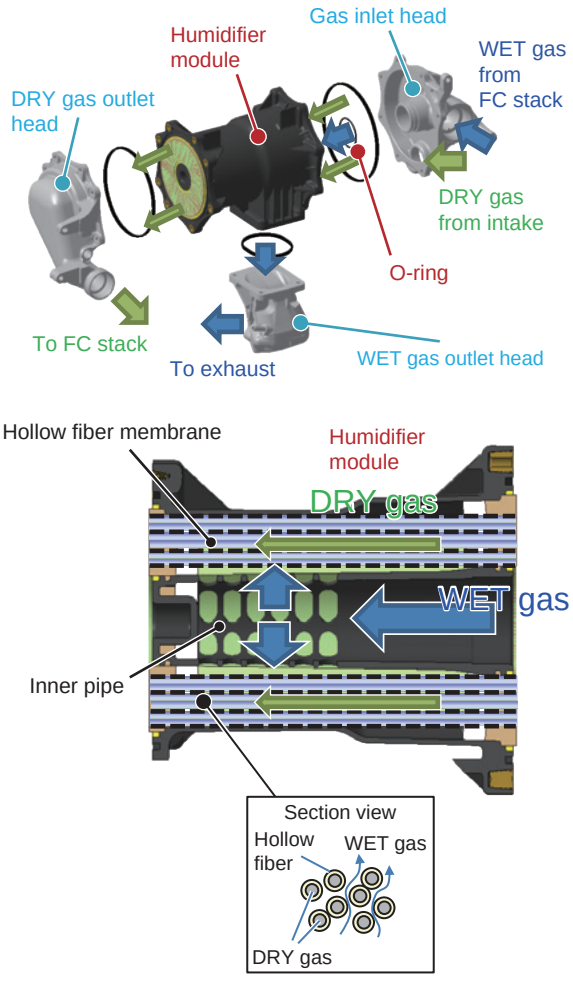
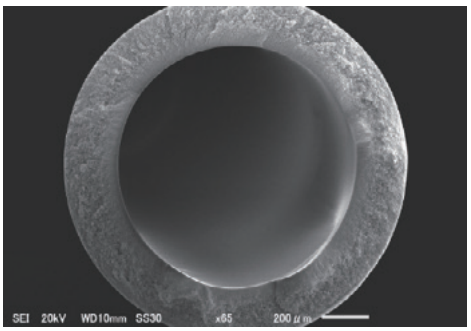


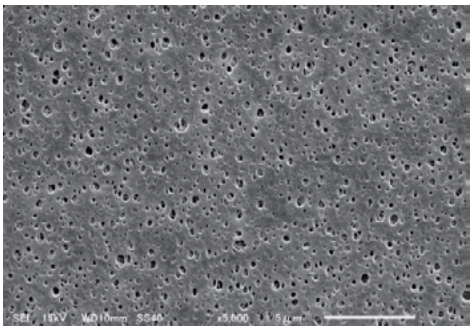
Fig. 3 Structure of humidifier module

membranes such as proton exchange membranes and dissolution diffusion membranes require thinning to increase the water vapor permeability, in porous membranes, the pore diameter acts instead of the thickness. This means that both differential pressure strength and humidification performance can be achieved by providing membrane thickness, which makes porous membranes suitable for use in fuel cell systems.

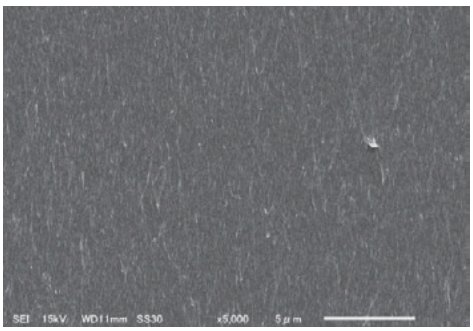
Next, the mechanism of water transfer in the porous membrane is explained[7]. Figure 5 shows the mechanism of water transfer by the pores. The water in the WET gas is attracted to the membrane surface by the adsorption phenomenon, and that water then moves toward the DRY gas by capillary transfer inside the pores. The water that passed through the pores enters the DRY gas by evaporative diffusion due to the sudden drop in pressure. This continuous process is the mechanism of humidification.



(a) Membrane cross section 65X magnification



(b) Outer surface 5000X magnification



(c) Inner surface 5000X magnification

Fig. 4 Magnified views of hollow fiber membrane

3.2. Overview of One-dimensional Humidifier Model

This section describes an overview of the one-dimensional humidifier model for accurately estimating the water transfer rate by the humidifier. Figure 6 shows the flowchart of the one-dimensional humidifier model.

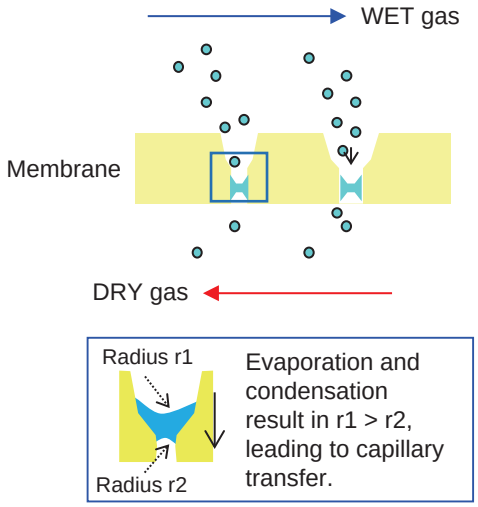


Fig. 5 Mechanism of water transfer

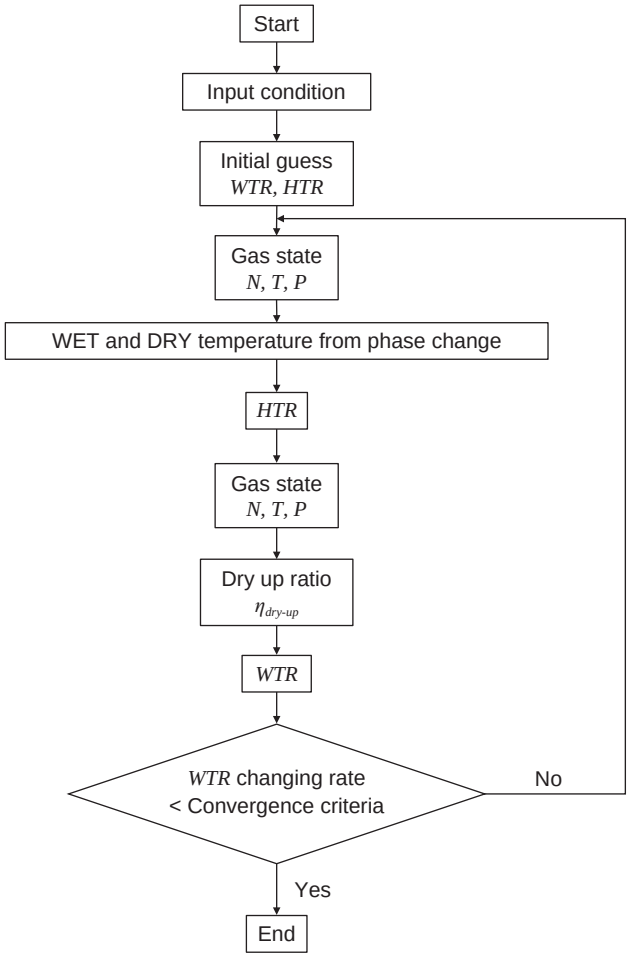


Fig. 6 Flowchart of humidifier model

The initial condition is a simple calculation of the water vapor and temperature distributions inside the humidifier, using the gas states at the inlet and outlet of the humidifier to be calculated as the inputs. Next, the gas temperature distribution is obtained from the heat transfer rate (HTR) between the WET gas and DRY gas and the latent heat of evaporation due to phase change between water vapor and liquid water, and the water transfer rate (WTR) is calculated based on the water vapor partial pressure and humidity in each part. In addition, due to the influence of the dry-up phenomenon, the dry-up ratio ($\eta_{dry\text{-}up}$) described in Section 3.4 is obtained from the gas temperature and humidity and taken into account in the WTR calculation.

The WTR of the membrane and the water vapor partial pressure distribution in the axial direction of the hollow fibers have a strong mutual influence. Therefore, accuracy was enhanced by discretizing and calculating in one dimension in the axial direction of the hollow fibers, as shown in Fig. 7. This was also done for the relationship between heat transfer and temperature.

3.3. Water Transfer

This section describes the method of modeling the phenomena inside the humidifier. Water transfer is a permeation phenomenon with the difference in water vapor partial pressure between the WET gas and DRY gas as the driving force. The water transfer rate N_{wtr} [mol/s] is expressed by Eq. (2) using the membrane surface area S [m^2], the water vapor partial pressures in the WET gas $P_{v,wet}$ [Pa] and the DRY gas $P_{v,dry}$ [Pa], and the permeation resistance in bulk $R_{mt,total}$ [s/m].

$$N_{wtr} = \frac{S}{R_{mt,total}} \cdot \frac{P_{v,wet} - P_{v,dry}}{RT} \tag{2}$$

Based on the three-resistance model used to explain the process of mass transfer inside the membrane[8], this permeation resistance is considered to be the sum of three resistances in series: (i) evaporation resistance, (ii) capillary transfer resistance, and (iii) adsorption resistance (Fig. 8). The evaporation resistance and adsorption resistance can be expressed as shown in Eq. (3) and Eq. (4) by the boundary layer equation and dimensional analysis[9]. The flow in the vicinity of the hollow fibers has a Reynolds number of 1000 or less and can be regarded as laminar flow, and thus the laminar flow equation was adopted for the dimensionless number multiplier. The capillary transfer resistance is expressed here by Eq. (5) using the membrane-specific value k_m.

Evaporation resistance:

$$R_{mt,dry} = d_{mem\text{-}inner} / (\alpha_{dry} Re^{0.5} Sc^{1/3} D_{H_2O,Air}) \tag{3}$$

Adsorption resistance:

$$R_{mt,wet} = d_{wet,asm} / (\alpha_{wet} Re^{0.5} Sc^{1/3} D_{H_2O,Air}) \tag{4}$$

Capillary transfer resistance:

$$R_{mt,m} = 1/k_m \tag{5}$$

3.4. Dry-up Phenomenon

This section describes the details and modeling of the dry-up phenomenon.

Figure 9 shows the relationship between the WTR and the water content in the WET gas by comparing the values estimated by the model and the actual measurement results using the test apparatus described in Chapter 4. From Eq. (1) to Eq. (5), if the capillary transfer resistance is assumed to be constant, the WTR is nearly proportional to the water vapor partial pressure in the WET gas, and is expected to exhibit characteristics like the blue dashed line. However, the actual WTR was smaller than the expected transfer rate, as shown by the green dots. This indicates an increase in the capillary transfer resistance due to the dry-up phenomenon.

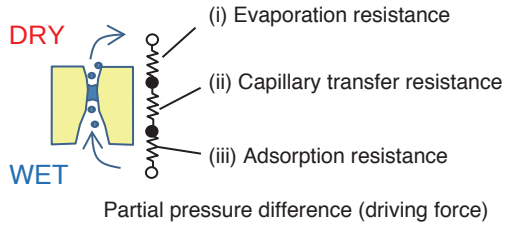


Fig. 8 Three-resistance model for water transfer

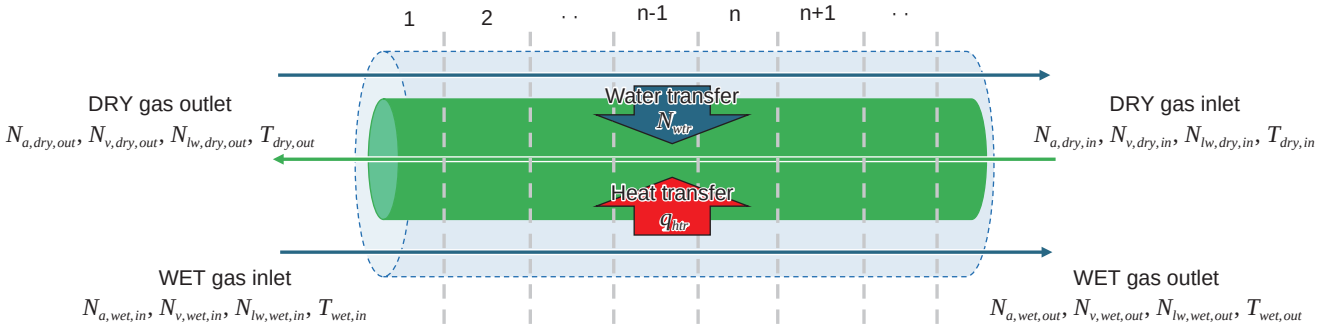


Fig. 7 Discretization of hollow fibers

Based on previous research on the mechanism of gas separation in porous membranes[10], the following hypothesis was made about the mechanism of the drop in humidification performance due to the dry-up phenomenon. Figure 10 shows the mechanism of capillary transfer of water in porous material. The condensed water in the pores moves in the liquid phase with the gradient of the capillary attraction force produced by the difference in the Meniscus radius as the driving force, as shown in Fig. 10(a). When there is less water in the pores, the difference in the Meniscus radius becomes smaller, as shown in Fig. 10(b), and the transfer rate drops. Furthermore, evaporation produces vacancies on both sides inside the pores, and water vapor moves in these areas in the gas phase. Movement in the gas phase is Knudsen diffusion, in which the molecules move due to the pressure gradient while encountering resistance due to collision with the walls. However, the resistance is larger than that for movement in the liquid phase, such that resistance is added and the capillary transfer resistance increases. In pores with no condensate, movement is only by Knudsen diffusion, as shown in Fig. 10(c), and capillary transfer almost ceases to function.

The water vapor condenses inside the pores according to Kelvin's equation of condensation represented by Eq. (6)[11]. When the RH of the gas inside the pores is outside the condensation range for the pore diameter and contact angle of the membrane, the condensate evaporates from inside the pores. Figure 11 shows the relationship between the RH of the WET gas and the pore diameter at the condensation limit. This shows that as the RH of the WET gas drops, the condensate evaporates from inside the pores at pore diameters larger than the pore diameter at the condensation limit. Figure 12 shows the pore diameter distribution per unit area of the porous membrane of the humidifier. Pores of various diameters are distributed in the membrane, and the condensate evaporates from an increasing number of pores as the RH of the WET gas drops and the pore diameter at the condensation limit becomes smaller. For pores in this state, the capillary transfer resistance increases as a result of less condensate, or the condensate disappears

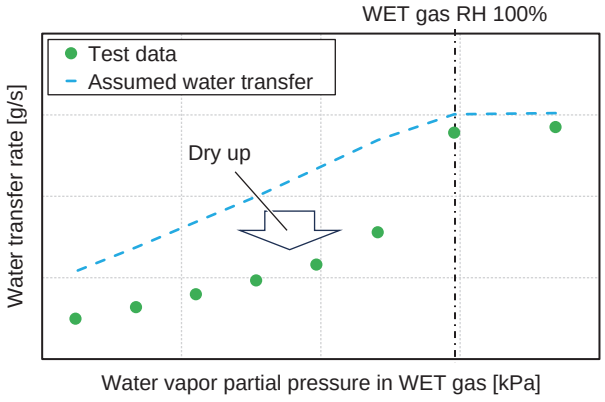


Fig. 9 Characteristics of dry up

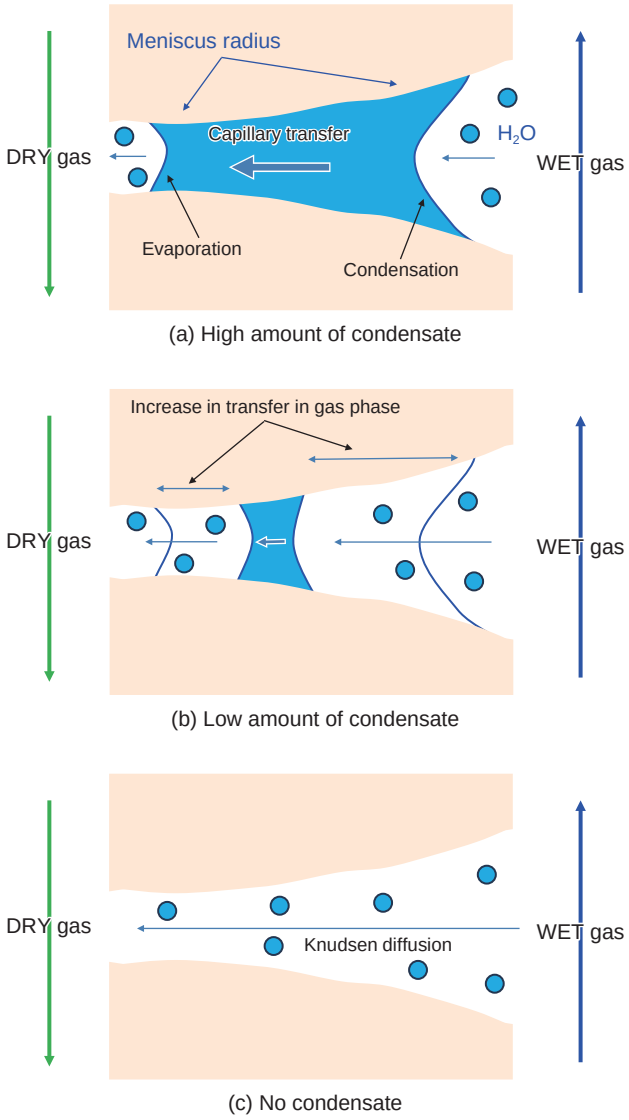


Fig. 10 Mechanism of capillary transfer

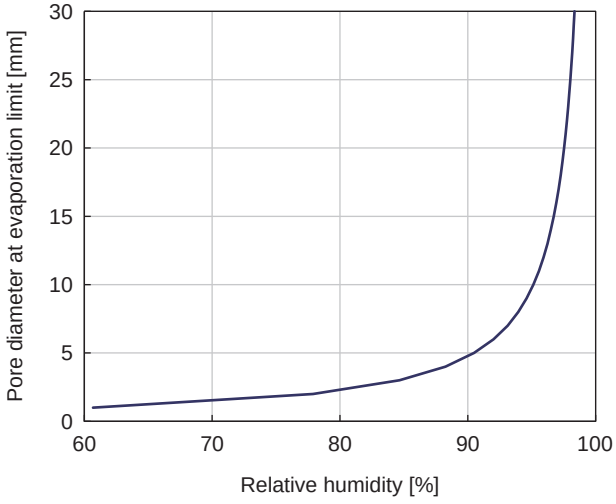


Fig. 11 Relationship between RH and pore diameter at condensation limit

and capillary transfer ceases to function, which is a factor resulting in lower humidification performance.

$$\ln \frac{RH}{100} = -\frac{2\gamma V}{rRT}\cos\theta \qquad (6)$$

Here, the ratio of the number of pores at the condensation limit calculated from the Kelvin equation to the total number of pores in the porous membrane is defined as the dry-up ratio. In order to reproduce the drop in humidification performance due to the dry-up phenomenon in the model, the dry-up ratio is taken into account in the capillary transfer resistance in Eq. (5). It was observed with the test apparatus described in Chapter 4 that the capillary transfer resistance increases exponentially as the dry-up ratio increases, and thus a fitting parameter $\alpha_{dry\text{-}up}$ was set and this relationship was expressed by Eq. (7). $\alpha_{dry\text{-}up}$ uses the same value regardless of the operating conditions or humidifier specifications.

$$R_{mt,mem} = 1/\left(\left(1-\eta_{dry\text{-}up}\right)^{\alpha_{dry\text{-}up}} k_m + \eta_{dry\text{-}up} k_K\right) \qquad (7)$$

The capillary transfer resistance is influenced by the condensate in the pores, and thus a time lag was observed in the change in humidification characteristics due to the transition between the dry and wet conditions. Figure 13 shows the measured relationship between the humidifier weight and the WTR when the temperature of the DRY gas supplied to the humidifier is continuously varied to repeat the cycle of dry and wet conditions.

(A) is the state in which high-temperature DRY gas is flowed in, resulting in the dry condition. When the temperature of the DRY gas is lowered in this condition, the (B) wet condition results and the weight increases due to condensate. When the temperature of the DRY gas is raised to dry again, the (C) condition results in which the weight drops due to evaporation, but the WTR is about the same as that in the wet condition. As shown here, hysteresis was confirmed in the relationship between weight change and the WTR, and the rate of drop in humidification performance due to evaporation and the rate of rise in humidification performance due to condensation were found to differ.

Figure 14 shows the drying process of condensate in the pores as the factor for this phenomenon. In this drying process, the evaporation of water is slower in the pores, and thus the condensate in areas that do not contribute to capillary transfer, such as the porous membrane surface, evaporates first. Therefore, it was thought that the capillary transfer resistance does not increase and the WTR is maintained until the condensate in the pores begins to evaporate.

A key to estimating the water transfer rate under transient conditions is to reproduce this hysteresis of change in the capillary transfer resistance. Therefore, in

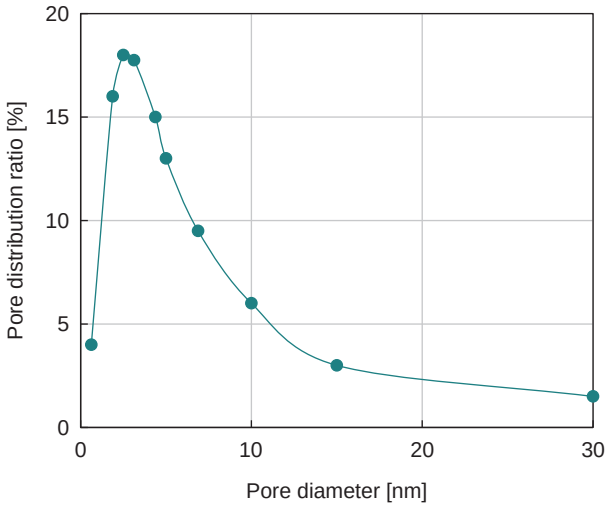


Fig. 12 Pore diameter distribution in membrane

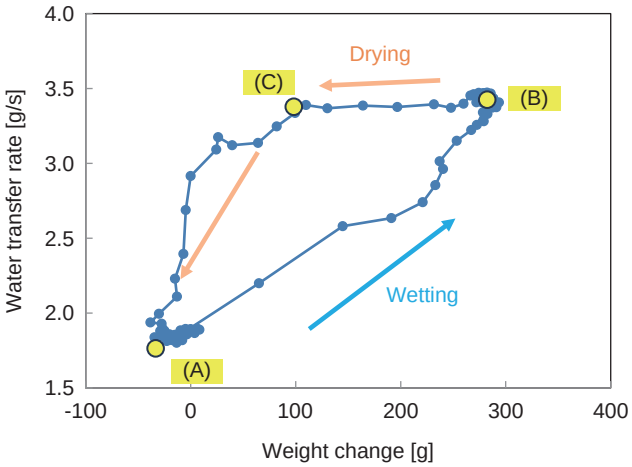


Fig. 13 Hysteresis of weight change versus water transfer

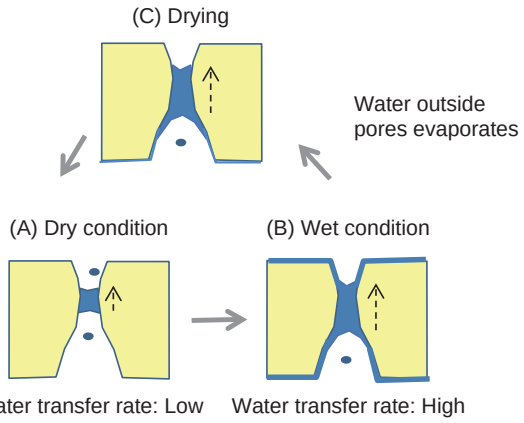


Fig. 14 Condensate during transition between dry and wet conditions

order to reproduce this time lag, the change in the dry-up ratio was defined by the first-order time-lag equations expressed by Eq. (8) and Eq. (9). As the condensation rate and evaporation rate have different characteristics, separate equations were used to enable separate coefficient settings.

Evaporation rate:

$$\frac{\partial \eta_{dry\text{-}up}}{\partial t} = \alpha_{eva} \left(\eta_{dry\text{-}up} - \eta_{dry\text{-}up}^{steady\text{-}state} \right) \quad (8)$$

Condensation rate:

$$\frac{\partial \eta_{dry\text{-}up}}{\partial t} = \alpha_{con} \left(\eta_{dry\text{-}up} - \eta_{dry\text{-}up}^{steady\text{-}state} \right) \quad (9)$$

3.5. Heat Transfer and Phase Change

Heat exchange between the WET gas and DRY gas is heat transfer with the temperature difference as the driving force. Like water transfer, it can be considered as series resistance, and is the sum of three resistances: heat transfer resistance from the WET gas to the WET side face of the membrane, heat transfer resistance from the WET side to the DRY side of the membrane, and heat transfer resistance from the DRY side face of the membrane to the DRY gas.

Furthermore, in heat transfer inside the humidifier module, the latent heat of evaporation influences the temperature distribution inside the module, and thus it is necessary to consider the evaporation of the condensate contained in the gas. The amount of evaporation N_{eva} [mol/s] can be expressed by Eq. (10) using dimensional analysis and boundary layer theory[12]. Therefore, the amount of heat generated was calculated from the amount of evaporation N_{eva} and the latent heat of evaporation.

$$N_{eva} = \beta D_{Air,H_2O} \left(2 + 0.37 Re^{0.61} Sc^{0.51}\right) \frac{P_{sat,v,wet} - P_{v,wet}}{RT} \quad (10)$$

4. Verification of Humidifier Model Accuracy

The overall mechanism of humidification was modeled from the equations derived thus far, and a one-dimensional humidifier model was constructed. Chapter 4 compares the values estimated by this humidifier model and the actual WTR measurement data, and verifies the estimation accuracy of the model.

4.1. Verification of Model Accuracy by Humidifier Evaluation Tests

In order to verify the accuracy of the model under steady-state conditions, the model results were compared with the WTR measurement results obtained using a humidifier unit evaluation test apparatus. Figures 15 and 16 show the overall configuration of the humidifier test apparatus. In

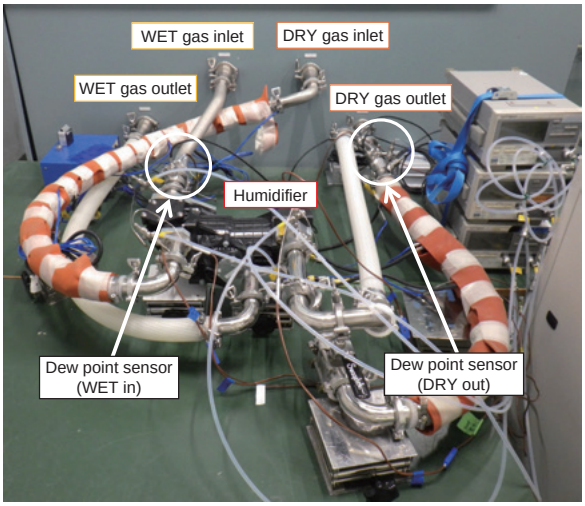


Fig. 16 Configuration around humidifier

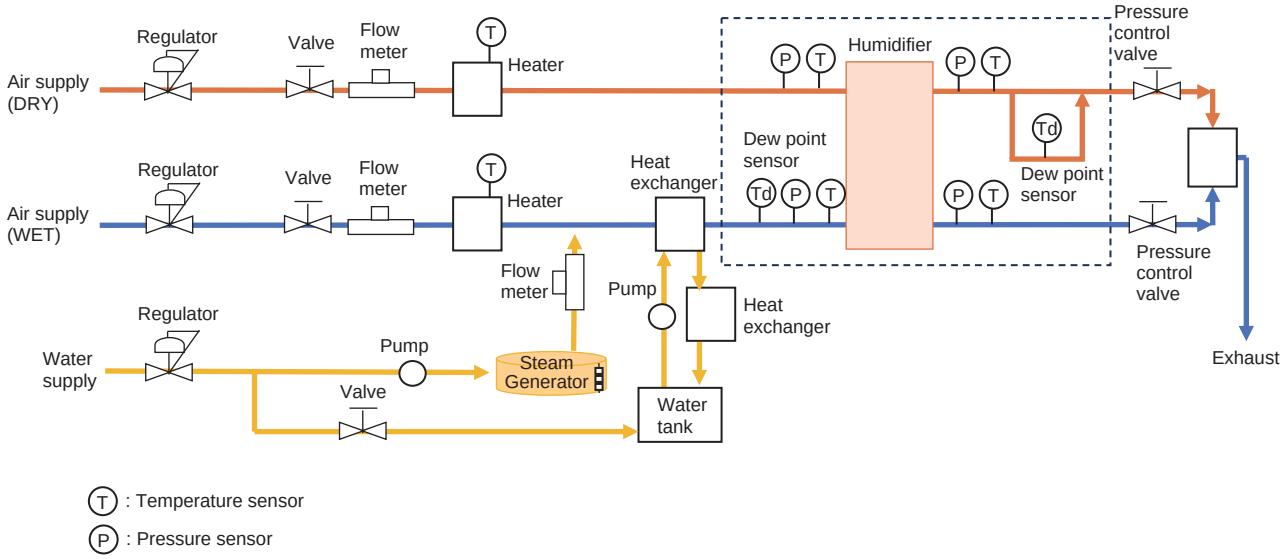


Fig. 15 Humidifier evaluation test apparatus

Table 1 Gas conditions for humidifier evaluation test

Condition No.	Dry inlet temperature	Dry inlet pressure	Dry air flow rate	Dry water vapor flow rate	Wet inlet temperature	Wet inlet pressure	Wet air flow rate	Wet water vapor flow rate	Inlet wet ratio *
	K	kPaA	mol/s	mol/s	K	kPaA	mol/s	mol/s	%
1	333.2	237.0	2.87	0.000567	358.9	208.0	2.47	0.937	96.1
2	323.2	167.1	1.90	0.000533	351.2	140.0	1.66	0.712	96.2
3	313.7	145.7	1.52	0.000500	348.5	121.0	1.32	0.613	98.6
4	314.9	135.7	1.14	0.000400	349.7	116.0	0.97	0.547	101.7
5	315.4	125.8	0.76	0.000283	347.3	112.0	0.66	0.357	106.1
6	314.2	117.7	0.59	0.000233	340.7	107.0	0.50	0.190	105.7
7	313.4	112.0	0.38	0.000167	335.1	105.0	0.32	0.103	117.7
8	313.5	108.1	0.24	0.000100	332.0	103.4	0.20	0.060	126.7
9	313.2	105.5	0.14	0.000067	328.1	103.1	0.14	0.028	113.6

* Inlet wet ratio above 100% indicates presence of two-phase (liquid-gas) state. Inlet wet ratio up to 100% is equivalent to relative humidity (RH) .

Table 2 Gas conditions for humidifier evaluation test

Condition No.	Dry inlet temperature	Dry inlet pressure	Dry air flow rate	Dry water vapor flow rate	Wet inlet temperature	Wet inlet pressure	Wet air flow rate	Wet water vapor flow rate	Wet inlet water contents	Inlet wet ratio *
	K	kPaA	mol/s	mol/s	K	kPaA	mol/s	mol/s	g/s	%
10	338.4	224.0	1.756	0.00037	351.1	180.0	1.56	0.497	37.9	119.3
11								0.497	30.8	102.6
12								0.433	26.0	89.9
13								0.373	22.4	80.0
14								0.317	19.0	70.6

* Inlet wet ratio above 100% indicates presence of two-phase (liquid-gas) state. Inlet wet ratio up to 100% is equivalent to relative humidity (RH).

order to measure the WTR due to the humidifier, a method of flowing in the generated water vapor and mixing it into the dry air is adopted. The configuration enables realization of the predetermined test conditions by controlling the air flow rates with mass flow meters and adjusting the amount of water vapor generated to achieve the target humidity. Although this test apparatus is limited to steady-state conditions, evaluation can be performed under various operating conditions including low-humidity conditions. The accuracy of the model was verified by measuring the humidifier characteristics using this test apparatus and comparing them with the calculation results of the humidifier model under the same conditions.

Table 1 shows the supply air conditions assuming operating conditions from high load to low load in the fuel cell system. In the humidifier unit test, the WTR was measured while performing steady-state operation with the test apparatus set to these gas conditions. The gas conditions were set in the humidifier model as the input conditions, and the water transfer rate was calculated. Figure 17 compares the humidifier model and test results. As shown in the graph, it was confirmed that the humidifier model can estimate the WTR at an accuracy of ±15% or less under all conditions.

Next, the accuracy was also verified under conditions where the dry-up phenomenon may occur. As shown in Table 2, tests and model calculations were performed even under gas conditions with a WET gas RH of less than 100%, and the results were compared. Conditions No. 12 to 14 are the region in which the dry-up phenomenon may

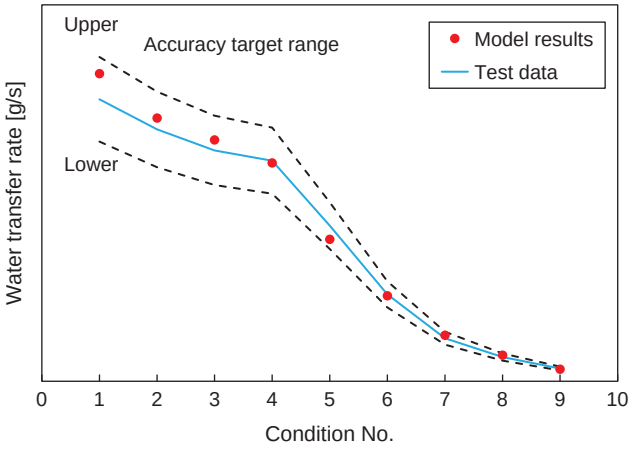


Fig. 17 Comparison of humidifier model and test results

occur. Figure 18 shows the comparison results. Here, the calculation results did not achieve the target accuracy when not considering the increase in the capillary transfer resistance. However, it was confirmed that the humidifier model that considers the dry-up phenomenon accurately reproduces the drop in WTR and can estimate the water transfer rate at the target accuracy of ±15% or less.

4.2. Verification of Model Accuracy in Fuel Cell System

As verification of the humidifier model accuracy under transient conditions, the model results were compared with measurement results of the RH of the supply air in fuel cell system operation. The fuel cell system performed power generation simulating the U.S. Environmental Protection Agency's (EPA) city driving mode, and the RH of the supply air was measured by attaching Vaisala Corporation's HUMICAP HMT337 dew point measurement instrument to the humidifier DRY gas outlet piping. Figure 19 compares the time series data of the RH measurement results and the model calculation results. This confirmed that the model can estimate RH at the target accuracy of ±15% or less even under transient conditions.

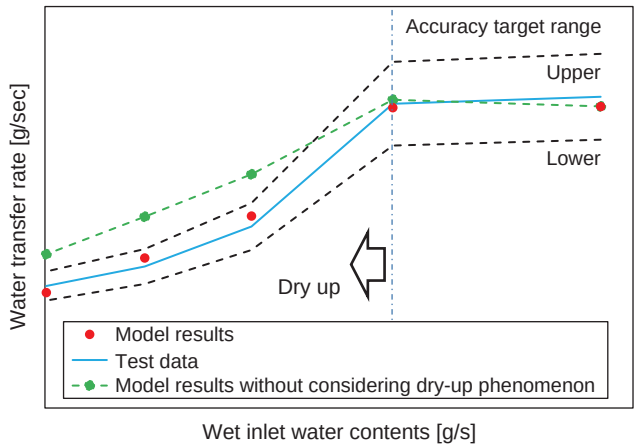


Fig. 18 Comparison of humidifier model and test results in dry up conditions

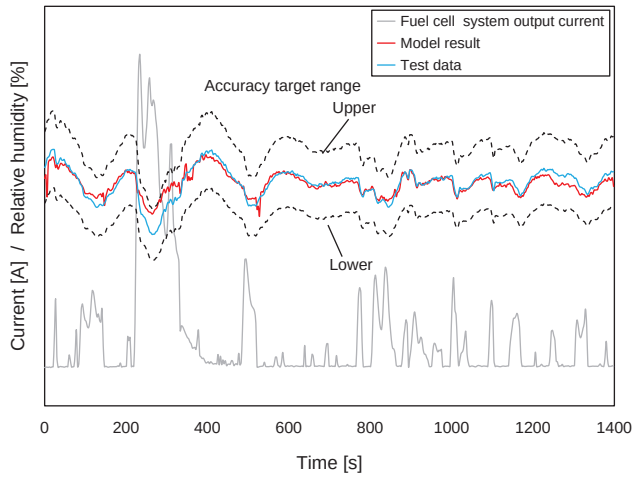


Fig. 19 Comparison of humidifier model and test results in mode operation

In Honda's new fuel cell system, this one-dimensional humidifier model was converted to an approximation function, and a control model that provides accuracy while lowering the calculation load was implemented. Highly accurate water content control is achieved by controlling the coolant temperature based on the amount of water vapor calculated by this control model[13].

5. Conclusion

A one-dimensional humidifier model that estimates the RH of the air supplied to the fuel cell stack from the operating conditions was constructed for use in performance design and control optimization of fuel cell systems.

(1) The water transfer, heat transfer, and water phase change phenomena inside a porous hollow fiber membrane humidifier are expressed mathematically.
(2) The drop in the WTR and the response time lag of that drop were modeled, focusing on the dry-up phenomenon.
(3) The accuracy of the model was verified by comparing the model calculation results with the WTR measurement values in humidifier unit evaluation tests and measurement results of the RH of the supply air in bench mode operation of the fuel cell system. It was confirmed that the WTR due to the humidifier can be estimated at the set target accuracy of ±15% or less under both steady-state conditions including the dry-up phenomenon and transient conditions in the fuel cell system.

References

(1) Zatoń, M., Rozière, J., Jones, D. J.: Current understanding of chemical degradation mechanisms of perfluorosulfonic acid membranes and their mitigation strategies: a review, Sustainable Energy & Fuels, Royal Society of Chemistry, Vol. 1, Issue 3, p. 409-438, (2017), doi: 10.1039/C7SE00038C
(2) Perry, M. L., Daring, R. M., Kandoi, S., Patterson, T. W., Reiser, C.: Operating Requirements for Durable Polymer-Electrolyte Fuel Cell Stacks, Polymer Electrolyte Fuel Cell Durability, Springer, p. 399-417, (2009), doi: 10.1007/978-0-387-85536-3_20
(3) Jinnouchi, R.; Nenryo Denchi no Genri to Ouyou, Asakura Publishing Co., Ltd., p. 132-136, (2023) (in Japanese)
(4) Vu, H. N., Nguyen, X. L., Han, J., Yu, S.: A study on vapor transport characteristics in hollow-fiber membrane humidifier with empirical mass transfer coefficient, International Journal of Heat and Mass Transfer, Vol. 177, p. 1-12, (2021), doi: 10.1016/j.ijheatmasstransfer.2021.121549

(5) Nguyen, X. L., Vu, H. N., Yu, S.: Parametric understanding of vapor transport of hollow fiber membranes for design of a membrane humidifier, Renewable Energy, Vol. 177, p. 1293-1307, (2021), doi: 10.1016/j.renene.2021.06.003
(6) https://www.nok.co.jp/product/film/kashitu.html, (accessed 2024/7/16)
(7) Asaeda, M.: Nano-Pore Technology in Ceramics. Separation Mechanisms of Molecular Mixtures by Porous Ceramic Membranes., Ceramics Japan: bulletin of the Ceramic Society of Japan, Vol. 29, No. 11, p. 967-970, (1994)
(8) Haraya, K.: Gas Separation Process with Membrane, Membrane, Vol. 13, No. 2, p. 83-92, (1988), doi: 10.5360/membrane.13.83
(9) Asano, K.,: Bussitsu Idou no Kiso to Ouyou, Fick no Housoku kara Taseibunkei Zyouryuu made, Maruzen Publishing Co., Ltd., p. 72-73, (2004) (in Japanese)
(10) Asaeda, M.: Gas separation using inorganic porous solid membrane, Membrane, Vol. 10, No. 5, p. 297-304, (1985), doi: 10.5360/membrane.10.297
(11) Chikazawa, M., Takei, T.: Adsorption and Capillary Condensation -Surface Structure and Properties of Condensed Liquid-, Hyomen Kagaku, Vol. 14, No. 9, p. 526-532, (1993), doi: 10.1380/jsssj.14.526
(12) Asano, K.,: Bussitsu Idou no Kiso to Ouyou, Fick no Housoku kara Taseibunkei Zyouryuu made, Maruzen Publishing Co., Ltd., p. 122-123, (2004) (in Japanese)
(13) Ozaki, H., Yamazaki, K., Ogawa, T., Maniwa, S., Miura, T., Huston, T. W.: Development of New Fuel Cell System, Honda R&D Technical Review, Vol. 37, p. 13-19

List of Symbols

d	Pore diameter [m]
$D_{H2O,Air}$	Diffusion coefficient between air and vapor [m^2/s]
k	Transfer coefficient [m/s]
N	Molar flow rate [mol/s]
P	Pressure [Pa]
q_{htr}	Heat transfer rate [J/s]
r	Radius of curvature of pore [m]
R	Gas constant [$J \cdot mol^{-1} \cdot K^{-1}$]
R_{mt}	Transfer resistance [s/m]
Re	Reynolds number
S	Membrane surface area [m^2]
Sc	Schmidt number
T	Temperature [K]
t	Time [s]
V	Molar volume of water [m^3/mol]
α	Fitting coefficient
β	Fitting coefficient
γ	Surface tension of water [N/m]
$\eta_{dry\text{-}up}$	Dry up rate
θ	Contact angle [degree]

Subscripts

a	Air
asm	Assumption
con	Condensation
dry	DRY side
dry-up	Dry up
eva	Evaporation
in	Inlet
K	Knudsen diffusion
l	Liquid water
m	Capillary transfer in membrane
mem-inner	Membrane inner
out	Outlet
sat	Saturation
steady-stat	Steady state
total	Total
v	Vapor
wet	WET side
wtr	Water transfer

■ Author ■


Shuto MANIWA


Yohei HIDAKA


Koichi KIMURA


Nobuki KOIWA

Application of Acoustic Emission Technology to Damage Analysis of High-Pressure Container for Fuel Cell Vehicles

Takanori SUZUKI, Ph.D.[1] Takashi KUWAYAMA[1] Masamichi KAWABE[1]
Ichiro HARADA[1] Toshihiko KANEZAKI, Ph.D.[1]

ABSTRACT

Evaluation tests are conducted in order to verify the design accuracy of vehicle-mounted high-pressure containers that use carbon fiber-reinforced plastic layers. We have developed a method to identify the state of damage generated in carbon fiber-reinforced plastic layers that eventually leads to bursting in these tests, in order to enhance the design accuracy of such containers.

For this method, we used acoustic emission technology and processed the measured results into dimensionless data. This enabled us to set threshold values for the appearance of major damage that is the prelude to bursting. For the first time in the world, this makes it possible to terminate the test directly before the bursting takes place.

Applying this technology will enhance the design of high-pressure containers by enabling a precise analysis of the state of damage in the carbon fiber-reinforced plastic layer of a high-pressure container.

1. Background and Purpose

In recent years, fuel cell systems have started to be considered and implemented as a source of electrical power in a range of applications, including for moving vehicles. Among such applications, fuel cells for vehicles are considered particularly promising, as such types of vehicles do not emit greenhouse gases during operation (see Fig. 1).

Recently in vehicle applications, it has become commonplace to store hydrogen, which serves as the fuel, as a high-pressure gas at 70 MPa. The high-pressure containers used are divided into four types, from Type 1 to Type 4, and are shown in Fig. 2.

Type 1 high-pressure containers are totally metal. Types 2 and 3 high-pressure containers are made with a metal liner surrounded by a layer of higher-strength carbon fiber-reinforced plastic (CFRP) in order to reduce size and weight. Finally, Type 4 high-pressure containers consist of a plastic liner surrounded by a CFRP layer. As Type 3 and Type 4 containers are compact and relatively lightweight, they are used as vehicle-mounted high-pressure containers. Currently, the Type 4 high-pressure container in particular is being widely used.

International standards are in place that stipulate the necessary performance of vehicle-mounted high-pressure containers, including global unified standards relating to safety (Global Technical Regulation No. 13: GTR13)(1) and UN regulations (United Nations Regulation No. 134: UNR134)(2). In Japan, while high-pressure containers are generally regulated by the High Pressure Gas Safety Act, the Act on Vehicles for Road Transportation regulates vehicle-mounted high-pressure containers. The international regulations mentioned previously have been ratified and are applicable under Japanese law.

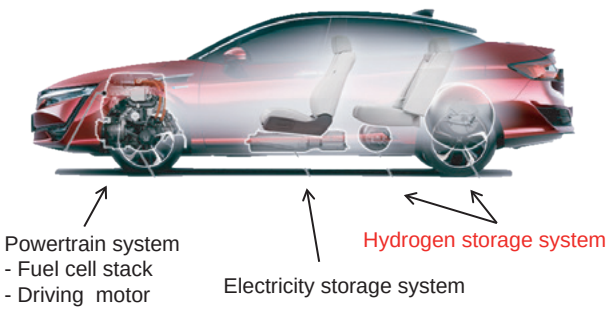


Fig. 1 Layout of major components of fuel cell vehicle

[1] Innovative Research Excellence, Power Unit & Energy
E-mail: takanori_suzuki@jp.honda

The cost of high-pressure containers continues to be an issue in the widespread uptake of fuel cell vehicles (FCV) [3]. An effective way to reduce the cost of high-pressure containers is to reduce the use of expensive CFRP. As well, reducing the amount of material used helps to reduce the weight of the high-pressure container, and so various initiatives are being pursued for its achievement.

In basic terms, the amount of CFRP used depends on the ratio of the expected pressure to the carbon fiber (CF) strength. The functionality and durability of high-pressure containers are stipulated by laws and regulations. It is necessary to reduce the amount of CFRP as much as possible while still meeting these stipulations. Also, in order to achieve this, an important development task is to establish a high level of CFRP layer design technology.

The aim of our development was to establish a high-pressure container damage analysis technology to enhance the design precision of the CFRP layers of high-pressure containers.

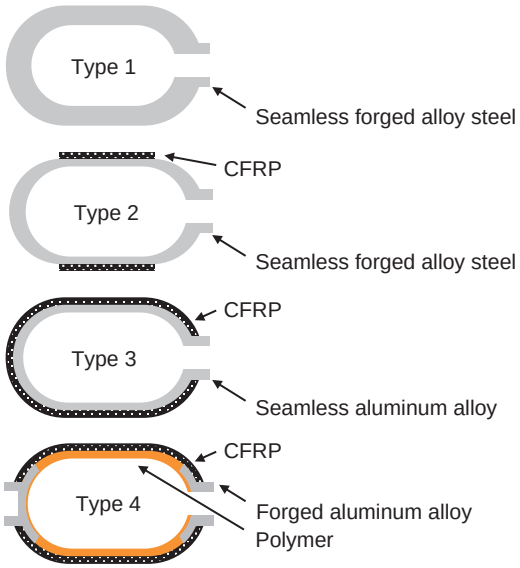


Fig. 2 Types and structures of high-pressure containers

2. Technology Development Goals

The accuracy of strength estimates and lifespan forecasts of the CRFP layers in high-pressure containers is not high. Therefore, the thickness of the CFRP layer is designed to provide a sufficient safety factor, and thus there is room to the design better by increasing accuracy.

Computer-aided engineering (CAE) is deployed in CFRP layer strength design. Based on this, prototype high-pressure containers are created and evaluated in testing, and the results are compared to the estimated values in order to enhance the accuracy of the forecasts. In other words, the development is a repeated trial-and-error process, as depicted in Fig. 3.

In many cases, the high-pressure containers rupture into many small pieces, making it challenging to perform a detailed causal analysis of the origin and progression of the bursting of the prototype high-pressure containers. As a result, a high technological hurdle exists to feeding damage analysis results back into the design forecasting technology, creating a major challenge in improving CFRP layer strength forecasting technology.

It is important, therefore, to terminate the evaluation test just prior to the bursting of the high-pressure container, so that the state of the damage leading up to the final bursting can be properly understood. The methods for performing hydraulic pressure-induced burst tests and durability tests in high-pressure containers are stipulated in the GTR. Although the maximum pressurization rate in the tests is 1.4 MPa/s, many containers burst suddenly and without warning during the test, and in burst testing in particular, it is challenging to stop just prior to the burst.

Given the above, it was believed that the following technologies were additionally required.

(1) Technology to terminate the test before bursting

(2) Technology to identify the location of damage

In order to achieve this, the authors turned to acoustic emissions (AE) technology and enhanced the development process to enable detailed measurements of damage progression, as shown in Fig. 4. This report will focus on the particularly important first of the additional technologies mentioned above, (1) Technology to terminate the test before bursting.

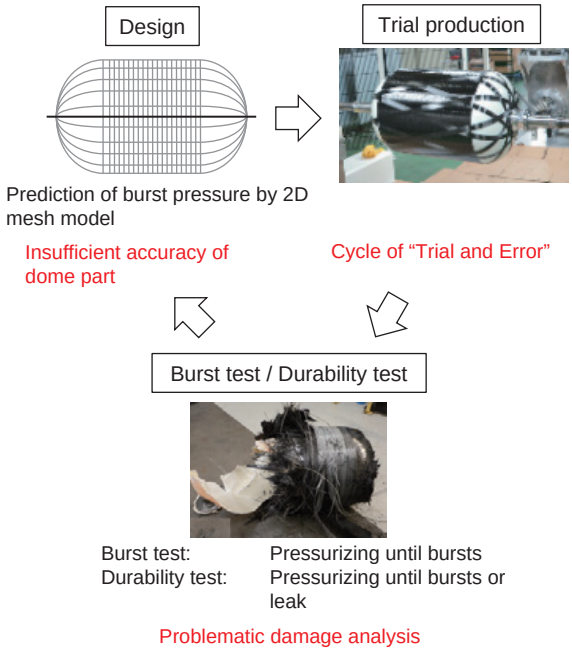


Fig. 3 Conventional high-pressure container development process

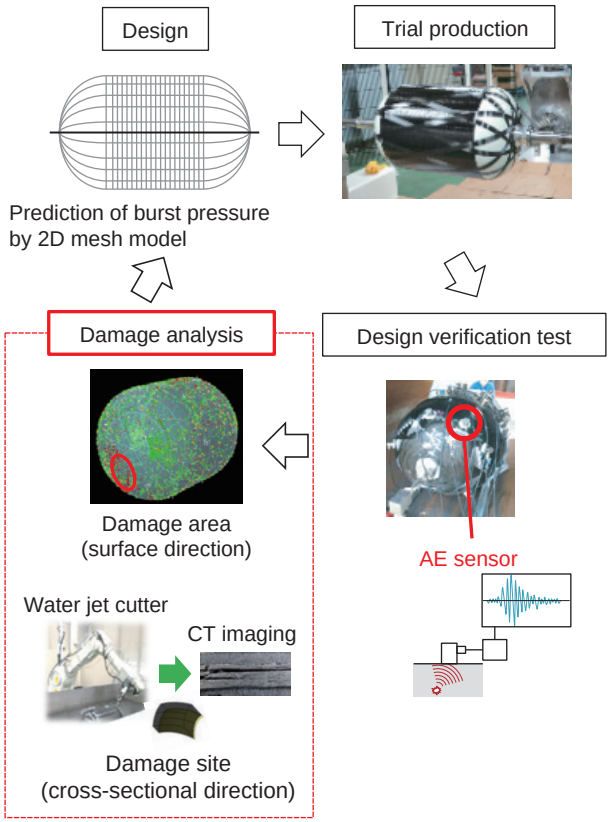


Fig. 4 Enhanced high-pressure container development process

3. AE Technology

AE technology[4)-8)] is one of the technologies that are used for the nondestructive testing of structures, such as building structures or storage tanks. AE is a phenomenon in which the elastic energy stored within a structure is released as sound waves when that structure is deformed or damaged. AE waves refer to the elastic waves that travel through the target object and are detected. The strength and frequency of the sound waves vary according to the scale of damage and the material, and so they are often used to clarify the damage mechanisms of strengthening members.

AE waves are detected by sensors mounted on the surface of the high-pressure container and interpreted as a composite of multiple waves as shown in Fig. 5. Measurement noise can then be removed by setting appropriate threshold values, and the number of small waves that exceed the threshold value is defined as the count number. The energy of the AE waves is equivalent to the calculated surface area based on the AE wave duration time and amplitude.

In a high-pressure container, the CFRP layer is made of bundles of CF (filaments) with resin infused between the fibers. It is believed that damage to the CFRP layer progresses according to a process like that shown in Fig. 6. Specifically, it is assumed that damage in the form of cracks and delamination in the resin forms in the early stages of use of the high-pressure container. As this increases and expands, the CF starts to undergo breakage, until finally the container bursts when a large amount of breakage has developed in the CF. By detecting the AE waves that are generated during this process, the authors believed it would be possible to analyze the process of damage to the CFRP layer.

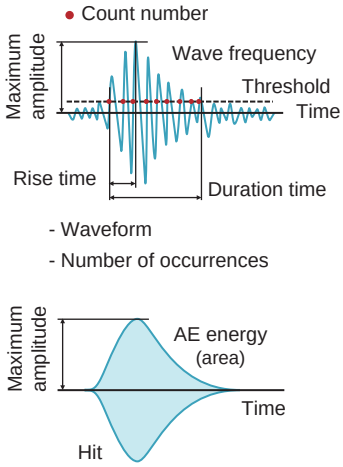


Fig. 5 AE waves and parameters

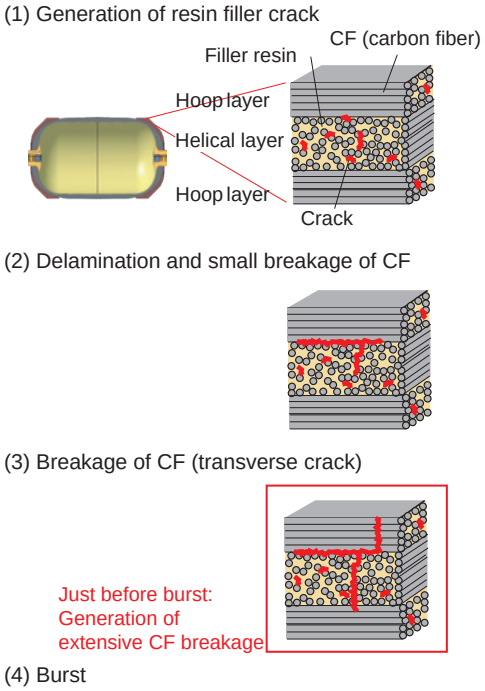


Fig. 6 Images of damage process in CFRP layer of high-pressure container

4. Technology Application and Results

To develop a technology that would use AE to stop a test just before bursting, hydraulic burst tests were conducted on vehicle-mounted high-pressure containers. In the hydraulic burst test, a high-pressure pump was used to fill and release water into and from a high-pressure container in order to change the internal pressure at a constant rate and thus evaluate the high-pressure container's strength and durability. The conditions were stipulated according to the high-pressure container codes and standards.

Two types of high-pressure containers were used in the tests, both sharing the same liner but with different CFRP layers. (Type A had an outer diameter of 530 mm and a length of 920 mm, while Type B was 550 mm and 920 mm, respectively.) In this report, the AE measuring devices, the measurement and analysis software, and the AE sensors were commercially available products. The templates needed to make the measurements, such as the basic shape of the measured object and propagation velocity, were as provided. (Measurement device: Vallen System MB19; Software: Vallen VisualAE R2019.0926.3; AE sensor: Vallen System VS150-RIC)

Figure 7 shows an example of the changes in the duration time, count number, and AE energy of the AE waves that were detected when the internal pressure of a Type A high-pressure container was increased at a constant rate. The horizontal axis shows the pressure in the high-pressure container, and the vertical axis shows the AE energy, count number, and duration time of the AE wave as detected from above. In the graph, AE waves with dimensionless AE energy from 20 up to less than 100 are shown as yellow dots, those of 100 or more are shown as red dots, and all others are shown as green dots. The dimensionless AE energy is as determined by Eq. (1) below.

The results show that as pressure increases, the highest values on the vertical axis remain almost constant (as marked by each chart's horizontal white dashed line) up to around 150 MPa, which is indicated by the vertical pink dashed line. A sudden increase in the values is observed around 150 MPa, and AE waves with steadily higher values are detected after this point, with greater pressures leading to an increasing number of yellow dots. Finally, bursting occurs at approximately 167 MPa, as indicated by the solid pink line, with an extremely large increase in the values.

The integrated count number and integrated AE energy results are shown in Fig. 8, making it easier to understand the circumstances leading up to bursting. The solid blue line shows the pressure in the high-pressure container for the given moment. The dot colors have the same meaning as in Fig. 7.

In the pressure range below approximately 150 MPa, the series of points starts by following a constant slope, as shown by the solid white line.

The line of points then rises abruptly and gradually increases thereafter. Eventually, there is another rapid rise, as seen in the upward solid red line, before bursting takes place.

The slope of the straight line in this Fig. 8 from the initial period up to an integrated count number of about 1.3×10^5 (at a pressure of about 150 MPa) represents the average AE energy of the small waves that make up the AE waves. After this, the linear relationship state as seen in the early stages of the test is defined as the steady state.

The same kind of test was conducted on several high-pressure containers of both Type A and Type B specifications, and the results are shown in Fig. 9.

As in Fig. 8, in Fig. 9 the slopes tend to rise at a constant rate from the start of the test up to a certain integrated count number.

However, the slopes of the steady-state straight lines obtained from the various high-pressure containers differ

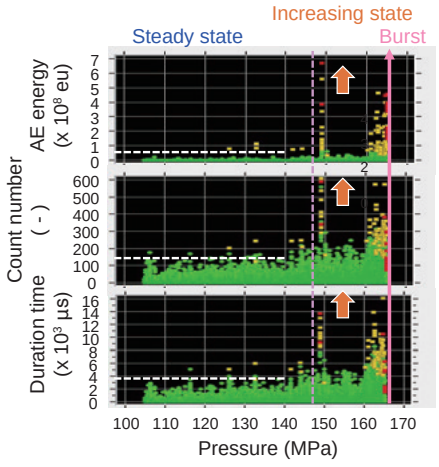


Fig. 7 AE detection status in burst test (high-pressure container: Type A)

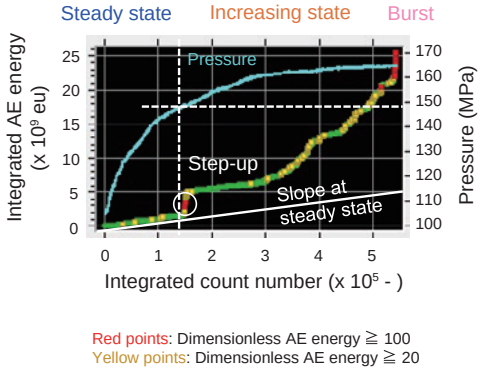


Fig. 8 Changes of integrated energy and pressure in burst test (high-pressure container: Type A)

greatly. This is hypothesized to be caused by differences in sensor installation conditions and the ensuing sensitivity differences, AE propagation characteristics, and other variables. Therefore, to enable a unified comparative evaluation, we tried to standardize the slope of the straight line that is seen at the beginning of the pressure increases in Figs. 8 and 9.

By focusing on the average AE energy of all the waves that comprise the measured AE waves as shown in Fig. 5 and comparing it to the ratio of the average AE energy of the AE component waves under steady-state conditions, it was hypothesized that it would be possible to determine the severity of the damage in the CFRP layer. That is to say, the average value per AE energy count number at steady state was used to define the dimensionless AE energy according to the following formula.

$$\text{Dimensionless AE energy} = \left(\frac{E'}{\text{Count number}}\right) \Big/ \left(\frac{\sum E'}{\sum \text{Count number}}\right)_{\text{Steady state}} \quad (1)$$

Here, E' is the AE energy calculated from the measured AE waves and is the apparent AE energy including various noise sources in the test and measurements, relative to the true AE energy (E).

Figure 10 shows the results of the measurements from Fig. 8 readjusted relative to the pressure and dimensionless AE energy. After taking an overall look at the various data such as high-pressure container burst pressures, the dimensionless AE energy at which a large amount of damage leading to bursting takes place was set at 100. Dimensionless AE energy was less than approximately 20 at steady-state conditions up to about 150 MPa. So, as in Figs. 7 and 8, in Fig. 10 steady-state dimensionless AE energy of less than 20 is shown with a green dot, AE energy from 20 up to less than 100, indicating major damage, is shown with a yellow dot, and AE energy of 100 or more is shown with a red dot.

Figure 11 shows the results of the comparison between the burst pressure and the pressure that appears when dimensionless AE energy exceeding 100 appears in the measured AE waves, for the burst pressures that occur for the different high-pressure containers tested in burst tests. This figure shows that the ratio for all examples was less than 1. This confirms that the test could be stopped just before bursting if the threshold value for determining the dimensionless AE energy bursting is set appropriately. This technology has made it possible to secure a test object in a state just prior to bursting, making it possible to analyze the progression of damage with a detailed analysis of the CFRP layer.

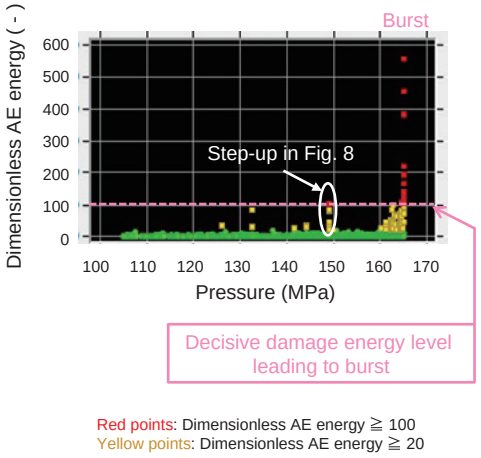


Fig. 10 Results of damage analysis using dimensionless AE energy (high-pressure container: Type A)

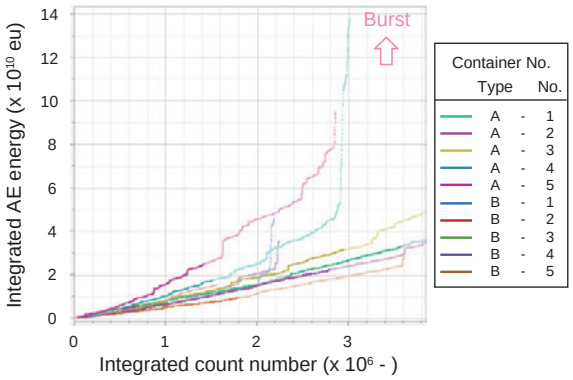


Fig. 9 Changes of integrated energy in burst tests of various high-pressure containers

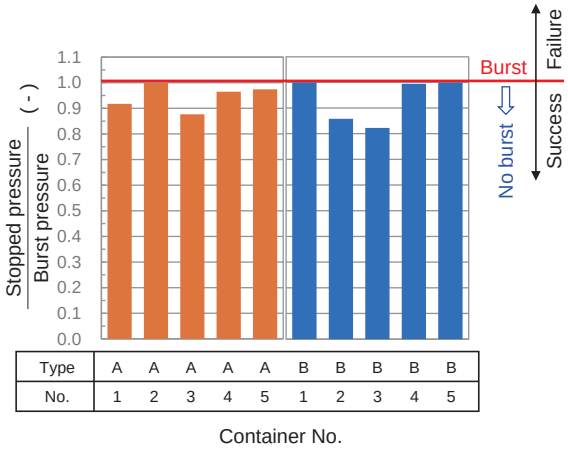


Fig. 11 Validation results of shutdown technology just before burst

5. Conclusion

In order to reduce the weight and cost of high-pressure containers mounted in fuel cell systems in moving vehicles, a high-accuracy CFRP layer design technology is required. To enhance the design accuracy, therefore, we have proposed a method using AE technology to identify the presence of CFRP layer damage that eventually leads to bursting in tests that can involve the bursting of high-pressure containers.

We focused on dimensionless AE energy and used experimental methods to exclude variations between high-pressure containers and individual tests, so as to establish a threshold value for shutdown decisions that can be applied to high-pressure tanks of a range of specifications. Using this value, we achieved a world-first technology to terminate a test just prior to bursting.

By providing a precise understanding of the damage process in the CFRP layer of high-pressure containers, this technology can be expected to enhance the design technology of high-pressure containers, reduce their weight and cost, and shorten development times.

As mentioned in Chapter 2, as well, we are studying technology to identify the location of damage by analyzing the differences in arrival times of the AE waves obtained in testing, as well as technology to identify damaged materials by analyzing the wave frequency of AE waves. We believe that this AE technology can contribute to further enhancements in design accuracy by advancing understanding of the damage process in CFRP layers in greater detail.

References

(1) https://unece.org/sites/default/files/2023-07/ECE-TRANS-180-Add.13-Amend1e.pdf, (2023/7/17)
(2) https://unece.org/sites/default/files/2022-07/R134am4e.pdf, (2022/3/21)
(3) https://www.nedo.go.jp/content/100956710.pdf, (2023/2/9)
(4) Niwa, Y., Kobayashi, S., Otsu, M.: STUDIES OF SOURCE LOCATION BY ACCOUSTIC EMISSION, Proceedings of the Japan Society of Civil Engineers, Vol. 276, p. 135-147 (1978) (in Japanese)
(5) Suzuki, M., Nakanishi, H., Iwamoto, M., Jinen, E., Maekawa, Z., Mori, A., Sun, F.: Studies on Fracture Mechanisms of CFRP by Acoustic Emission Method, Transactions of the Japan Society of Mechanical Engineers Series A, Vol. 53, No. 492, p. 1459-1466 (1987) (in Japanese)
(6) Kawasaki, H., Takizawa, M., Nakajima, T., Nakamura, H., Okazaki, J., Nakagawa, K.: Suiatsu Hirou Shiken ni yoru Kouatsu Suiso you CFRP Chikuatsuki he no AE Shiken Tekiyousei Kentou, IIC REVIEW, No. 52, p. 23-28 (2014) (in Japanese)
(7) Omori, M., Kawasaki, T., Omori, S., Nakamura, H., Sasaki, T.: AE ha Jyuushin Shuuhasuu wo mochi ita CFRP zai no Sonshou Hyouka Kenkyuu, Reinforced Plastics, Vol. 63, No. 9, p. 434-439 (2017) (in Japanese)
(8) Nakajima, T., Kawasaki, H., Sato, A.: Experimental Consideration about AE Sources Location of a Thin CFRP Vessel Pressure Test, Transactions of the Japan Society of Mechanical Engineers Series A, Vol. 79, No. 797, p. 115-118 (2013) (in Japanese)

■ Author ■


Takanori SUZUKI


Takashi KUWAYAMA


Masamichi KAWABE


Ichiro HARADA


Toshihiko KANEZAKI

Development of Power Exporter e: 6000, External Power Output Device, with Three-phase 200 V AC Output Function

Yuuna YAHAGI[1] Tomoyuki KOZU[1] Takuya ODAKA[2]
Kenta YAGASAKI[3] Takahiro FUKUI[1] Kosuke IHARA[3]

ABSTRACT

The less-expensive and more versatile Power Exporter e: 6000 was developed based on the Power Exporter 9000 external power output device. A lower price was achieved while maintaining high quality by optimizing power output in response to market needs, reducing the number of parts in line with the reduced power output, and addressing change points with minimal cost. In addition, the first known function to provide three-phase 200 V AC output with three linked units has been added to realize Vehicle to Load and Vehicle to Home as an electrical facility for general use, thereby expanding use applications to large electrical equipment such as industrial equipment. The power supply cable length was extended and the control was modified to conform to the "Electric Vehicle V2L DC Charge/Discharge System Guidelines" to enhance connectivity with even more EVs, including those of other automakers.

1. Introduction

Honda aims to achieve carbon neutrality for all products and corporate activities by 2050. To help achieve this, the company has set a target of a sales ratio of 100% for EV/FCV in the automobile market by 2040[(1)]. The EV market is in an expansion trend worldwide, and the need to utilize electricity stored in vehicles is also expected to expand accordingly.

Since 2016, Honda has sold the Power Exporter 9000[(3)] (PE9000) portable external power output device, the first such device known to conform to the Guidelines of Charge/Discharge System for Electric Vehicle V2L DC version[(2)] (hereinafter, V2L Guidelines). Figure 1 shows the configuration of the external power output system. The voltage supplied from the EV is DC voltage, and this voltage fluctuates depending on the condition of the vehicle and the battery. This fluctuating DC voltage is converted to the prescribed DC voltage by a converter, and then converted into AC voltage by an inverter to supply electricity to electrical equipment. The PE9000 uses Honda's inverter technology developed for engine generators[(4), (5)], and features the ability to simultaneously output high-quality AC voltages of 100 V and 200 V. It can also supply large power output of 9 kVA quietly and odorlessly, enabling phase-free use as a power source for events and kitchen cars in normal times, and as a power source for evacuation centers and disaster response headquarters that have lost power in the event of a disaster, etc.

However, products with lower output and lower price than the PE9000 are currently the mainstream in Japan's external power output device market. Furthermore, the market for Business Continuity Planning (BCP) support for

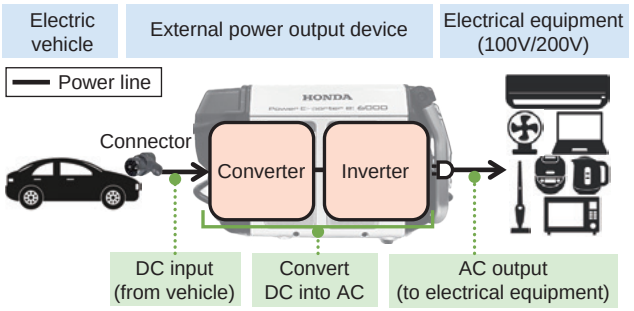


Fig. 1 Configuration of external power output system

[1] Innovative Research Excellence, Power Unit & Energy
E-mail: yuuna_yahagi@jp.honda
[2] Honda Racing Corporation
[3] Honda Motor Co., Ltd.

Table 1 Comparison of specifications

		PE6000	PE9000	A	B
Destination		Japan	Japan	Japan	Japan
Rated power (kVA)		6	9	3	4.5
Rated alternating current voltage (V)	Single-phase	100 / 200	100 / 200	100	100
	Three-phase	200	-	-	-
Receptacle		200 V × 1 100 V × 4	200 V × 1 100 V × 6	100 V × 2	100 V × 3
Mass (kg)		41	51	21	38
Volume (m^3)		0.128	0.128	0.073	0.093
Cable length (m)		2.1	1.2	2.0	2.0
Applicable standard	Charge/discharge system guidelines for electric vehicles V2L DC version	2.1	2.1	2.1	2.1
	CHAdeMO version	2.0	1.0	2.0	2.0

small and medium-sized business establishments is expected to expand in the future. As this BCP support anticipates the use of equipment such as shown in Fig. 2 (as of October 2023, according to Honda's research), it was thought that a 6 kVA class external power output device would be needed. In addition, with the expansion of the external power output device market, there are demands to enable use in a wider variety of devices, and the addition of three-phase 200 V AC (hereinafter, three-phase AC) output function that can operate large electrical equipment is expected. Meanwhile, the increase in EVs that conform to the V2L Guidelines is providing greater opportunity for use in combination with various vehicles, and there are also market demands to enhance the ease of connection with vehicles and increase versatility.



Examples of power consumption

2 air conditioners	1,600 W
20 ceiling lights	1,600 W
10 desktop PCs	1,000 W
2 laptops	60 W
1 electric kettle	1,000 W
1 TV	150 W
Total	5,410 W

Fig. 2 Example of instantaneous power consumption in BCP of small and medium-sized office

2. Development Goals

The Power Exporter e: 6000 (PE6000) external power output device was developed based on the PE9000 as a low-priced product with a rated output of 6 kVA, and further evolved to meet market demands. Figure 3 shows an external view of the PE6000 connected with an electric vehicle. While maintaining the functions and high power supply quality of the PE9000, development and manufacturing costs were minimized and a low price was achieved by using 7% fewer parts than the PE9000 and reusing 88% of the PE9000's parts. In addition, the main development items were set as follows to meet market demands and make the PE6000 a more competitive product.

(1) Addition of the first known three-phase 200 V AC output function
(2) Increased versatility in vehicle connectivity

Table 1 lists the main specifications of the PE6000, PE9000, and competitors' products.



Fig. 3 External view of PE6000 with electric vehicle

3. Introduction of Developed Technologies

3.1. Three-phase 200 V AC Output Function

A three-phase AC output function was added to the PE6000. Three-phase AC is a type of commercial power supply stipulated by Japan's Electricity Business Act, and is a three-phase power supply with a line voltage of 182 V to 222 V and a phase difference between lines of 120 degrees. As three-phase power supply can operate large electrical equipment such as elevators and industrial equipment, implementation of this function in external power output devices is expected as a response to power outages. However, when operating large electrical equipment that exceeds 10 kW with conventional three-phase AC generators, Japanese law stipulates that notification of the safety regulations be provided to a national body and a chief engineer be appointed, and there were issues with operation in the event of an emergency. Therefore, this development

constructed technology enabling the combination of PE6000 units to enable proper and easy handling of large-output three-phase power sources.

3.1.1. Principle of generation of three-phase AC

Three-phase AC can be generated by synthesizing three sine waves called U-phase, V-phase, and W-phase. Figure 4 shows the system diagram, and Fig. 5 shows an external view of the three-phase AC output function. In this system, three EVs and three PE6000 units that conform to the V2L Guidelines[2] are combined, and the two inverters mounted in each PE6000 are used to generate three-phase AC. The three PE6000s are designated Units A, B, and C, and the two inverters mounted in each unit are designated Inverter 1 and Inverter 2. When started in three-phase output mode, the phase difference between Inverter 1 and Inverter 2 is set to 120 degrees. If the start-up order of the three PE6000s is set to Unit A, B, and then C, Inverter 1 of Unit A outputs the U-phase, and Inverter 2 outputs the V-phase. Inverter 1 of Unit B that starts next outputs the V-phase by synchronizing with Inverter 2 of the previously started Unit A, and Inverter 2 outputs the W-phase. Likewise, Inverter 1 of Unit C outputs the W-phase, and Inverter 2 outputs the U-phase. The AC waveforms output from each PE6000 are then connected with a current collecting box to obtain three-phase AC power rated at 16.4 kVA (line current 52 A). This technology is an application of real-time communication synchronous control[4] and parallel synchronous control[5] cultivated through engine generators. Each technology is described in detail below.

Real-time communication synchronous control is a technology that sets the phase difference between the output waveforms of two inverters in the same device to an arbitrary angle, and outputs and maintains it with high accuracy. In a previous dual-voltage inverter generator[4], the phase difference of the 100 V AC waveforms output by Inverters 1 and 2 is set to 180 degrees. As a result, the phases of the positive and negative peaks of the output waveforms of the two inverters match, and thus 200 V AC output can be obtained by taking this difference. The PE6000 also performs similar control in single-phase mode.

Parallel synchronous control is a technology that enables synchronous operation of parallel-connected inverter generators without signal communication lines. Two inverters that output the same phase detect the phase difference between the voltage and the current, and slightly increase or decrease the output frequency based on the detected phase difference to approach each other, thereby maintaining waveform synchronization without signal communication lines. In a previous inverter generator that supports parallel operation[5], this technology is used to automatically synchronize generators connected with a dedicated cable to synthesize power equivalent to two units.

As the developed system combines three vehicles and

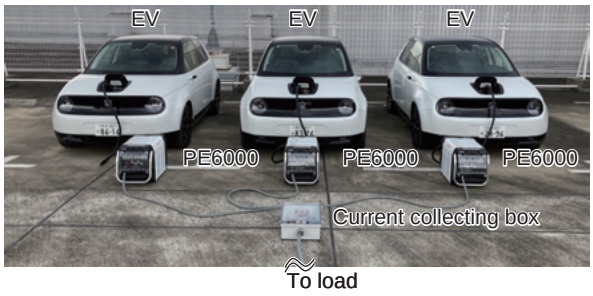


Fig. 5 External view of parallel three-phase 200 V AC output system

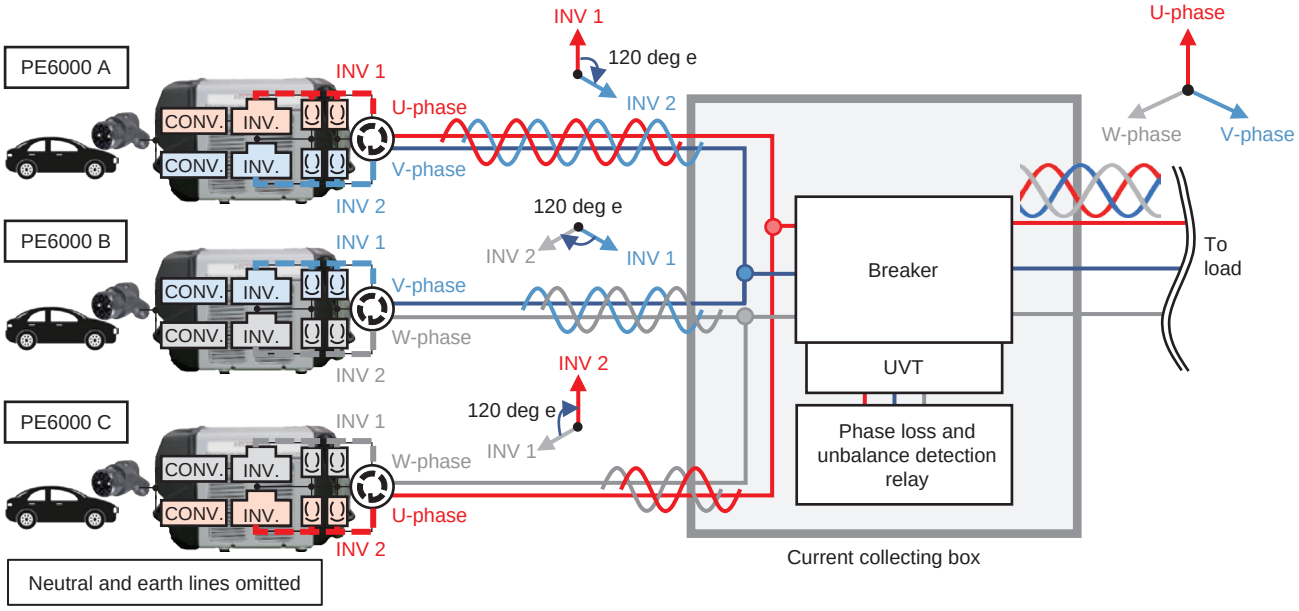


Fig. 4 System configuration of parallel three-phase 200 V AC output

Table 2 Conditions of single output test

Vehicle	Honda e (Honda)
Output power	No load
Power factor	—
Frequency (Hz)	50

three PE6000 units, there is the possibility that the output of one or two of the three PE6000 units may stop due to a vehicle power shortage or the overheating protection function of the PE6000, etc. In this case, the U-, V-, and W-phases would be lost or unbalanced, possibly resulting in damage to the connected electrical equipment. Therefore, the current collecting box is equipped with a phase loss and unbalance detection relay and an Under Voltage Trip device (UVT), and functions have been added to activate a breaker to stop power output in the event of phase loss or unbalance. In addition, functions have been added to notify the user with the indicator lamps of the PE6000 that power output has stopped.

3.1.2. Actual verification of three-phase AC output

It was confirmed that the PE6000 can output sine waves with the newly set phase difference of 120 degrees under the conditions shown in Table 2. Figure 6 shows the respective AC voltage waveforms output in single-phase mode and three-phase mode, and Table 3 shows the measurement results. The difference θ_{diff} between the electrical angles of the inverters can be obtained by Eq. (1) below.

$$\theta_{diff} = \frac{T_{diff}}{T} \times 360 \text{ (deg e)} \quad (1)$$

T: Cycle (msec)
T_{diff}: Time difference of zero-cross timing (msec)

Table 3 Results of single output test

Output mode setting	Single-phase	Three-phase
One cycle of sine wave T (msec)	20.00	20.00
Time difference of zero-cross timing T_{diff} (msec)	10.00	6.67
Difference of electric angles θ_{diff} (calculated value) (deg e)	180.0	120.0

Table 4 Conditions of three-phase output test

Vehicles	3 cars, 3 Honda e cars
Output power (kVA)	16.4
Line current (A)	52
Power factor	Inductive load 0.8
Frequency (Hz)	50

The phase difference of the output waveforms of two inverters started in single-phase mode was 180 degrees, the phase difference of the waveforms started in three-phase mode was 120 degrees, and the phase difference could be accurately controlled to the setting by real-time communication synchronous control.

Next, three vehicles and three PE6000 units were combined, and the three-phase AC output waveform was checked under the test conditions shown in Table 4 that assume an inductive load such as a motor. Figure 7 shows the line voltage waveform at a rated output of 16.4 kVA, and Table 5 shows the measurement results. The three-phase sine waves were synchronized by parallel

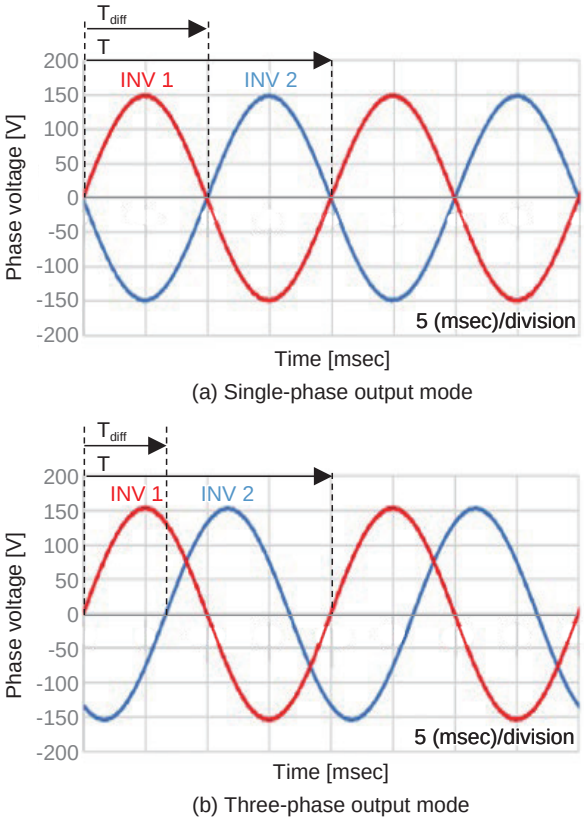


Fig. 6 Comparison of phase differences in single output waveforms for each mode

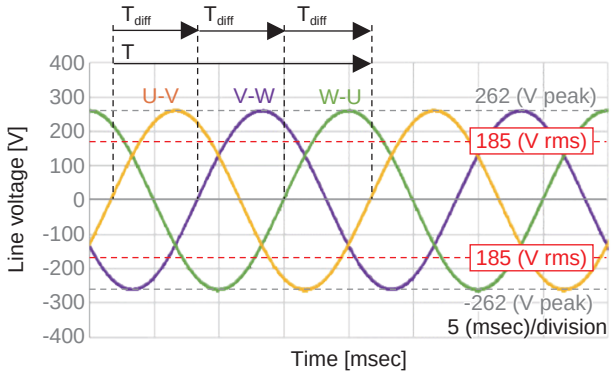


Fig. 7 Three-phase output waveform

Table 5 Results of three-phase output test

	U-V	V-W	W-U
Line voltage (V rms)	185	185	185
One cycle of sine wave T (msec)	20.00		
Time difference of zero-cross timing T_{diff} (msec)	6.67	6.67	6.67
Difference of electric angles θ_{diff} (calculated value) (deg e)	120.0	120.0	120.0

synchronous control, and an AC waveform with a line voltage of 185 V and a phase difference of 120 degrees, which is within the provisions of the Electricity Business Act, could be output.

The above technologies realize a three-phase AC output function and enable use in large electrical equipment such as industrial equipment. In addition, the power output per unit is 10 kW or less, the total power output is less than 50 kW, and the system conforms to the interpretation of technical standard for electrical facilities (Article 199-2)[6]. This realizes Vehicle to Load and Vehicle to Home (V2L2H) as an electrical facility for general use, which does not require notification to a national body or appointment a chief engineer, even though the power output exceeds 10 kW. Furthermore, the same unit can be switched between single-phase and three-phase for use, enabling use in a wider variety of situations than a dedicated three-phase power source unit.

3.2. Versatility of Vehicle Connectivity

The PE6000 and PE9000 are portable external power output devices that comply with the V2L Guidelines[2], and have the configuration shown in Fig. 8 where the power supply connector is plugged into the power supply port of the vehicle, and the vehicle and the Power Exporter main unit are connected by the power supply connector cable. As the PE9000 was developed exclusively for the CLARITY FUEL CELL, the cable length was set to 1.2 m, which is suitable for the former. However, with the spread of EVs, the number of vehicles that conform to the V2L Guidelines is increasing, and opportunities to use the PE9000 in combination with vehicles other than the CLARITY FUEL CELL are also increasing. As a result, issues with usability have become apparent, with the shortness of the cable making it a challenge to connect depending on the position of the power supply port of the vehicle. In order to expand versatility, the cable was lengthened, the electromagnetic lock system was changed accordingly, and the resulting issues were addressed. These three points are introduced below.

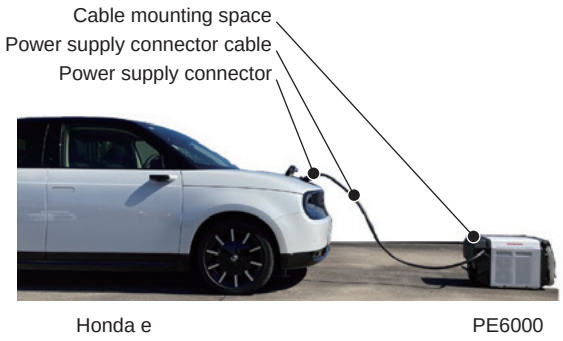


Fig. 8 External view of power supply connector and cable

Table 6 Comparison of specifications of power supply connectors

		PE6000	PE9000
Required maximum current (A)		36	54
Rated current (A)		37	100
Rated voltage (VDC)		Below 500	DC450
Mass (kg)		2.2	3.2
Cable	Length (m)	2.1	1.2
	Diameter (mm)	ϕ23.4 (typical)	ϕ26.3 (typical)
	HV+/- conductor size (mm^2)	5.5 (10 AWG)	22
	Mass (kg/m)	0.5	1.0

3.2.1. Longer power supply connector cable

The cable was lengthened without increasing the storage space by reducing the cable diameter and increasing the number of loops when storing the cable. Table 6 shows the specifications of the power supply connector. As the PE9000 has large power output of 9 kVA, a thick cable diameter of φ26.3 mm is needed. The cable diameter of the PE6000 was reduced to φ23.4 mm in accordance with the reduced power output. Furthermore, the cable storage specification winds the cable in three loops while gradually reducing the winding radius, as shown in Fig. 9. The space created by the smaller cable diameter was utilized by changing the winding specification, and achieved storage of the lengthened cable.

However, the reduced winding radius of the third loop in order to store the lengthened cable resulted in interference between the cable and surrounding parts, and reduced workability when storing the cable. This issue was addressed by verification using a 3D model to clarify the connector storage angle at which there is no interference between the cable and surrounding parts, and by designing a new holder.

The above measures enabled the installation of a 2.1 m power supply connector cable, the longest known for a portable external power output device compatible with the V2L Guidelines, while reusing the PE9000 frame parts other than the holder to reduce costs. This achieved a package that is easy to connect with a wider variety of vehicles.

3.2.2. Change of electromagnetic lock system

For safety performance reasons, the power supply connector is equipped with an electromagnetic lock using

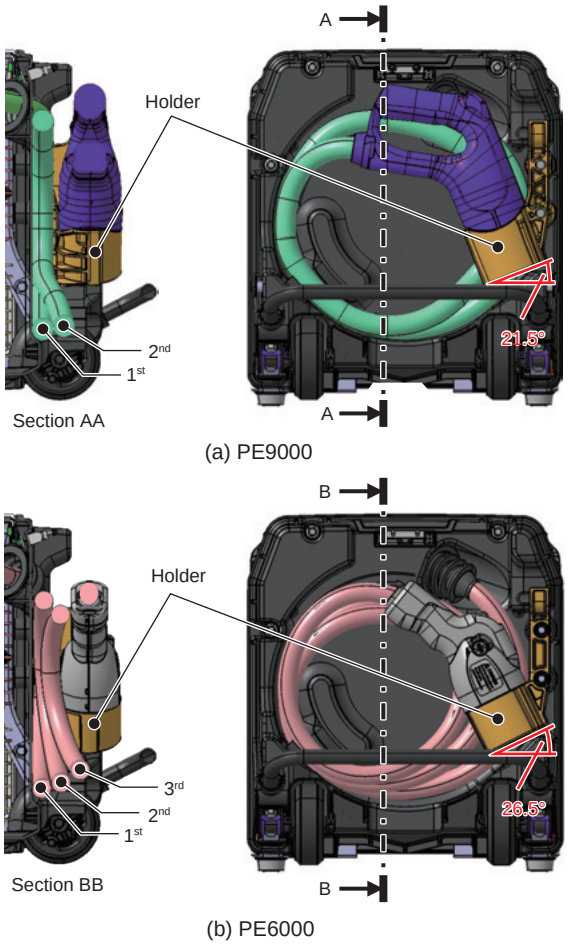


Fig. 9 Power supply connector cable storage status

a solenoid so that the mating between the vehicle and the power supply connector is not released during power supply. Due to the reduction in the power supply connector cable diameter, the electromagnetic lock system of the power supply connector was changed.

The V2L Guidelines stipulate that the electromagnetic lock specification should be a constantly energized type if the cross-sectional area of the conductor of the high-voltage cable of the power supply connector is 22 mm^2 or more, or a self-holding type[7] if it is less than 22 mm^2. Therefore, as shown in Table 6, the large power output PE9000 that has a large cable diameter is a constantly energized type, whereas the PE6000 adopts a self-holding type because of the smaller cable diameter. Figure 10 shows the state transition diagram of the electromagnetic lock using a solenoid. In contrast to the constantly energized type that constantly consumes electric power while locked, the self-holding type consumes electric power only when switching between locked and unlocked, which has the advantage of being able to reduce the amount of electric power consumed by the electromagnetic lock. Compared with the PE9000, the electromagnetic lock of the PE6000 can reduce electric power consumption by 98.4% (0.31 Wh) when power is continuously supplied for 5 minutes, and by 99.7% (1.89 Wh) when power is continuously supplied for 30 minutes.

On the other hand, the addition of circuits was an issue in adoption of the self-holding type. The constantly energized type can control switching and detection of the lock state with a single circuit, but this calls for three circuits for the self-holding type. This development added a control circuit to the Electrical Control Unit (ECU) to

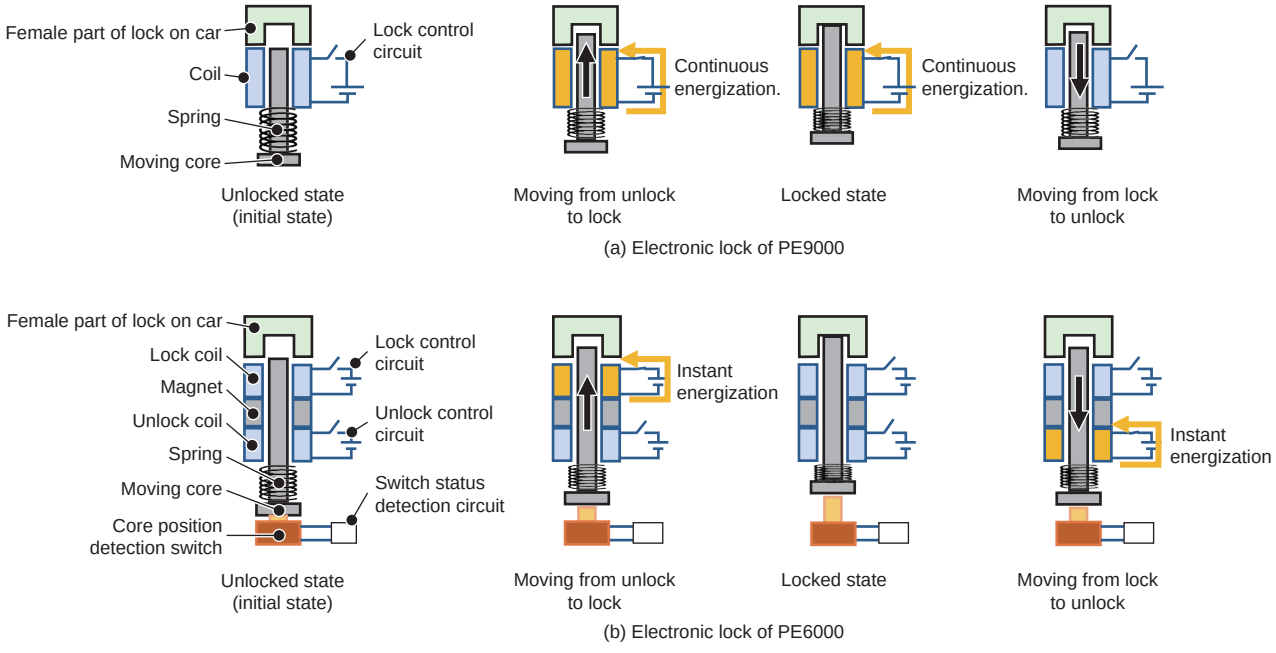


Fig. 10 State transition diagram of electromagnetic lock using solenoid

support the change in the electromagnetic lock. At this time, the board pattern was revised to maintain the board size, which enabled reuse of the ECU case and contributed to cost reduction without impacting the ECU layout and mounted components.

3.2.3. Response to issues due to change in lock system

The PE6000 and PE9000 are battery-less external power output devices without internal 12 V power supply. Therefore, the ECU is started and the electromagnetic lock is operated by receiving 12 V power supply from the vehicle. This 12 V power is supplied via the power supply connector or a 12 V accessory socket according to the specifications of the connected vehicle. Figure 11 shows an outline of connection when 12 V power is supplied from a 12 V accessory socket.

The constantly energized type PE9000 does not need 12 V power supply when switching from locked to unlocked, while the self-holding type PE6000 requires 12 V power supply as described above. Thus, the situation where the power supply connector cannot be disconnected may occur when the cable connected to the 12 V accessory socket is disconnected during power supply, when the power supply of the 12 V accessory socket is stopped by vehicle control, in case of irregular high-voltage battery start-up, or when the high-voltage cable has a broken wire.

This development addressed events where the power supply connector cannot be disconnected with the following two items.

First, a function was added to notify the loss of 12 V power during power supply by the lamp action of the indicator lamps. The notification enables the user to notice that the cable has been disconnected or the vehicle 12 V power supply has stopped, and to restore the 12 V power supply needed to unlock before performing the stop operation. This helps reduce events where the power supply connector cannot be disconnected.

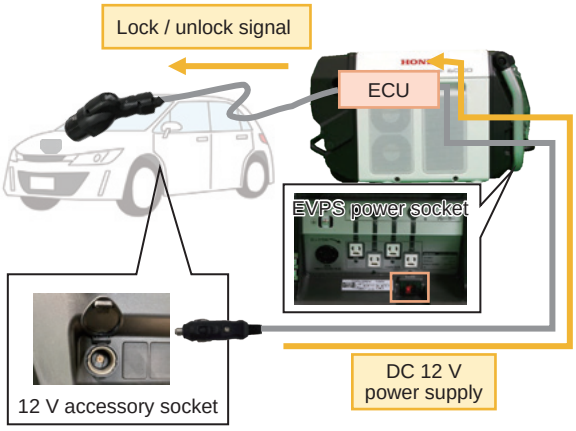


Fig. 11 System configuration of control power supply from 12 V accessory socket

Second, electromagnetic lock control was developed that enables removal of the power supply connector even if it could not be disconnected because the stop operation was performed in the condition with the 12 V power supply lost without noticing the above notification. When the power supply connector cannot be disconnected, the user restarts the PE6000 after restoring the 12 V power supply. Regardless of the state of the electromagnetic lock, the PE6000 performs self-diagnosis at start-up to determine whether the high-voltage battery has started up irregularly or the high-voltage cable has a broken wire. Based on the self-diagnosis results, if the power supply connector could not be removed due to a loss of 12 V power supply, the unlock operation is performed and normal operation is restored. However, if the power supply connector could not be removed due to an irregularity in the high-voltage system, the locked state is continued. Thus, normal operation is restored only when proper circumstances are confirmed, and the power supply connector can be disconnected as usual after power supply is completed.

The above technology enabled changing to a self-holding type without installing a 12 V battery.

4. Conclusion

The PE6000 was developed based on the PE9000 external power output device, and realized a low price by optimizing the power output while maintaining high quality and adding new functions. Sales commenced from September 2023. Despite the low price, the PE6000 achieved the development items set in response to market needs to provide expanded versatility and become a highly competitive product.

(1) The PE6000 is considered the first such device to add a three-phase AC output function. Combination of three units enables the provision of a large power output of 16.4 kVA, expanding use applications to power supply for industrial equipment, etc.

(2) The versatility of vehicle connectivity has been expanded by extending the length of the power supply connector cable to 2.1 m, considered the longest for a portable external power output device compatible with the V2L Guidelines. In addition, technical issues due to this change were addressed with minimal cost, which helped to realize the low price.

It is thought that the above technology will expand the range of use in V2L2H and enable the proposal of an even greater range of phase-free use. Honda is confident that the PE6000 will help support people's lives and lead to the expansion of customer joy.

References

(1) https://global.honda/en/sustainability/integratedreport/, (accessed 2024/5/31)

(2) CHAdeMO Association, Guidelines of Charge /

Discharge System for Electric Vehicle V2L DC version, (2015)
(3) Tsuno, K., Komatsu, T., Funaki, M., Shin, M., Kanazawa, H., Ogushi, K.: Development of High-output, Portable External Power Output System for Use with Next-generation Environment Vehicles, Honda R&D Technical Review, Vol. 28, No. 2, p. 37-44
(4) Nakamura, M., Kasagi, S., Hirose, T., Shinkawa, Y., Asai, K., Kamimura, K.: Development of EM7000is Dual-voltage Inverter Generator, Honda R&D Technical Review, Vol. 16, No. 2, p. 55-64
(5) Fujii, S., Shimizu, M., Nakamura, M.: Development of Sine Wave Inverter Generating System, HONDA R&D Technical Review, Vol. 8, p. 70-76
(6) https://www.meti.go.jp/policy/safety_security/industrial_safety/law/files/dengikaishaku.pdf, (accessed 2024/5/31)
(7) Jikohojigata Sorenoid, Mekatoro Tsuushin, Shindengen Mechatronics Co., Ltd., No. 35, p. 1-4, (2021) (in Japanese), https://smt.shindengen.co.jp/product/download/pdf/smtcom35.pdf, (accessed 2024/5/31)

■ Author ■


Yuuna YAHAGI


Tomoyuki KOZU


Takuya ODAKA


Kenta YAGASAKI


Takahiro FUKUI


Kosuke IHARA

Enhancement of Feeling in Turn Focusing on Pitching Behavior

Naoto OHKUBO[1]

ABSTRACT

In order to provide a natural feeling in turn for general drivers in daily driving, a method was examined for adjusting the pitching behavior produced by steering in control of acceleration and deceleration linked with lateral motion. In consideration of the characteristic that the pitch angle response is twice the steering frequency, a control law was devised to reduce unnatural feeling in turn. The effect of the control law and the controlled variable was verified by simulation, and it was confirmed that the timing at which the pitching behavior occurs can be adjusted without impacting the rolling behavior. Next, actual vehicle tests were conducted, and the vehicle behavior was confirmed to be similar to that in the simulation. In addition, sensory evaluation showed that the method is effective in enhancing the feeling in turn, and that there is an appropriate value for the control strength.

1. Introduction

Numerous control devices are applied to the chassis area to enhance vehicle dynamic performance. Typical examples include control of the front and rear wheel steering angles to enhance maneuverability at low vehicle speeds and stability at high vehicle speeds[(1), (2)], ABS control that helps decrease tire locking in sudden braking, and yaw moment control by lateral distribution of the braking and driving forces[(3), (4)], all of which have increased stability and responsiveness.

In control by braking, the yaw moment control installed as standard equipment has enhanced stability performance, and application is also spreading to various areas other than emergency avoidance[(5), (6)]. However, increasing the usage frequency of braking devices necessitates consideration of factors such as durability and quietness, so it has not been widely applied to the operation area used by general drivers in daily driving (Fig. 1).

In control by the power plant, it is known that when acceleration and deceleration are performed in turning, a yaw moment is generated due to weight transfer between the front and rear wheels[(7)], and technology has been reported that provides driving enjoyment and a good driving feel in the daily operation area by controlling acceleration and deceleration linked with lateral motion[(8)] to assist the turning operation and realize a "smooth G connection"[(9)].

With the electrification of power plants, the application range of vehicle dynamic control that makes use of the good responsiveness of the motor is expanding. This makes it also necessary to consider the unnatural feeling produced by control intervention.

In addition, it has been reported that pitching behavior also occurs along with yaw and rolling behavior in turning, and that the temporal difference between rolling and pitching behavior impacts the turning sensation[(10)].

This study therefore defined the sensation of turning without unnatural feeling in response to the driver's steering wheel operation as "feeling in turn," and examined a method to enhance the feeling in turn and reduce the unnatural feeling produced by control intervention, focusing on pitching behavior in turning within the aforementioned technology to control acceleration and deceleration linked with lateral motion.

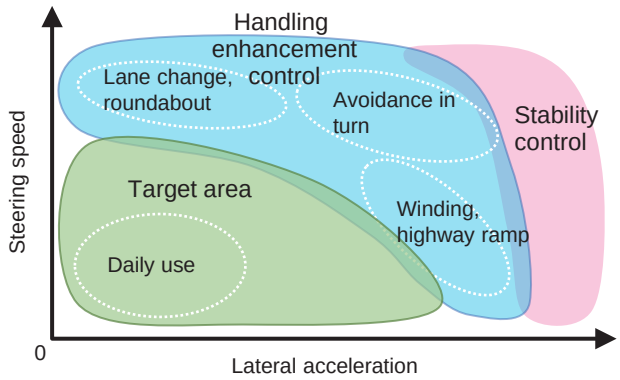


Fig. 1 Target scene

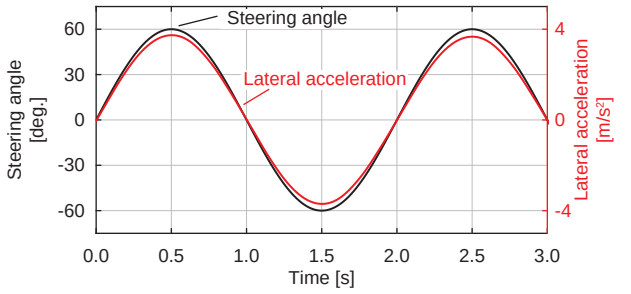
[1] Honda Motor Co., Ltd.
E-mail: naoto_ohkubo@jp.honda

2. Pitching Motion Produced by Steering

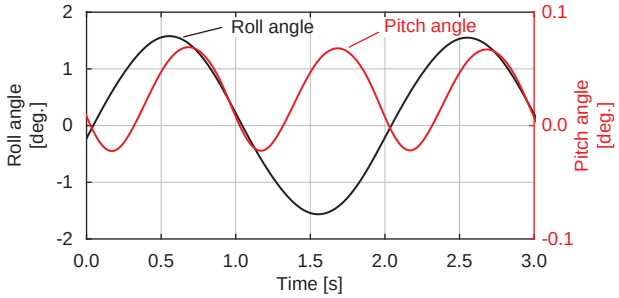
It is known that when acceleration and deceleration occur in turning, weight transfer occurs between the front and rear wheels, and a yaw moment is generated[7]. In longitudinal force control linked with lateral motion, a yaw moment that promotes turning is generated by the longitudinal force on the deceleration side. However, a pitching moment is also generated at the same time, which also contributes to pitching behavior.

Figure 2 shows an example of the lateral acceleration and the roll angle and pitch angle responses in sinusoidal steering input. Here, the lateral acceleration and roll angle can be seen to respond symmetrically to the left and right steering directions. In contrast, the pitch angle has characteristics such that it responds independently to the steering direction and has a response frequency twice the steering frequency.

It was therefore thought that if the temporal difference between the rolling and pitching behavior could be adjusted by controlling the longitudinal force to adjust the phase of the pitching behavior, this would be effective to enhance the feeling in turn.



(a) Steering angle and lateral acceleration



(b) Roll angle and pitch angle

Fig. 2 Example of vehicle motion during sinusoidal steering input

3. Control for Enhancement of Feeling in Turn

3.1. Modeling of Pitching Motion

In order to perform control that adjusts the phase of the pitching behavior by longitudinal force control, it is necessary to incorporate the pitching motion characteristics into the control law. However, taking the pitching motion into account increases the complexity of the vehicle model.

An approximate equation was thus derived that reproduces the aforementioned pitching motion characteristics with a minimum model, and a control law based on that approximate equation was examined.

First, the pitching motion produced by steering is summarized as Eq. (1).

$$I_Y\ddot{\theta} = -hF_X + M_{YJ} + M_{YS} \tag{1}$$

On the right side of Eq. (1) here, F_X is the longitudinal force, and M_{YJ} and M_{YS} are the respective pitching moments generated by the jacking force and the suspension. The pitching moments are positive in the forward downward direction as shown in Fig. 3, and the gyro moment, tire vertical spring stiffness, unsprung mass, and anti-dive/lift/squat that contribute little to steering and pitching motion were ignored.

The longitudinal force F_X is the force acting in the x-axis direction of the vehicle body, and only the longitudinal force generated by turning is targeted. In steering, the cornering drag generated by the lateral force of the front wheels acts as the longitudinal force F_X, so longitudinal acceleration occurs in the direction to decelerate the vehicle body.

As the side-slip angle is small, by treating the lateral and cornering forces as equal, the longitudinal force due to cornering drag can be written as shown in Eq. (2) using the front wheel cornering force and the front wheel steering angle.

$$F_X = -F_{Yf}\delta \tag{2}$$

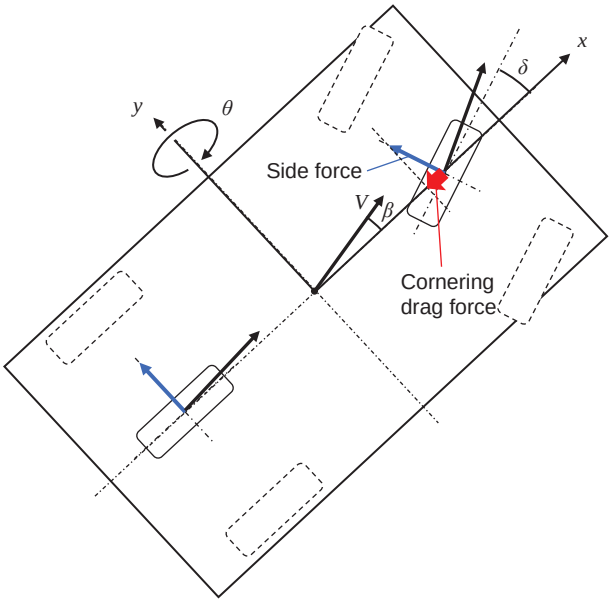


Fig. 3 Cornering drag force

The front wheel cornering force is described concisely using the lateral acceleration Y_G in the steady state as Eq. (3).

$$F_{Yf} = \frac{l_r}{l} mY_G \tag{3}$$

By substituting Eq. (3) into Eq. (2), the cornering drag becomes as shown in Eq. (4).

$$F_X = -\frac{l_r}{l} mY_G\delta \tag{4}$$

Here, if the lateral acceleration gain G_Y relative to the front wheel steering angle is used, Eq. (4) can also be described as Eq. (5).

$$F_X = -\frac{l_r}{l} mG_Y\delta^2 \tag{5}$$

From Eq. (5), the cornering drag is proportional to the square of the front wheel steering angle, so it is independent of the steering direction and the response frequency is twice the steering frequency. These characteristics match the pitching motion characteristics shown in Fig. 2.

Next, the pitching moment M_{YJ} generated by the jacking force, which is the second term on the right side of Eq. (1), can be expressed as Eq. (6) using the roll center height, track width, center of gravity height, and cornering force.

$$M_{YJ} = 2\frac{h}{mg}\left(\frac{2}{T}\right)^2\left(-h_f {F_{Yf}}^2 + h_r {F_{Yr}}^2\right) \tag{6}$$

Here, obtaining the rear wheel cornering force in the same way as in Eq. (3) and substituting it into Eq. (6) results in Eq. (7).

$$M_{YJ} = 2\frac{mh}{g}\left(\frac{2}{T}\right)^2\left(-h_f\frac{l_r}{l} + h_r\frac{l_f}{l}\right){Y_G}^2 \tag{7}$$

From Eq. (7), the pitching moment generated by the jacking force is generated according to the square of the lateral acceleration. In addition, like Eq. (5), if the lateral acceleration gain G_Y relative to the front wheel steering angle is used, Eq. (7) can also be described as Eq. (8).

$$M_{YJ} = 2\frac{mh}{g}\left(\frac{2}{T}\right)^2\left(-h_f\frac{l_r}{l} + h_r\frac{l_f}{l}\right)(G_Y\delta)^2 \tag{8}$$

Since Eq. (8) is also proportional to the square of the front wheel steering angle, the pitching moment generated by the jacking force is also consistent with the pitching motion characteristics.

The pitching moment M_{YS} generated by the suspension, which is the third term on the right side of Eq. (1), can be expressed as Eq. (9) using the pitch damping coefficient and pitch stiffness of the suspension.

$$M_{YS} = -C_\theta\dot{\theta} - K_\theta\theta \tag{9}$$

Therefore, the basic relationship between steering and pitching motion can be obtained as Eq. (10) by substituting the approximate equations (4), (7), and (9) into Eq. (1).

$$I_Y\ddot{\theta} = h\frac{l_r}{l} mY_G\delta + 2\frac{mh}{g}\left(\frac{2}{T}\right)^2\left(-h_f\frac{l_r}{l} + h_r\frac{l_f}{l}\right){Y_G}^2 - C_\theta\dot{\theta} - K_\theta\theta \tag{10}$$

From Eq. (10), an approximate equation was obtained that can concisely express the characteristics of the pitching motion produced by steering.

3.2. Derivation of Control Law

Next, it was thought that if the phase of the pitching behavior in response to the steering input could be adjusted by longitudinal force control, this would be effective to enhance the feeling in turn. Therefore, the approximate equation obtained in the previous section was used to examine a control law that advances the forward downward pitching behavior among the behaviors when increasing the steering angle such as turn-in as shown in Fig. 4.

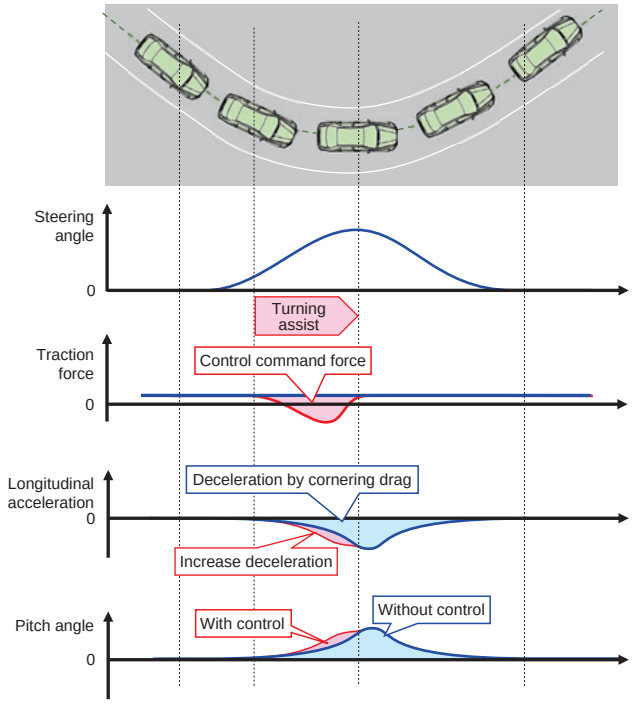


Fig. 4 Example of control law operation

The first term on the right side of Eq. (10) is the pitching moment proportional to the longitudinal force generated by cornering drag. It is thought that if the phase of the pitching moment can be advanced using this term, the pitch angle response characteristic shown in Fig. 2(b) can be retained, enhancing the feeling in turn while reducing the unnatural feeling produced by control intervention.

Addition of an item that advances the phase with the time constant τ_C to the first term on the right side of Eq. (10) in order to advance the pitching behavior results in Eq. (11).

$$I_Y\ddot{\theta} = h\frac{l_r}{l}m\left(Y_G\delta + \tau_C\frac{d}{dt}(Y_G\delta)\right) + 2\frac{mh}{g}\left(\frac{2}{T}\right)^2\left(-h_f\frac{l_r}{l} + h_r\frac{l_f}{l}\right)Y_G{}^2 - C_\theta\dot{\theta} - K_\theta\theta \tag{11}$$

However, for the pitching motion when longitudinal force control is performed, the pitching moment F_{XC} generated by the control command force is added to Eq. (10), resulting in Eq. (12).

$$I_Y\ddot{\theta} = h\frac{l_r}{l}mY_G\delta + 2\frac{mh}{g}\left(\frac{2}{T}\right)^2\left(-h_f\frac{l_r}{l} + h_r\frac{l_f}{l}\right)Y_G{}^2 - C_\theta\dot{\theta} - K_\theta\theta - hF_{XC} \tag{12}$$

Furthermore, substituting Eq. (11) into Eq. (12) and summarizing obtained Eq. (13) as the control command force for advancing the pitching behavior.

$$F_{XC} = -\frac{l_r}{l}m\tau_C\frac{d}{dt}(Y_G\delta) \tag{13}$$

In Eq. (13), the product of the lateral acceleration and the front wheel steering angle is differentiated, so the longitudinal force that advances the pitch phase acts on the deceleration side when increasing the steering angle, and on the acceleration side when decreasing the steering angle. This control law is intended to advance the pitching behavior in turn-in, so Eq. (14) is used so that the control command force of Eq. (13) acts only on the deceleration side when increasing the steering angle.

$$F_{XC}{}' = min\left(-\frac{l_r}{l}m\tau_C\frac{d}{dt}(Y_G\delta), 0\right) \tag{14}$$

Here, by substituting Eq. (5), the control command force of Eq. (14) can also be described as Eq. (15).

$$F_{XC}{}' = min\left(-\frac{l_r}{l}m\tau_C\frac{d}{dt}(G_Y\delta^2), 0\right) \tag{15}$$

Like Eq. (5), the right side of Eq. (15) includes an element of the square of the front wheel steering angle, so the control command force is independent of the steering direction and the response frequency is twice the steering frequency.

From the above, a control law was established that adjusts the phase of the pitching behavior in turn-in by longitudinal force control using the time constant τ_C.

4. Simulation Results

The control effects of the control law were verified by simulation.

The vehicle model used in the simulation had ten degrees of freedom consisting of six sprung degrees of freedom and four unsprung degrees of freedom for each wheel (up and down). The model took into account jacking due to the roll center height, anti-dive angle, and anti-squat angle, and the tire characteristics were such that the cornering power was linear to the load.

The vehicle model used the specification values of a D-segment hybrid EV sedan. The control command force was applied to the vehicle body as longitudinal force at the wheel center, and the power plant response delay was considered as delay time.

As shown in Fig. 5(a), a J-turn at a vehicle speed of 50 km/h was used as the test mode, and the control operation and vehicle behavior in turn-in were verified.

In order to confirm the control effect, cases with and without control were compared. Four different time constant τ_C schemes were used for cases with control: reference scheme 1 that was the smallest value for which a significant difference was observed, and then 2.5, 5, and 10 times that value.

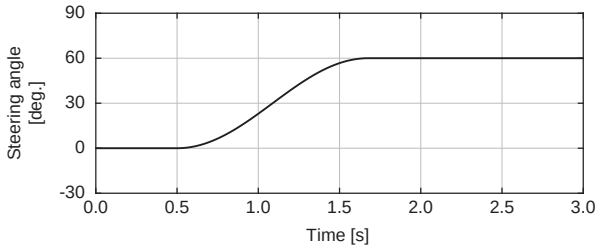
Figure 5 shows the simulation results.

The longitudinal force in Fig. 5(c) was output as the control command force when increasing the steering angle from straight running, and as the time constant τ_C increased, the control command force also increased.

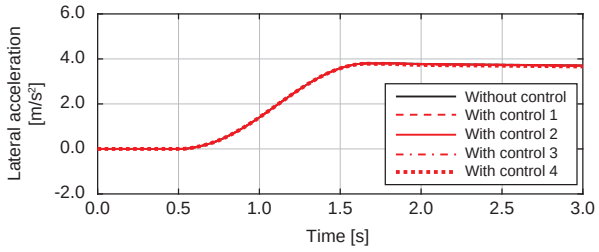
At this time, the longitudinal acceleration in Fig. 5(d) rose faster and the peak also became larger as the time constant τ_C increased.

The pitch angle in Fig. 5(f) also exhibited changes similar to the longitudinal acceleration at this time, but it was confirmed that the roll angle in Fig. 5(e) was unaffected.

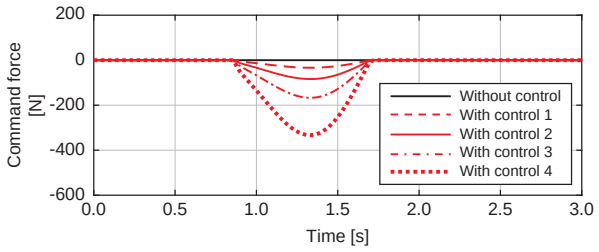
This confirmed that the longitudinal acceleration and the pitch angle can be controlled by the time constant τ_C.



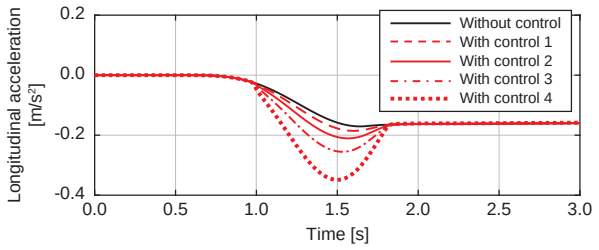
(a) Steering angle



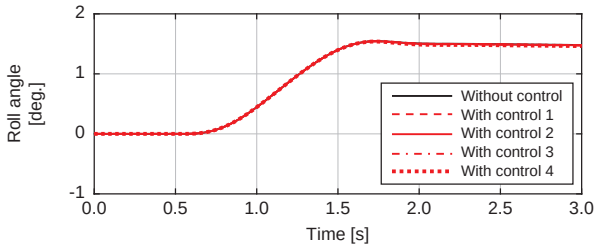
(b) Lateral acceleration



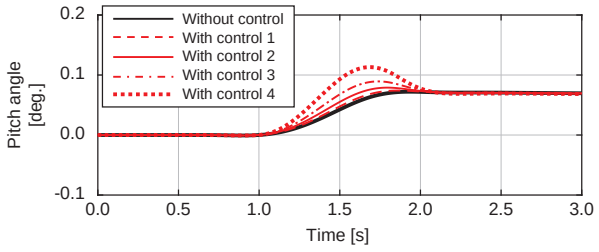
(c) Control command force



(d) Longitudinal acceleration



(e) Roll angle



(f) Pitch angle

Fig. 5 Simulation results

5. Actual Vehicle Test Results

Next, verification was performed by actual vehicle tests.

The test vehicle used the D-segment hybrid EV sedan that was the basis for the simulation vehicle model. The control command force was given as the modified value of the driving force of the electric power plant system. As shown in Fig. 6(a), a J-turn at a vehicle speed of 50 km/h was used as the test mode, and the control operation and vehicle behavior in turn-in were verified.

A steering robot was used to steer the vehicle in order to standardize the steering input for each measurement, and the roll and pitch angles were measured using vehicle-to-ground laser displacement meters.

As in the simulation, cases with and without control were compared, and the cases with control used the same time constant τ_C schemes.

Figure 6 shows the measurement results of the actual vehicle tests.

The control command force in Fig. 6(c) output when increasing the steering angle from straight running changed in a similar manner to the simulation when the time constant τ_C was changed.

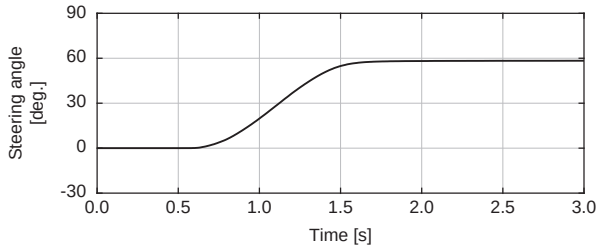
The longitudinal acceleration in Fig. 6(d) also changed in a similar manner, and it was further confirmed that the roll angle in Fig. 6(e) was unaffected as in the simulation.

From these results, it can be inferred that the pitch angle in Fig. 6(f) also changes in a similar manner, and schemes 3 and 4 with larger control command force changed in a similar manner to the simulation. In contrast, schemes 1 and 2 with smaller control command force deviated from the trends in the simulation due to the impact of measurement error.

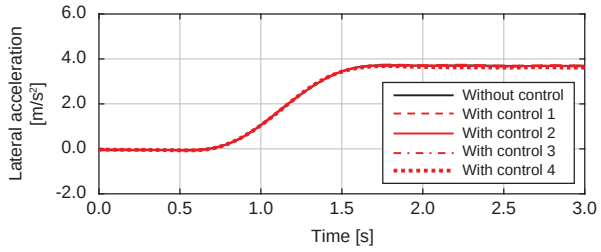
Next, sensory evaluation was conducted by the expert driver assigned to this control development, and it was confirmed that as the time constant τ_C increased, the feeling in turn was enhanced compared to the case without control. However, when the time constant τ_C was increased further, the unnatural feeling increased, indicating that there is an appropriate value for the control strength.

In addition, to verify the control effect, sensory evaluation was also conducted by multiple test drivers not assigned to control development. Here, the value judged to be appropriate by the expert driver assigned to this development was used as the time constant τ_C setting for the case with control. As a result, comments were received that the feeling in turn with control was enhanced compared to without control.

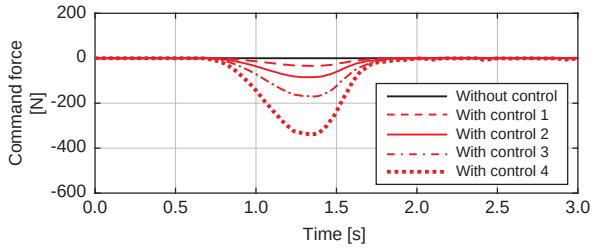
From the above, although the effect of the devised control law to enhance feeling in turn could not be quantitatively demonstrated in terms of pitch angle, the effect was confirmed by the quantitative value of longitudinal acceleration and by sensory evaluation.



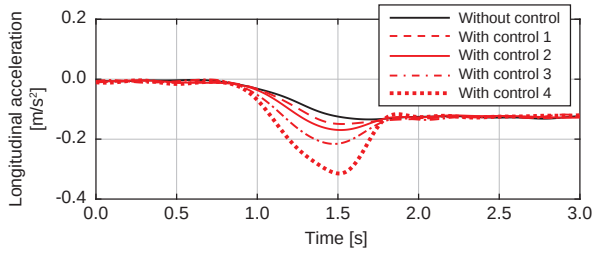
(a) Steering angle



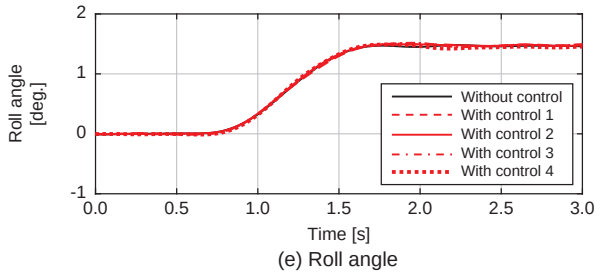
(b) Lateral acceleration



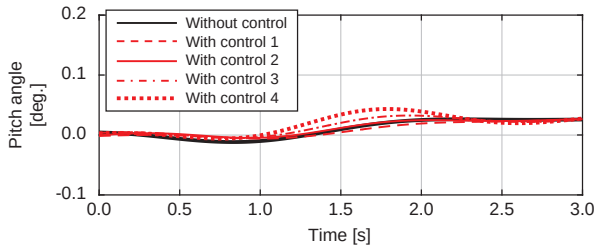
(c) Control command force



(d) Longitudinal acceleration



(e) Roll angle



(f) Pitch angle

Fig. 6 Actual vehicle test results

6. Conclusion

In order to provide good feeling in turn with natural pitching behavior in the operation area used by general drivers in daily driving, a method was examined to enhance the feeling in turn and reduce the unnatural feeling produced by control intervention, focusing on pitching behavior in turning.

(1) An approximate equation was derived that reproduces the aforementioned pitching motion characteristic with a minimum model, and a control law based on that approximate equation was examined.

(2) A control law was devised that reduces the unnatural feeling in turn. This was done by incorporating the characteristics that the pitching behavior is independent of the steering direction and twice the steering frequency into the control law, and retaining the pitch angle response characteristics.

(3) It was confirmed by simulation that the timing at which the pitch angle occurs can be effectively adjusted without impacting the roll angle.

(4) Vehicle behavior similar to that in the simulation was also confirmed in actual vehicle tests.

(5) Sensory evaluation by multiple drivers using an actual vehicle indicated that the control law is effective in enhancing the feeling in turn.

References

(1) Abe, M., Kohata, T., Kawamoto, Y., Nonaga, I., Tsurumiya, O.: Electronic Control Four-Wheel Steering system, Proceedings. JSAE Annual Congress, Issue 921, Vol. 1, p. 131-134, (1992)

(2) Suzumura, M., Kojo, T., Matsuda, M., Kawamuro, J., Fukui, K., Sugawara, T.: Development of Front Steering Control System, Proceedings. JSAE Annual Congress, Issue 34-03, p. 5-8, (2003)

(3) Yamamoto, M.: Vehicle stability control (VSC) System to prevent lateral skid, JSAE Symposium Text, No. 96-02, p. 9-17, (1996)

(4) Kitamura, K., Shibahata, Y., Wada, K., Honda, K., Kuwahara, K., Okuma, S., Kajiwara, H., Kuriki, N.: Developing of active torque transfer system, Proceedings. JSAE Annual congress, Issue 971, p. 13-16, (1997)

(5) Suzuki, T., Hosaka, M., Kujubu, N., Isono, Y., Miyashita, N., Matsumoto, S., Naito, G.: Konaringu Sutabiriti Asisuto Kinou no Kaihatsu, Proceedings. JSAE Annual Congress, Issue 27-10, p. 7-12, (2010) (in Japanese)

(6) Kojima, T., Futamura, T., Ohmura, K.: Development of Agile Handling Assist, Honda R&D Technical Review, Vol. 26, No. 1, p.49-57

(7) Shimada, K., Shibahata, Y.: Analysis of Vehicle Maneuverability by β-Yaw Moment Diagram. Comparison of Three Different Active Control

Methods., Proceedings. JSAE Annual Congress, Issue 933, p. 199-202, (1993)
(8) Yamakado, M., Abe, M.: Study on handling characteristics of longitudinal acceleration controlled vehicle combined with lateral motion-Proposal of Acceleration (G) Vectoring Control for the improvement of vehicle agility and stability-, Proceedings. JSAE Annual Congress, Issue 8-08, p. 9-14, (2008)
(9) Umetsu, D., Abe, M., Yamakado, M., Kano, Y., Takahara, Y., Kato, F., Yoshioka, T., Sunahara, O., Takahashi, J.: Kououtou Enjin wo mochiita Ryousangata G-Vectoring Seigyo Sharyou no Kaihatsu, Proceedings, 2016 JSAE Annual Congress (Spring), p. 1310-1314, (2016) (in Japanese)
(10) Sakai, H., Hozumi, J., Yamamoto, Y., Sano, K., Tomita, K.: Damping Control to Enhance Transient Cornering Feel -Control to Synchronize Pitching with Rolling Utilized Kalman Filter-, Proceedings. JSAE Annual Congress, Issue 145-11, p. 13-18, (2011)

List of Symbols

m	Vehicle mass
I_Y	Pitching moment of inertia around center of gravity
l	Wheelbase
l_f	Distance of front axle to center of gravity
l_r	Distance of rear axle to center of gravity
T	Track width
h	Center of gravity height
h_f	Front axle roll center height
h_r	Rear axle roll center height
C_θ	Suspension pitch damping coefficient
K_θ	Suspension pitch stiffness
F_{Yf}	Front wheel cornering force
F_{Yr}	Rear wheel cornering force
F_X	Longitudinal force
F_{XC}	Control command force
F_{XC}'	Control command force limited to deceleration side
M_{YS}	Pitching moment by suspension
M_{YJ}	Pitching moment by jacking force
M_Z	Yawing moment
Y_G	Lateral acceleration
G_Y	Lateral acceleration gain for front wheel steering angle
g	Gravity acceleration
$\ddot{\theta}$	Pitch angular acceleration
$\dot{\theta}$	Pitch angular velocity
θ	Pitch angle
δ	Front wheel steering angle

■ Author ■



Naoto OHKUBO

γ' Precipitation-hardened Cobalt-free Heat-resistant Steel Strip for Exhaust Gaskets Work at 900°C

Hiroki YAMAMOTO[1] Isamu SAITO[2]
Yoshiki KUMAGAI[3] Yoshinori SUMI[3]

ABSTRACT

We have developed a new steel strip for gaskets that can seal exhaust gas in 900°C environments. The concept for the material specified the seemingly conflicting requirements of high performance through the active use of γ'-Ni_3 (Ti, Al) as a strengthening phase for high-temperature stability, together with a higher melting point for manufacturability. To enhance the relaxation properties, alloying elements that raised the amount and stability of strengthening phase γ' and suppressed the precipitation of the harmful phase η-Ni_3Ti were investigated using thermodynamic calculations, and 5.9 at% of Ti+Al and a ratio of 1.0 of Al/Ti were selected. In addition, to enhance hot rollability, the melting point was increased by reducing Nb and Cr contents as compared to Alloy 718. To maintain initial springiness and the stability of γ' at high temperatures, the cold rolling reduction ratio was set at 30% to 40%. As a result, in heat load tests at 900°C, gaskets made of the developed alloy performed at the same level as Alloy 718 gaskets at 750°C.

1. Introduction

With the goal of mitigating global warming, Japan and other developed nations have declared their aim to realize carbon neutral societies with zero greenhouse gas emissions (net total of emissions and absorption) by 2050[(1)]. Through electrification, the automobile industry is working to bring carbon emissions from driven vehicles to zero. However, there are a large number of issues that need to be addressed before this can become widespread, and it is also important to further develop internal combustion engines, which for now remain the dominant powertrain systems.

Europe is considering expanding the Real Driving Emission (RDE) driving conditions, imposing stricter limits, and enacting other measures under Euro 7, the next round of automobile exhaust gas regulations. In this context, in order to simultaneously enhance thermal efficiency and reduce exhaust gas emissions in internal combustion engines, stoichiometric air-fuel ratio operation is necessary across the full range without enrichment controls, as such controls have the effect of cooling the fuel. The result is that exhaust gas temperatures, which have traditionally been around 900°C, will exceed 1000°C. This will increase the demand for materials that can provide component functionality and durability in these high-temperature environments[(2)]. Accordingly, exhaust components need to have high heat resistance, not only typical exhaust system components such as the turbocharger, catalytic converter, and exhaust pipe, but also the gaskets that are responsible for sealing in the gases where such components are utilized. A gasket is used between the turbocharger and the catalytic converter, where exhaust gas temperatures are about 100°C to 150°C lower than those at the engine outlet. Therefore, if the temperatures of such exhaust gases are expected to increase from 900°C to 1050°C, the gasket needs to provide sealing functionality at 900°C, 150°C more than the former 750°C level.

As shown in Fig. 1, the developed gasket consists of multiple layers of 0.2 mm cold-rolled material formed with ridges (beads). This multi-layered gasket is bolted in place between the flanges of the turbocharger and catalytic converter. The gasket's bead seal mechanism is shown in Fig. 2. During initial installation, the bolting force compresses the beads between the flanges, generating a surface pressure that seals in the exhaust gases.

During driving, heat from the exhaust gas may cause thermal deformation of the flanges, tending to create gaps between the flanges where the bolts are widely spaced. In response, the springiness in the gasket beads makes them conform to the gaps, thus maintaining the surface pressure and the exhaust gas seal. In terms of sealing the gases, therefore, the higher the bead height that remains after

[1] Material Research Center
[2] Honda Motor Co., Ltd.
[3] Daido Steel Co., Ltd.

repeated engine operation (remaining bead), the greater the sealing surface pressure, the better the beads can conform to the gaps in the flanges that may occur during driving, and thus the better the gas sealing functionality.

In order to secure this remaining bead height, it is necessary to not only have high initial springiness (hardness), but also to suppress the relaxation phenomenon that may occur when the seal pressure generated by the flange connection changes over time. Hereinafter, this will be referred as the relaxation properties. Therefore, in order to provide sufficient sealing functionality for this gasket, a material that has reliable relaxation properties at the target temperature of 900°C is required.

As shown in Fig. 3, gaskets are made from steel strips that are manufactured in a series of steps from ingot casting and blooming to hot rolling followed by cold rolling. The strips are then subjected to bead forming and shape punching to produce the desired shape. Typically, any attempt to increase relaxation properties at high temperatures affects the hot and cold rollability, making it is necessary to also consider the product's manufacturability.

Given all of the above, we set out to develop a high-heat-resistant steel strip with reliable relaxation properties at 900°C that also take manufacturability into account.

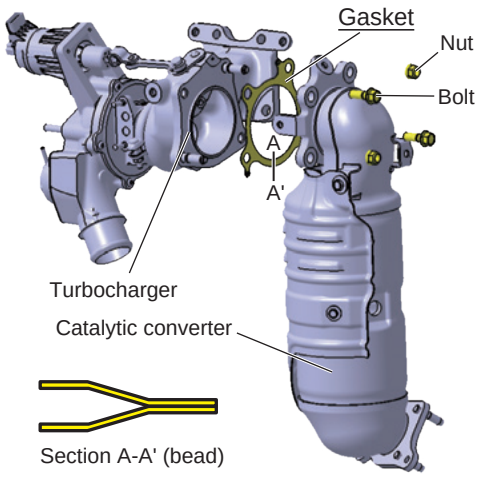


Fig. 1 Gasket in exhaust system

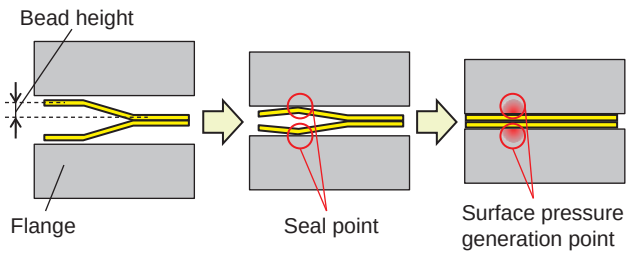


Fig. 2 Assembly flow and sealing mechanism of gasket

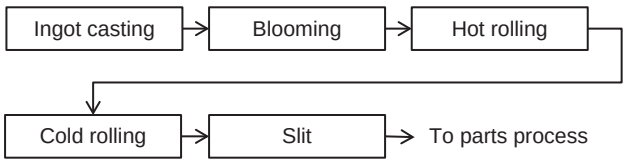


Fig. 3 Outline of steel strip manufacturing process

2. Development Goals and Setting of Target Values

One example of a general-purpose gasket material currently used between exhaust system components is the Ni-based superalloy Alloy 718 (AMS5596). This is a precipitation hardening type alloy, which is one of the alloy-strengthening mechanisms. γ''-Ni_3Nb, an intermetallic compound of Ni and Nb, and γ'-Ni_3 (Al, Ti), an intermetallic compound of Ni, Al, and Ti, are the strengthening phases[3]. The alloy has reliable relaxation properties under high-stress and high-temperature environments. This alloy is therefore used for gaskets between the turbocharger and catalytic converter in current engines, in which 750°C temperatures can be expected. When this alloy is exposed to temperature ranges above 750°C for certain periods of time, however, one of the strengthening phases, γ''-Ni_3Nb, transforms into δ-Ni_3Nb, with a different crystal structure[4], and the alloy's relaxation properties degrade as a result. Therefore, in order to develop a high-heat-resistant strip in which relaxation properties are maintained at the anticipated running temperature increase from 750°C to 900°C that may occur due to future increases in exhaust gas temperatures, it was decided to actively pursue the use of γ' rather γ''[5] as the strengthening phase, due to its greater thermodynamic stability.

There is concern however that the higher stability of γ' in high-heat-resistance strips may make the hot rolling process shown in Fig. 3 more challenging to carry out. In hot rolling processes that are typically conducted in the temperature range of 700°C to 1200°C, a high-heat-resistant strip exhibits high deformation resistance because of the issue of making γ' particles fully dissolved[6], and this can lead to cracking and so on. To address this issue and enhance hot-rollability, an existing Ni-based superalloy such as Alloy 263, which has a higher heat resistance than Alloy 718, for example, can lower the solvus temperature of γ' with the addition of Co[7]. However, in recent years, Co is attracting increasing attention for its impact on people and the environment, and so to avoid using Co in this development, the concept of having a high melting point that can expand the upper limit of the hot rolling temperature range was incorporated into the alloy design.

Cold rolling is performed after the strip hot rolling. In cold rolling, increasing the rolling reduction ratio promotes strain hardening (dislocation strengthening) resulting

from accumulated crystal defects (dislocations) in the crystals, producing higher initial springiness. However, introducing excessive dislocations increases the driving force of microstructural changes and is detrimental to high-temperature relaxation properties. Therefore, cold rolling conditions were also assessed. In terms of the performance target of the gasket for which the developed alloy would be used, the goal was to maintain a remaining bead height of 56 μm at 900°C, the same remaining bead height for an Alloy 718 gasket at 750°C, in a heat load test of a single-layer gasket modeled on that mounted between the turbocharger and catalytic converter of a current market vehicle. The processing capacity of a mass-production hot-rolling mill was considered, and manufacturing targets were set to provide a hot working temperature range of 350°C or higher in a Gleeble test that simulates hot-rollability.

3. Alloy Design

In order to achieve the performance and manufacturing targets, thermodynamic calculations were performed to determine the optimal amount of alloying element that would enhance the high-temperature stability of γ' and increase the melting point of the alloy, starting with a base of the standard composition of Alloy 718, Fe-51Ni-19Cr-5.1Nb-0.5Al-1.0Ti-3Mo (mass%). For this investigation, thermodynamic calculations were performed using Thermo-Calc with ThermoTech's thermodynamics database Ni8.

3.1. Stabilized γ' Design for Enhanced Functionality

With regard to the role of each alloying element in Ni-based superalloys, Ti, Al, Nb, etc. stabilize strengthening phase γ' (Nb also stabilizes γ'', however), while Cr, Mo, etc. perform solid solution strengthening of the matrix[8]. One of the goals of this development was to investigate the optimal quantities of Al and Ti needed to stabilize γ'. Based on the standard composition of Alloy 718, the Ti/Al ratio was fixed at 1.0 atomic percent, and the relationship between the γ' mole fraction and solvus temperature was plotted for varying amounts of Ti+Al. The results are shown in Fig. 4.

As the amount of Ti+Al increases, the γ' solvus temperature rises, and it is necessary to add Ti+Al of 3 at% or more to stabilize γ' at 900°C. On the other hand, the concern exists that if too much Ti+Al is added, the hot workability will degrade with the rise in the solvus temperature. In existing precipitation-hardened-wrought Ni-based superalloys used at 700°C or higher, the amount of precipitation of γ' is set at between 20% and 30%[9]. Accordingly, in this development, the amount of Al+Ti was set at close to 6 at%, with the aim of achieving 25% of γ'.

In addition to the total amount of Ti+Al, the Ti/Al ratio is also an important parameter for the stability of γ'[10]. The ratio value has an impact not only on γ', but also on the stability of the Ni and Ti intermetallic compound, η-Ni_3Ti. Typically, in Ni-based superalloys η precipitates in a plate shape and reduces high-temperature strength[11]. For this reason, it is preferable to have a design that avoids precipitation. Therefore, the mole fractions of γ' and η were calculated at 900°C against the Ti/Al ratio at a fixed Ti+Al amount of 6 at% (Fig. 5). Accordingly, the amount of γ' increases as the Ti/Al ratio increases, up to around Ti/Al = 1. Above this, however, γ' starts to decrease and η is formed and begins to increase. Based on these calculations and a consideration of the balance between the amounts of γ' and η, the Ti/Al ratio was set at about 1.

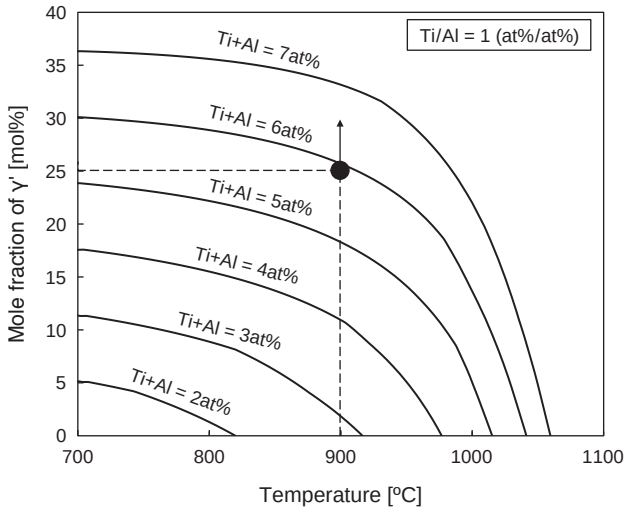


Fig. 4 Relationship between temperature and γ' mole fraction of Fe-51Ni-19Cr-5.1Nb-3Mo-Al-Ti (mass%) with various Ti+Al contents (at%)

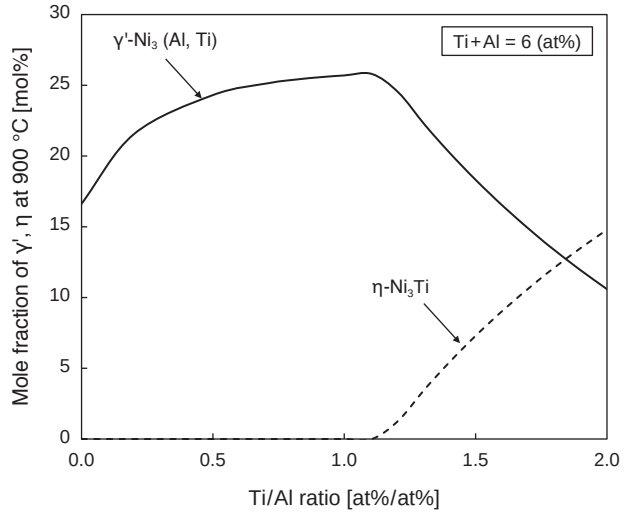


Fig. 5 Relationship between Ti/Al ratio (at%/at%) and γ'/η mole fraction at 900°C of Fe-51Ni-19Cr-5.1Nb-3Mo-Al-Ti (mass%)

Table 1 Chemical compositions of developed alloy and Alloy 718

	Chemical composition [mass%]							Ti+Al [at%]	Ti/Al [at%/at%]
	Ni	Cr	Fe	Nb	Al	Ti	Mo		
Developed alloy	50	15	Balance	1.3	1.4	2.5	1	5.9	1.0
Alloy 718	51	19	Balance	5.1	0.5	1.0	3	2.3	1.1

3.2. Higher Melting Point Design to Enhance Hot Workability

As discussed in Chapter 2, due to the concern that stabilizing γ' decreases hot workability, it was decided to enhance ductility at high temperatures above 1000°C, at which γ' can be fully dissolved, to secure a sufficient hot working temperature range. Since high-temperature embrittlement has a major impact on the decrease in ductility at high temperatures, a study was conducted to reduce the amount of elements in order to increase the melting point, with which this is correlated. With regard to the alloying element groups, as Ni, Al, and Ti constitute γ' and thereby impact performance, the focus was turned to Nb and Cr, other elements that are highly sensitive to melting point effects. Nb was studied first, and a phase diagram was calculated based on an Alloy 718 component with the amount of Nb on the horizontal axis (Fig. 6). This showed that for every 1 mass% reduction in the amount of Nb added, the melting point (solidus temperature) rose about 28°C. In Alloy 718, Nb is the alloying element that stabilizes γ", which is the main strengthening phase of the alloy. In this development, however, γ' was being used instead as the main strengthening phase, and so reducing the amount of Nb was expected to have only a small effect on the alloy's relaxation properties. However, a certain amount of Nb was considered necessary, because greatly decreasing the amount of Nb has been shown to decrease the stability of γ' and the solvus temperature of γ' (γ' - solvus). Therefore, to help prevent the formation of harmful phase δ at the anticipated service temperature of 750°C to 900°C for the alloy being developed, Nb was reduced to 1.3 mass%, where the δ solvus temperature (δ - solvus) is below 750°C.

Next, Fig. 7 shows the calculated phase diagram with the amount of Cr on the horizontal axis. This shows that for Cr, as well, each additional 1 mass% results in an approximately 10°C rise in the melting point, and so the amount of Cr was reduced to 15 mass%, still within a range that did not degrade oxidation resistance.

3.3. Composition of Developed Alloy

Table 1 shows the developed alloy composition, taking into consideration performance and manufacturability, and as based on preceding Sections 3.1 and 3.2. The Mo element contributes to solid solution strengthening, which is one of the strengthening mechanisms for alloys. However, because precipitation hardening of γ' was mainly being used in the developed alloy, and Mo is a rare metal and has presented an increasing resource risk in recent years, the amount was reduced compared to Alloy 718. The solvus temperature and melting point of γ' in the developed alloy are 994°C and

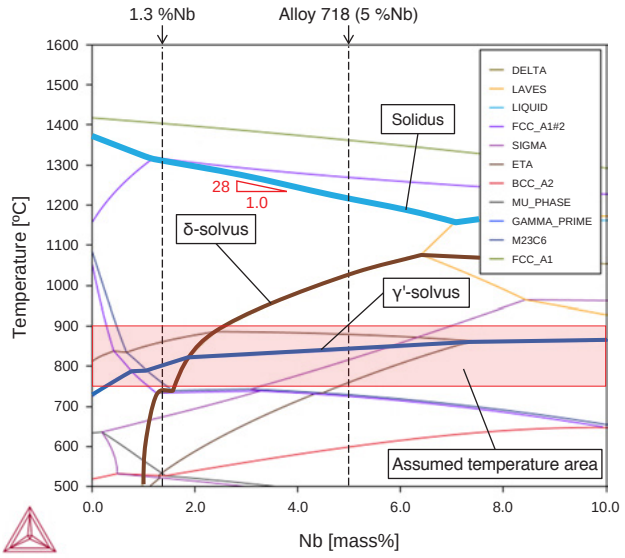


Fig. 6 Calculated vertical section of Fe-51Ni-19Cr-3Mo-0.5Al-1Ti-Nb (mass%)

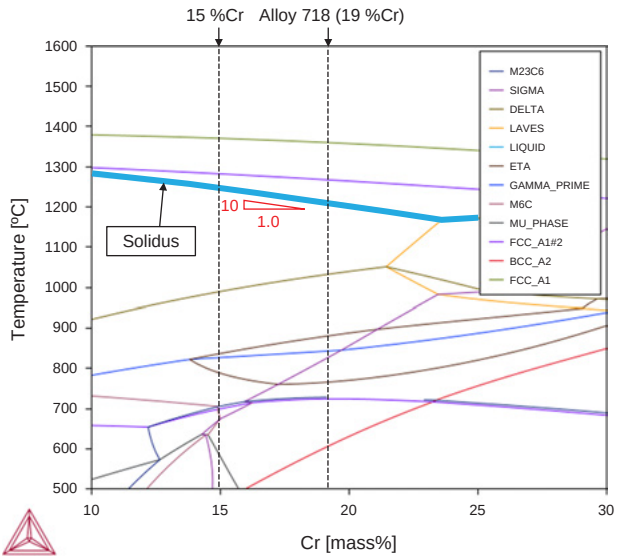


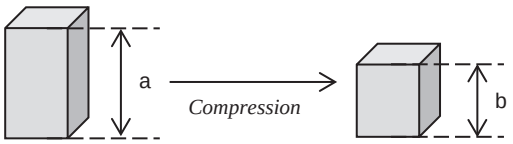
Fig. 7 Calculated vertical section of Fe-51Ni-3Mo-0.5Al-1Ti-5.1Nb-Cr (mass%)

1292°C, respectively, as calculated by Thermo-Calc. Both parameters are higher than the 835°C and 1204°C figures for Alloy 718, confirming that the component composition meets both performance and hot workability considerations.

4. Cold Rolling Condition Setting

As described in Chapter 2, in consideration of initial springiness, it is preferable to increase hardness with the highest possible cold rolling reduction ratio. However, excessive cold rolling promotes the precipitation of η, reducing the high-temperature strength of the alloy[12]. Since this, in turn, prompts concerns about reduced relaxation properties, it is necessary to clarify the cold rolling reduction range within which there is no effect on the stability of γ', and to establish an upper value. For this study, the compression ratio of prismatic test pieces stood in for the cold rolling reduction ratio, and the samples were created as shown in Fig. 8 for heat exposure tests. The stability of γ' was subsequently assessed, based on the hardness and microstructural observation, and the cold rolling reduction ratio established.

For the test method, compressed samples were first prepared at various compression ratios. They were then exposed to high temperatures in a muffle furnace for extended periods of time, before being cooled in water. The target temperature exposure was 900°C, and the time was set at 50 hours, sufficient for high-temperature relaxation to stabilize[13]. A Vickers hardness test was then used to measure five points in the center cross-section of the samples at each compression ratio. The structure was examined for the presence of γ' and η with a scanning electron microscope (SEM). Figure 9 plots the hardness after heat exposure against the compression ratio of the prismatic test pieces. The plots are the averages, and the upper and lower lines respectively show the maximum and minimum values for each temperature. The results showed that the hardness increased due to strain hardening as the compression ratio increased, but at over 40%, hardness after thermal exposure decreased, while the variation of hardness increased greatly. To analyze the reason for, the state of precipitation of γ' and η were observed with an SEM in samples with 0% and 50% compression ratios (Fig. 10).



$$Compression\ ratio = \frac{b}{a} \times 100$$

Fig. 8 Preparation method of compressed sample

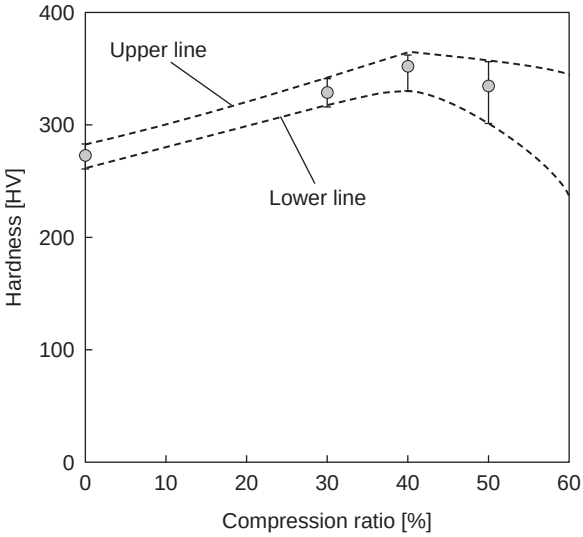
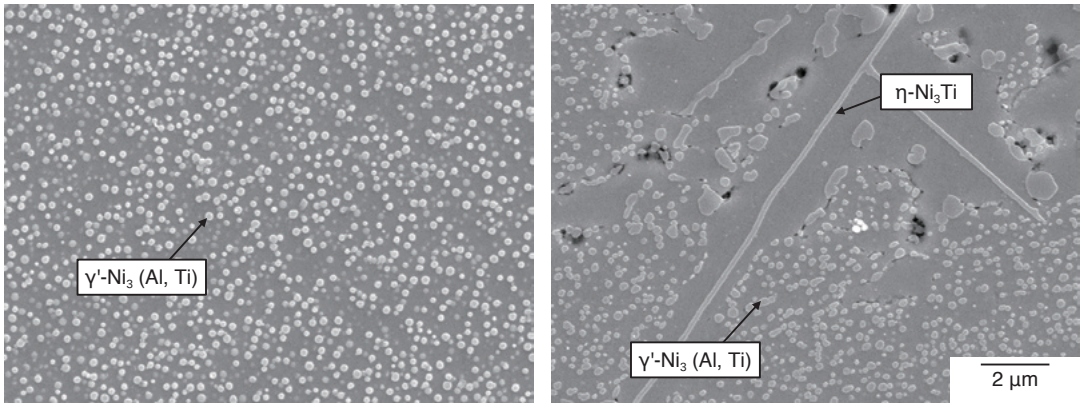


Fig. 9 Relationship between compression ratio of developed alloy and hardness after exposure at 900°C for 50 hours



(a) Compression ratio 0% (b) Compression ratio 50%

Fig. 10 Secondary electron images of developed alloy after compression and exposure at 900°C for 50 hours

In the sample with 0% compression ratio, homogeneous distribution of fine γ' particles within the grain interior were observed, while in that with 50% compression ratio, needle-like η particles were observed in addition to the γ' particles. In addition, areas with no γ' particle precipitation were confirmed in areas close to the needle-like η particles.

These results suggest that the reason that hardness decreases when the compression ratio exceeds 40% is the occurrence of areas without γ' precipitation, and the reason for the increased variation in hardness is the variation in the structure, which includes mixed areas of γ' precipitation and γ' non-precipitation. Based on these results, the cold rolling reduction ratio was set at between 30% and 40%, to secure the stability of γ' while taking into account initial springiness.

5. High-temperature Property Test Method and Results

Up to Chapter 4, it was confirmed that the examined alloy composition and cold rolling reduction ratio satisfied the development targets for performance and manufacturing. With regard to performance, the characteristics of the developed alloy and Alloy 718 were compared with a relaxation test using standard round bar test pieces.

5.1. Relaxation Assessment Testing

The alloy configured in Section 3.3 was hot forged into round bars and solution treated at the assumed annealing temperature during cold rolling. The round bars were then cold swaged to introduce a plastic strain equivalent to 30% to 40%. This was followed by heat treatment for 50 hours at each of the test temperatures described below to produce round bar test pieces as depicted in Fig. 11.

The relaxation tests were conducted in accordance with ASTM E328-13[14]. Change in stress over time was recorded for up to a maximum of 50 hours with a gauge length of 12 mm and a tensile strain of 1%. The test temperatures were 800°C, 850°C, and 900°C, and the same tests were performed on Alloy 718 for comparison.

The results of the relaxation testing are shown in Fig. 12. At 900°C, the residual stress of Alloy 718 was zero, while that of the developed alloy remained at about 35 MPa. This confirmed that the developed material has better high-temperature relaxation properties than Alloy 718. The enhancement in the residual stress in the high-temperature range is presumed to be due to γ' remaining stable as a strengthening phase up until 900°C, which suppresses stress relaxation at high temperatures, as per the development concept.

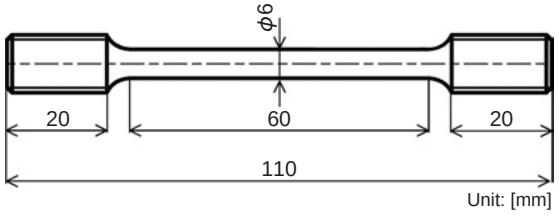


Fig. 11 Sample shape for relaxation test

5.2. Assessment Test for Hot-rollability

The test pieces were made from round bars hot forged in the same ways as the pieces in Section 5.1, then machined into parallel lengths of 20 mm with a diameter of 4.5 mm. First, the test pieces were placed inside a Gleeble testing machine and heated for 100 seconds until reaching 1150°C, at which temperature γ' particles completely dissolved, then held for 60 seconds. Next, the test pieces were cooled or heated to the test temperature (from 900°C to 1200°C) at a rate of 10°C/s, and held for 60 seconds. They were then subjected to a tensile test with a crosshead speed of 50.8 mm/s. The evaluation metric was established as the temperature range at which ruptures may occur with 50% or higher reduction of area. This temperature range is the range where hot rolling can be performed[15]. The results were then compared to Alloy 718 (Fig. 13). In addition, the temperature dependence of the γ' mole fraction and liquid phase of the developed alloy and Alloy 718 were calculated using Thermo-Calc (Fig. 14).

Figure 13 shows that the developed alloy has a lower reduction of area from the low-temperature side up to 950°C, but has a higher value in higher temperature ranges. The reason for this may be seen in Fig. 14, which shows that the developed alloy has a higher γ' mole fraction at the low-temperature end compared to Alloy 718. This means that during the test γ' precipitates more easily, decreasing ductility. At the high-temperature end, however, the melting point, which corresponds to the start of high-temperature

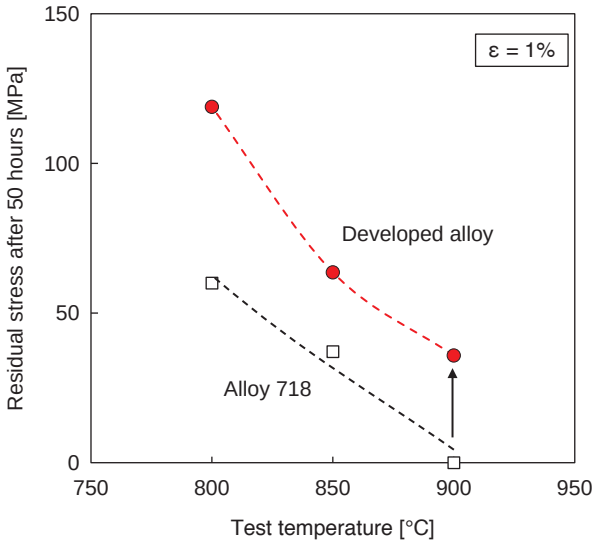


Fig. 12 Relaxation properties of developed alloy and Alloy 718 using round bar test pieces

embrittlement, is higher, and this is assumed to maintain ductility.

It follows from the above then that the developed alloy has, compared to Alloy 718, a higher temperature range in which hot rolling is possible, in line with the design intent of the higher melting point. These results confirm that the temperature range at which hot rolling is possible is approximately 450°C, and that the development target of 350°C or higher has been achieved.

5.3. Gasket Heat Load Test

Using equipment that could be expected to be used in mass production, prototypes of the developed strips were created using the alloy composition and cold rolling ratio configured in Chapters 3 and 4. Gaskets with a bead height of 0.45 mm were fabricated from both the prototype strips and Alloy 718 strips. As shown in Fig. 15, the gaskets were mounted between flat jigs made of SUS303, 20 mm thick with M10 holes, secured with bolts, and exposed to the air at specified temperatures for 50 hours.

After the test ended, the remaining bead height was assessed and compared to the Alloy 718 gasket. The bead measurement location was an area in which the distance between bolts was large (Area A), an area that is more challenging to seal. Figure 16 shows the results.

At 900°C, the remaining bead height for the Alloy 718 gasket was 0 μm, while that of the developed alloy was 64 μm. This was presumed to be because strengthening phase γ' in the developed alloy continued to exist stably up to 900°C, thus providing confirmation of the development concept. The results showed that the remaining bead height of the developed alloy at 900°C exceeded the 56 μm remaining bead height of Alloy 718 at 750°C, confirming that the developed target had been achieved.

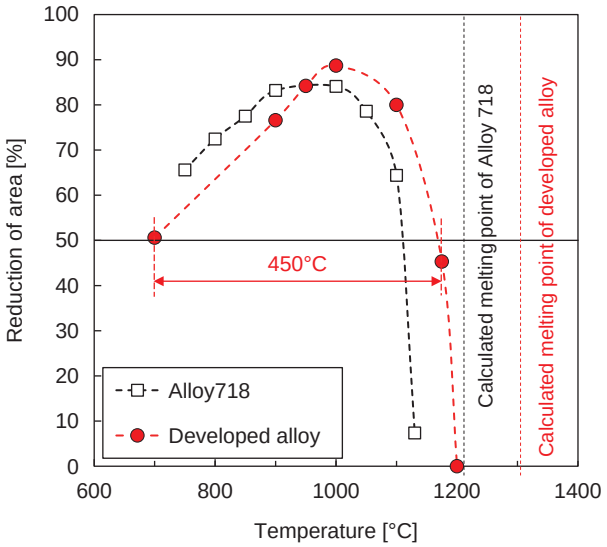


Fig. 13 Result of Gleeble test for developed alloy and Alloy 718

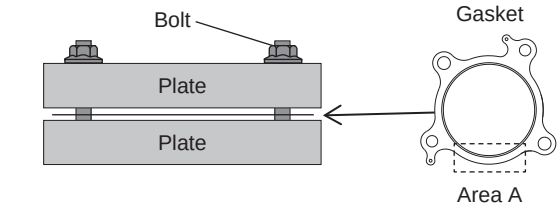


Fig. 15 Layout of gasket test and evaluated bead area after heat exposure

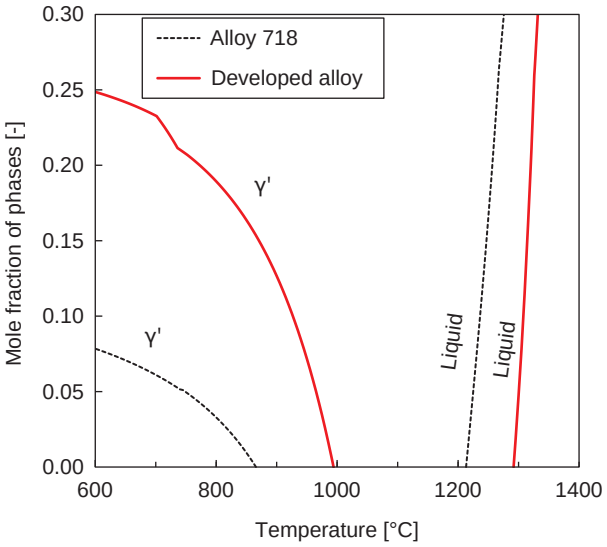


Fig. 14 Calculated mole fraction of γ' and liquid phases for developed alloy and Alloy 718

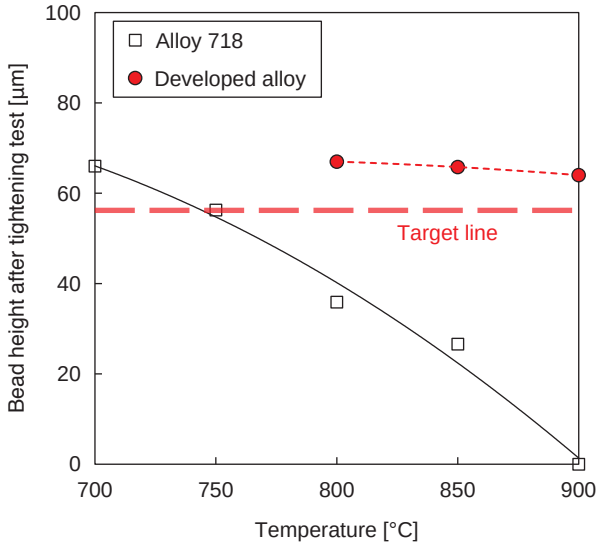


Fig. 16 Result of tightening test after exposure at each temperature

6. Conclusions

In order to develop a strip for gaskets that can provide sealing up to 900°C as required for compliance with future exhaust gas regulations, we have developed a Co-free strip, based on the composition of Alloy 718, that makes active use of γ' as the strengthening phase.

(1) From calculations using Thermo-Calc, setting Ti+Al at 5.9 at% and the Al/Ti ratio to 1.0 (at%/at%) maximized the amount of γ', which enhanced relaxation properties and suppressed the precipitation of harmful phase η, which degrades said properties.
(2) At the same time, based on Thermo-Calc melting point calculations, the amounts of Nb and Cr were reduced compared to Alloy 718 to 1.3 mass% and 15 mass%, respectively, thereby raising the melting point and helping to ensure the possibility of hot rolling at temperatures at or above 450°C.
(3) In consideration of the initial spring properties and stability of γ' during use, the cold rolling reduction ratio was set from 30% to 40% in order to suppress precipitation of η and the formation of areas without γ' precipitation at 900°C.
(4) In heat load tests, it was confirmed that gaskets made of the developed alloy and manufactured with equipment expected to be used in mass production, maintained a remaining bead height at 900°C that was equivalent to the remaining bead height at 750 °C of a gasket made of Alloy 718.

References

(1) https://www.meti.go.jp/shingikai/sankoshin/sangyo_gijutsu/chikyu_kankyo/pdf/2022_001_03_00.pdf, (2022/5/27)
(2) Komori, K.: Trend of Exhaust System Material and It's Future Development, Journal of The Japan Welding Society, Vol. 72, Issue 7, p. 546-551, (2003) (in Japanese)
(3) Kulawik, K., Buffat, P. A., Kruk, A., Wusatowska-Sarnek, A. M., Czyrska-Filemonowicz, A.: Imaging and characterization of γ' and γ'' nanoparticles in Inconel 718 by EDX elemental mapping and FIB-SEM tomography, Materials Characterization, Vol. 100, p. 74-80, (2015)
(4) Reed, R. C.: The Superalloys: Fundamentals and Applications, Cambridge University Press, p. 49-51, (2006)
(5) Reed, R. C.: The Superalloys: Fundamentals and Applications, Cambridge University Press, p. 40-49, (2006)
(6) Cremisio, R. S., McQueen, H. J.: Some observations of hot working behavior of superalloys according to various types of hot workability tests, Superalloys, G-1-G-36, (1972)
(7) Sims, C. T., Stoloff, N. S., Hagel, W. C.: Superalloys II: High-Temperature Materials for Aerospace and Industrial Power, Wiley-Interscience, p. 107-109, (1987)
(8) Fujita, T., Shibata, K.: Nikkeru-ki Chougoukin ni okeru Goukin Genso no Yakuwari, Bulletin of the Japan Institute of Metals, Vol. 16, No. 4, p. 231-239, (1977) (in Japanese)
(9) Reed, R. C.: The Superalloys: Fundamentals and Applications, Cambridge University Press, p. 238-239, (2006)
(10) Ueta, S., Noda, T., Okabe, M., Ishida, M., Oketani, H.: Development of Cold-formable Iron-based Superalloy for Exhaust Valves of Motorcycles, DENKI-SEIKO, Vol. 70, No. 3, p. 205-214, (1999) (in Japanese)
(11) Detrois, M., Jablonski, P. D., Hawk, J. A.: The effect of η phase precipitates on the creep behavior of alloy 263 and variants, Materials Science and Engineering: A, Vol. 799, No. 2, Article 140337, (2021)
(12) Farvizi, M., Asgari, S.: Effects of cold work prior to aging on microstructure of AEREX^{TM}350 superalloy, Materials Science and Engineering: A, Vol. 480, Issues 1-2, p. 434-438, (2008)
(13) Katsurai, T., Nishiyama, T., Hamano, S.: Development of High-heat-resistant High-nitrogen Containing Austenitic Stainless Steel for Exhaust Gasket, Honda R&D Technical Review, Vol. 15, No. 2, p. 167-174
(14) ASTM E328-13: Standard Test Methods for Stress Relaxation for Materials and Structures, (2013)
(15) Sato, K., Saka, T., Ohno, T., Noda, T.: Development of Low-Nickel Heat-Resistance Alloy for Exhaust Valves, HONDA R&D Technical Review, Vol. 9, p. 185-190, (in Japanese)

■ Author ■


Hiroki YAMAMOTO


Isamu SAITO


Yoshiki KUMAGAI


Yoshinori SUMI

Evaluation of Anodized Aluminum Corrosion Resistance by Constant Current Anodic Polarization Test

Hideaki MIYASHITA[1] Kohei TOMITA[2]
Yuki YAMAGUCHI[1] Takahiro KUWABARA[1]

ABSTRACT

A method was developed that can estimate the corrosion resistance of anodized aluminum regardless of the aluminum material or treatment conditions. It was confirmed that the constant current anodic polarization method can be used to evaluate the state of voids and foreign matter in anodized aluminum and the corrosion resistance by measuring the initial potential increase rate when a constant current is applied to anodized aluminum.

In addition, the change in the initial potential increase rate showed that the factor lowering the corrosion resistance of anodized aluminum due to an increase in the amount of added contents in aluminum alloys is rooted in the change in the anodized aluminum structure.

This method can estimate the corrosion resistance of anodized aluminum in a short time, enabling determination of the specifications of anodized aluminum at an early stage.

1. Introduction

How to secure sustainable growth in consideration of the global environment is an ongoing issue, and calls for a transformation from a resource-wasting society to a recycling-oriented society(1).

Anti-corrosion technology is important for the effective use of limited resources. The actual loss amount due to corrosion in Japan varies depending on the calculation method, but it is estimated that the amount will exceed 4 trillion yen annually in 2015(1).

Anti-corrosion technology is also important for long-term effective use of automobiles. However, the application of aluminum, magnesium, and carbon-fiber reinforced plastics is increasing due to the shift to multi-material aimed at weight and cost reduction, and corrosion at contact points between different materials is also becoming an issue. Particular care is needed for aluminum, which is a metal with a relatively low natural potential that often promotes galvanic corrosion at contact points with different materials. Plating treatment and coating are often applied as countermeasures to enhance electrical insulating properties. However, there are an increasing number of cases in which anodizing treatment is applied to provide electrical insulating properties by artificially forming a thick and stable oxide film on the aluminum surface by an electrochemical reaction.

Anodizing treatment is usually performed in the order of washing, electrolysis, and sealing. An oxide film composed of a barrier layer directly above the aluminum material and a porous layer having fine porous holes as shown in Fig. 1 is formed by electrolysis. Although the overall film thickness ranges from several μm to several tens of μm, the thickness of the barrier layer and the hole diameter and wall thickness of the porous layer are all on the order of several

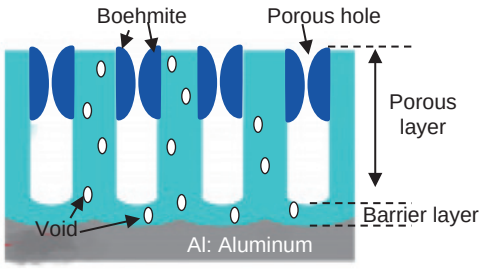


Fig. 1 Cross-sectional view of anodized aluminum

[1] Honda Motor Co., Ltd.
E-mail: hideaki_miyashita@jp.honda
[2] Material Research Center

tens of nm. In addition, fine voids are also generated from gases and impurities in the aluminum material[2), (4)].

If porous holes and voids are present, moisture easily reaches the aluminum base material in a water-exposed environment, making it a challenge to obtain stable corrosion resistance. Therefore, corrosion resistance is enhanced by immersing the part in boiling water or nickel acetate solution, etc. after electrolysis to modify the surface of the oxide film into a hydroxide called boehmite by a hydration reaction, and applying sealing treatment to seal the porous holes and voids.

Previously, anodized aluminum often used A6061-T6 and AC4CH-T6 materials, which have fewer impurities, but use of recycled materials with greater amounts of impurities such as AC2B-T6 and ADC12-F materials is increasing, and anodizing treatment is increasingly applied to those materials.

However, when the corrosion resistance of anodized aluminum using various aluminum materials was actually evaluated, different anodizing treatment conditions and material composition resulted in different corrosion resistance, and there were cases where the target corrosion resistance could not be obtained. For this reason, the corrosion resistance of anodized aluminum has been evaluated and determined by subjecting the treated parts to long-term tests such as the cyclic corrosion test (CCT) and actual vehicle rust durability tests. However, these tests call for testing periods of tens of days to several months.

2. Development Goals

Figure 2 shows an example of observation of the vicinity of the barrier layer of a test piece using a transmission electron microscope (TEM). This test piece was made of A6063-T5 material, which is one of the A6000 series alloys that are said to have fewer impurities and more easily grow regular barrier and porous layers, and was anodized with oxalic acid.

The fine voids generated during electrolysis remain even after the sealing treatment, so it is presumed that moisture enters the interior through the gaps of these voids and porous holes and reaches the aluminum base material, producing corrosion of the anodized aluminum.

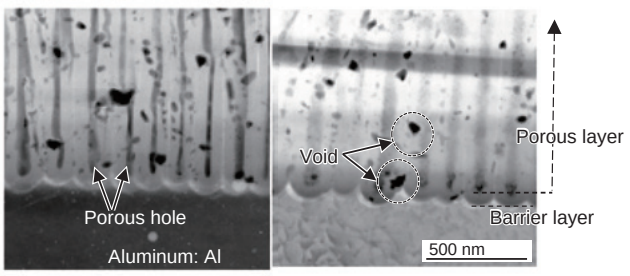


Fig. 2 Example of observation of anodized aluminum cross-section of A6063-T5 material using TEM

Although the state of the voids and porous holes can be observed by TEM, only a narrow range can be observed at one time, and it is not easy to grasp the state of the entire anodized aluminum layer. Therefore, focus was placed on electrochemical testing as a method to evaluate the structure of the entire anodized aluminum layer[(2)-(8)]. Takahashi et al.[(2)] stated that when a constant anode current is applied, the potential increases at a faster rate when there are smaller and fewer voids in the anodized aluminum, and more gradually as the size and number of voids increase. Therefore, it was thought that the constant current anodic polarization test could be used to evaluate the corrosion resistance of anodized aluminum, which is influenced by the size and number of voids.

3. Test Method

Anodized aluminum test pieces were fabricated using multiple aluminum materials. The potential behavior was measured by constant current anodic polarization tests, the rust occurred cycle was measured by CCT, and the relationship between the two was compared and evaluated.

3.1. Polarization Test

Figure 3 shows the polarization test device.

Current application and potential data recording used the HZ-7000 made by Meiden Hokuto Corporation.

The test piece was set so that it directly faced a platinum counter electrode at an interval of 10 mm as the anode, and the tip of a Luggin capillary into which the Ag/AgCl reference electrode was inserted was positioned between the two.

Past studies used a boric acid solution in many cases, but this test was conducted with the same 5% salt water as that used in the CCT test heated and held at 50°C in accordance with the corrosion test environment. After setting the test piece and holding for about 10 minutes, a constant anode current was applied, and the potential was measured every

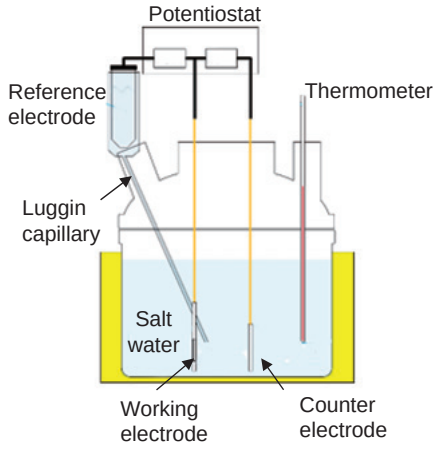


Fig. 3 Device of polarization test

0.01 seconds, which is the minimum measurement interval of the device. The anode current was set to 10 μA/cm^2 so as not to exceed the ±15V potential measurement range of the measuring instrument.

As the potential increases, some of the Al^{3+} and O^{2-} ions move from stable lattice positions to high-energy interstitial positions and the current flows more easily. As a result, a clear difference in potential behavior was observed immediately after current application[(2)], and the initial potential increase rate (IPIR) was calculated by dividing the potential difference between 0.01 and 0.02 seconds by the time difference.

3.2. Test Pieces

Table 1 shows the added content of the four types of materials evaluated in this study. Test pieces were fabricated with these materials under different anodizing treatment conditions and evaluated.

Figure 4 shows the test piece shape before anodizing treatment.

The entire surface was milled to help reduce differences in anodized aluminum quality due to different surface shapes, and an M5 screw hole was provided in one corner for connecting to the anode.

Figure 5 shows a test piece used for the polarization test. The anodized test piece was cut to a size of 45 × 45 mm, and the anodized aluminum in the part where the electrode rod was attached was peeled off with a router, etc.

Polyimide tape with a 30 × 30 mm range hollowed out was attached in the center, and a copper electrode rod with a resin-coated alligator clip was attached to the part where the anodized aluminum was peeled off.

After that, a Formed In Place Gasket (FIPG) was applied to areas except for the opening of the polyimide tape and dried at room temperature until it was no longer sticky as waterproofing.

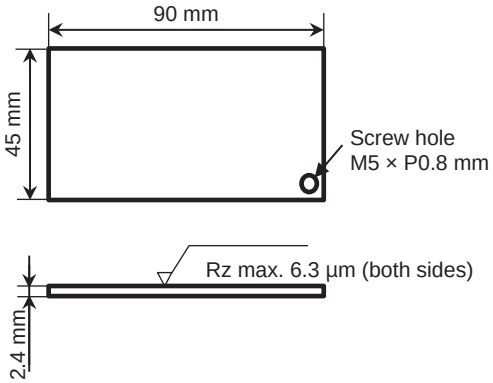


Fig. 4 Shape of aluminum test piece before anodizing treatment

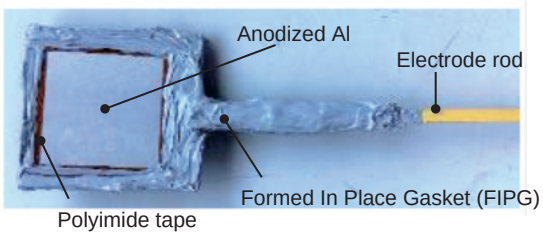


Fig. 5 Test piece for polarization test

Table 1 Added content of anodized Al materials

Material	Added content (wt%)				
	Cu	Si	Mg	Zn	Fe
ADC12-F	1.8	10.1	0.21	0.63	0.77
AC2B-T6	3.0	7.0	0.31	0.01	0.16
AC4CH-T6	0.02	6.9	0.33	0.004	0.08
A6061-T6	0.19	0.48	0.98	0.01	0.46

Table 2 Anodizing treatment conditions

No.	Electrolyte	Current density (A/dm^2)	Minimum thickness (μm)	Sealing treatment
1	Sulfuric acid	2.0	3.0	Nickel acetate
2			1.5	
3			8.0	
4			20.0	
5			3.0	None
6				Water
7	Oxalic acid	4.0		Nickel acetate

3.3. Anodizing Treatment Conditions

Table 2 shows the anodizing treatment conditions. When corrosion resistance is emphasized, the No. 1 condition is often selected: after degreasing and washing, electrolysis is performed in a sulfuric acid solution to provide a film thickness of at least 3 μm, and finally sealing treatment is performed with a nickel acetate solution. Therefore, using this as the basic condition, test pieces were fabricated with different electrolyte, film thickness, and sealing treatment.

The film thickness and sealing treatment were selected as evaluation parameters because they were thought to influence the time it took for salt water to enter the anodized aluminum layer and reach the aluminum base material. The film thickness was adjusted by the electrolysis time.

It is known that when oxalic acid is used as the electrolyte, the barrier layer and porous walls are thicker than when sulfuric acid is used, and it was thought that this could help reduce the impact of the voids and enhance corrosion resistance, so it was also selected as an evaluation parameter. In that case, the anodized aluminum does not grow at the same current density as with sulfuric acid, so electrolysis was performed with the current density changed to 4 A/dm^2.

After cutting and polishing the center part of the test

piece, it was observed with an optical microscope, and the film thickness of the thinnest part was used as the typical value.

3.4. Corrosion Test

The back surface and a range of about 5 mm around the outer circumference of the anodized test piece were masked with polyester tape, and the test piece was placed in the CCT tester so that it was 70 degrees to the horizontal. The CCT was conducted under Honda's original conditions of 24 hours per cycle combining salt spray, wet, dry, and keeping at low temperature, and the progress was observed.

The JIS H8679-1 Rating Number Method[9] was used to determine corrosion resistance, and the number of CCT cycles at which corrosion corresponding to a rating number (RN) of 9.8 occurred was set as the Rust Occurred Cycle (ROC).

4. Test Results and Discussion

4.1. Impact of Anodizing Treatment Conditions

The impact of anodizing treatment conditions on IPIR and ROC was verified using AC4CH-T6 material, which is often applied to aluminum wheels and power unit parts due to the ease in obtaining the anti-corrosion effects of anodized aluminum.

Figure 6 shows the constant current anodic polarization curves for No. 1, No. 5, and No. 7, which exhibited greatly different ROC.

The larger the ROC and the higher the corrosion resistance, the larger the slope of the initial potential increase, which suggests a faster IPIR.

Table 3 and Fig. 7 show the results of calculating the IPIR for each condition and comparing it with the ROC. IPIR and ROC were positively correlated for all samples with different anodizing treatment conditions, and results enabling evaluation of the corrosion resistance of anodized aluminum by the constant current anodic polarization method were obtained.

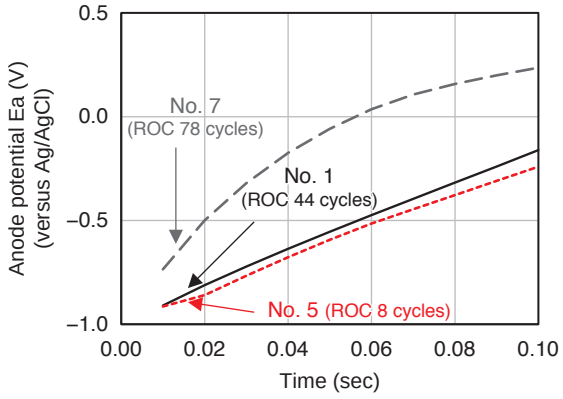


Fig. 6 Relationship between anode potential Ea and polarization time of No. 1, No. 5, and No. 7

Table 3 Evaluation results of AC4CH-T6 anodized test pieces

No	Differences from condition No. 1	IPIR (V/sec)	ROC (n)
1	—	9.4	44
2	Thin	6.6	11
3	Thick	13.9	60
4	Very thick	17.0	80
5	No seal	5.4	8
6	Boiling water seal	8.2	14
7	Using oxalic acid	17.2	78

Table 4 Evaluation results of each test piece under anodized condition No. 1

No.	Material	Subtotal of added content (wt%)	IPIR (V/sec)	ROC (n)
1	ADC12-F	13.51	3.9	5
2	AC2B-T6	10.48	7.1	20
3	AC4CH-T6	7.33	9.4	44
4	A6061-T6	2.12	18.3	72

4.2. Impact of Aluminum Material Composition

Test pieces were fabricated by anodizing ADC12-F, AC2B-T6, and A6061-T6 materials in the same manner as AC4CH-T6 material and evaluated.

Table 4 shows the relationship between the subtotal of added content, IPIR, and ROC for each material anodized under condition No. 1 in Table 2.

Figure 8 shows the relationship between IPIR and ROC. A positive correlation was observed between IPIR and ROC, and it was confirmed that the corrosion resistance of anodized aluminum differs greatly depending on the material composition even with the same anodizing treatment conditions.

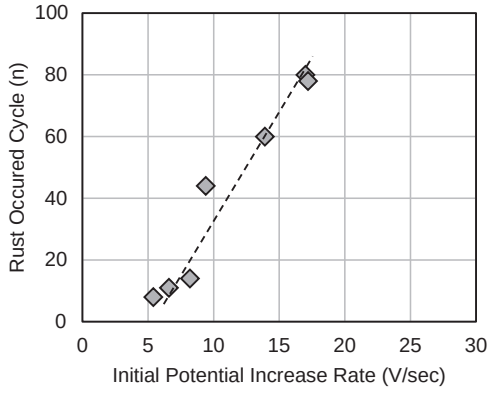


Fig. 7 Relationship between Rust Occurred Cycle and Initial Potential Increase Rate of anodized AC4CH-T6

Figure 9 shows the relationship between the amount of added content and IPIR. In this case, a negative correlation was observed between the amount of added content and IPIR.

Figure 10 shows the results of observation of the anodized aluminum cross section of A6061-T6 and ADC12-F materials using an optical microscope.

In the ADC12-F material, voids and Si that is thought to have remained in the anodized layer without dissolving during electrolysis are present at a level that can be confirmed even with an optical microscope. Si itself has high electrical resistance and does not allow current to flow easily, and it is thought that like voids, Si remaining as foreign matter in anodized aluminum lowers the quality of the anodized aluminum.

This showed that the reason why IPIR and ROC differ greatly depending on the aluminum material composition is that the added content not only forms voids but also exists as foreign matter in the anodized aluminum, and their impact can be evaluated by the constant current anodic polarization method.

This result is thought to show the validity of the estimation mechanism whereby the IPIR obtained by the constant current anodic polarization method is an indicator of the state of voids and foreign matter in anodized aluminum, and that moisture reaches the aluminum base material via those voids and foreign matter and corrosion occurs.

Figure 11 shows the relationship between IPIR and ROC for all anodized test pieces fabricated in this study. The larger the IPIR value, the larger the ROC, which confirmed a strong positive correlation.

From this, it was found that measurement of IPIR by the constant current anodic polarization method enables evaluation and estimation of the corrosion resistance of anodized aluminum regardless of differences in anodizing treatment conditions and material composition.

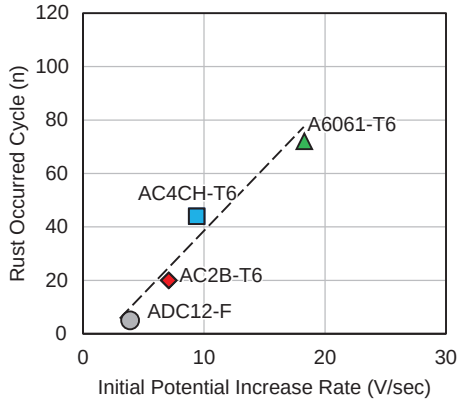


Fig. 8 Relationship between Initial Potential Increase Rate and Rust Occurred Cycle under condition No. 1

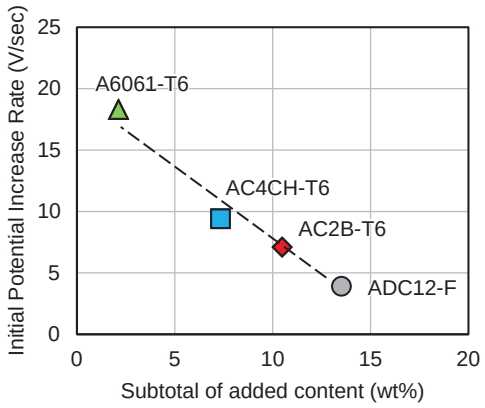


Fig. 9 Relationship between Initial Potential Increase Rate and subtotal of added content under condition No. 1

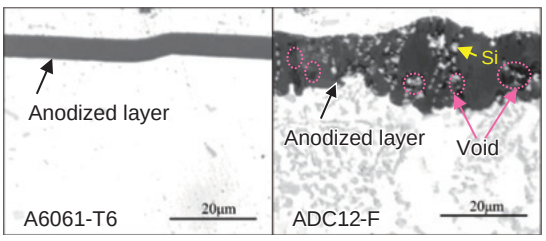


Fig. 10 Cross-sectional structure of A6061-T6 and ADC12-F test pieces anodized under condition No. 1

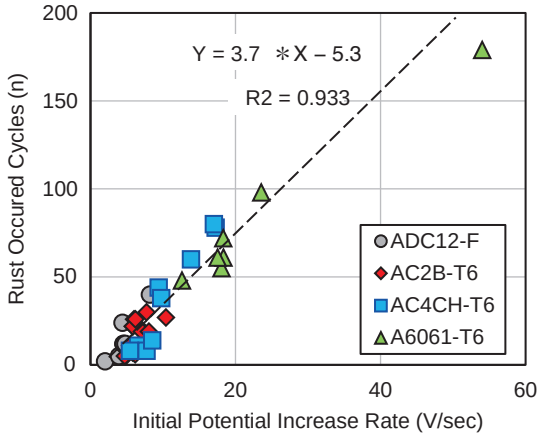


Fig. 11 Relationship between Initial Potential Increase Rate and Rust Occurred Cycle of all anodized test pieces

5. Conclusion

The following results were obtained by fabricating anodized test pieces from multiple aluminum materials under various conditions, and measuring, comparing, and verifying the potential behavior obtained by the constant current anodic polarization method and the rust occurred

cycle in CCT.

(1) When anodized aluminum is treated by constant current anodic polarization, the potential increase behavior immediately after current application changes according to differences in the aluminum materials and the anodizing treatment conditions.
(2) There is a strong positive correlation between the IPIR and the ROC in CCT, and the corrosion resistance of anodized aluminum can be estimated based on the differences in the anodizing treatment conditions and aluminum materials.
(3) The change in the IPIR showed that the factor lowering the corrosion resistance of anodized aluminum due to an increase in the amount of added content in aluminum materials is rooted in the change in the anodized aluminum structure.
(4) It was found that by measuring IPIR, the time needed to evaluate the corrosion resistance of anodized aluminum, which previously took up to several months, can be shortened to about one or two days. This enables determination of the specifications of anodizing treatment at an early stage.

References

(1) Committee on Cost of Corrosion in Japan, Japan Society of Corrosion Engineering, Japan Association of Corrosion Control: Cost of Corrosion in Japan, Zairyo-to-Kankyo, Vol. 69, No. 11, p. 283-306, (2020) (in Japanese)
(2) Takahashi, H., Fujiwara, K.: Electrochemical Analysis of Imperfections in Anodic Oxide Films on Aluminum, Hyomen Kagaku, Vol. 15, No. 7, p. 433-439, (1994) (in Japanese)
(3) Yamada, M., Kikuchi, T., Sakairi, M., Takahashi, H.: Breakdown of Anodic Oxide Films on Aluminum, Journal of The Surface Finishing Society of Japan, Vol. 58, No. 6, p. 331-336, (2007) (in Japanese)
(4) Ono, S.: Structure and Growth Mechanism of Anodic Oxide Films Formed on Aluminum and Their Gas Emission Property in Vacuum, Journal of the Vacuum Society of Japan, Vol. 52, No. 12, p. 637-644, (2009) (in Japanese)
(5) Masuda, T.: Anodo Sanka Porasu Arumina no Bisai Kozo Hyouka to Netsu shori ni yoru α- Arumina Menburen no Sakusei, Doctoral dissertation of Kogakuin University, 145p., (2015) (in Japanese)
(6) Asoh, T., Ono, S.: Fundamental Technology that Support Functionalization of Alumite, Journal of The Surface Finishing Society of Japan, Vol. 65, No. 9, p. 406-413, (2014) (in Japanese)
(7) Takahashi, H., Kumagai, H., Nagayama, M.: Estimation of the Microstructure of Anodic Porous Oxide Films on Aluminum by the Pore-filling Method I. Analysis of Film Structure Formed by Two-Step Anodizing, Journal of the Metal Finishing Society of Japan, Vol. 36, No. 11, p. 478-482, (1985) (in Japanese)
(8) Ono, S., Masuko, N.: Dissolution behavior of the barrier layer of porous anodic films formed on aluminum studied by pore-filling technique, Journal of Japan Institute of Light Metals, Vol. 43, No. 9, p. 447-452, (1993) (in Japanese)
(9) JIS H 8629-1: Anodizing of aluminium and its alloys --Rating system for the evaluation of pitting corrosion-- Part 1: Rating number method, (2013)

Author


Hideaki MIYASHITA


Kohei TOMITA


Yuki YAMAGUCHI


Takahiro KUWABARA

Automated Test Scheduling Using Vehicle Routing Problem Methodology

Atsushi ARISAKA[1] Takeshi MIYAZAKI[1] Kazuki FUKUI[2]

ABSTRACT

In order to shorten the development period and help reduce development costs for new vehicle models, a method for automated scheduling of actual vehicle tests was devised that helps to minimize the number of test vehicles and calculate the shortest test schedule. Use of mathematical optimization methodology for collision test scheduling and use of the vehicle routing problem solution in particular in mathematical optimization methodology for function test scheduling enabled incorporation of the constraints into the automated calculations to be considered. Simple applications were created and verified using the applications with a spreadsheet software. As a result, a scheduling task that previously took an expert 90 hours could be accomplished in 6 hours.

1. Introduction

Continuing advances in technologies such as CAE and performance design technology are enabling theoretical examination of many performance items[(1)-(3)]. In addition to enhancing performance, automakers are also working to shorten development periods and use fewer test vehicles in order to suppress development costs.

However, it is not easy to estimate all performances, and some items are required by law to be confirmed using actual vehicles, and thus confirmation tests with actual vehicles are conducted prior to mass production.

The number of confirmation tests continues to rise due to tightening of laws and regulations and the diversification of specifications and equipment such as destinations, engines, transmissions, and control.

Confirmation tests using collision test facilities (hereinafter, collision tests) and performance confirmation tests that do not use collision test facilities (hereinafter, function tests) have been conducted with different vehicles.

However, in order to use fewer test vehicles, there are demands to use vehicles that have undergone function tests in collision tests.

Furthermore, adjustment of collision test facilities is becoming an issue in collision tests due to increasing numbers of models being developed at the same time, and adjustment of schedules is becoming an issue in function tests due to restrictions on the timing and order of various confirmation items.

Therefore, the test schedule is prepared in advance, all the function and collision tests are assigned to the test facilities and test vehicles, and whether the tests can be completed within the set time period (hereinafter, test deadline) is examined.

However, in actual vehicle development, some 1000 confirmation tests are conducted with around 50 test vehicles even for a full model change with relatively few variations, and testers often make individual requests for some function tests. As a result, it takes two weeks to a month for even an experienced person to create a test schedule, and test scheduling is an issue in new model development.

In existing studies, some methods have been reported to automatically create the shortest collision test schedule by giving the number of test vehicles, the number of confirmation tests, and the number of days and the order needed for each test as constraints[(4), (5)].

These methods use the mathematical optimization methodology in Operations Research (OR) to create a test schedule automatically. Figure 1 shows an example of a schedule for conducting four collision tests and some function tests with seven test vehicles.

In these methods, simple conditions can be considered such as conducting tests A and D first, but function tests cannot be conducted using the same vehicles after collision tests, and thus it is necessary to plan the function test schedule with different test vehicles.

In addition, complex conditions need to be considered in

[1] Honda Motor Co., Ltd.

E-mail: atsushi_arisaka@jp.honda

[2] FLECT Co.,Ltd.

function tests, such as tests that need to be conducted first, tests with a decided order among multiple tests, and tests with timings that can be consolidated to shorten the test period.

This makes it a challenge to automatically create an overall schedule that includes function tests in addition to collision tests in actual development.

Therefore, this study examined a method to automatically create the shortest test schedule that takes into account all the tests, using the number of collision test facilities and the number of test vehicles as conditions for calculation, and given the respective numbers of collision tests and function tests, the number of days needed for each test, and the test order.

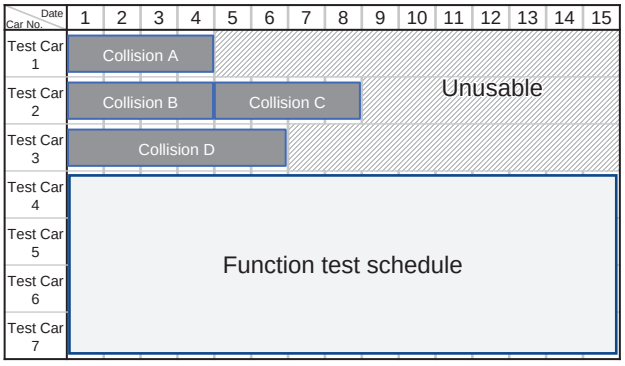


Fig. 1 Example of collision and function test schedule

2. Scheduling of Collision Tests

2.1. Helping Prevent Test Overlap

Multiple tests cannot be conducted at the same time with the same test vehicle. Therefore, the constraint to prohibit overlap of the periods of the tests conducted on each test vehicle is expressed by Eq. (1).

$$\text{Non-overlap}\left(\{I(s_t, P_t, x_{t,v})\}_{t\in\mathcal{T}}\right), \forall v \in \mathcal{V} \qquad (1)$$

where $I(s, P, x)$ is an interval variable representing the period of the number of test days P from the test start time s, t is the test, s_t is a variable representing the start date and time of test t, P_t is a constant representing the number of test days of test t, $x_{t,v}$ is a binary variable that is 1 when test t is conducted with test vehicle v and 0 otherwise, $\mathcal{T}$ is the set of tests, and $\mathcal{V}$ is the set of test vehicles. Non-overlap$(\cdot)$ is a special constraint called a global constraint[6], which does not permit overlap of the given interval variables.

This constraint helps to prevent multiple tests from being assigned to a single test vehicle at the same time.

2.2. Setting the Test Start Timings

Some tests can be conducted immediately after the test vehicle is assembled, whereas others cannot be conducted until the necessary parts are ready.

If the date and time that test vehicle v becomes available is assumed to be the delivery date Q_v, Q_v needs to satisfy the following equation.

$$x_{t,v} = 1 \Rightarrow s_t \geq Q_v, \qquad \forall t \in \mathcal{T}, \qquad \forall v \in \mathcal{V} \qquad (2)$$

The symbol "$\Rightarrow$" in Eq. (2) represents the logical implication, and the constraint on the right side is satisfied when test t is assigned to test vehicle v, as indicated by the left side. In other words, this means that the start date and time of test t should be the delivery date and time of test vehicle v or later.

The constraint for the case that the test cannot be conducted unless the parts are ready is expressed by the following equation.

$$s_t \geq R_t, \qquad \forall t \in \mathcal{T} \qquad (3)$$

where R_t is a constant representing the time that test t can be started, and sets information such as the date and time that facilities become available and the date and time that the parts needed for the test are delivered.

These constraints enable setting of the timing at which the test can be started.

2.3. Consideration of Test Vehicle Damage

Some tests cannot be conducted using vehicles that have been damaged in other collision tests.

First, the constraint expressed by the following equation is added to achieve consistency among decision variables.

$$x_{t,v} = 1 \Rightarrow w_t = v, \qquad \forall t \in \mathcal{T}, \qquad \forall v \in \mathcal{V} \qquad (4)$$

where w_t is a variable expressing the test vehicle assigned to test t.

Equation (4) indicates that when test t is assigned to test vehicle v, that test vehicle is set to w_t. Furthermore, by setting the constraint of Eq. (5), if tests t_1 and t_2 are to be conducted with the same test vehicle, t_2 can only be performed before t_1 in which the vehicle is damaged.

$$w_{t_1} = w_{t_2} \Rightarrow s_{t_2} + P_{t_2} \leq s_{t_1} \qquad (5)$$

With these constraints, the damage condition of the test vehicles can be considered before assigning another test.

2.4. Optimization of Number of Test Vehicles

Equation (6) expresses the objective function representing the sum of the penalties in order to use the fewest test vehicles possible.

$$\min \sum_{v\in\mathcal{V}} C_v^V u_v \qquad (6)$$

$$x_{t,v} \le u_v, \qquad \forall t \in \mathcal{T} \tag{7}$$

where C_v^V represents the penalty constant applied when test vehicle v is used in a collision test, and u_v is a binary variable that indicates whether test vehicle v was used in the collision test. The value of u_v is 1 if the vehicle v is used in the collision test and 0 otherwise. Under the constraint of Eq. (7), if any collision test is assigned to test vehicle v, u_v = 1 and the penalty in Eq. (6) becomes larger.

The above objective function and constraint enable helping to minimize the number of test vehicles.

2.5. Consideration of Test Deadlines

In order to use fewer test vehicles, it is desirable to conduct as many tests as possible with a single test vehicle before the test deadlines. This is achieved by setting an object function Eq. (8) that considers the test deadline.

$$\min \sum_{t \in \mathcal{T}} C_t^T o_t \tag{8}$$

$$s_t + P_t \le D_t + o_t, \qquad t \in \mathcal{T} \tag{9}$$

where C_t^T is a constant representing the penalty applied for the delay of test t from its test deadline, D_t is a constant representing the deadline for test item t, and o_t is a variable representing the delay of test t from its deadline.

Under the constraint of Eq. (9), the delay of each test is expressed as o_t. Equation (8) helps to minimize the total delay, enabling assignment of all the tests within the deadlines.

2.6. Order of Each Collision Test

Collision tests include tests such as for occupant protection, safety equipment, and low-speed collision, and these tests are conducted in a certain order. When conducting tests in that order, it is also necessary to set intervals of a certain time period or more, as shown by U in Fig. 2.

Therefore, the constraint expressed by Eq. (10) was added to provide an interval between the nth test t_n and the (n+1)th test t_{n+1}.

$$s_{t_n} + U_{t_n,t_{n+1}} \le s_{t_{n+1}} \tag{10}$$

where $U_{t_n,t_{n+1}}$ is a constant representing the length of the interval provided between the nth test t_n and the (n+1)th test t_{n+1}, as shown in Fig. 2.

This condition enabled to fix the order of each collision test with the necessary intervals.

2.7. Consideration of Capacity of Collision Test Facilities

The capacity of collision test facilities is limited, making it necessary to establish an upper limit on multiple tests using the same resources simultaneously.

Therefore, considering the total number of facilities to be used as a constraint results in Eq. (11).

$$\text{Cumulative}\left(\{I(s_t, P_t, 1)\}_{t \in \mathcal{T}_g}, L_g\right), \qquad \forall g \in G \tag{11}$$

Cumulative($\{I_t\}_t$,L) is a constraint that upper bounds the overlap of the interval variables given by $\{I_t\}_t$ to L.

Here, G is the set of resources, and $\mathcal{T}_g \subset \mathcal{T}$ is the set of test items that use the resources $g \in G$.

While general resources can by expressed by Eq. (11), most collision test schedules consist of the three processes of preparation, hit, and post-process, as shown in Fig. 3. For this reason, the period occupying the collision test facilities is one day in the test duration. Assuming that up to two hits can be conducted in a single day, the constraint of Eq. (11) is specialized as shown in Eq. (12).

$$\text{Cumulative}\left(\{I(s_t + P_t^{\text{Prep}}, P_t^{\text{Hit}}, 1)\}_{t \in \mathcal{T}}, 2\right) \tag{12}$$

where P_t^{Prep} is Preparation in Fig. 3 and represents the preparation period of test t, and P_t^{Hit} is Hit in Fig. 3 and represents the collision test period.

Addition of this constraint enabled consideration of the capacity of test facilities.

2.8. Preserving Time for Function Tests

When using the same test vehicles in both collision and function tests, the function tests cannot be conducted after the collision test, making it necessary to conduct them before the collision test.

To achieve this, it is necessary to make the period r_t in

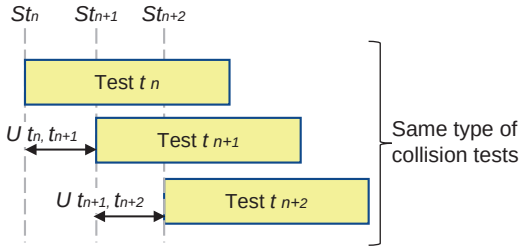


Fig. 2 Sequence of collision tests and start-time offsets

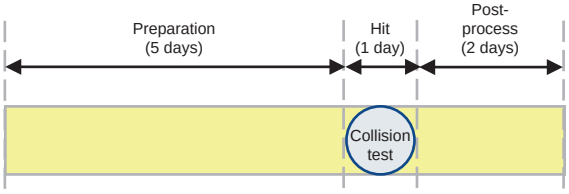


Fig. 3 Schedule for front collision tests

Fig. 4 smaller and shift the test completion time as much as possible toward the test deadline to increase the number of days available for the function tests before the collision tests. Therefore, the objective function and constraint expressed by Eq. (13) and Eq. (14) were set.

$$\min \sum_{t \in \mathcal{T}} C_t^R r_t \tag{13}$$

$$D_t - s_t - P_t \leq r_t, \qquad \forall t \in \mathcal{T} \tag{14}$$

where D_t is the test deadline, r_t is a variable representing the reduction in the number of days available for other tests due to test t, and P_t is the duration of test t. In addition, C_t^R is a constant representing the penalty for the reduction in the number of days available for other tests.

This objective function and constraint enable assignment of the collision tests to help maximize the number of days available for the function tests before the collision tests.

Consideration of the above constraints and the objective functions in the developed OR model enabled automated collision test scheduling that preserves time for function tests such as shown in Fig. 5.

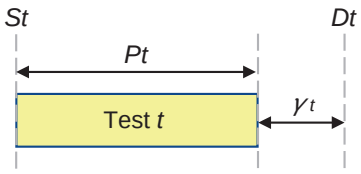


Fig. 4 Reduction of vehicle-days due to collision tests

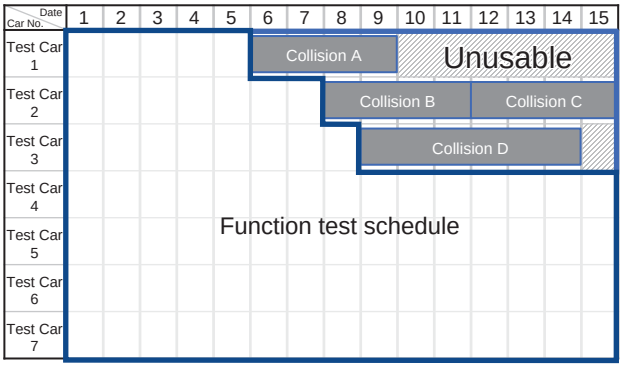


Fig. 5 Example of collision test schedule with days available for function tests

3. Scheduling of Function Tests

3.1. Approach

The task of assigning performance tests one by one to each test vehicle is thought to be similar to selecting the path on the transition network of test items conducted on a certain test vehicle, as shown in the upper part of Fig. 6.

For example, by interpreting Start and End in Fig. 6 as nodes that represent the start and end of test vehicle usage and other nodes as test items, the path through the nodes from the Start node to the End node on this network can be seen as a test schedule such as shown in the lower part of Fig. 6.

The size of the penalty for each transition is set when considering this network. For example, in the case of transition within the same test category such as the transition from Test A to Test B in Fig. 7, there is no test vehicle handover work, and thus a smaller penalty is set. However, if the test category differs such as the transition from Test A to Test C or D, a larger penalty is set.

Use of this approach to find a test schedule that efficiently allocates each test to the test vehicles was found to be similar to the Vehicle Routing Problem (VRP) [7], which is a mathematical optimization method that determines the route to be taken by a delivery vehicle to complete delivery by the size of the total penalty. Therefore,

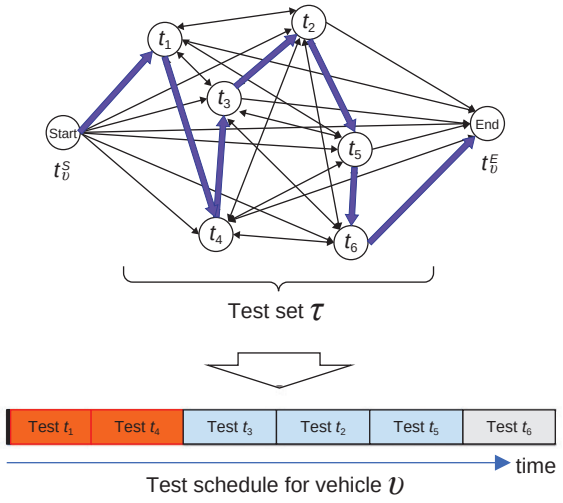


Fig. 6 Correspondence between test network and test schedule

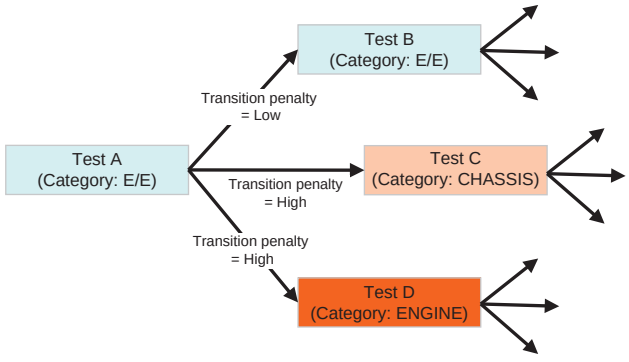


Fig. 7 Transition penalties

as a new approach, some fast solving methods for VRP were incorporated into function test scheduling.

3.2. Helping Prevent Test Overlap

Like the collision tests, multiple function tests cannot be conducted at the same time with a single test vehicle.

Equations (15) and (16) are constraints indicating that the transition is necessarily from a single test to another single test on the test network from the first test to the last test. Each test need to appear only once on the transition path from the first test to the last test on the test network.

$$\sum_{a \in \mathcal{A}_t^O} y_a = 1, \qquad \forall t \in \mathcal{T} \cap \{t_v^S\}_{v \in \mathcal{V}} \tag{15}$$

$$\sum_{a \in \mathcal{A}_t^I} y_a = 1, \qquad \forall t \in \mathcal{T} \cap \{t_v^E\}_{v \in \mathcal{V}} \tag{16}$$

where $\mathcal{A}_t^O$ is the set of directed links from the test t node, $\mathcal{A}_t^I$ is the set of directed links to the test t node, y_a is a binary variable that is 1 if passing through link a and 0 otherwise, t_v^S represents the start node of vehicle v, and t_v^E represents the end node of vehicle v.

This condition enables helping to prevent test overlap.

3.3. Setting the Test Start Times

Equations (17) to (20) express the passage of dates and times that tests are conducted and are constraints representing the consistency of the time change from the first test to the last test.

$$y_{(t_v^S, t)} = 1 \Rightarrow s_t \geq Q_v, \qquad \forall t \in \mathcal{T}, \qquad \forall t \in \mathcal{T} \tag{17}$$

$$y_{(t_1, t_2)} = 1 \Rightarrow s_{t_1} + P_{t_1} \leq s_{t_2}, \qquad \forall t_1, t_2 \in \mathcal{T} \tag{18}$$

$$y_{(t, t_v^E)} = 1 \Rightarrow s_t + P_t = e_v, \qquad \forall t \in \mathcal{T}, \qquad \forall v \in \mathcal{V} \tag{19}$$

$$y_{(t_v^S, t_v^E)} = 1 \Rightarrow e_v = Q_v, \qquad \forall v \in \mathcal{V} \tag{20}$$

where Q_v is the delivery time of vehicle v, and e_v is a variable representing the time at which vehicle v usage ends.

Of these, Eq. (17) is the constraint that the tests can be conducted only after delivery.

The above constraints enabled defining the start of the tests.

3.4. Consideration of Damage

It is not possible for some tests to be conducted after a collision test or after a function test in which the vehicle is damaged. First, the constraints of Eq. (21) to Eq. (23) define the consistency between the flow of the test vehicle on the test network and the variable w_t that represents the assignment of the test vehicle to the test t.

$$y_{(t_v^S, t)} = 1 \Rightarrow w_t = v, \qquad \forall t \in \mathcal{T}, \forall v \in \mathcal{V} \tag{21}$$

$$y_{(t, t_v^E)} = 1 \Rightarrow w_t = v, \qquad \forall t \in \mathcal{T}, \forall v \in \mathcal{V} \tag{22}$$

$$y_{(t_1, t_2)} = 1 \Rightarrow w_{t_1} = w_{t_2}, \qquad \forall t_1, t_2 \in \mathcal{T} \tag{23}$$

The above equations and the aforementioned Eq. (5) enable consideration of damage to test vehicles in test execution.

The above basic VRP constraints that define the test vehicle transitions between tests and the consistency of time[8] enable assignment of all the tests to all the test vehicles, in consideration of helping to prevent test overlap, test start dates and times, and damaged test vehicles.

3.5. Handling of High-Priority Tests

Some function tests need to be performed as early as possible, including those that impact other test conditions such as aerodynamic tests, and those that impact other tests such as initial confirmation of engine performance.

The objective function and constraint expressed by Eq. (24) and Eq. (25) were set to conduct such high-priority tests as early as possible. Here, $\mathcal{T}^P$ is the set of high-priority tests, C_t^P is a constant representing the penalty applied for the delay of the start time of high-priority test t, B_t is a constant representing the earliest start time for high-priority test t, and o_t^P is a variable representing the difference between the start time s_t of high-priority test t and the earliest available start time B_t.

$$\min \sum_{t \in \mathcal{T}^P} C_t^P o_t^P \tag{24}$$

$$s_t - B_t \leq o_t^P \tag{25}$$

This objective function and constraint enable assignment of high-priority tests as early as possible.

3.6. Handling of Tests with a Decided Order

Some tests are conducted in a certain order such as Tests J and K in Fig. 8. For example, driving performance tests may be performed after making the suspension settings. In these cases, the order in which two tests t_1 and t_2 are conducted can be specified by precedence constraint of Eq. (26).

$$s_{t_1} + P_{t_1} + M_{t_1, t_2} \leq s_{t_2} \tag{26}$$

where M_{t_1, t_2} is a constant representing the time period between test t_1 and test t_2.

Furthermore, when it is necessary to conduct tests t_1 and t_2 with the same test vehicle, the constraint of Eq. (27) is added.

$$w_{t_1} = w_{t_2} \tag{27}$$

Equations (26) and Eq. (27) enable assignment of consecutive tests to the same test vehicle.

3.7. Enhancing Efficiency by Consecutive Same Category Tests

As mentioned above, when the category that uses a test vehicle switches, additional workload is incurred for test vehicle handover between different categories. Therefore, the same test vehicle should be consecutively assigned to tests in the same category as much as possible. This corresponds to "Same category tests" in Fig. 8.

For this purpose, the objective function of Eq. (28) was set so that the proper penalty for the selection of transitions between tests is set to achieve the least switching between categories.

$$\min \sum_{a \in \mathcal{A}} C_a^A y_a \tag{28}$$

where $a = (t,t') \in \mathcal{A}$ is the set of directed links representing the transition from test t to test t', and C_a^A is a constant representing the penalty incurred with the test transition represented by directed link a.

Less switching between categories can be achieved by setting the above objective function.

3.8. Test Completion Within the Deadline

All tests should be scheduled to be completed within the test deadlines. However, due to the large number of tests and the many constrains, not all tests may fit, and the initially planned test deadline may be exceeded as shown in Fig. 9.

In order to achieve the smallest total of the delay of each test from the test deadline, a condition to achieve the earliest overall end time was added to the objective function that considers the completion deadline of Eq. (8) which was also considered in the collision tests.

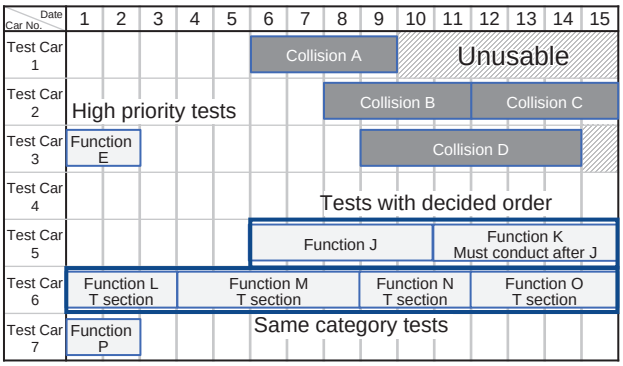


Fig. 8 Arrangement of function tests

$$\min \max\{e_v\}_{v \in \mathcal{V}} \tag{29}$$

This results in the earliest completion of all tests.

The VRP method was incorporated into function test scheduling, the basic VRP constraints that define the test vehicle transitions between tests and the consistency of time were set, and constraints and objective functions specific to function tests were added. This enabled automated function test scheduling that satisfies the conditions for function test transitions.

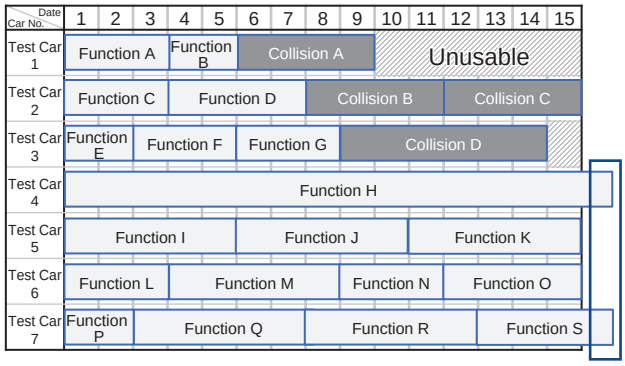


Fig. 9 Example of schedule exceeding deadline

4. Verification

When actually performing calculations, it is necessary to give the necessary conditions, create an input/output function to check the calculation results, and create applications to execute the mathematical optimization calculations for OR and VRP.

To this end, spreadsheet software was used in the input/output interface to enable description of the test vehicle information, test information, and information of the conditions related to the test schedule.

It was decided to create two different applications for OR and VRP using a popular programming language. The programming language was the commonly used Python, and the calculations were executed with a computer (Xeon Platinum 8000 Series, clock frequency: 3.6 GHz, memory: 8 GB).

Figure 10 shows an example of the calculation result.

This is an example of a full model change with relatively few variations, but even so, 45 test vehicles and 931 tests are scheduled.

It previously took 90 hours or more for an expert to manually create such a test schedule, but when calculated on a computer with the aforementioned specifications, test scheduling could be accomplished in about 6 hours.

The calculation time is thought to vary depending on the number of test vehicles and the number of tests. However, as shown in Fig. 11, it was confirmed that automation of

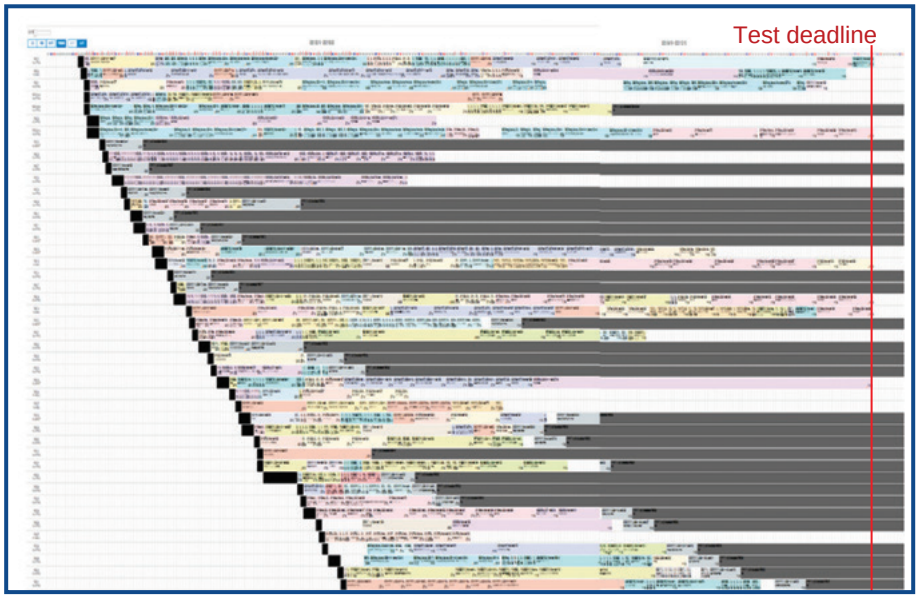


Fig. 10 Calculation result

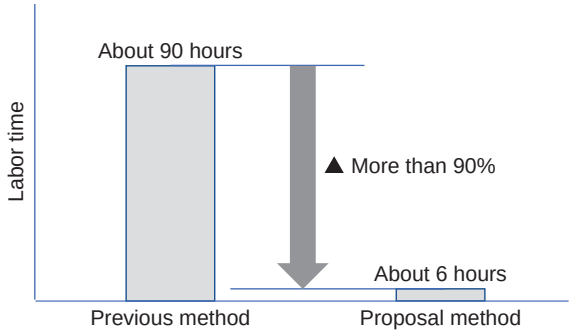


Fig. 11 Comparison between previous scheduling time and proposal scheduling time

test scheduling by the mathematical optimization methods of OR and VRP shortens the calculation time by 90% or more compared with manual scheduling by an expert.

5. Conclusion

This study examined a method to automatically create the shortest test schedule, using the number of collision test facilities and the number of test vehicles as conditions for calculation, and given the respective numbers of collision tests and function tests, the number of days needed for each test, and the test order. The results are summarized below.

(1) A method was established that incorporates the mathematical optimization methods of OR and especially VRP to automatically create the shortest test schedule.

(2) Definition of the constraints and objective functions of collision tests by the OR method enabled automated collision test scheduling that preserves time for function tests.

(3) Definition of basic VRP constraints that define the test vehicle transitions between tests and the consistency of time, and constraints and objective functions that represent the conditions between function tests enabled automated function test scheduling.

(4) In order to verify automated test scheduling, automated test scheduling applications that consider all the test conditions of the collision tests and function tests were created.

(5) Automated test scheduling was performed using existing vehicle model data and information, and it was confirmed that the scheduling time was shortened by 90% or more.

References

(1) Toyoshima, T., Matsuzawa, T., Ito, K., Endo, Y., Takano, H., Ushimura, T.: Development of Chassis Performance Design Technologies for MBD of Mass-production Vehicles, Honda R&D Technical Review, Vol. 29, No. 1, p. 52-62

(2) Fujimoto, S., Tojo, K., Kusunoki, S., Saito, T.: Proposal of Development Process Using DSM and Simulation, Honda R&D Technical Review, Vol. 29, No. 1, p. 106-116

(3) Yasuhara, S., Yoshimoto, T., Okada, H.: Modeling and Utilizing Expert's Knouwledge, Experience, and Thinking in Automobile Development, Honda R&D Technical Review, Vol. 32, No. 2, p. 91-98

(4) Reich, D., Shi, Y., Epelman, M., Cohn, A., Barnes, E.,

Arthurs, K., Klampfl, E.: Scheduling Crash Tests at Ford Motor Company, Interfaces, Vol. 46, No. 5, p. 365-462, (2016), doi: 10.1287/inte.2016.0855
(5) Shi, Y., Reich, D., Epelman, M., Klampfl, E., Cohn, A.: An analytical approach to prototype vehicle test scheduling, Omega, Vol. 67, p. 168-176, (2017), doi: 10.1016/j.omega.2016.05.003
(6) Beldiceanu, N., Carlsson, M., Rampon, J-X.: Global Constraint Catalog, HAL, 1406p., (2005), https://hal.science/hal-00485396
(7) Braekers, K., Ramaekers, K., Nieuwenhuyse, I. V.: The vehicle routing problem: State of the art classification and review, Computers & Industrial Engineering, Vol. 99, p. 300-313, (2016), doi: 10.1016/j.cie.2015.12.007
(8) El-Sherbeny, N. A.: Vehicle routing with time windows: An overview of exact, heuristic and metaheuristic methods, Journal of King Saud University - Science, Vol. 22, Issue 3, p. 123-131, (2010), doi: 10.1016/j.jksus.2010.03.002

■ Author ■


Atsushi ARISAKA


Takeshi MIYAZAKI


Kazuki FUKUI

Honda R&D Co., Ltd.
Honda R&D Technical Review Editorial Committee

Material Research Center, Honda R&D Co., Ltd.
Innovative Research Excellence, Honda R&D Co., Ltd.
Innovative Research Excellence, Power Unit & Energy, Honda R&D Co., Ltd.
Solution System Development Center, Honda R&D Co., Ltd.
Motorcycle and Power Product Operations, Honda Motor Co., Ltd.
Automobile Development Center / BEV Development Center, Honda Motor Co., Ltd.

Editorial Afterword

Thank you for reading Honda R&D Technical Review Vol. 37 to the end. I wish to extend my congratulations and gratitude to the authors and everyone else who worked hard to produce it.

Over the past 25 years, it has been my honor to be involved in peer reviewing this journal, both as an editorial committee member and chairman of the Innovative Research Excellence, Power Unit & Energy within the editorial committee. In all that time, I have always kept one thought in particular in mind: the knowledge that research papers outlive their authors.

When I wrote my first paper, a senior colleague told me: "Your research paper will outlive you, so you should write it carefully." At first, I thought he was exaggerating. But as the years have passed, I've felt more and more the import of his words. With each issue, over 800 copies of this journal are distributed not just within Honda, but also to corporations, universities, libraries, and other institutions. It is also made available to the public online. The National Diet Library permanently archives books, research papers, and other works published in Japan. Naturally, the Honda R&D Technical Review is one of these.

The technology and results of the authors are thus communicated widely to future generations, and I have pursued the peer preview process with a keen awareness of its significance. For those writing a paper for the first time, responding to the comments of the peer review can be an onerous task. But the skills that the author acquires in bringing a paper to completion are invaluable, and difficult to acquire any other way. It is always my hope that such skills become great assets in the authors' future careers.

As we navigate this era of once-in-a-century transformation, Honda's technological fields are expanding dramatically, and the pace of technological innovation is ever accelerating. It is my hope that this journal will bring your technology to the world, build a broader network of engineers and researchers around the world, and contribute to further research and development.

Hiromi MATSUURA

©2025 Honda R&D Co., Ltd. (All rights reserved)

ISSN 1881-6223

Published by:
Honda R&D Co., Ltd.
1-4-1, Chuo Wako-shi, Saitama-ken,
351-0193, Japan

Edited by:
Honda R&D Co., Ltd.
Honda R&D Technical Review Editorial Committee

Printed:
Mar. 1, 2025

Honda R&D Co., Ltd.